Searching for Brown Dwarf Companions

November 2008

Avril C. Day-Jones

A report submitted in partial fulfillment of the requirements of the University of Hertfordshire for the degree of Doctor of Philosophy.

Abstract

In this thesis I present the search for ultracool dwarf companions to main sequence stars, subgiants and white dwarfs. The ultracool dwarfs identified here are benchmark objects, with known ages and distances.

The online data archives, the two micron all sky survey (2MASS) and SuperCOSMOS were searched for ultracool companions to white dwarfs, where one M9±1 companion to a DA white dwarf is spectroscopically confirmed as the widest separated system of its kind known to date. The age of the M9±1 is constrained to a minium age of 1.94Gyrs, based on the estimated age of the white dwarf from a spectroscopically derived $T_{\rm eff}$ and log g and an initial-final mass relation. This search was extended using the next generation surveys, the sloan digital sky survey (SDSS) and the UK infrared deep sky survey (UKIDSS), where potential white dwarf + ultracool dwarf binary systems from this search are presented. A handful of these candidate systems were followed-up with second epoch near infrared (NIR) imaging. A new white dwarf with a spectroscopic M4 companion and a possible wide tertiary ultracool component is here confirmed.

Also undertaken was a pilot imaging survey in the NIR, to search for ultracool companions to subgiants in the southern hemisphere using the Anglo-Australian telescope. The candidates from that search, as well as the subsequent follow-up of systems through second epoch NIR/optical imaging and methane imaging are presented. No systems are confirmed from the current data but a number of good candidates remain to be followed-up and look encouraging.

A search for widely separated ultracool objects selected from 2MASS as companions to Hipparcos main-sequence stars was also undertaken. 16 candidate systems were revealed, five of which had been previously identified and two new L0±2 companions are here confirmed, as companions to the F5V spectroscopic system HD120005 and the M dwarf GD 605. The properties of HD120005C were calculated using the DUSTY and COND models from the Lyon group, and the age of the systems were inferred from the primary members. For GD 605B no age constraint could be placed due to the lack of information available about the primary, but HD120005C has an estimated age of 2-4Gyr.

In the final part of this thesis I investigate correlations with NIR broadband colours ($J-H$, $H-K$ and $J-K$) with respect to properties, $T_{\rm eff}$, log g and [Fe/H] for the benchmark ultracool dwarfs, both confirmed from the searches undertaken in this work and those available from the literature. This resulted in an observed correlation with NIR colour and $T_{\rm eff}$, which is presented here. I find no correlation however with NIR colours and log g or [Fe/H], due in part to a lack of suitable benchmarks. I show that despite the current lack of good benchmark objects, this work has the potential to allow UCD properties to be measured from observable characteristics, and suggest that expanding this study should reveal many more benchmarks where true correlation between properties and observables can be better investigated.

Acknowledgments

I would like to extend a thank you to all the people who have provided help and support throughout my Ph.D. no matter how large or small, your help was always appreciated.

I firstly need to thank my supervisors David Pinfield, Hugh Jones and Ralf Napiwotzki for their constant support and help with every aspect of the Ph.D, for their patience and understanding and for teaching me the skills needed to succeed.

I could also not have done this Ph.D. without the support, both emotionally and financially from all of my immediate and extended family.

I also owe a very big thank you to James Jenkins, who helped me with many scientific and computing aspects throughout my Ph.D, as well as his tireless support, encouragement, motivation and constant belief in me throughout.

I would also like to thank my fellow students and inhabitants of Starlink for their help, support and hundreds of cups of tea over the last 3 years, with a special thanks to Bob Chapman, Stuart Folkes, Douglas Weights and Krispian Lowe for all their many hours of help with IDL, IRAF and LATEX.

I also extend a thank you to the staff and grad students at Penn State University, who made it possible for me to work there during the summer of 2008 and for the fantastic experience I had while I was there.

I also owe thanks to Harriet Parsons, Simon Weston, Andy Gallagher and Joanna Goodger for providing a temporary roof and their sofas/floors for the last months of my write up.

Thank You to you all!

I would like to dedicate this thesis to my grandmother Joyceline Pay, who passed away during the last weeks of writing this thesis, I know she would have been proud to see it come to fruition.

Contents

1 Background **17**

1.1 Introduction 17

1.1.1 Properties of brown and ultracool dwarfs 18

1.2 Benchmark ultracool dwarfs 23

1.2.1 Ultracool formation scenarios 24

1.3 The ultracool IMF and birthrate 26

1.3.1 The substellar initial mass function 26

1.3.2 The substellar birth rate 28

1.3.3 Ultracool evolution 30

1.4 Understanding and interpretation of ultracool atmospheres 31

1.4.1 Atmospheric models 32

1.4.2 Benchmark UCDs as members of binary systems 35

1.4.3 Stellar evolution beyond the main-sequence 37

1.5 Motivation and thesis structure 43

2 Selection Techniques **45**

2.1 Selecting white dwarfs 46

2.1.1 White dwarfs in SuperCOSMOS 46

2.1.2 White dwarfs in SDSS 47

2.2 Selecting ultracool dwarfs 50

2.2.1 L dwarfs in 2MASS 50

2.2.2 L and T dwarfs in UKIDSS 52

3 Ultracool companions to white dwarfs **57**

3.1 Selecting candidate binary pairs . . . 57

3.2 Searching SuperCOSMOS and 2MASS . . . 58

3.2.1 Proper motions of candidate systems . . . 62

3.3 A wide WD + UCD binary . . . 63

3.3.1 Spectral classification of UCDc-1: 2MASSJ0030-3739 . . . 63

3.3.2 Spectral classification of WDc-1: 2MASSJ0030-3740 . . . 68

3.3.3 A randomly aligned pair? . . . 72

3.3.4 Binary age . . . 73

3.3.5 UCD properties . . . 74

3.4 Searching SDSS and UKIDSS . . . 74

3.4.1 Simulated numbers of WD + UCD binaries . . . 74

3.4.2 Binary selection . . . 76

3.4.3 Candidate WD + UCD systems . . . 79

3.4.4 Second epoch imaging and proper motion analysis of candidate UCDs 81

3.4.5 A candidate wide L dwarf companion to a spectroscopic WD + M dwarf binary . . . 94

3.5 Summary of chapter . . . 100

4 Ultracool companions to Subgiants **101**

4.1 A pilot survey of southern Hipparcos subgiants . . . 101

4.1.1 Selection of subgiants . . . 101

4.1.2 Simulated populations . . . 102

4.2 The pilot survey . . . 104

4.2.1 Observing strategy . . . 107

4.2.2 Extraction and calibration of photometry . . . 107

4.2.3 Selection of good candidate systems . . . 111

4.3 Follow-up Observations . . . 114

4.3.1 Second epoch imaging . . . 117

4.3.2 Methane imaging . . . 119

4.4 Discussion . . . 124

5 Ultracool companions to main-sequence stars **127**

5.1 Selection of Hipparcos main-sequence + UCD wide binary systems 127

5.2 Spectroscopic follow-up observations 131

5.2.1 Reduction and extraction of data 131

5.3 Spectral classifications 134

5.3.1 Cand 13 134

5.3.2 Cand 10 136

5.4 Parameters of the systems 139

5.4.1 Gl605 139

5.4.2 HD120005 141

5.5 Discussion 142

6 Further discussion and conclusions **145**

6.1 The ultracool mass-age distribution 145

6.2 The current benchmark population 146

6.2.1 Open clusters and moving groups 150

6.2.2 UCDs in binaries 157

6.2.3 Field UCDs 164

6.3 Discussion 166

6.3.1 The effects of gravity and metallicity on observed UCD properties . 170

6.3.2 Correlations with colour and physical properties 172

6.4 Future Work 182

List of Figures

1.1 Optical spectra of an M9, L3 and L8 types from Kirkpatrick et al. (1999). . 20
1.2 NIR spectra of M7-L2 dwarfs from Reid et al. (2001). 21
1.3 NIR spectra of L3.5-L8 dwarfs from Reid et al. (2001). 21
1.4 NIR spectra of T dwarfs from Burgasser et al. (2003). 22
1.5 Main-sequence mass function from Miller & Scalo (1979). 27
1.6 Pleiades mass function from Lodieu et al. (2007) 29
1.7 Bolometric luminosity functions from Allen et al. (2005). 30
1.8 Comparison of $\Phi(T_{\rm eff})$ for different birth rate scenarios from Burgasser et al. (2004). 31
1.9 Cooling tracks for brown dwarfs, stars and planets taken from Burrows et al. (1997). 32
1.10 Hertzsprung-Russell diagram 36
1.11 Cooling tracks for DA WDs from Chabrier et al. (2000). 41
1.12 The initial-final-mass-relation for WDs from Dobbie et al. (2006). 41

2.1 A reduced proper motion diagram of WD candidates from SuperCOSMOS 48
2.2 A reduced proper motion diagram of WDs from SDSS DR2 from Kilic et al. (2006). 50
2.3 A $u-g$ against $g-r$ two colour diagram of WDs selected from SDSS (DR6) 51
2.4 A $J-H$ against $H-K$ two colour diagram of L dwarfs from DWARFARCHIVES.ORG. 53
2.5 A $Y-J$ against $J-H$ two colour diagram showing L and T dwarf selection regions. 55

3.1 A WD M_B against $B-R$ absolute colour-magnitude diagram for McCook & Sion (1999) WDs with known parallax. 59
3.2 Separation area probed by 2MASS and SuperCOSMOS for WD + UCD binaries. 60

3.3 An M_J against $J-K$ absolute colour-magnitude diagram showing companion UCD candidates. 62

3.4 SuperCOSMOS and 2MASS images show UCDc-1 (2MASSJ0030 − 3739) and WDc-1 (2MASSJ0030 − 3740). 64

3.5 J- band spectra of UCDc-1 (2MASSJ0030 − 3739) 66

3.6 H- band spectra of UCDc-1 (2MASSJ0030 − 3739) 66

3.7 Optical spectrum of the confirmed white dwarf WDc-1 (2MASSJ0030−3740). 69

3.8 Model atmosphere fit to the Balmer lines of 2MASSJ0030 − 3740. 71

3.9 Simulated WD + UCD J- against g- magnitude diagram from Pinfield et al. (2006) 76

3.10 A WD M_g against $g-r$ colour-magnitude diagram for McCook & Sion (1999) WDs with known parallax 77

3.11 A UCD colour-magnitude diagram for L and T dwarfs with known parallax from DWARFARCHIVES.ORG. 78

3.12 Left: $i-z$ against spectral type relation. Right: $z-J$ against spectral type relation from Hawley et al. (2002). 80

3.13 Colour-colour relations for M, L and T dwarfs from Hawley et al. (2002).. . 80

3.14 Left: A $Y-J$ against $J-H$ two-colour diagram. Right: An M_J against $J-H$ CMD of UCD candidate components of potential wide WD + UCD binaries. 82

3.15 A $u-g$ against $g-r$ two colour diagram showing WD candidate components of potential wide WD + UCD binaries. 83

3.16 SDSS spectra of the WD candidate nBIN7. 95

3.17 Model DA4 WD SDSS spectra combined with M0-L0 spectra. 97

3.18 Model DA5 WD SDSS spectra combined with M0-L0 spectra. 98

3.19 Model DA4 WD SDSS combined with an M4 spectra. 99

3.20 M4 component of the convolved spectra of nBIN7. 99

4.1 Subgiant selection.(a) An M_V against $B-V$ diagram of Hipparcos stars with $V < 13.0$ and $\pi/\sigma \geq 4$. (b) Theoretical isochrones from Girardi et al. (2000) for solar metallicity. 103

4.2 Simulated distance - magnitude distribution of UCD companions to Hipparcos subgiants from Pinfield at al. (2006). 105

4.3 Predicted separation-distance distribution of subgiant + UCD binaries. . . 106

4.4 A diagram showing the imaging strategy used for the subgiant survey on AAT/IRIS2. 108

4.5 An airmass curve for standard star observations. 110

4.6 A $J-H$ against Δ magnitude plot showing the zero point calibration using 2MASS objects for the J- band for one IRIS2 imaging field. 111

4.7 A plot of magnitude against the difference in flux between two aperture sizes in the J- band for objects in one image. 112

4.8 A $J-H$ against $Y-J$ two-colour diagram, showing the position of main sequence stars, M, L and T dwarfs. 114

4.9 Left: A $J-H$ against $Z-J$ two-colour diagram, showing candidate L and T dwarfs. Right: A M_J against $J-H$ CMD of L and T dwarf candidates. 115

4.10 Plot from Tinney et al. (2005) showing the position of the methane filters; CH_4s and CH_4l. 120

4.11 A CH_4s-CH_4l colour against spectral type plot from Tinney et al. (2005).121

4.12 A CH_4s-CH_4l against CH_4s CMD for Cand T18. 123

5.1 Top: M_J against $J-K$ CMD for candidate L dwarf companions to Hipparcos stars. Bottom: A distance - separation plot for the candidate main-sequence + L dwarf binary systems. 129

5.2 A vector point diagram of four candidate main sequence + L dwarf common proper motion systems. 131

5.3 The ZJ spectrum of Cand 13. 132

5.4 The HK spectrum of Cand 13. 133

5.5 The HK spectrum of Cand 10. 133

5.6 The ZJ spectrum of Cand 13 overplotted with template spectra (M7, M8, M9, L0.5, L1 and L2 type) from Cushing, Rayner & Vacca (2005). 137

5.7 The HK spectrum of Cand 13, overplotted with template spectra (M7, M8, M9, L0.5, L1 and L2 type) from Cushing, Rayner & Vacca (2005). 138

5.8 The HK band spectrum of Cand 10, overplotted with template spectra (M7, M8, M9, L0.5, L1 and L2 type) from Cushing, Rayner & Vacca (2005).140

6.1 Simulations of the UCD mass-age population from Pinfield et al. (2006) for 2MASS and UKIDSS. 147

6.2 Simulations of the UCD mass-age population from Pinfield et al. (2006) for UCD companions to WDs and subgiants. 148

6.3 The mass-age distribution of benchmark UCDs from the literature and both confirmed and candidate objects presented in this work 167

6.4 $T_{\rm eff}$ against log g for benchmark UCDs taken from the literature and both confirmed and candidate objects presented in this work. 168

6.5 $T_{\rm eff}$ against Fe/H for benchmark UCDs taken from the literature and both confirmed and candidate objects presented in this work. 169

6.6 M_J against $J-K$ colour space showing the dependence of metallicity and gravity on models from Burrows et al. (2006) for their COND and DUSTY models. 173

6.7 $T_{\rm eff}$ against $J-K$ space predictions of the DUSTY and COND models from Burrows et al. (2006). 173

6.8 Left: M_J as a function of spectral type and Right: M_J as a function of $J-K$ colour for L and T dwarfs from Knapp et al. (2004). 174

6.9 $T_{\rm eff}$ against colour plot of benchmark L dwarfs with NIR $J-H$, $H-K$ and $J-K$ colours. 175

6.10 $T_{\rm eff}$ against colour plot of benchmark T dwarfs with NIR $J-H$, $H-K$ and $J-K$ colours. 175

6.11 Colour against log g, where the colour-$T_{\rm eff}$ trend has been subtracted from the colour, for benchmark L dwarfs with NIR $J-H$, $H-K$ and $J-K$ colours. 177

6.12 Colour against log g, where the colour-$T_{\rm eff}$ trend has been subtracted from the colour, for benchmark T dwarfs with NIR $J-H$, $H-K$ and $J-K$ colours. 177

6.13 Colour against Fe/H, where the colour-$T_{\rm eff}$ trend has been subtracted from the colour, for benchmark L dwarfs with NIR $J-H$, $H-K$ and $J-K$ colours. 178

6.14 Colour against Fe/H, where the colour-$T_{\rm eff}$ trend has been subtracted from the colour, for benchmark T dwarfs with NIR $J-H$, $H-K$ and $J-K$ colours. 178

6.15 Improved $T_{\rm eff}$ against colour plot, where the effects of log g and Fe/H have been removed for the benchmark L dwarfs with NIR $J-H$, $H-K$ and $J-K$ colours. 181

List of Tables

1.1 The classification scheme for WDs from Sion et al. (1983). 40

2.1 Galactic co-ordinates of contaminated and overcrowded regions removed. . 52

3.1 Candidate UCD + WD binary systems from SuperCOSMOS and 2MASS. 61

3.2 Estimated spectral types for 2MASSJ0030 − 3739. 68

3.3 Fit results and derived quantities for WD mass, cooling age and absolute magnitude for 2MASSJ0030 − 3740. 70

3.4 Parameters of the binary 2MASSJ0030 − 3739 + 2MASSJ0030 − 3740 and its components. 75

3.5 Parameters of the WD component of the WD + UCD binary candidates with optical counterparts selected from SDSS and UKIDSS. 84

3.6 Parameters of the UCD component of the WD + UCD binary candidates with optical counterparts selected from SDSS and UKIDSS. 85

3.7 Parameters of the WD component of the WD + late M dwarf binary candidates selected from SDSS and UKIDSS. 86

3.8 Parameters of the UCD component of the WD + late M dwarf binary candidates selected from SDSS and UKIDSS. 87

3.9 Parameters of the WD component of the WD + UCD i- band drop out binary candidates selected from SDSS and UKIDSS. 88

3.10 Parameters of the UCD component of the WD + UCD i- band drop out binary candidates selected from SDSS and UKIDSS. 89

3.11 Parameters of the WD component of the WD + UCD non-optical detection binary candidates selected from SDSS and UKIDSS. 90

3.12 Parameters of the UCD component of the WD + UCD non-optical detection binary candidates selected from SDSS and UKIDSS. 92

3.13 Proper motion analysis for followed up candidate WD + UCD binary pairs from SDSS and UKIDSS 94

4.1 Candidate subgiant + UCD binary systems. 116

4.2 Proper motion measurements of candidate L and early T dwarfs. 119
4.3 The status of UCD candidates (confirmed or not). 126

5.1 Widely separated main sequence + L dwarf candidate systems. 130
5.2 Spectral ratios for Cand 13 135
5.3 Equivalent widths for Cand 13 135
5.4 Spectral ratios for Cand 10 139
5.5 Parameters of the system HD12005 143

6.1 Subgiant + UCD candidates with age and mass constraints estimated from the Lyon group DUSTY and COND models. 151
6.2 Main-sequence + UCD Candidates with known ages and masses derived from the Lyon group DUSTY and COND models. 152
6.3 Cluster and Moving Group UCDs. 155
6.4 Pleiades cluster UCDs. 156
6.5 UCD in binaries 161
6.6 UCD + WD binaries 163
6.7 Field UCDs with age estimates 165
6.8 Parameters of fitting equations for colours of T dwarfs. 180
6.9 Parameters of fitting equations for colours of L dwarfs. 180

Chapter 1

Background

.

In this chapter the background knowledge relevant to the later chapters in this thesis is discussed. In brief the main topics here include an overview of the understanding and interpretation of ultracool dwarf (UCD) and brown dwarf (BD) atmospheres, formation scenarios, the ultracool contribution to the initial mass function and the birth rate of L and T dwarfs are also discussed in context. A particular emphasis is given to benchmark UCDs, why they are needed, how they will be used and where they can be found.

1.1 Introduction

In just over a decade nearly 700 UCDs have been discovered since those that were first confirmed (Tiede 1 (M8); Rebolo, Zapatero-Osorio & Martin 1995 and Gliese 229B (T6.5); Nakajima et al. 1995). This is in large thanks to the rise of deep large area surveys such as the Two Micron All Sky Survey (2MASS), the Sloan Digital Sky Survey (SDSS) and more recently the UK Infrared Deep Sky Survey (UKIDSS). These populations have helped shape the understanding of ultracool dwarfs and extended the classification system for substellar objects including the creation of two new spectral types L and T. The latest M dwarfs (∼M7-9) have effective temperature ($T_{\rm eff}$) reaching down to ∼2300K. At lower $T_{\rm eff}$ (∼2300-1400 K) are the L dwarfs, which have very dusty upper atmospheres and generally very red colours. T dwarfs are even cooler having $T_{\rm eff}$ in the range ∼1400-600 K, where the low $T_{\rm eff}$ limit is currently defined by the recently discovered T8+ dwarfs, ULAS J0034-0052 (Warren et al. 2007), CFBDS J005910.90-011401.3 (Delorme et al. 2008) and ULAS

1335 (Burningham et al. 2008). T dwarf spectra are dominated by strong water vapour and methane bands, and generally appear bluer in the near infrared (NIR) (Geballe et al. 2003; Burgasser, Burrows & Kirkpatrick 2006).

The physics of ultracool atmospheres is complex and very difficult to accurately model. Atmospheric dust formation is particularly challenging for theory (Allard et al. 2001; Burrows, Sudarsky & Hubeny 2006) and there are a variety of other important issues that are not well understood, including the completeness of CH_4/H_2O molecular opacities, their dependence on $T_{\rm eff}$, gravity and metallicity (e.g. Jones et al. 2005; Burgasser et al. 2006; Liu, Leggett & Chiu 2007), as well as the possible presence of vertical mixing in such atmospheres (Saumon et al. 2007). The emergent spectra from ultracool atmospheres are likely strongly affected by factors such as gravity and metallicity (e.g. Knapp et al. 2004; Burgasser et al. 2006; Metchev & Hillenbrand 2006), which highlights the need for an improved understanding of such effects if physical properties (e.g. mass, age and composition) are to be constrained observationally (e.g. spectroscopically).

Discovering UCDs whose properties can be inferred indirectly (without the need for atmospheric models) is an excellent way to provide a test-bed for theory and observationally pin down how physical properties affect spectra. Such UCDs are referred to as 'benchmark' objects (e.g. Pinfield et al. 2006). A population of benchmark UCDs with a broad range of atmospheric properties will be invaluable in the task of determining the full extent of spectral sensitivity to variations in UCD physical properties. However, such benchmarks are not common and the constraints on their properties are not always particularly strong.

1.1.1 Properties of brown and ultracool dwarfs

BDs were first theorised by Kumar (1963) as a cool extension of the main-sequence, beyond the M7 type. They are not massive enough to ignite or burn hydrogen in their core, such that an upper mass limit would correspond approximately to $0.075M_{\odot}$ (Chabrier et al. 2000a), although it is possible for this limit to change with metallicity (if the BD is metal poor then it can have a larger mass). The lower end of the mass limit remains ill defined approaching the planetary mass regime. The difference between BDs and giant planets is commonly assumed to be the way in which they form. It was originally suspected that BDs form in the same way as stars, from the fragmentation of a gas cloud (as shown by the simulations of Bate 1998) and that giant planets form via accretion onto rocky cores

in a proto-planetary disk (e.g. Pollack et al. 1996). However the formation mechanisms for both types of object are not fully understood. The currently adopted lower mass limit is taken from the deuterium burning minimum mass ($0.013M_{\odot}$), which draws the distinction that all BDs burn deuterium at some point during their lifetime. However Bate (2005) showed that the minimum mass (i.e. the deuterium burning limit) of a BD can change by 3-9 M_{Jup} from simulating clouds where the opacity limit is set by the clouds metallicity, such that metallicity can drive this mass up towards $0.015M_{\odot}$. This has also been challenged more recently by the discovery of planetary mass objects in Orion (Lucas et al. 2006; Weights et al. 2008) and 2MASS1207B, an $8\pm2M_{Jup}$ L dwarf (Mohanty et al. 2007).

For ages of a few Gyr, these masses correspond to temperatures generally less than ∼2300K (Kirkpatrick et al. 1999b) encompassing two new spectral classifications, the L and T dwarfs (Kirkpatrick et al. 1999b; Martín et al. 1999). Traditionally spectral typing is done using optical spectra as is typically done for L dwarfs, following the conventions of Kirkpatrick et al. (1999b). However, as L dwarfs are faint at these wavelengths it is often easier to use NIR spectra. Indeed T dwarfs are very faint in the optical and are thus formally classified in the NIR following the classification scheme of Burgasser et al. (2006). In general L and T dwarfs are BDs but objects later than ∼M7 can be referred to as UCDs. From an M dwarf a UCD is expected to cool and evolve through the L to the T dwarf sequence and to cooler temperatures (Kirkpatrick et al. 1999b).

L dwarfs

L dwarfs have temperatures between ∼2300-1400K, such that the peak of their flux is more red-ward than main-sequence stars. Their spectra tend to exhibit strong H_2O absorption, along with metal-oxide (TiO and ViO), metal (CaH and FeH) and alkali band (Na, K, Cs, Rb) features, which along with the effects of low temperature cause opacities which redden their colours. GD 165B, a companion to a white dwarf (Becklin & Zuckerman 1988) is often taken as the prototype L dwarf. Shown in Fig. 1.1 is an example of the spectra of late M through to L dwarfs at optical wavelengths, highlighted are some of the identifying features specifically of L dwarfs, including water vapour and alkali metal lines. Fig 1.2 and 1.3 show the NIR spectrum of late M and L dwarfs, where it can clearly be seen that for later L types the spectra around 1.5 μm becomes much more enhanced.

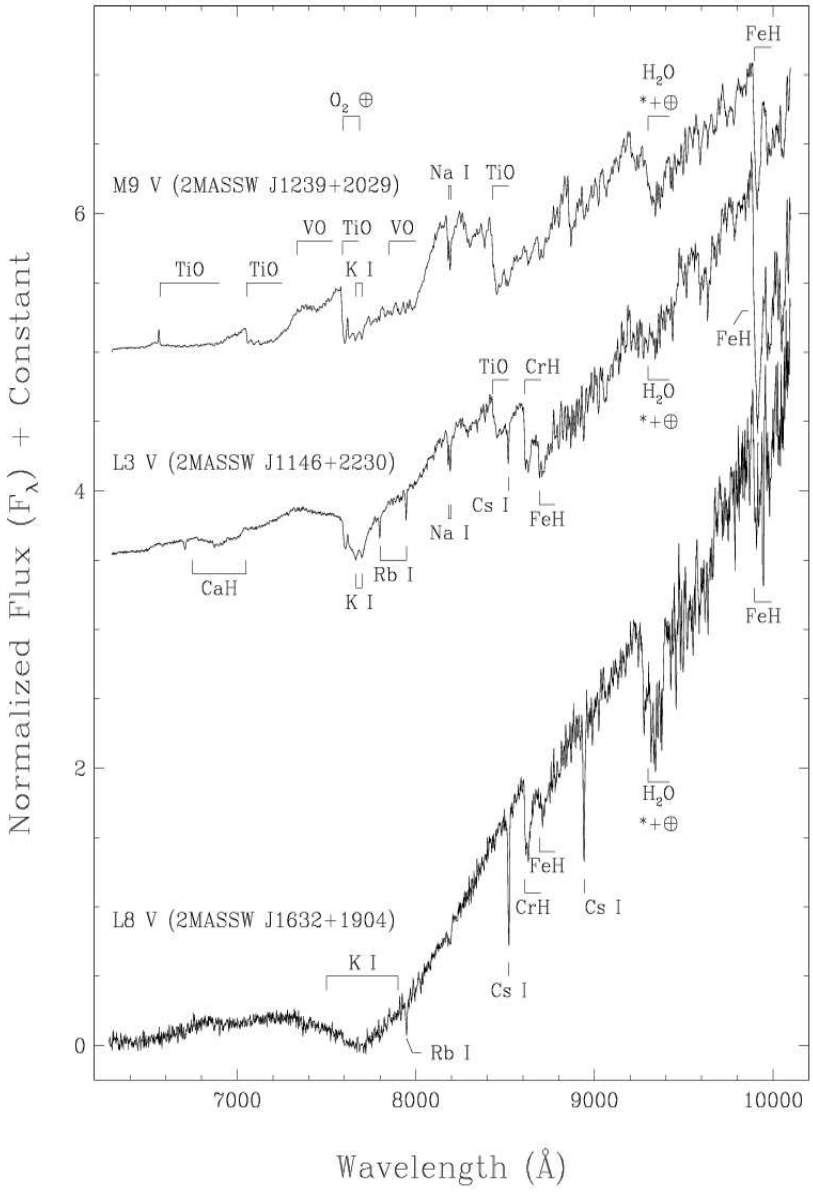

Figure 1.1: Optical spectra of an M9, L3 and L8 type, showing water vapour and alkali metal features from Kirkpatrick et al. (1999).

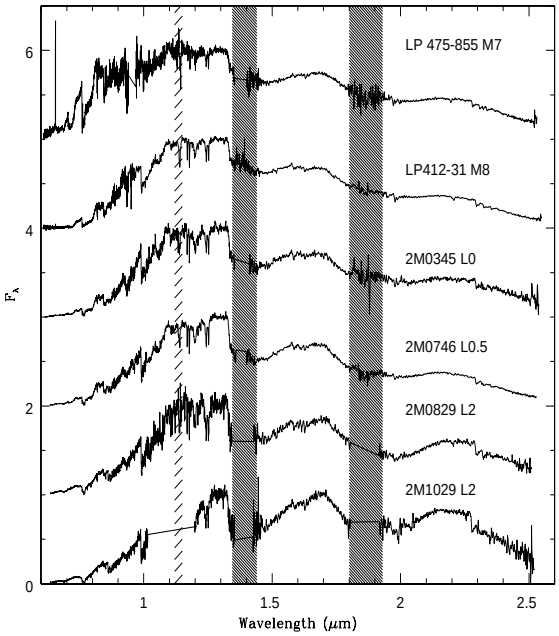

Figure 1.2: NIR spectra of M7-L2 dwarfs from Reid et al. (2001). The shaded regions show areas affected by terrestrial water vapour absorption. Refer to Figs. 1.1 and 1.4 for spectral features.

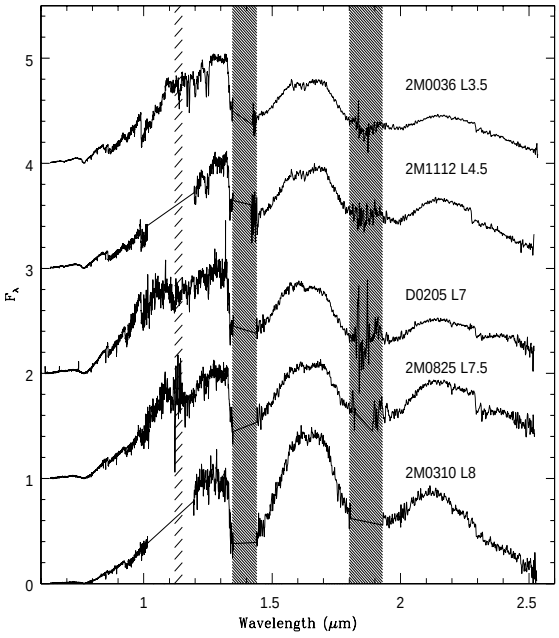

Figure 1.3: NIR spectra of L3.5-L8 dwarfs from Reid et al. (2001). The shaded regions show areas affected by terrestrial water vapour absorption. Refer to Figs. 1.1 and 1.4 for spectral features.

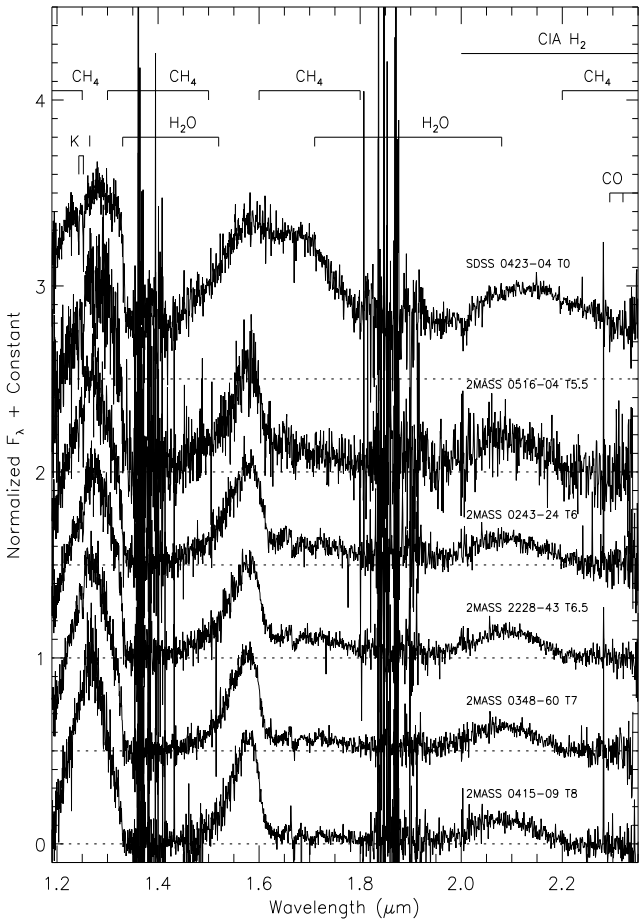

Figure 1.4: NIR spectra of T dwarfs from Burgasser et al. (2003).

T dwarfs

T dwarfs are cooler than Ls, with a typical range in temperature of ∼1400-600K or cooler (Burningham et al. 2008), where their spectra become dominated by CH_4 absorption. At these temperatures the FeH bands seen in L dwarfs disappear. T dwarfs develop much bluer NIR colours as the dust layers present themselves below the photosphere, such that the effects of dust reddening in L dwarfs no longer occur. Also noticeable is the strong absorption of H_2O and CH_4. Like GD 165B, Gl 229B, one of the first confirmed BDs is taken as the prototype T dwarf. Examples of T dwarf spectra are shown in Fig. 1.4, where the H_2O and CH_4 features are indicated.

These spectral classifications are further split into sub-classes of L0-L9 and T0-T9. These classifications are based mainly on the strength of the CH_4 and H_2O absorption and employ flux comparisons to determine a dwarfs position within the sub-classification scheme. Band passes of determined widths are centred on features of interest and regions of slope, their integrated fluxes determined and then compared with relations between these bandpass flux estimates of known spectral type, e.g. Geballe et al. (2003) use four regions in the NIR spectra, centred at 1.15 and 1.50μm (H_2O features) and 1.60

and 2.20μm (CH_4 features). More recently other features such as FeH are also used to generate more accurate relations within the L and T sub-classes (Slesnick, Hillenbrand & Carpenter 2004). Another method is to use the equivalent widths of the potassium lines at $\sim$1.18μm (Reid et al. 2001a). For the very late T dwarfs that are now being discovered (ULAS J0034-0052 Warren et al. 2007 and CFBDS J005910.90-011401.3 Delorme et al. 2008) a further spectral class beyond T will be needed. Pre-emptively coined 'Y-dwarfs' by Kirkpatrick et al. (1999b) they are expected to be characteristically different from T dwarfs. Such changes may result from the emergence of ammonia absorption in the NIR, or effects due to the condensation of water clouds at $\sim$400K (similar to those seen in Jupiter).

1.2 Benchmark ultracool dwarfs

There is no official criteria for what constitutes a benchmark UCD in the literature, other than the fact that it has some known properties. In the context of this thesis however, benchmark UCDs are those that have a known age. This parameter is vitally important for the understanding of UCD properties and how they evolve with time. Currently it is not possible to calculate the age of an isolated UCD in the field (with the exception of very young objects that show lithium in their spectra) as models are not yet robust enough for this prediction. Benchmark UCDs are thus vital to the calibration of such models and are likely to be the testbeds for interpreting UCD atmospheric effects, which could lead to the accurate prediction of physical properties from observable characteristics. Potentially a UCD with an indicated age constraint is likely to be useful, when considering overall trends. These are discussed in the later chapters of this thesis, where all known UCDs with an age estimate are presented. However, if the age of the UCD is not very accurate then the associated properties may not be particularly useful for calibrating models. The ideal benchmark UCD should have an age accurate to 10% (Pinfield et al. 2006). These benchmarks are the subject of the searches in this thesis. Where such benchmarks may be found, as well as the application for the use of such benchmarks are described in the following sections.

1.2.1 Ultracool formation scenarios

The formation of UCDs is still not well understood, but it is likely that they form initially like stars (core collapse and accretion) but never acquire enough mass to ignite stable hydrogen burning, only burning deuterium for a limited period of time, such that their formation may take a slightly different course to those of normal stars. Briefly described here are the four main types of theorised formation mechanisms, these include formation by turbulent fragmentation, disc fragmentation, photo-erosion and ejection.

Turbulent Fragmentation

Formation of UCDs via turbulent fragmentation was first proposed by Padoan & Nordlund (2002), who suggested that very low-mass cores could be formed during the process of fragmentation in a turbulent cloud, which would then go on to produce very low-mass objects. Their simulations show that turbulent flows commonly gives rise to variations in the mass density distribution allowing substellar mass cores to be dense enough to collapse and form UCDs.

Disk Fragmentation

It may also be possible for UCDs to form from initially massive prestellar cores via fragmentation of a large circumstellar disk (Bate, Bonnell & Bromm 2003). Whitworth & Goodwin (2005) state that this theory could be possible for large disks ($\sim$1000AU) where the separation between the two components is relatively large ($\geq$100AU), but would not work for stars with smaller disks, where the temperature and surface density are higher, such that the photo-fragments (small forming cores) are unable to cool fast enough to condense out to form a UCD in the disk. This formation mechanism may also explain the $'$brown dwarf desert$'$ (the observed trend where UCDs are not found at separations of $<$ 5AU from a main-sequence star binary companion Grether & Lineweaver 2006) as UCDs formed in this fashion must have large separations. Whitworth & Stamatellos (2006) also support this theory of formation but suggest that a massive enough circumstellar disk is likely to be rare and short-lived, converting into UCDs quickly on a dynamical timescale of only $\sim 10^4$yr.

Ejection

The theory of UCD formation through embryo ejection or liberation was first suggested by Reipurth & Clarke (2001). They postulated that UCDs form from prestellar cores that are ejected from dynamically interacting multiple systems before they have had time to accrete enough mass to ignite hydrogen. UCDs formed in this manner would exhibit no kinematic imprint and are likely to be found as isolated objects, as shown in the simulations of Bate et al. (see http://www.ukaff.ac.uk/starcluster). This formation mechanism also requires a large amount of initial formation by fragmentation and core collapse to produce the protostellar embryo that is ejected from the system. It cannot however explain the large number of close UCD binaries that have been observed (Pinfield et al. 2003).

Photo-erosion

The fourth formation mechanism is the theory of photo-erosion, whereby UCDs form in the presence of a higher mass star embedded in a HII region. The higher mass object causes compression waves and an ionisation front that photo-erodes surrounding low mass cores. This theory produces UCDs for a wide range of initial conditions and predicts close UCD binaries. However, the process is inefficient as it requires a massive protostellar core to be eroded to form a single UCD, and can only work in the presence of an OB type star to produce the high levels of UV needed for this formation mechanism to work (Whitworth & Goodwin 2005).

None of the methods outlined here can, by themselves predict all the observed dynamics of UCDs (the numbers of isolated and both close and wide binary systems) and it seems likely that a combination of these mechanisms is responsible for at least some of the UCDs discovered to date, possibly being dependent on environment, epoch and metallicity, as reflected by collective UCD properties that are seen by observations. Indeed Goodwin & Whitworth (2007) favour a combination of formation scenarios, suggesting that UCDs are initially binary companions formed by gravitational fragmentation of the outer parts ($R > 100$ AU) of the protostellar disc of a low-mass hydrogen-burning star. These are then gently disrupted by passing stars, rather than violent interaction as suggested by Reipurth & Clarke (2001). UCDs formed in this way would have velocity dispersions and spatial distributions similar to that of higher-mass stars and they would likely be able to retain discs and sustain accretion and outflows. This also implies that most stars

and UCDs should form in binary or multiple systems, which is supported by observations (Pinfield et al. 2003), thus studies of UCDs in binaries could potentially be revealing about their formation mechanisms.

1.3 The ultracool IMF and birthrate

To fully understand the nature of UCDs (other than the treatment of dust) and their contribution to the galaxy, there are several important factors that need to be understood in order to answer these questions. How do they form? at what rate does this happen? how do they evolve? and what is their contribution to the very low mass end of the mass function (MF) and the initial mass functions (IMF)? The current knowledge on these factors are briefly outlined below.

1.3.1 The substellar initial mass function

The IMF describes the distribution of newly formed stars as a function of mass, which can be described as a power law of the form $M^{-\alpha}$. Salpeter (1955) showed that α=2.35 for stars equal to or larger than $M_{\odot}$, this is referred to as the Salpeter function and states that the number of stars of each mass range decreases with increasing mass. This form of the IMF stays fairly uniform regardless of environment for stars M>$M_{\odot}$. Miller & Scalo (1979) and Scalo (1986) expanded on this work for stars < $M_{\odot}$, suggesting that the IMF flattens for lower masses where α=0 for stars below $M_{\odot}$, as shown in Fig. 1.5. Kroupa (2001) however suggests that α=2.3 to half a solar mass but then reduces to α=1.3 for masses 0.5<$M_{\odot}$<0.08 and to α=0.3 below 0.08$M_{\odot}$. Traditionally the IMF is estimated from a luminosity function and a mass-luminosity relation, this is a problem however for UCDs, as the initial heat from gravitational contraction is slowly radiated away with time, such that the UCD mass-luminosity relation is a factor of age. Currently neither the mass, nor the age can be calculated from luminosity alone, making it difficult to calculate an IMF for field UCDs, as a history of the star formation along with an accurate age is needed. This was attempted by Reid et al. (1999), who calculated an IMF for stars in the solar neighbourhood from 2MASS and showed evidence for a substellar IMF that is shallower than the Salpeter IMF. However the models they use (Burrows et al. 1997b) are geared towards dust-free atmospheres and do not represent the characteristics of dustier

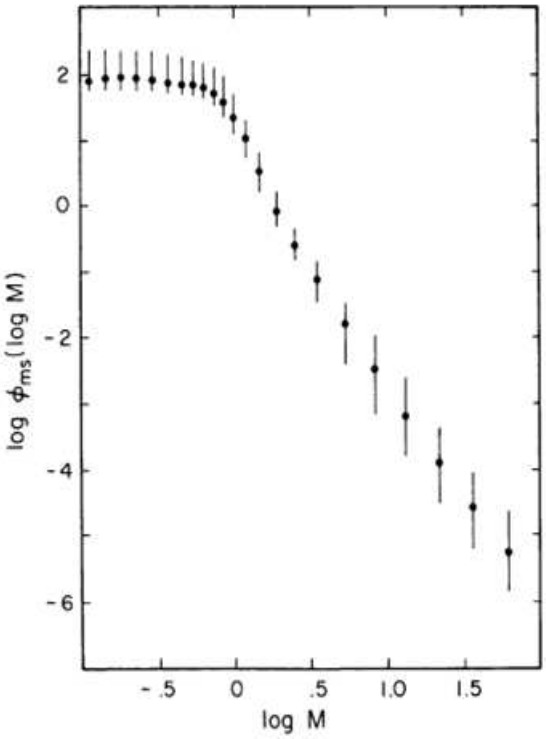

Figure 1.5: The present day mass function of main-sequence field stars from Miller & Scalo (1979), where the MF $\phi_{ms}(log\ M)$ as the number of stars ($pc^{-2}logM$).

L dwarfs. Allen et al. (2005) took a slightly different approach and calculated the IMF for M<0.08$M_\odot$ to be in the range -0.6< α <0.6 using Bayesian techniques.

The problems associated with determining the IMF for field UCDs could potentially be solved by determining the ages of UCDs and obtaining theoretical masses using evolutionary models. This may be done by observing open cluster populations where stars and UCDs of different masses with well defined ages would be abundant. There are however potential difficulties when observing objects in clusters such as sources of extinction, uncertainties in age and distance, and contamination from non-members. Studies of young clusters have been performed by Andersen et al. (2008) who looked at the IMF in young clusters including IC348, where Luhman et al. (2003b) found that the IMF rises as a Salpeter function from high/intermediate masses down to $\sim M_\odot$ and then rises more slowly to a mass around M=0.1-0.2$M_\odot$, turning over and declining into the substellar regime. They also looked at the IMF in Taurus (Briceño et al. 2002, Luhman et al. 2003a) and find that it appears to rise quickly to a peak of $\sim$0.8$M_\odot$ and then steadily declines to lower masses. The trend of a falling mass function in the ultracool regime is generally shared with the observations in other clusters (Chameleon1; Luhman 2007, Pleiades; Lodieu et al. 2007a; Chabrier 2003; Moraux et al. 2003, Orion; Hillenbrand 1997; Luhman et al. 2000; Muench et al. 2002 and NGC2024; Levine et al. 2006) as can be seen in Fig. 1.6, showing the MF of the Pleiades (Lodieu et al. 2007a). The different

forms of the IMF in these clusters all show subtle differences, suggesting that they might be sensitive to initial condition. These differences however, may also be able to help pin down the formation mechanisms for UCDs.

The recent simulations and studies of late T dwarfs (>T4) in the field from the UKIDSS LAS by Pinfield et al. (2008) suggest that a log normal form of the MF agrees best with both their observations and observations of clusters (e.g. Pleiades MF from Chabrier 2003; Lodieu et al. 2007a). The slope of the function appears to steepen, increasing as mass decreases, suggesting a function that is consistent with an α=0 power law around a mass of $\sim$0.04M$_{\odot}$. This would also suggest that as T dwarfs probe lower mass ranges, the mass function may differ for L dwarfs from that of T dwarfs and that T dwarfs may be more sensitive to changes in the IMF, as shown by the simulations of Allen et al. (2005) in Fig. 1.7. The findings of Pinfield et al. (2008) indicate that for the field population the substellar MF is most consistent with an α=-1.0 and α=0.0 for L and T dwarf populations, respectively.

1.3.2 The substellar birth rate

The birth rate is the number density of stars born per unit time and determines the MF and IMF. For main-sequence stars the MF is thought to stay constant with time (Miller & Scalo 1979) but remains undefined for substellar objects. Burgasser (2004) made Monte Carlo simulations of five UCD birth rate scenarios, including a constant birth rate (flat), similar to that taken for galactic star formation, an exponential birth rate, such that the star formation rate scales with average gas density. They also consider an empirical birth rate in the form of a series of star formation bursts, which would agree with the apparent increase in star formation $\sim$400 Myr ago (Barry 1988). A fourth scenario is a stochastic birth rate, where star formation occurs only in young clusters and only for a series of short-lived bursts, producing an equal amount of UCDs at each event. Finally they consider a halo birth rate where only UCDs born over a 1 Gyr range, occurring 9 Gyr ago and that represent the halo population. These five scenarios are all compared for α=0.5, where they shows that there is little difference between the majority of scenarios and that only the extreme exponential and halo birth rates show any strong dissimilarities, as these scenarios produce a larger number of older, more evolved UCDs. They also suggest that UCDs in the $T_{\rm eff}$ range 1200-2000K (L and early T dwarfs) may be more sensitive to the birth rate than later type T dwarfs, as shown by Fig. 1.8. Using a number of late T dwarfs

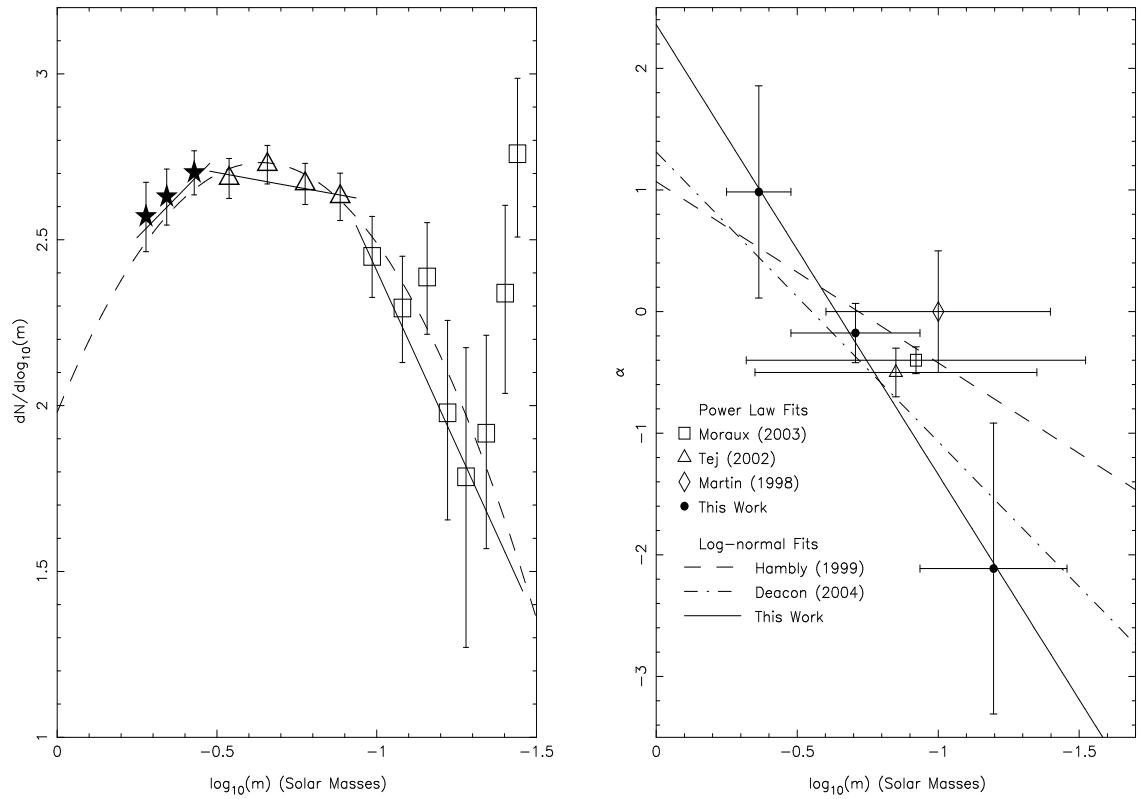

Figure 1.6: Left: The Pleiades mass function from Lodieu et al. 2007a of UKIDSS GCS DR1. The solid lines show segments of a best fit power law where α=0.98 $\pm$ 0.87 for 0.563-0.333M$_{\odot}$ (filled stars),α=-0.18 $\pm$ 0.24 for 0.333-0.116M$_{\odot}$ (open triangles) and α=-2.11 $\pm$ 1.20 for 0.116-0.035M$_{\odot}$ (open squares). Right: A plot of α for the Pleiades mass function, showing the power law fits from different studies. The filled circles are from Lodieu et al. 2007a, open squares from Moraux et al. 2003, open triangles from Tej et al. 2002 and open diamonds from Martín et al. 1998. The solid line shows the studies from Lodieu et al. 2007a, dashed lines are from studies by Hambly et al. 1999 and dot-dashed line from Deacon & Hambl 2004.

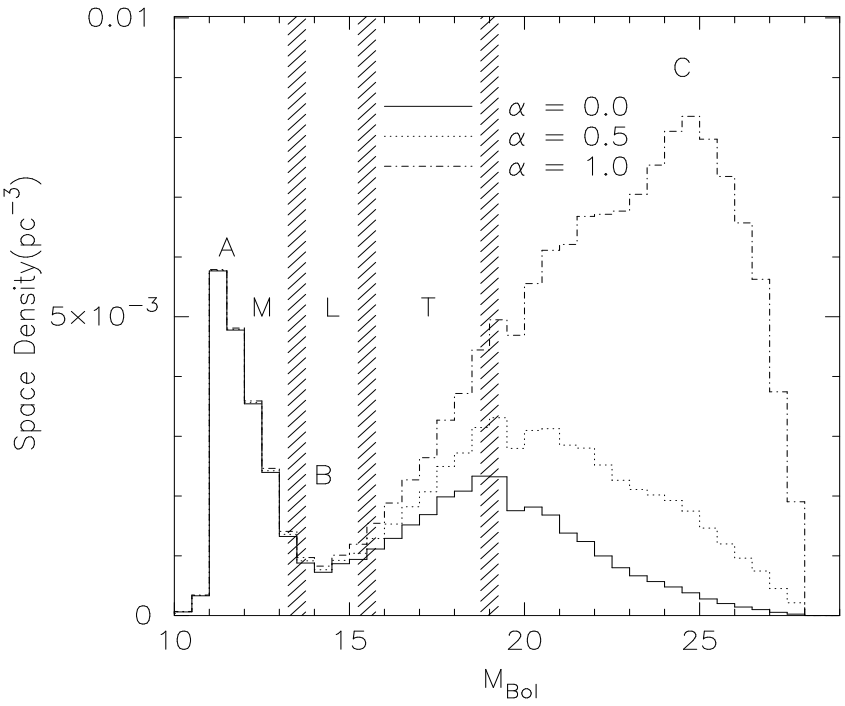

Figure 1.7: Three bolometric luminosity functions from Allen et al. (2005) comparing models of $\alpha = 0.0$ (solid line), 0.5 (dotted line) and 1.0 (dot-dashed line) for M, L and T dwarfs.

discovered from the UKIDSS LAS, Pinfield et al. (2008) suggest from observations that an IMF of the form $\alpha \geq 0$ is unlikely and favour a range of -1.0<α<-0.5. Analysis of a larger sample of L and early T dwarfs, over short $T_{\rm eff}$=100K bins in the range 1100-1500K, would be able to rule out at least extreme scenarios (e.g. exponential or halo birth rates).

1.3.3 Ultracool evolution

BDs and UCDs are not massive enough to burn hydrogen, but instead burn deuterium for some fraction of their lifetime. For the most massive UCDs this can be as short as 10Myr, at which point deuterium burning within the core will cease and the UCD will be supported by electron degeneracy pressure. They then simply cool and radiate away their internal thermal energy. Fig. 1.9 shows the cooling tracks for low-mass stars, brown dwarfs and exoplanets, taken from Burrows et al. (1997a). UCDs have masses between those of low-mass stars and exoplanets and as a result their cooling tracks appear like a mixture of the two cases. The kinks in the tracks for the higher mass objects relate to the switch-off of deuterium burning in the particular type of object. It is clear that

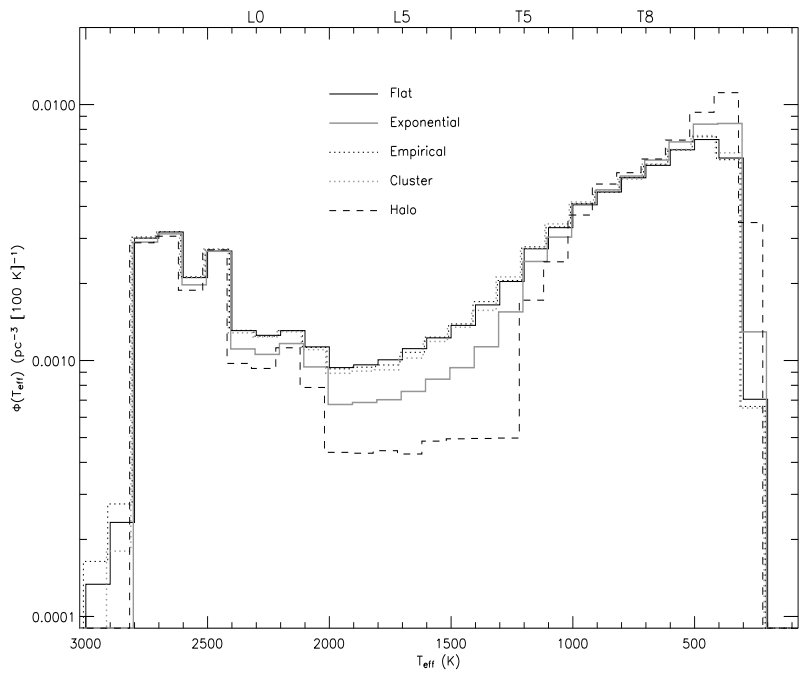

Figure 1.8: Comparison of $\Phi(T_{\rm eff})$ for α=0.5 for different birth rate scenarios from Burgasser et al. (2004) as disussed in the text. These include a flat/constant (solid black line), exponential (gray solid line), empirial (black dtted line), a stocastic/cluster (gray dotted line) and a halo (black dashed line) birth rate. The constant, empirical and cluster birth rates show nearly identical distribuations, where as the exponential and halo distributions show significant variations in the $T_{\rm eff}$ range 1200-2000 K.

UCDs and stars differ in the region where this occurs but UCDs unlike stars continue cooling indefinitely, similar to exoplanets. Throughout this cooling time the UCD will evolve through the L sequence to the T sequence and to cooler temperatures over billions of years. This means that very old UCDs are difficult to image as they are intrinsically fainter than their younger field counterparts.

1.4 Understanding and interpretation of ultracool atmospheres

One of the most notable characteristics of UCDs from the observation of their spectra and photometry is that dust grains composed of Al_2O_3 (corundum), $MgSiO_3$, $CaSiO_3$, VO, TiO and other metal oxides and silicates can form and condensate out in their upper atmospheres. The cool temperatures of UCDs provide the right environment for heavier elements to form in their atmospheres, thus allowing more complex chemistry to occur, similar to that seen in the gas giant planets like Jupiter. This has profound effects on the observable characteristics of UCDs, causing large changes in their colours and the

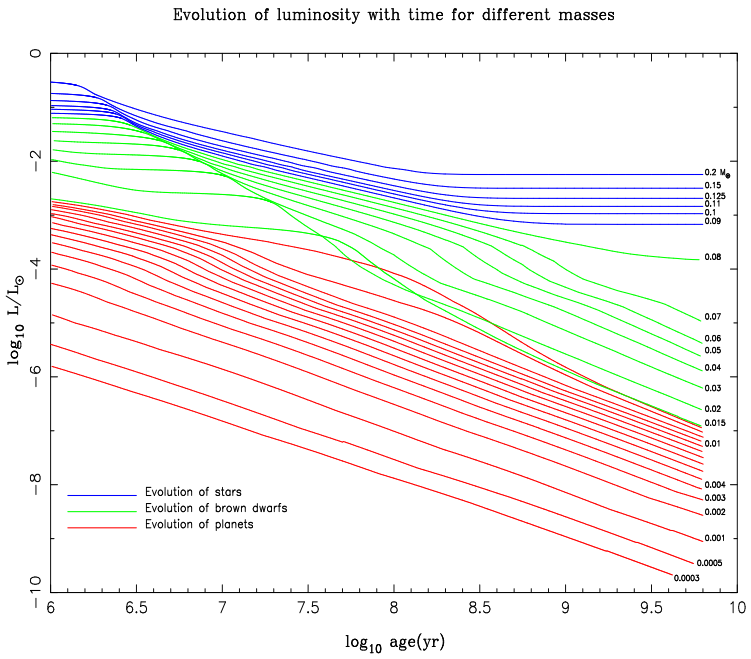

Figure 1.9: Cooling tracks for brown dwarfs, stars and planets taken from Burrows et al. (1997).

emergence of features such as water vapour and methane in their spectra. The key to understanding the changes within the spectra of these cool, substellar objects lies in the understanding of their complex atmospheres and how dust affects not only their physical but observable characteristics.

1.4.1 Atmospheric models

The spectra of UCDs are dictated by their atmospheric physics and properties, and a proper understanding thereof should thus allow accurate predictions of UCD properties and ultimately their evolutionary behaviour. Several models have been produced that try to explain the changes in the spectral and photometric characteristics that are observed for L and T dwarfs and to explain what happens at the transition between the two subclasses. These models can have very different effects on the resulting spectra and colours, depending on how they treat dust in the atmosphere (e.g. the amount of dust, grain size and composition). Traditionally stellar modelling relied on gray models that lacked any inclusion of dust, but clearly this is not the case for UCDs, where dust plays a significant role in the underlying physics, shaping their appearance.

Lyon (Phoenix) group models

The NextGen models (Baraffe et al. 1998) were some of the first models produced to try and physically describe the appearance of UCDs, they do not include dust grains, but take into account opacities, however they tend only to be useful for $T_{\rm eff}$>1700K. The latest results from the Lyon group present two model scenarios, one to explain the hotter, redder L dwarfs, known as the DUSTY models (Chabrier et al. 2000a; Baraffe et al. 2002) and the COND (condensate) models (Allard et al. 2001; Baraffe et al. 2003) that try to explain the cooler, bluer T dwarfs (both models are for solar metallicity scenarios). The models use mixtures of several hundred gas and liquid species and opacities of more than 30 types of sub-micron sized dust grains, including Aluminium, Magnesium and Calcium silicates. For this they assume that dust forms in equilibrium with the gas phase. The DUSTY models are applied to temperatures ∼3000-1400K and log g=3.5-6.0 and take into account both the formation and opacity caused by dust grains. They describe reasonably well the NIR colours and spectra of early-mid L dwarfs, where $T_{\rm eff}$>1800K but the predicted optical colours show discrepancies from observations on the order of 0.2-0.3 mags. The COND models take into account the formation of dust but no effects of atmopheric opacity, representing the dust-free appearance and general bluer colours of T dwarfs. This model is presented for $T_{\rm eff}$ from 3000-700K and log g=2.5-6.0. The properties of UCDs with $T_{\rm eff}$≤1300K are better described by the COND models than the DUSTY models. These models both struggle to reproduce observations seen at the transition between late L to early T dwarfs, suggesting that at this stage dust seen in the photosphere of L dwarfs primarily forms lower in the atmosphere of T dwarfs, and gravitationally settles below the photosphere, with the observed atmosphere being relatively dust-free. They state that these models used together represent extremes that might be expected in the properties of UCDs.

AMES models

The AMES group (Marley et al. 2002; Saumon et al. 2003) produced models using a self-consistent treatment of cloud formation. They suggest that $i-z$ colour is extremely sensitive to chemical equilibrium assumptions, having an affect of up to ∼2 mags on colour. They consider not only the sedimentation of condensates but also the efficiency of the process to help explain both L and T dwarfs and the L/T transition with the same model, for solar metallicity. As such they attempt to represent an intermediate

between the DUSTY and COND extremes. In this case the cloud decks are confined to a fraction of the pressure scale height and the models assume that it is sedimentation that controls vertical mixing in the clouds, causing the observed turnover in $J-K$ colour with decreasing $T_{\rm eff}$. They also take into account grain sizes between 10-100μm and assume that if the grain size is less than the observed wavelength of light, Rayleigh scattering dominates and has little affect on opacity. The problems with this model are that while it predicts the overall trend seen by observations, the finer details are not matched, e.g. the peak of the model value in $J-K$ is not as red as that observed, and the models predict a move to bluer colours that is much slower than is actually observed.

Tsuji models

The models of Tsuji, Nakajima & Yanagisawa (2004) use an empirical unified cloud model for cases of log g=4.5-5.5, where they assume the dust column density is relative to that of the gas column density in the photosphere for this range of log g. Their initial models assumed that dust forms everywhere, as long as the thermodynamic conditions are right for condensation (Tsuji, Ohnaka & Aoki 1996). However this was only good for predicting the colours of late M and early L dwarfs. Their latest models include the segregation of dust from gaseous mixing at a corresponding critical temperature (T_{CR}; related to the temperature of condensation). Dust then remains in the photosphere of warm dwarfs where $T_{\rm eff}>T_{CR}$ is optically thick. In cooler dwarfs where $T_{\rm eff}<T_{CR}$, producing an optically thin region and the dust is segregated and precipitated. This model represents the L/T transition reasonably well on a colour-magnitude diagram and from spectra, however the detailed behaviour does not match observations (e.g. see the $J-K$, M$_J$ diagram in Tsuji & Nakajima 2003).

Tuscon models

Burrows, Sudarsky & Hubeny (2006) use a model of refractory clouds, coupled with the latest gas-phase molecular opacities for dust molecules, similar to those used by the Lyon group. They also look at the effects of gravity and metallicity and vary grain size, cloud scale height and cloud distribution, applicable over a $T_{\rm eff}$=2200-700K range. They show generally good agreement with the observed spectra of NIR colours for early-mid L and mid-late T dwarfs and by varying gravity parameters get a closer fit to the L/T transition than other models. However they do not reproduce the apparent brightening seen in the

J- band at the transition, nor the dimming at very late T. They suggest that the L/T transition is likely related to gravity and possibly metallicity but needs better explanation.

As yet no self-consistent model has been presented that can reproduce the observed characteristics of L and T dwarfs and how they evolve from one type to the other consistently in both optical and NIR colours and spectra. It seems evident that the treatment of dust plays a vital part in fully understanding the underlying physical processes at work. Also the affects of gravity and metallicity are largely ignored by the models, with the exception of the latest Burrows models and may also play a significant role.

1.4.2 Benchmark UCDs as members of binary systems

What is needed to help the models explain the characteristics being observed are benchmark UCDs, where the age and distance can be measured or determined without the need to refer to synthetic spectra, which struggle to accurately predict true characteristics. There are several ways in which benchmark UCDs could be found. Firstly young ($\leq$1 Gyr) benchmark objects could be found as members of clusters and moving groups, where UCDs associated with a cluster (through shared kinematic properties) have a well constrained age and a known metallicity. Very young clusters, e.g. the Orion nebula cluster also provide the nursery environments, where UCD formation and the properties of very young UCDs can be studied. The distance to which these young benchmarks can be observed is generally larger than that of field UCDs, as they are much brighter at these very young ($\sim$1Myr) ages. However for the older, more evolved population it is somewhat more difficult to constrain the age, as this can not, in general be done for isolated field UCDs. The best source of benchmark objects comes from UCDs as members of binary systems, where the age can be inferred from the primary component, as members of binary systems are expected to have formed from the same nascent cloud. Of particular use are eclipsing binaries where the mass and radius can be calculated from the dynamics of the system, though depending on the parent star it may be difficult to measure the age accurately.

The ideal primary for a binary system containing a UCD, would be a star whose age can be accurately constrained, in particular binaries can be discovered in large numbers from photometric surveys, e.g. SuperCOSMOS, SDSS, 2MASS and UKIDSS (described in Chapter 2). Wide binaries with a separation >1000 AU are known to be quite common around main-sequence stars. Gizis et al. (2001) found an L-dwarf companion fraction

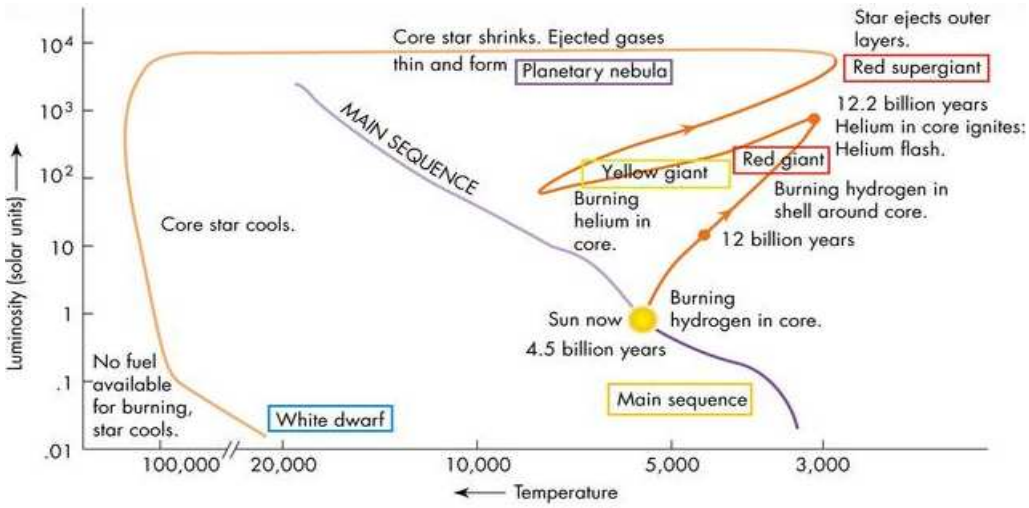

Figure 1.10: Hertzsprung-Russell diagram showing the evolution for a solar type star (www.skyserver.sdss.org).

of 1.5%, from which a UCD companion fraction of 18±14% was calculated. However, they only used a sample of three L dwarf companions to main-sequence stars to infer this fraction. Pinfield et al. (2006) on the other hand find a larger L dwarf companion fraction of $2.7^{+0.7}_{-0.5}$%, using a larger sample of 14 common proper motion companions to Hipparcos stars out to a limiting magnitude of $J = 16.1$, which a wide companion UCD fraction of 34^{+9}_{-6}% is inferred, assuming the fraction of UCDs detected as L dwarfs is =0.08 (the companion MF for an α=1 from Gizis et al. 2001). Thus wide companion UCDs to main-sequence stars should be sufficiently numerous to provide a useful population for study. The problem with main-sequence stars however is that their ages can be largely uncertain. The later stages of stellar evolution however may prove more reliable age indicators, for example the subgiant phase is very short compared to the MS lifetime and the age of a star in this phase can be fairly well constrained. The white dwarf (WD) phase is also well understood and the cooling age of a WD can be accurately measured, along with the age of the progenitor that can be accuratly calculated from models.

1.4.3 Stellar evolution beyond the main-sequence

Subgiants

Stars of mass $0.8 \leq M_{\odot} \leq 8.0$ spends the majority of their lifetime on the main-sequence of the Hertsrung-Russell diagram (HR; as shown in Fig. 1.10). Once a star has used up all of its fuel, it ceases to fuse hydrogen in its core, causing the core to contract, increasing the stars central temperature enough to cause hydrogen fusion to occur in the a shell of hydrogen surrounding the core, which is now helium rich. The star starts to expand, increasing both in diameter and in brightness. However the star's temperature and colours stay relatively consistant with its main-sequence counterpart. At this point the star leaves the main-sequence and evolves rapidly, moving horizontally across the HR diagram before joining the base of the red giant branch. The time it occupies this phase is very brief and with comparison to evolutionary models, its age can be accurately determined. During this point of the stars evolution it has not undergone any mixing or $'$dredging up$'$ of materials, where the outer convective layers start to penetrate the inner layers, mixing materials formed closer to the core and bringing them from the lower layers up to the surface. This would wipe out any original metallicity information, as the star would make its way to the giant phase.

As subgiants have not yet undergone this dredge-up phase their metallicity can still be accurately measured by comparisons with evolutionary models. Theoretical predictions of subgiant evolution are sensitive to metallicity, where the largest uncertanties arise from the extent of convective core overshooting (Roxburgh 1989) that occurs for different masses. This uncertainty is yielding to accurate observational constraints via the study of different aged open clusters (e.g. VandenBerg & Stetson 2004). UCD companions to subgiants have been previously identified by Wilson et al. (2001), who confirmed an L dwarf companion to an F7IV-V star primary from 2MASS. They find that subgiants give better age constraints ($\pm$30 %) compared to F dwarf main-sequence stars (from their fig. 4.). This subgiant has only just left the main-sequence, but fully fledged subgiants are likely to have better age constraints. Indeed subgiants with accurately measured metallicity [Fe/H] accurate to 0.1 dex (Ibukiyama & Arimoto 2002) and either a distance known to within 5% or log g to 0.1 dex could allow the subgiant age to be constrained to within 10% accuracy (Thorén, Edvardsson & Gustafsson 2004), making them excellent age calibrators. Such UCD companions to subgiants will have an accurate measurable metallicity as well as age. $T_{\rm eff}$ and log g could also then be measured, giving a UCD with

well defined properties.

The red giant and asymptotic giant phases

As the star evolves along the red giant branch, slowly burning the hydrogen in the shell around the helium rich core, the star continues to increase expanding rapidly. The surface temperature of the star then decreases as the star has expanded. When the temperature decreases lower than 5000 K dredge up can occur. During this time the helium core contracts and the internal temperature increases. When it has contracted so much that it is now gravitationally suported by electron degeneracy pressure. As the pressure suporting the star is no longer dependent on temperature the core continues to generate energy and increase heating in a run-away situation, known as the helium flash. Burning of helium then takes place in the core. Once most of the helium has been converted to carbon and oxygen in the core, a shell of helium and hydrogen around it is produced. The star again expands to become a red giant once more, with a radius comparable to 1 astronomical unit. At this point the star leaves the red giant branch and joins the lower part of the asymptotic giant branch (ABG). The star again increases in temperature and luminosity, moving back towards the left hand side of the main-sequence. After the helium shell has run out of fuel the star cools but increases in luminosity and its main source of energy production is shell hydrogen burning around the inert helium shell. Over a very short period (10,000-100,000 yr) the helium shell can 'switch on' again and the hydrogen shell burning switches off, creating another helium flash or thermal pulse. Several of these, on short timescales can occur, causing additional dregde-up of materials. The increased luminosity results in high radiation pressure, causing a strong stellar wind. Eventually the star looses most of its envelope and shrinks with constant luminosity. The temperature increases to 10^8K and the circumstellar envelope becomes visible as a planetary nebula. Near the hottest point of this post-AGB evolution the nuclear energy generation ceases and it remains a hot WD with a Carbon-Oxygen core, surounded by layers of hydrogen and helium (Prialnik 2000; Boehm-Vitense 1992).

White dwarfs

When the star looses the majority of mass, during the planetray nebula phase, it does so at a random phase of the thermal pulse cycle. For the majority of stars this occurs during the hydrogen buring phase, which occurs for a longer period of time than helium burning. The star is thus left with a thin layer of helium and an outer layer of hydrogen and exhibits strong hydrogen lines in its spectrum, and is classified as a DA WD. However if the star undergoes a helium flash after leaving the AGB phase then it will be left with a helium layer, stripping away the hydrogen. These helium atmosphere WDs show helium lines in their spectra, however the majority ($\sim$85%; Althaus et al. 2009) of WDs form with hydrogen atmospheres. The remaining WDs have predominatly helium atmospheres, and are classified by their atmospheric content. The most basic helium rich WD just shows helium lines in its spectra and no hydrogen line, this type of DB WD has temperatures between 12,000-30,000 K. The helium can also be in an ionised form (a DO WD) if it is hot enough, having a temperature in the range 45,000-100,000 K. Helium atmosphere white dwarfs with temperatures cooler than 12,000 K however, will have a featureless spectrum (a DC WD). It is also possible to see additional metal lines in the WD atmosphere (DZ white dwarfs), however the reasons for this are not fully understood. It has been sugested that these could be the result of circumstellar disks (Farihi, Zuckerman & Becklin 2008). There is also a very small fraction (0.1%) of white dwarfs that have carbon atmospheres (DQ WD), which are thought also to have formed if the WD undergoes a very late thermal pulse during the early stages of cooling, where it re-enters the WD stage in a 'born-again' phase. Gravitational settling is thought to cause the star to go from a helium rich DO into a DB and then DQ as it cools and carbon difuses up from the core (Dufour et al. 2008). Table. 1.1 show the characteristics of the different spectral types of WDs from Sion et al. (1983). The different phases from the main-sequence are illustrated in the HR diagram in Fig. 1.10.

White dwarf maximum mass and evolution

The WD itself has no nuclear energy source so the energy it radiates at its surface comes from thermal energy stored in ions that is supported by pressure from degenerate electrons. These degenerate electrons are in the form of a gas in the WD which is homogeneous and isothermal. As the density and pressure increase within the WD, the degenerate gas becomes relativistic. The maximum mass of a WD is set by the mass-radius relation that

Table 1.1: The classification scheme for WDs from Sion et al. (1983).

Type	Spectral Features
DA	Shows strong hydrogen (HI) lines.
DB	Shows strong neutral Helium (HeI) & no HI lines.
DO	Shows ionised Helium (HeII) lines.
DC	Shows a continuous spectra.
DZ	Shows strong metal lines & no Hi,HeI/HeII or Carbon lines.
DQ	Shows strong atomic or molecular carbon (C) lines.
DX	Has a peculiar or unclassifiable spectra.

was first defined by (Chandrasekhar 1931) and means that a WD of mass $>1.4M_{\odot}$ can not be supported against gravity. This also means that as the mass increases the physical size of a WD must decrease.

The mass-radius relation can also be used to relate the luminosity to mass. As luminosity depends upon surface temperature and radius, this implies that as a WD cools it simply fades, evolving along a specific track as illustrated by the evolutionary models of Chabrier et al. (2000b), shown in Fig. 1.11. High mass WDs ($\geq 0.65M_{\odot}$) will have relatively high mass main-sequence progenitors, which would have had a relatively short main-sequence lifetime (using initial-final-mass relations [IFMR], e.g. Dobbie et al. 2006 and main-sequence lifetime estimates) and the total age of the WD will essentially be the same as the cooling age of the WD. Lower mass WDs come from lower mass main-sequence progenitors, where the main-sequence lifetime is less accurately known and could be up to $\sim$10 Gyr old, with a minimum age likely greater than 1 Gyr, for an average main-sequence star in the field. Hot WD atmospheres of pure hydrogen can be well modelled (Hubeny & Lanz 1995) to constrain $T_{\rm eff}$ and $\log g$ from accurately fitting synthetic spectra to Balmer lines in the optical (Claver et al. 2001; Dobbie et al. 2005), such that WD cooling ages can be determined from $T_{\rm eff}$ and $\log g$ (assuming a mass-radius relation) and evolutionary models. Thus higher mass WDs are more desirable for constraining the ages of UCD companions, as illustrated by the IFMR shown in Fig. 1.12. It is not possible however, to establish the metallicity of the WD progenitor from observations since the surface composition of the WD is not representative of its main-sequence progenitor composition.

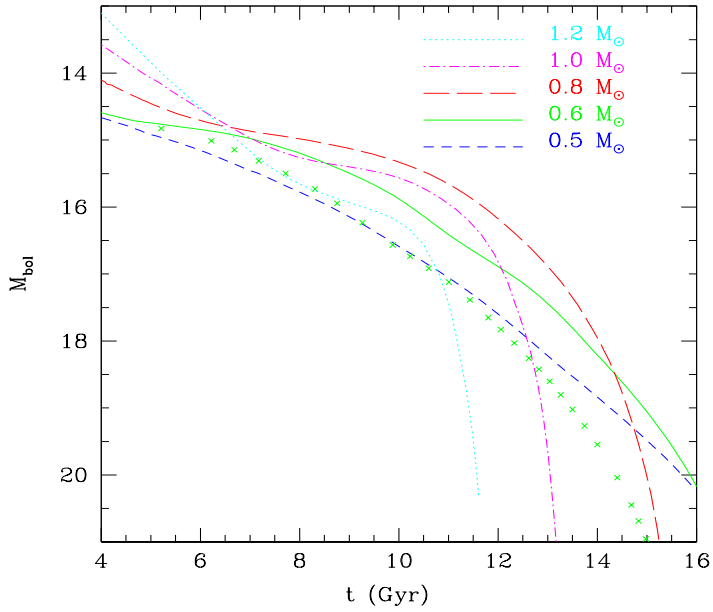

Figure 1.11: Cooling tracks for DA WDs of different mass from Chabrier et al. (2000).

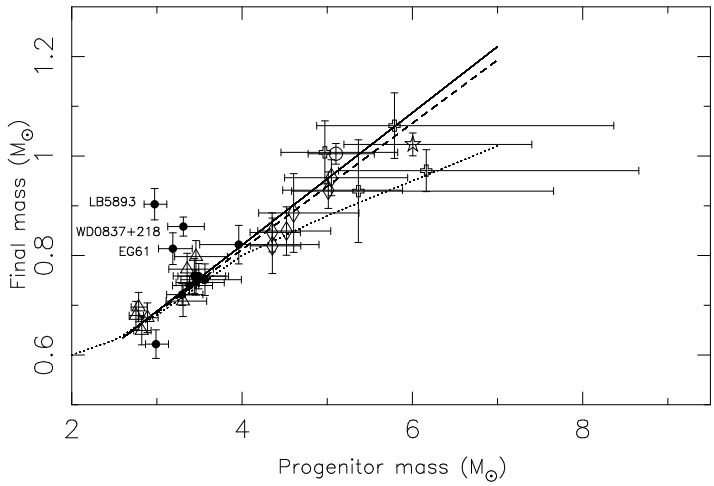

Figure 1.12: The initial-final-mass-relation from Dobbie et al. (2006) for Hyades WDs (open triangles), Praesepe (black circles), M35 (open diamonds), NGC2516 (open crosses) and the Pleiades (open stars). Linear fit to the data is shown by the solid line (fit to CO core), dashed line (fit to C core) and the relations of (Weidemann 2000) (dotted) overplotted.

Previously identified white dwarf + ultracool dwarf systems

There have been several searches to find UCD companions to WDs. Despite this, only a small number of detached UCD + WD binaries have been identified; GD 165B(L4 Zuckerman & Becklin 1992), GD 1400(L6/7; Farihi & Christopher 2004; Dobbie et al. 2005), WD 0137 − 349(L8; Maxted et al. 2006; Burleigh et al. 2006a) and PG1234+482 (L0; Steele et al. 2007; Mullally et al. 2007). The two components in GD 16 are separated by 120 AU and the separation of the components in GD 1400 and PG 1234 + 482 are currently unknown, and WD 0137 − 349 is a close binary (semi-major axis $a = 0.65\,R_{\odot}$). Farihi, Becklin & Zuckerman (2005) and Farihi, Hoard & Wachter (2006) also identified three late M companions to WDs; WD2151 − 015 (M8 at 23 AU), WD2351 − 335 (M8 at 2054 AU) and WD1241 − 010 (M9 at 284 AU). The widest system previously known was an M8.5 dwarf in a triple system – a wide companion to the M4/WD binary LHS 4039 and LHS 4040 (Scholz et al. 2004), with a separation of 2200AU. There are several other known UCD + WD binaries, however these are cataclysmic variables (e.g. SDSS 1035; Littlefair et al. 2006, SDSS1212; Burleigh et al. 2006b, Farihi, Burleigh & Hoard 2008, EF Eri; Howell, Nelson & Rappaport 2001) and are unlikely to provide the type of information that will be useful as benchmarks, as they have either evolved to low masses via mass transfer or their ages cannot be determined because of ongoing interaction. The components of CVs are also not directly observable due to obsuration by the accretion disk formed around the system.

Recent analysis from Farihi, Becklin & Zuckerman (2008) shows that the fraction of L dwarf companions at separations within a few hundred AU of WDs is <0.6%. Despite this, UCDs in wide binary systems are not uncommon (revealed through common proper motion) around main-sequence stars at wider separations of 1000 − 5000 AU (Gizis et al. 2001; Pinfield et al. 2006). However, when a star sheds its envelope during the post-main-sequence evolution, it may be expected that a UCD companion could migrate outwards to even wider separation (Jeans 1924; Burleigh, Clarke & Hodgkin 2002) and UCD + WD binaries could thus have separations of up to a few tens of thousands of AU. Although some of the widest binaries may be dynamically broken apart quite rapidly by gravitational interactions with neighbouring stars, some systems may survive, offering a significant repository of benchmark UCDs.

1.5 Motivation and thesis structure

The aim of the work in this thesis is to uncover benchmark UCDs as members of binary systems, where the primary member of the binary has a calibratable age. The UCDs discovered will be able to aid the calibration of UCD properties, allowing models to be refined, enabling them to reproduce observable properties with greater accuracy than is currently possible. This thesis is split into six chapters outlining the main project components I have worked on over the course of the Ph.D and are organised in the following structure:

Chapter 2: Describes the techniques used to select UCDs and WDs from available online data resources and catalogues, including the SuperCOSMOS, SDSS (for WDs) and the 2MASS and UKIDSS (for UCDs) sky surveys, using a combination of colour, magnitude and proper motion constraints. Presented here are the sets of candidate objects that are searched for potential binary systems.

Chapter 3: Outlines the search for widely separated UCD companions to WDs, including the results from a search of SuperCOSMOS and 2MASS for common proper motion systems. One system is confirmed, spectroscopically and has been published (Day-Jones et al. 2008), its properties and usefulness as a benchmark are also discussed. Also presented are candidate systems from SDSS (DR6) and UKIDSS (DR3), and preliminary follow-up for several of these systems, including a spectroscopic WD + M4 dwarf system with a potential wide UCD companion.

Chapter 4: Describes a pilot NIR imaging survey of subgiant stars in the southern hemisphere for widely separated UCD companions. Presented are the results from the follow-up program and the candidate systems identified.

Chapter 5: Presents the confirmation of two UCD companions to main-sequence stars, where their properties are derived and ages for the systems are calculated and assessed for suitability as benchmark objects.

Chapter 6: Discusses the findings of the various searches for UCD companions and compares them with other benchmark UCDs from the literature, where trends with properties (temperature, gravity and metallicity) are explored as functions of observable characteristics to assess current potential for the use of benchmark UCDs and highlight useful future directions.

Chapter 2

Selection Techniques

Online data archives provide an easy and efficient way to access large amounts of data that cover a wide area of sky and allow one to select objects of interest, such as WDs and UCDs here. UCDs are well characterised by their colours, especially in the near infrared (NIR), where surveys such as the 2 Micron All Sky Survey (2MASS; Skrutskie et al. 2006) and the UK Infrared Deep Sky Survey (UKIDSS; Lawrence et al. 2007) are particularly sensitive to such objects, as they are brightest at these wavelengths. These surveys provide the largest and deepest search area available in the NIR to date, thus providing an excellent way of selecting large numbers of stars and UCDs.

WDs can also be successfully selected via their colours and proper motions from optical surveys such as the SuperCOSMOS Sky Survey and the Sloan Digital Sky Survey (SDSS; Hambly, Digby & Oppenheimer 2005; Kleinman et al. 2004; Eisenstein et al. 2006), making them the ideal searching facilities for selecting WDs.

These surveys provide an invaluable tool for selecting candidate WDs and UCDs, which could make up components of widely separated WD + UCD binaries. The techniques used to select potential WD candidates from the SuperCOSMOS and the SDSS surveys and UCD candidates from the 2MASS and UKIDSS sky surveys are described in the following sections.

2.1 Selecting white dwarfs

2.1.1 White dwarfs in SuperCOSMOS

The online data archive SuperCOSMOS is a compilation of digitised sky survey plates taken with the UK Schmidt and ESO Schmidt (in the south) and with the Palomar Schmidt (in the north) telescopes. The database is accessed through the SuperCOSMOS Science Archive (SSA); http://surveys.roe.ac.uk/ssa) where data can be obtained through the use of Structured Query Language (SQL). Initially the SSA covered 5000 degrees^2 of sky, primarily covering the southern hemisphere from -60° to +3° DEC, in B-, I- and two R- band epochs, with R- limiting magnitudes of 21.0 and 21.5, respectively. These two epochs are taken using slightly different filters, the $R59$ and $R63$ filters, whose wavelength coverage varies slightly from those of the Cousins R- band, but can be easily converted using colour relations. As of August 2008 the survey is now complete and covers the whole sky, however work presented here made use of the southern release only.

Candidate WDs were selected from the SSA, following a similar technique to that of Knox, Hawkins & Hambly (1999). Candidates were selected based on their position on a reduced proper motion (RPM) diagram, a technique that reduces the proper motion to a linear velocity, such that reduced proper motion (in the R- band) is expressed as $\mathrm{H}_R = R + 5\log\mu + 5$, thus enabling it to be used as a proxy for absolute magnitude and hence distance, taking advantage of the fact that nearby objects in general have higher proper motion. WDs occupy a distinct region of the RPM diagram and have successfully been selected via this method (Hambly, Digby & Oppenheimer 2005). Fig. 2.1 shows a SuperCOSMOS RPM diagram with the location of WDs. An initial SSA sample (shown as dots) was a magnitude selected sample ($R \leq$20) to avoid sources near the plate limit. Potential candidates were also selected to be moving sources by requiring proper motion (PM)$\geq$10 mas/yr, PM$\sigma_{PM}\geq$5 and to be stellar-like sources, requiring a database object to have a class=2. In addition the galactic plane was avoided (requiring $|b| \geq$25°) to minimise confusion due to crowded fields, and SSA I- band coverage was also required ($\delta \leq$+3°), which offers possible additional epochs for nearby UCD candidates (see §3.2.1). Quality constraints on the database photometry were also imposed requiring the flag qual$\leq$1040 in each of the B-, R- and I- bands ensuring that the object is unlikely to be a bright star artifact. The main-sequence and WD sequence can be clearly seen in Fig. 2.1, and display

good separation for $B-R \leq 1.3$. To further illustrate the location of the WD sequence, overplotted are the positions of WDs from the spectroscopically confirmed McCook & Sion WD catalogue (McCook & Sion 1999; here after MS99), along with pre-WDs (i.e. sdO stars) and Halo objects from Leggett (1992). Also overplotted are subdwarf B stars, hot, cool and extreme subdwarfs from Kilkenny, Heber & Drilling (1988), Stark & Wade (2003), Yong & Lambert (2003) and Monet et al. (1992) respectively, which can have high velocity dispersions and can masquerade as WDs in RPM diagrams. The overplotted populations help confirm the location of the WD sequence for $B-R \leq 1.3$ and allow the location of WDs to be assessed out to redder colour. The final RPM selection criteria were chosen to strike the best balance between WD selection and contamination minimisation, and are shown in Fig. 2.1 by dashed lines. At the red end in particular, an attempt to include as many WD candidates as possible was made, while minimising contamination from cool subdwarfs.

The RPM selection criteria are:

$$H_R \geq 8.9(B-R) + 10.5 \text{ for } B-R \leq 0.65 \text{ and}$$
$$H_R \geq 4.1(B-R) + 12.5 \text{ for } B-R > 0.65.$$

This selection criteria resulted in a sample of 1532 WD candidates.

2.1.2 White dwarfs in SDSS

The Sloan Digital Sky Survey (SDSS; www.sdss.org) is currently undertaking a 5 year mission to survey a quarter of the sky, mostly in the northern galactic pole (b>30°) and a 2x50 degree strip in the southern galactic pole region. These areas are being surveyed in 5 optical bands *u*-, *g*-, *r*-, *i*- and *z*- at central wavelengths 0.35, 0.46, 0.61, 0.74 and 0.89 μm, with limiting magnitudes 22.0, 22.2, 22.2, 21.3, 20.5, respectively. The survey uses the 2.5 metre Sloan telescope, located at Apache Point Observatory in New Mexico. SDSS uses CCD technology to obtain highly sensitive measurements and more accurate images than photographic counterparts like SuperCOSMOS.

Candidate WDs were selected from the SDSS using two selection techniques, firstly bluer WDs ($u-g < 0.6$) were selected from their $u-g$ and $g-r$ colours only based on those used by Kleinman et al. (2004) and Eisenstein et al. (2006), who successfully selected WDs in this bluer $u-g$ colour regime, based on their colours alone. Secondly redder WDs ($u-g > 0.6$) were selected from their *u*-, *g*- and *r*- colours along with a reduced proper

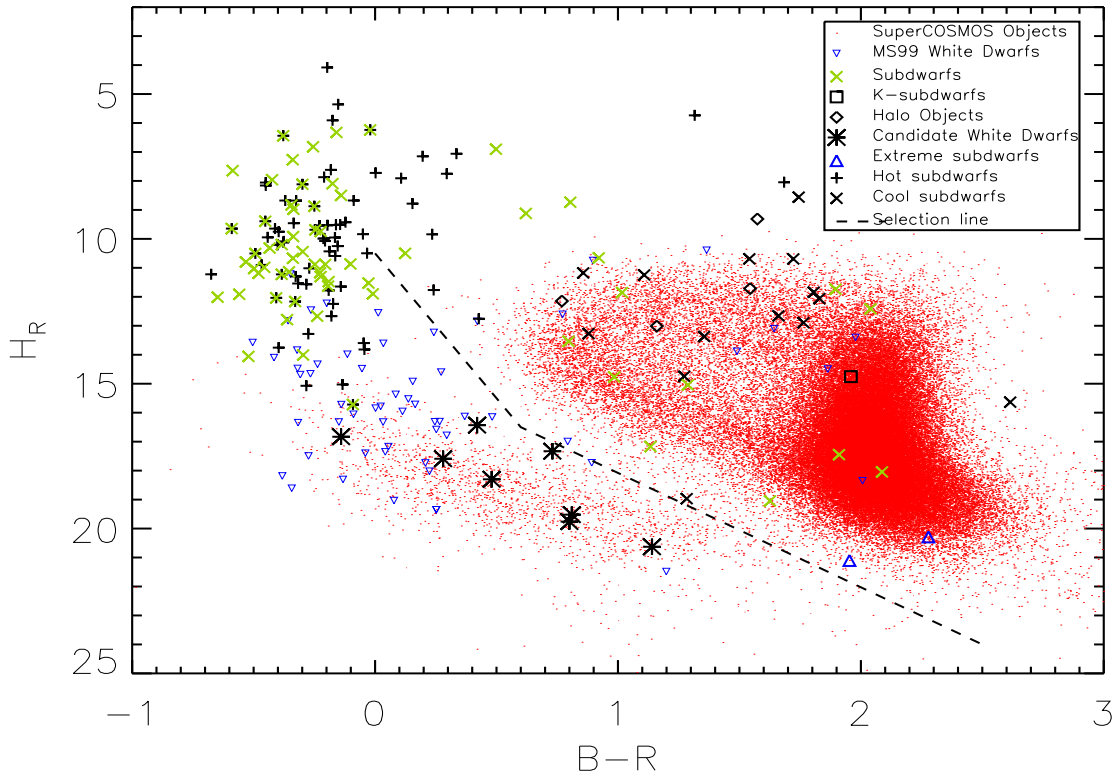

Figure 2.1: A reduced proper potion (RPM) diagram showing how WD candidates were selected from SuperCOSMOS. Candidate WDs were chosen from amongst an initial SuperCOSMOS sample (points) using a cut in colour-RPM space (RPM=$\mathrm{H}_R = R+5\log\mu+5$), which is overplotted in the figure as a dashed line. Highlighted are spectroscopically confirmed WDs from MS99 (upside down triangles), hot subdwarfs (plus signs), cool subdwarfs (crosses) and extreme subdwarfs (triangles) to help delineate the WD sequence. The location of some halo objects (diamonds and squares) are also indicated. Also shown are the WD components of the eight candidate UCD + WD binaries (stars) (see §3.2).

motion constraint (as there is some overlap with main-sequence stars at these redder $u-g$ colours), using the same method described in §2.1.1. The RPM selection adopted here is based on that of Kilic et al. (2006), as shown in Fig. 2.2, where the chosen selection regions are shown as dashed red lines and overplotted with spectroscopically confirmed WDs in SDSS to highlight the WD sequence. In addition, data quality flags were used requiring that objects were classified as being stellar like (phototype = 'star') and that they were not close to the edge of the image (photoflags 'edge' = 0) since objects near the edge of images can be distorted in shape. To reduce the contamination from extra galactic sources with similar colours to WDs, two additional flags were used to select only close-by objects, by use of the redshift flag (z) where if measured $z < 0.01$. Also QSOs were removed from the sample using the spectral class flag such that specClass$\neq$ 3. Finally spectroscopically identified WDs in SDSS (ObjType = 8, where 8 indicates a WD as classified by SDSS) were also included in the list of candidates, yielding a sample of 22,087 WD candidates which are shown in Fig. 2.3. Of the selections the blue WDs are likely to have the most amount of contamination as they are selected based on their colour alone. To estimate the level of contamination that might be expected, a magnitude limited sub-sample of the blue WDs of u$\leq$20 (where 95% of objects have measured proper motion measurements in SDSS) was constructed. The objects in this sample were then put through the reduced proper motion criteria used to select the red WD sample. This should provide a list of more probable WDs. 65% of the sub-sample had a reduced proper motion consistent with being WD like, suggesting that the level of contamination is likely on the order of $\sim$35%. It is expected that for fainter candidates this level of contamination should also hold.

The colour selection criteria for blue ($u-g<0.6$) WDs are:

$$u < 21.5,\ -2.0 < g-r < 1.2$$
$$\text{and}$$
$$(u-g < 0.7,\ g-r < -0.1) \text{ or } (u-g < 0.6 \text{ and } g-r > -0.1)$$

The colour selection criteria for red ($u-g>0.6$) WDs are:

$$u < 21.5,\ -2.0 < g-r < 1.2$$
$$\text{and}$$
$$(u-g > 0.7,\ g-r < -0.1) \text{ or } (u-g > 0.6,\ g-r > -0.1)$$
$$\text{and}$$

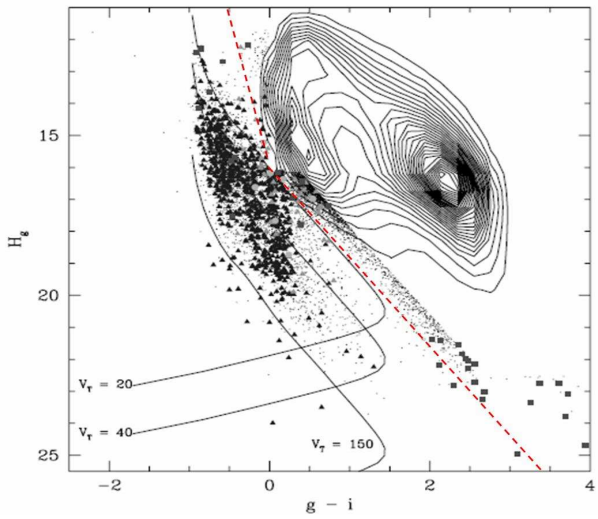

Figure 2.2: A reduced proper motion diagram, where $H_g = g + 5log\mu + 5$ from Kilic et al. (2006) for stars from SDSS DR2 showing WDs (dark triangles), WDs + late type star binaries (light triangles), subdwarfs (squares) and quasars (circles). Also shown are WD cooling tracks for different tangential velocities $V_T = 20 - 40$ (solid lines) and for halo objects (V_T). The sharp blue turnoff is due to i- band depression caused by opacity during the onset of collision induced absorption of molecular hydrogen for cool stars with pure hydrogen atmospheres (Hansen et al. 1998; Saumon et al. 1999). Candidate WDs were selected to the left of the selection line (red dashed line).

$$H_g > 10.0(g-i) + 16.0 \text{ for } H_g < 16.0 \text{ or}$$
$$H_g > 2.8(g-i) + 16.0 \text{ for } H_g > 16.0.$$

2.2 Selecting ultracool dwarfs

2.2.1 L dwarfs in 2MASS

The 2MASS completed its goal of scanning the whole sky in 2002 and released data of the NIR sky in three bands $J-$, $H-$ and $K-$, at central wavelengths 1.25, 1.65 and 2.17 μm respectively, producing a catalogue of over two terabytes of information and images. The survey was carried out on the 1.3 metre telescope at Mt Hopkins, Arizona and the 1.3 metre at CTIO in Chile, both of which have a three channel camera attached for simultaneous observing in all three bands. The catalogues can be accessed via an online search tool created for this data. This Gator facility allows one to access data for 300 million objects (http://irsa.ipac.caltech.edu/applications/Gator/) via an SQL form-based interface.

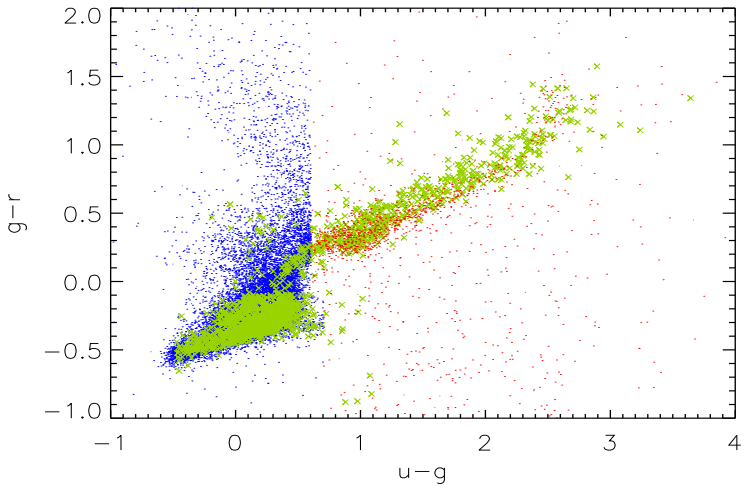

Figure 2.3: A $u-g$ against $g-r$ two colour diagram showing WDs selected from SDSS (DR6). Blue dots are candidates selected via colour only, red dots are candidates selected via colour and RPM constraints (see §2.1.2). Spectroscopically confirmed WDs are overplotted as green crosses to help define the location of the WD sequence.

UCD candidates were photometrically selected by their NIR colours from the 2MASS all sky point source catalogue. Colour cut criteria taken from Folkes et al. (2007), which are based on the colours of known L-dwarfs with reliable J- , H- and K- band 2MASS photometry (SNR≥20) from the Caltech cool dwarf archive (DWARFARCHIVES.ORG). These have much in common with other L dwarf searches (e.g. Kirkpatrick et al. 2000; Cruz et al. 2003) but use the following specific photometric criteria:

$$0.5 \leq J-H \leq 1.6$$
$$1.1 \leq J-K \leq 2.8$$
$$0.4 \leq H-K \leq 1.1$$
$$J-H \leq 1.75(H-K)+0.37$$
$$J-H \geq 1.65(H-K)-0.35$$
$$\text{and } J \leq 16.0.$$

Fig. 2.4 shows these colour cuts on a two-colour diagram, and also shows (as plus symbols) known L dwarfs from DWARFARCHIVES.ORG and those that have SNR≥20 are shown as green diamonds, that were used as a guide by Folkes et al. (2007).

An optical-NIR colour restriction was also imposed, using the USNO-A2.0 cross-match facility within the Gator, ruling out objects with $R-K$ <5.5 ($a=U$ combined with vr_m_opt-K >5.5, or nopt_mchs=0). Contamination from artefacts, extra-galactic sources and low quality photometric data were removed by requiring cc_flag=000 (no artifacts detected), gal_contam=0 and ph_qual≤CCC, where the measurements had jhk_snr>5. In addition a spatial density constraint was imposed so that the distance to the nearest

Table 2.1: Galactic co-ordinates of contaminated and overcrowded regions removed.

Region	$l_{\min}$	$l_{\max}$	$b_{\min}$	$b_{\max}$
SMC.....	300°	310°	-42°	-23°
LMC.....	270°	290°	-40°	-25°
.....	145°	220°	-42°	-20°
.....	20°	45°	-25°	-20°

star was > 6 arcsec (prox>6). This means that while the most crowded regions are avoided it imposes a lower limit on the separation of potential binary systems if the WD is detected at NIR colours. Known contaminants, such as minor planets and asteroids were also removed from the selection (mp_flg=0). As with the WD candidate selection, the areas searched lie away from the galactic plane ($|b|$ >25°) to avoid confusion from over crowding and contamination from reddened stars and giants. DEC $|\delta|$ >86° were also avoided, for which 2MASS suffers from incompleteness issues with its optical cross-matching. Additional areas surrounding the Small and Large Magellanic clouds were also ignored. Finally two additional uncatalogued, reddened regions were avoided following the approach of Cruz et al. (2003). These excluded regions are listed in Table 2.1, and the resultant sky coverage of the search is 13,216 square degrees, or 32% of the sky, giving a sample of 13,338 L dwarf candidates.

2.2.2 L and T dwarfs in UKIDSS

The UK Infrared Deep Sky Survey (UKIDSS) is a next generation NIR survey and operates in four NIR bands, including $J-$, $H-$ and $K-$ on the Mauna Kea filter system (Tokunaga & Vacca 2005) which will reach at least three magnitudes deeper than 2MASS, to K=18.5 (Hewett et al. 2006). The Y- band filter was also used, which is positioned blue-wards of the J- and covers the wavelength range 0.97-1.07μm, allowing high redshift quasars to be distinguished from UCDs (Warren & Hewett 2002). UKIDSS will survey 7500 degrees^2 of sky, covering a large proportion of the optical SDSS coverage, creating a complimentary NIR counterpart.

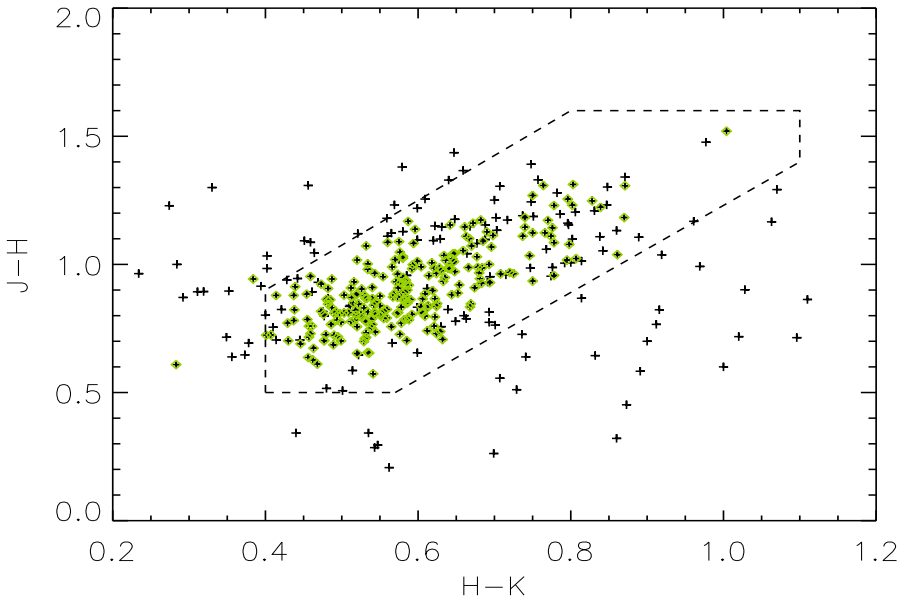

Figure 2.4: A $J-H$ against $H-K$ two colour diagram of L dwarfs from DWARFARCHIVES.ORG (plus symbols), overplotted with those where SNR$\geq$20 as green diamonds and overlaid with the selection area, defined in Folkes et al.(2007).

UKIDSS employs WFCAM, the Wide Field CAMera on the UK InfraRed Telescope (UKIRT; Casali et al. 2007) located in Hawaii, which started its 7 year project in May 2005, comprising of 5 individual surveys; the Galactic Plane Survey (GPS), the Galactic Clusters Survey (GCS), the Deep eXtra galactic Survey (DXS), the Ultra Deep Survey (UDS) and the Large Area Survey (LAS), which is most useful for this work. The first data release (early data release; EDR) to the ESO community was on February 10, 2006. The largest release to date, covering $\sim$900 degrees^2 was DR3 on 6 December 2007, which this work makes use of. Currently DR4 is available (as of July 1, 2008), adding an additional $\sim$200 degrees^2 to the total sky coverage.

Candidate L and T dwarfs were selected from the UKIDSS DR3 via the WFCAM science archive (http://surveys.roe.ac.uk/wsa; Hambly et al. 2008) based on their $Y-J$ and $J-H$ colours. The selection region in Y-, J- and H- colour space was devised from synthesised colours of M, L and T dwarfs from Hewett et al. (2006), who derive colours from spectra covering wavelengths from i- to K-. The colours of L and T dwarfs in 2MASS also show a similar trend that in general L dwarfs have red $J-H$ and $Y-J$ colours and T dwarfs appear to have neutral or bluer colours as T_{eff} decreases (Burgasser et al. 2002). Models predict that cooler objects ($T_{eff} < 700K$) will remain blue having

$J - H < 0.0$, however there is some disagreement with predictions for $Y - J$ colours. The cloud-free COND models (Allard et al. 2001; Baraffe et al. 2003) and the newer Lyon-Settl models (Allard et al. 2008) predict blue-ward $Y - J$ colours, while the models of Burrows, Sudarsky & Lunine (2003) and Tsuji, Nakajima & Yanagisawa (2004) predict redder colours, as shown in Fig. 2.5. These model colours were also used to help define the colour selection of UKIDSS T dwarfs by Lodieu et al. (2007b) and Pinfield et al.(2008), who have successfully identified 20+ mid to late T dwarfs. The colours of confirmed T dwarfs along with synthesised colours were considered when choosing the selection regions for candidate UCDs, which is shown in Fig. 2.5 and meet the following photometric requirements:

Colour selection criteria for L dwarfs:

$$0.9 \leq Y - J \leq 1.5$$
$$0.4 \leq J - H \leq 1.2$$
$$\text{and } J \leq 19.0$$

Colour selection criteria for T dwarfs:

$$0.9 \leq Y - J \leq 1.25$$
$$-0.5 \leq J - H \leq 0.4$$
$$\text{and } J \leq 19.0$$

As with the 2MASS selection several quality flags were used to select only good candidates, ensuring objects were star-like (meanclass = -1), did not appear to be extended sources (using the ellipticity flags, requiring $Ell < 0.35$ in all $Y-, J-, H-$ and $K-$ bands) or sources of contamination from artifacts such as cross-talk (Dye et al. 2006) by requiring ppErrBits< 256 in all four bands. The last criterion ensures objects are detected at coherent positions in all four bands, so that offsets in RA and DEC from the master position are within 0.5 arcsec ($-0.5 \leq Xi \leq 0.5$ and $-0.5 \leq Eta \leq 0.5$). This selection resulted in a sample of 24,293 L and T candidates (plotted in Fig. 2.5).

These selection techniques have yielded 1532 WD candidates selected from SuperCOSMOS south, 22,087 WD candidates from SDSS DR6, 13,338 L dwarf candidates from the 2MASS all sky point source catalogue and 24,293 L and T dwarf candidates from UKIDSS DR3.

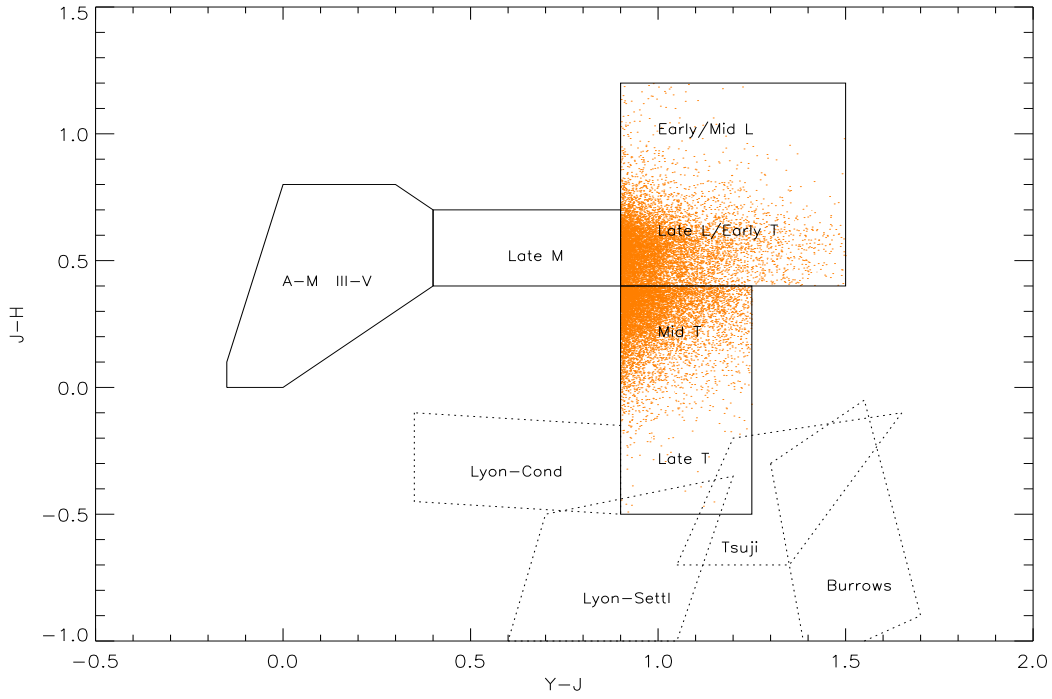

Figure 2.5: A $Y - J$ against $J - H$ two colour diagram showing the chosen selection regions for L (dotted line) and T dwarfs (dashed line), devised from predicted colours from Hewett et al. (2006) and model predictions (The Lyon-Cond models: Allard et al. 2001, Baraffe et al. 2003; Lyon-Settl models: Allard et al. 2008; Burrows et al. 2003 and Tsuji et al. 2004) for very cool objects ($T_{eff} < 700$K). Overplotted as orange points are candidate L and T dwarfs selected from UKIDSS DR3.

Chapter 3

Ultracool companions to white dwarfs

This chapter describes the process of selecting wide UCD + white dwarf (WD) binary systems from the selected samples of WD and UCD candidates (see §2). The candidate systems found using this method are presented, as well as the discovery of the widest separated WD+M9 UCD binary known to date, which has also been published in Day-Jones et al. (2008).

3.1 Selecting candidate binary pairs

To identify very widely separated UCD + WD binary candidates, a search was conducted to look for pairs with separations out to 20,000AU, allowing for an outward migration factor of ∼4 (during the post-main-sequence mass-loss phase of the WD) from the separations of known wide UCD + MS star binaries (5,000AU; see §1.4). To illustrate this choice, consider a WD of mass ∼0.6 $M_{\odot}$ (the mean of the WD mass distribution; Liebert, Bergeron & Holberg 2005). The progenitor mass would be ∼2.0 $M_{\odot}$ from the initial-final mass relation (e.g. Dobbie et al. 2006; Kalirai et al. 2008) so $M_{initial}/M_{final} \sim 4$ (Jeans 1924). This suggests that the projected maximum projected orbital separation could be up to ∼ 20,000AU. An additional constraint was imposed so that the photometry of any UCD and WD candidate pairs that were associated as candidate binaries was also consistent with both components being at the same distance. In order to do this reasonable distance constraints are required for both types of object.

3.2 Searching SuperCOSMOS and 2MASS

A distance constraint was placed on the WD candidates by constructing a CMD in the SuperCOSMOS colour system (M_B against $B-R$), using a combination of observed and theoretical WD photometry and distance measurements, this CMD is shown in Fig. 3.1. Known WDs were taken from McCook & Sion (1999), including all WDs with known parallax and distance uncertainties better than 20%. These objects are plotted as crosses with associated error bars in Fig. 3.1. In addition synthetic WD properties (luminosity, $T_{\rm eff}$ and $\log g$) were obtained for three different masses (0.5, 0.7 and 1.2 $\rm M_{\odot}$) over a range of disk ages, using equations from Schröder, Pauli & Napiwotzki (2004) and the mass–radius relation of Panei, Althaus & Benvenuto (2000). Synthetic WD photometric properties were then determined using a combination of colour–$T_{\rm eff}$ and bolometric correction–$T_{\rm eff}$ relations from models (Chabrier et al. 2000a) and observation (Kleinman et al. 2004). The photometry was transformed into the SuperCOSMOS system using relations given in Bessell (1986). These theoretical tracks are shown in Fig. 3.1 as dotted, dashed, and dot-dash lines respectively.

A region was defined for WDs on the CMD (shown by the solid lines) to take into account the spread seen in both observation and the models, while also offering a reasonably constrained WD sequence (that will yield useful distance constraints). Although some of the hottest WD model tracks lie slightly above the selection region, no such trend is seen by observations and the highest mass hot model points are completely contained within it. This is desirable since high mass WDs are more interesting in the context of benchmark UCDs (§1.2). Using this CMD as an aid for characterising WDs, the $B-R$ colour for each WD candidate was used to estimate a possible range in M_B, thus deriving a corresponding distance range consistent with the measured B- magnitude of each candidate.

Using the lower distance estimates to provide upper limits to the projected angular separation corresponding to 20,000AU at the distance of each of the WD candidates, a search was conducted for UCD candidates whose angular separation from the WDs was within the appropriate limit. As a proximity flag was used to select the UCDs from 2MASS, such that a UCD was selected at a separation of >6 arcsec from its nearest neighbour, this introduces a lower limit on the separation that can be searched for binary systems. To estimate how much of the total 20,000AU separation this affects, the distance of the WD candidates was calculated using the inferred absolute magnitude ($\rm M_B$) from

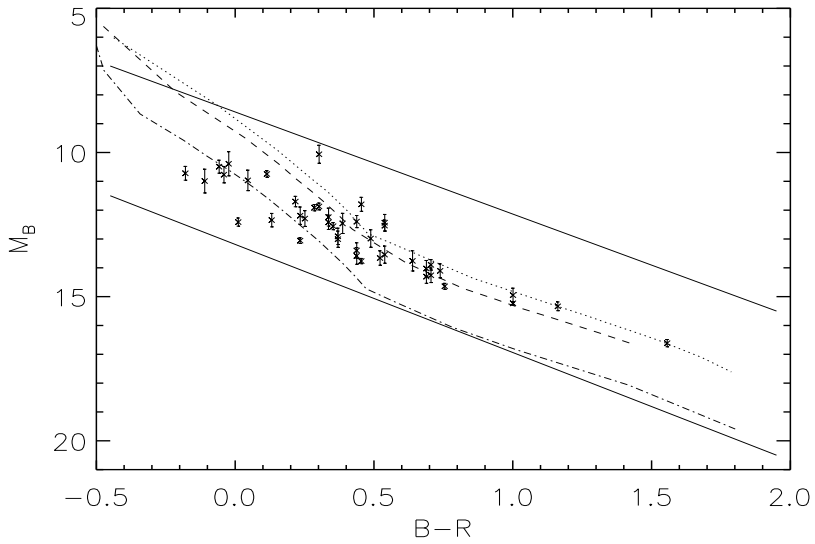

Figure 3.1: A WD M_B against $B-R$ absolute colour-magnitude diagram for MS99 WDs with known parallax (crosses with error bars). Photometry is on the SuperCOSMOS system. Overplotted are model cooling tracks (see §3.2) for WD masses of 0.5, 0.7 and 1.2 $M_\odot$ (dotted, dashed and dot-dashed lines respectively). The selected WD region in the CMD lies between the two solid lines.

the CMD in Fig. 3.1 and used to calculate the separation in AU , corresponding to a separation of 6 arcsec. The fraction of the 20,000AU separation that this affects was then calculated. Fig. 3.2 shows the affected region, where at a distance of 160pc a separation of $\leq$1000AU may be missed, and out to the maximum distance of the WD candidates ($\sim$300pc) a separation of $\leq$1900AU may be missed. In the context of wide binary systems (>1000AU) the search may be incomplete at the lower separations for distances >160pc. The percentage of the area surveyed corresponding to a separation limit of 20,000AU was also calculated and is illustrated in Fig. 3.2, where the total fraction of the 20,000AU separation area affected is shown to be less than 10% at 300pc.

In addition colour-magnitude information for the UCD was used to check for consistency between candidate binary pairs by using the WD distance estimates to convert UCD candidate J- band magnitudes into M_J. This assumes that the two objects are at the same distance. Any candidate UCD was then plotted on an M_J against $J-K$ CMD to see if it was located in the expected part of the diagram. Fig. 3.3 shows this NIR CMD with the location of previously spectroscopically confirmed UCDs (with parallax distances, shown as plus symbols), which along with the M_J range of L dwarfs from Knapp et al. (2004) was used to define the region that L dwarfs are expected to populate. A UCD CMD selection region was defined similar to that used by Pinfield et al. (2006),

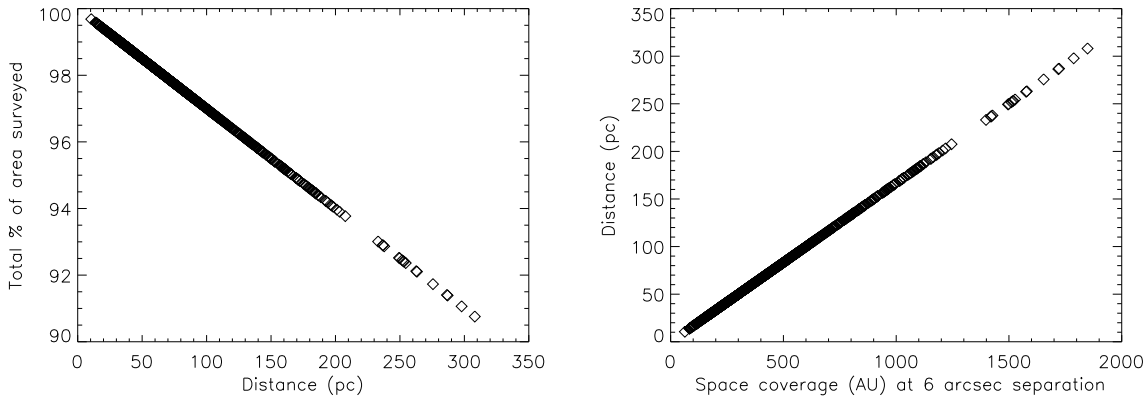

Figure 3.2: Left: The percentage of the 20,000AU separation limit searched for widely separated WD + UCD binaries from 2MASS combined with SuperCOSMOS, when a 6 arcsec minimum search radius is set (to reduce potential contamination in crowded areas of sky). Showing that at 300pc (max estimated distance for WD candidates) less than 10% of the search area is affected. Right: The separation coverage (in AU) corresponding to a minimum sky separation of 6 arcsec around the WD candidates. For wide (>1000AU) binary systems, a few systems at separations of 1000-1900AU may be missed at distances of 160-300pc.

which is shown as a dashed line box in Fig. 3.3. If UCD candidates lie outside this box, then their photometry is deemed inconsistent with a UCD at the same distance as the neighbouring candidate WD. All possible pairs were considered amongst the 1532 WD and 13,338 UCD candidates and assessed with the separation and photometric consistency tests. In this way 18 candidate UCD + WD binary systems were identified. These candidates were visually inspected using images from 2MASS, SuperCOSMOS and DENIS (where available). Seven of the UCD candidates had bright R- band counterparts and were therefore rejected since their $R-K$ colour was too blue to be L dwarfs; good L dwarf candidates have $R-K \geq 6$. Proper motion analysis using I- band SCHMIDT plates from SuperCOSMOS and 2MASS J- band images revealed that three of the remaining candidate pairs were non-common proper motion companions. The UCD and WD components from the eight remaining candidate pairs are presented in Table 3.1 and over-plotted as asterisks in Fig. 2.1 and 3.3. The clumping in the top left of the selection space in Fig. 3.3 reflects the greater sensitivity to closer, brighter late M and L dwarfs in 2MASS.

Table 3.1: Candidate UCD + WD binary systems. Coordinates are J2000. Photometry is from 2MASS, SuperCOSMOS and DENIS (where available). The last three columns show which UCD candidates have second epoch imaging (see §3.3), which pairs have been confirmed (or not) through common proper motion and which candidates have been confirmed as a UCD or WD with spectroscopy (see §3.3).

Name	RA	DEC	*B*-	*R*-	*I*-	*J*-	*H*-	*K*-	Sep (arcsec)	2nd epoch	CPM	Spec
UCDc-1	00 30 06.26	-37 39 48.2	-	-	18.30	15.2	14.4	13.8	89	IRIS2	Y	Y
WDc-1	00 30 11.90	-37 40 47.2	16.77	16.35	15.97	16.1	15.8	-				Y
UCDc-2	00 56 14.71	-40 36 03.6	-	-	-	15.8	15.0	14.3	922	IRIS2	N	-
WDc-2	00 57 18.72	-40 45 29.6	15.80	15.07	13.67	12.4	-	-				-
UCDc-3	03 02 07.70	-09 41 57.1	-	-	17.66	15.8	15.0	14.5	136	IRIS2	N	-
WDc-3	03 02 03.00	-09 43 54.9	17.63	17.35	17.34	-	-	-				-
UCDc-4	05 20 35.40	-18 54 27.7	-	-	17.64	15.9	15.1	14.7	145	IRIS2	N	-
WDc-4	05 20 40.03	-18 56 37.9	18.34	16.40	17.92	-	-	-				-
UCDc-5	10 12 35.59	-10 51 02.2	-	-	18.13	15.3	14.6	14.1	465	IRIS2	?	-
WDc-5	10 12 43.89	-10 43 33.8	19.48	18.34	17.87	-	-	-				-
UCDc-6	10 40 43.41	-16 48 20.5	-	-	-	15.9	15.2	14.8	124	IRIS2	?	-
WDc-6	10 40 39.17	-16 50 08.3	20.34	19.54	19.12	-	-	-				-
UCDc-7	14 05 37.54	-05 51 53.6	-	-	17.80	15.8	15.2	14.6	164	-	-	-
WDc-7	14 05 44.98	-05 49 51.9	16.66	16.80	16.87	-	-	-				-
UCDc-8	23 21 21.55	-13 26 28.3	-	-	-	14.5	13.5	13.1	73	IRIS2	?	-
WDc-8	23 21 14.38	-13 27 36.8	19.23	18.42	18.00	-	-	-				-

Notes - ? Indicates uncertainty due to a small measured motion and high uncertainties associated with the proper motion measurements (see text).

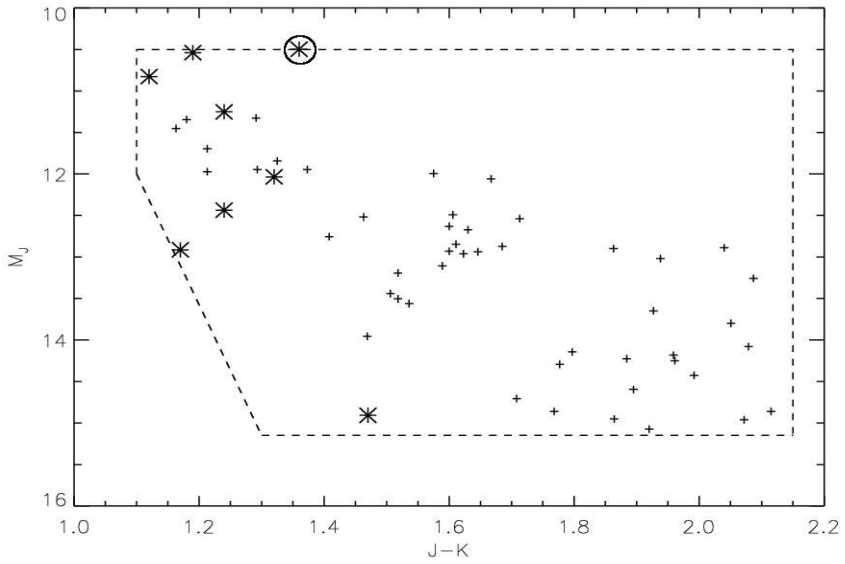

Figure 3.3: An M_J against $J-K$ colour-magnitude diagram showing the location of the companion UCD candidates (asterisks) when they are assumed to be at the same distance as their associated WD candidate. The UCD selection criteria is indicated with a dashed line and UCDs with known parallax from DWARFARCHIVES.ORG are plotted as plus signs. UCD-1 is also circled (see §3.3).

3.2.1 Proper motions of candidate systems

Second epoch images of candidate UCDs were taken with the Infrared Imager and Spectrograph, IRIS2 on the Anglo Australian Telescope (AAT) during service observations on 2006 July 7 and 2006 December 8, with J-, H- and K_s- band filters. The images were reduced using the standard ORACDR package for IRIS2; this included de-biasing to remove the CCD DC signal from the images, flatfielding to remove any pixel to pixel variations and any imperfections in the optics (i.e. dust). The data were dark subtracted, removing any thermal background inherent to the CCD and bad pixels were interpolated over to prevent inaccurate flux measurements in the areas they occupy on the image. Finally the jittered images (a 5 point jitter was used) were mosaiced together to create a final reduced image.

The IRAF routines GEOMAP and GEOXYTRAN were used to create a transformation of the X and Y position shift and scale between the available multi-epoch images, using an average of 15 reference stars. Proper motions were calculated by multiplying the motion (in pixels) by the pixel scale of IRIS2 (0.448 arcsec/pixel) and then dividing by the baseline (in yrs), to give a relative proper motion in arcsec/yr. In addition a correction was applied to the derived proper motions to account for the average (but small) proper

motion of the reference stars. Uncertainties were initially estimated from centroiding accuracies (typically 0.5 pixels) combined with the residuals associated with the derived transformations.

Amongst the eight candidate binary pairs, three of the UCD candidates were ruled out since they are not common proper motion companions (at $>3\,\sigma$), three remain uncertain due to the relatively small motion expected between epochs (compared to the uncertainties associated with the inter-epoch transforms) and one remains unobserved (see Table 3.1 for a summary of these results).

Second epoch IRIS2 measurements of candidate UCDc-1 (2MASS J0030 − 3739) revealed a significant motion over the 6.8 yr baseline between the 2MASS first epoch and the IRIS2 second epoch images. The large field of view of IRIS2 (7 x 7 arcmin) allowed the proper motion of both the UCD and the WD candidate to be measured from the same two-epoch image set, which clearly revealed the common proper motion. Final proper motion measurements and uncertainties were based on four individual measurements: pairing up J-, H- and K- band images from the 2MASS and IRIS2 epochs appropriately, as well as pairing up a SuperCOSMOS I- band as first epoch with the IRIS2 J- band image as second epoch. The last combination is over a relatively longer baseline of 15.86 yr, although this may suffer from larger chromatic effects due to the different bands. The final proper motions were an average of these four measurements and the associated uncertainties were estimated from their standard deviation. The measured proper motions of the pair are given in Table 3.4. Multi-band $BRIJHK$ 2 x 2 arcmin finder charts centred on 2MASSJ0030 − 3739 are shown in Fig. 3.4.

3.3 A wide WD + UCD binary

3.3.1 Spectral classification of UCDc-1: 2MASSJ0030-3739

Spectroscopic observations of one candidate (UCD-1; see Table 3.1) were also obtained with IRIS2 on the AAT on 2006 September 8. The long slit mode was used with a 1 arcsec slit width in the J- long and H- short grisms, covering wavelength ranges $1.1 - 1.33\,\mu$m and $1.46 - 1.81\,\mu$m with a dispersion of 0.225 nm/pixel and 0.341 nm/pixel, respectively ($R \sim 2400$). A total exposure time of 20 minutes in each band was obtained and the target was nodded along the slit in an "ABBA" pattern with individual exposure times of 300s. Standard dome flats and Xenon arcs were taken at the end of the night and an

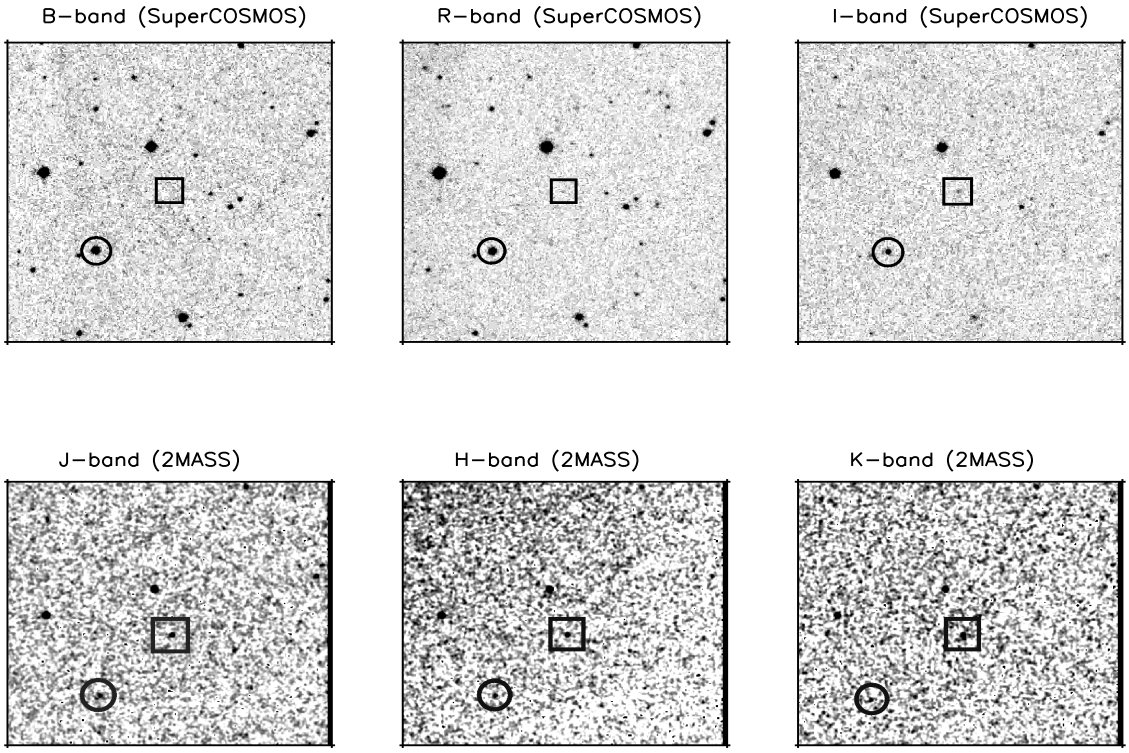

Figure 3.4: SuperCOSMOS and 2MASS images show UCDc-1 (2MASSJ0030 − 3739; squares) and WDc-1 (2MASSJ0030 − 3740; circles).

F5V star was observed at a similar airmass to the target to provide a telluric correction. The observing conditions were reasonable with an average seeing of $0.8 - 1.2$ arcsec.

Standard IRAF routines were used to reduce the spectra including flat fielding. A flatfield image was created from dome flat images by removing 'lamp on' images from 'lamp off' images, then median combining them using the IMARITH routine. This flatfield image was then normalised to $\sim$1 by creating a smoothed flatfield image, using the BOXCAR routine to provide the average flux in a box 11 pixels on each side. This was then divided out of the flatfield image to create a normalised masterflat. Each of the A and B images of the object, standard star and arcs were divided by the masterflat image. Cosmic rays and bad pixels were removed using an IDL program to identify bad pixels or groups of bad pixels and replace them with an average value in a 10 pixel box surrounding the bad pixel location. A-B pairs, containing a positive and negative object spectrum were extracted with APALL using a chebyshev function to fit the background and a third order Legendre function (where points of deviation were removed) to trace the fit to the spectrum. The wavelength calibration was done with a Xenon arc lamp spectrum, using IDENTIFY to reference the wavelength of the arc lines (from the line lists provided by the AAO; www.aao.gov.au/iris2) and the DISPCOR routine was used to correct the dispersion of the spectrum. This method was repeated for each of the differenced A-B pairs, and the wavelength calibrated spectra were median combined and flux calibrated by dividing the object spectrum by the telluric standard, then multiplying by the spectra of a blackbody, created from the BBODY routine in the STARLINK package FIGARO for a $T_{\rm eff}$= 6530K (appropriate for a F5V star; see Allen's astrophysical quantities). The annotated spectra are shown in Fig. 3.5 and Fig. 3.6.

Spectral ratios

An estimate of the spectral type for 2MASSJ0030 − 3739 was based on spectral ratios used in previously published work. The J- band spectral coverage is $1.1 - 1.35\,\mu$m. In this range the FeH ratio from Slesnick, Hillenbrand & Carpenter (2004) and the J- FeH and H_2O_A ratio from McLean et al. (2003) were used. A ratio of 0.854 for FeH was measured, where FeH is the ratio of the median flux at 1.20 and 1.23μm using a bandwidth of 0.01μm (1.20/1.23μm; bandwidth=0.01μm). Using the spectral type relation from Slesnick, Hillenbrand & Carpenter (2004), a spectral type of M9 was estimated from this ratio. The J- FeH (1.20/1.185μm; bandwidth = 0.04μm) ratio of 0.85 combined with the spectral type relations from fig. 12 of McLean et al. (2003) gives a spectral range M8-L3. At

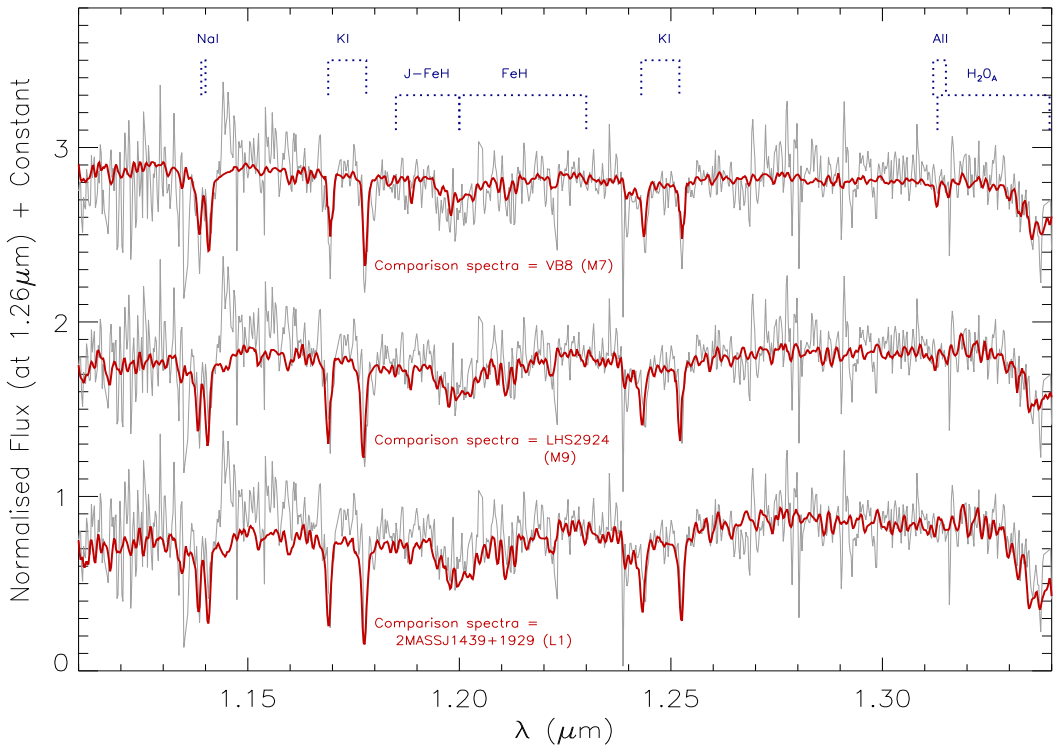

Figure 3.5: *J*- band spectra of 2MASSJ0030 − 3739 (thin grey line), shown with comparison spectra (thick line) of an M7, M9 and L1 type (top to bottom) from Cushing et al. (2005) overlaid. Also shown are the spectral ratios (J-FeH, FeH and H_2O_A) used for spectral typing and the features (NaI, KI and AlI) are shown.

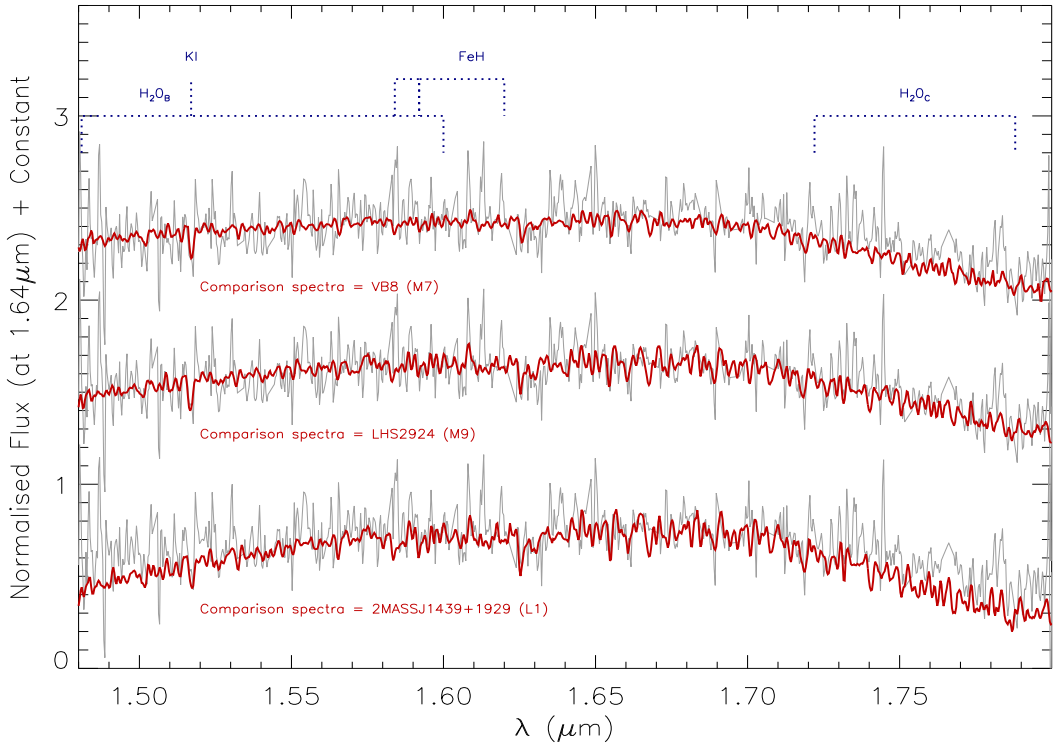

Figure 3.6: *H*- band spectra of 2MASSJ0030 − 3739 (thin grey line), shown with comparison spectra (thick line) of an M7, M9 and L1 type (top to bottom) from Cushing et al. (2005) overlaid. Also shown are the spectral ratios (FeH, H_2O_B and H_2O_C) used for spectral typing and the main KI feature.

the edge of the spectral coverage in the J- band, when strong water vapour absorption starts to appear, is the H_2O_A ratio (1.343/1.313; bandwidth = 0.004μm). This ratio was measured as 0.554. The relation between H_2O_A and spectral type in fig. 11 of McLean et al. (2003) indicates an ∼L1 type from this ratio.

The H- band spectrum covers wavelengths $1.45 - 1.81\,\mu$m, for which the H_2O ratios from Reid et al. (2001a)[H_2O_C] and McLean et al. (2003)[H_2O_B] were used. The H_2O_C ratio at 1.788/1.722μm with a bandwidth of 0.004μm was measured as 0.697 and indicates an L1.5 $\pm$2 type. The H_2O_B ratio (1.48/1.60μm; bandwidth=0.02μm) of 0.9 is consistent with an M8-M9 type. All of the spectral ratios considered are indicated by dotted lines in Fig. 3.5 and Fig. 3.6 and the spectral ratio results are summarised in Table 3.2.

Comparison to template spectra

Template spectra of known late M and early L dwarfs were used to make a comparison to the overall profile of $2MASSJ0030 - 3739$, as well as a comparison to the absorption in spectral features such as the KI (1.168, 1.179 and 1.243, 1.254 μm), NaI (1.138, 1.141 μm), AlI (1.311, 1.314 μm) doublets in the J- band and the blended KI doublet (1.517 μm) and FeH (1.58, 1.59 and 1.62 μm) in the H- band. In general alkali metal lines weaken at the M/L boundary (McLean et al. 2000), but the NaI, AlI, FeH and KI doublets are still clearly recognisable for the purposes of a comparison. The spectra of an M7(VB8), M9(LHS2924) and L1($2MASSJ1439 + 1929$) from Cushing, Rayner & Vacca (2005) were rebinned to the dispersion of the NIR spectra and normalised at 1.26 and 1.64 μm in the J- and H- bands respectively (Fig. 3.5 and 3.6). Visual inspection of the blended line features reveal the spectra are most consistent with an ∼M9 type.

Equivalent widths

Equivalent widths for the four neutral alkali (KI) lines present in the J- band spectra were calculated using the methods of McLean et al. (2003). An IDL program was used to interactively determine the equivalent width of each KI line, which were compared with those of McLean et al. (2003) to estimate a spectral type from each line (see their table 7). In order to reduce the amount of bias when selecting the reference continuum, the process was repeated 12 times using a continuum measured at different relative positions (within 0.05 Å from the centre of the line) and a mean of the measurements taken. A

Table 3.2: Estimated spectral types for 2MASSJ0030 − 3739.

Method	Reference	Spectral type
Ratio FeH (1.200/1.230 μm)	Slesnick ('04)	M9
$''$ J- FeH (1.185/1.200 μm)	McLean ('03)	M8-L3
$''$ H_2O_A (1.313/1.343 μm)	$''$	$\sim$L1
$''$ H_2O_C (1.722/1.788 μm)	Reid ('01)	L1.5 $\pm$2
$''$ H_2O_B (1.480/1.600 μm)	$''$	M8-M9
SC J-	...	M9 $\pm$1
SC H-	...	M9 $\pm$1
EW KI (@ 1.168 μm)	McLean ('03)	M8-M9
EW KI (@ 1.177 μm)	$''$	M7-M8
EW KI (@ 1.243 μm)	$''$	M7-M8
EW KI (@ 1.254 μm)	$''$	M7-M8
Notes: SC- Spectral Comparison, EW- Equivalent Width.		

width of 4.89 Å at the 1.168 μm line indicates an M8/9; while the other three KI line widths at 1.177, 1.243 and 1.254 μm are all consistent with an M7/8 type.

Analysis of the spectra of 2MASSJ0030 − 3739, through the use of spectral ratios, comparison to template spectra and equivalent widths are summarised in Table 3.2, and are consistent with a spectral type M9 $\pm$1. The relation between spectral type and absolute magnitude from Dahn et al. (2002) was used to calculate a range in M_J of 10.85−12.04 for the spectral range M8-L0. Thus, combining this with the measured J- band magnitude from 2MASS, it is estimated that 2MASSJ0030 − 3739 is at a distance of 41 − 75 pc.

3.3.2 Spectral classification of WDc-1: 2MASSJ0030-3740

A spectrum of WDc-1 (2MASSJ0030 − 3740) was obtained with FORS1 on the VLT on 2007 January 24, with Directors Discretionary Time in programme 278.C-5024(A), using the longslit mode in the optical wavelength range 3800 − 5200Å and a dispersion of 50 Å/mm. Three integrations of 600s were taken, giving a total exposure time of 30 minutes. Spectra of a DC WD and a standard F-type star were also taken and used for calibration. Sky flats were taken and HgCd arcs were used for wavelength calibration.

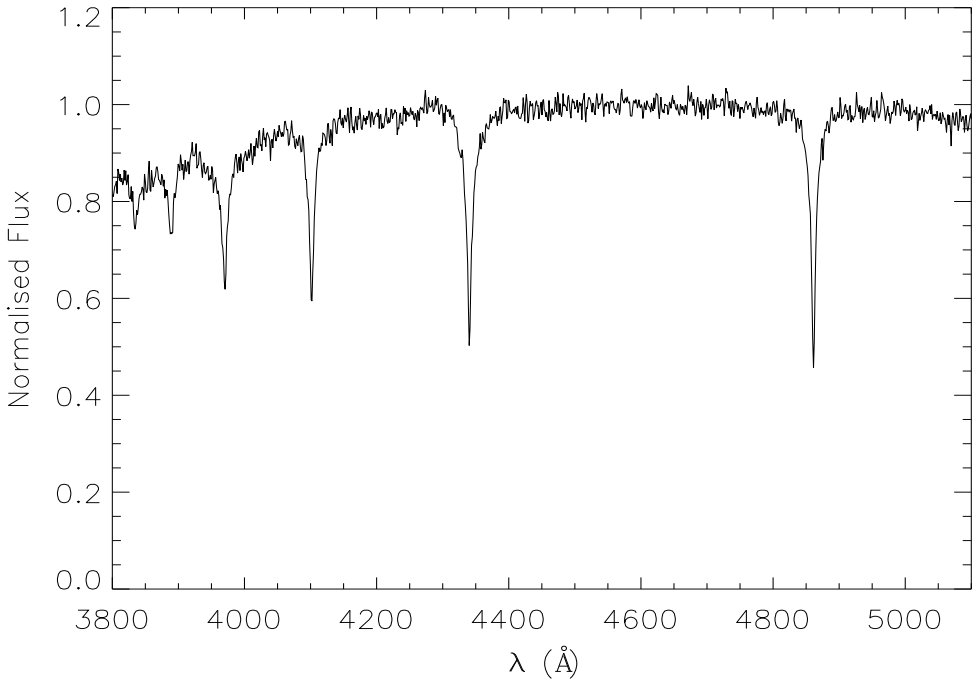

Figure 3.7: Optical spectrum of the confirmed white dwarf WDc-1 (2MASSJ0030 − 3740), flux calibrated and normalised at 4600Å.

Standard IRAF packages were used to reduce the spectra including debiasing (by creating a master bias frame from median combined images and subtracting this from the object, standard star, flat field and arc images), flat fielding and removal of bad pixels. The three spectra were then extracted and wavelength calibrated as described in §3.3.1. The resulting spectra of both WDc-1 and the standard were divided by the featureless DC WD spectrum, which has no intrinsic spectral features, enabling correction for the instrumental response. The standard star was then used for flux calibration and the final spectrum of 2MASSJ0030 − 3740 is shown in Fig. 3.7.

WD parameters, $T_{\rm eff}$ and log g were derived from a fit of the Balmer lines using the fitting routine FITPROF described in Napiwotzki, Green & Saffer (1999). The WD spectrum was modelled using an extensive grid of spectra computed with the model atmosphere code of Detlev Koester described in Finley, Koester & Basri (1997). Observational and theoretical Balmer line profiles were normalised to a linear continuum and the atmospheric parameters determined with a χ^2 algorithm. The best fit is shown in Fig. 3.8. The results are $T_{\rm eff} = 7600 \pm 20\,{\rm K}$ and $\log g = 8.09 \pm 0.04$ (formal uncertainties from the fit routine to one sigma).

Table 3.3: Fit results and derived quantities for WD mass, cooling age and absolute magnitude for the corrected and uncorrected case discussed in §3.3.2.

	$T_{\rm eff}$	log (g)	M	$t_{\rm cool}$	M_V
	K	dex	$M_\odot$	Gyr	
solution 1	7600	8.09	0.65	1.48	13.4
solution 2	7600	7.79	0.48	0.94	12.9

Realistic uncertainty estimates are often substantially larger than the formal statistical estimates. Napiwotzki et al. (1999) derived a relative uncertainty of 2.3% in $T_{\rm eff}$ and 0.075 dex in log g from a sample of DA WDs analysed using the same fitting method. This temperature uncertainty was adopted for the following estimates, but the gravity determination is likely subject to a systematic overestimate. The mass distribution of WDs peaks close to 0.6 $M_\odot$ (e.g. Napiwotzki, Green & Saffer 1999; Bergeron, Gianninas & Boudreault 2007), corresponding to log g values close to 8.0. Spectroscopic investigations applying the method have shown a trend of the log g distribution peaking at increasingly higher values for decreasing temperatures (Bergeron, Gianninas & Boudreault 2007). This trend starts at 11,500 K putting the WD analysed here in the affected region. Taken at face value, this would indicate on average higher masses for cool WDs. However, as argued by Bergeron, Gianninas & Boudreault (2007) and Engelbrecht & Koester (2007) this can be ruled out. A source of extra line broadening must be present in these stars. However, the exact nature of this mechanism is still under discussion and as pointed out in Bergeron, Gianninas & Boudreault (2007) anecdotal evidence suggests that some stars are affected and others are not.

A pragmatic approach was taken here, where a large sample of DA white dwarfs were used from observations taken in the course of the SPY programme (Napiwotzki et al. 2001) to derive an empirical correction. Spectra of these stars have been previously analysed using the same model grid and very similar analysis methods as for the WD discussed here. The estimated shift in log g distribution caused by the unknown mechanisms is 0.3 dex in the $T_{\rm eff} = 7500 - 8000$ K range. The corrected gravity is thus log g=7.79. As mentioned above it is not entirely clear whether all cool WDs are affected. Thus the corrected and uncorrected gravity values will be used for further discussion. WD masses and cooling ages were calculated by interpolation in the Benvenuto & Althaus (1999) cooling tracks for WDs with thick hydrogen envelopes. Results are listed in Table 3.3.

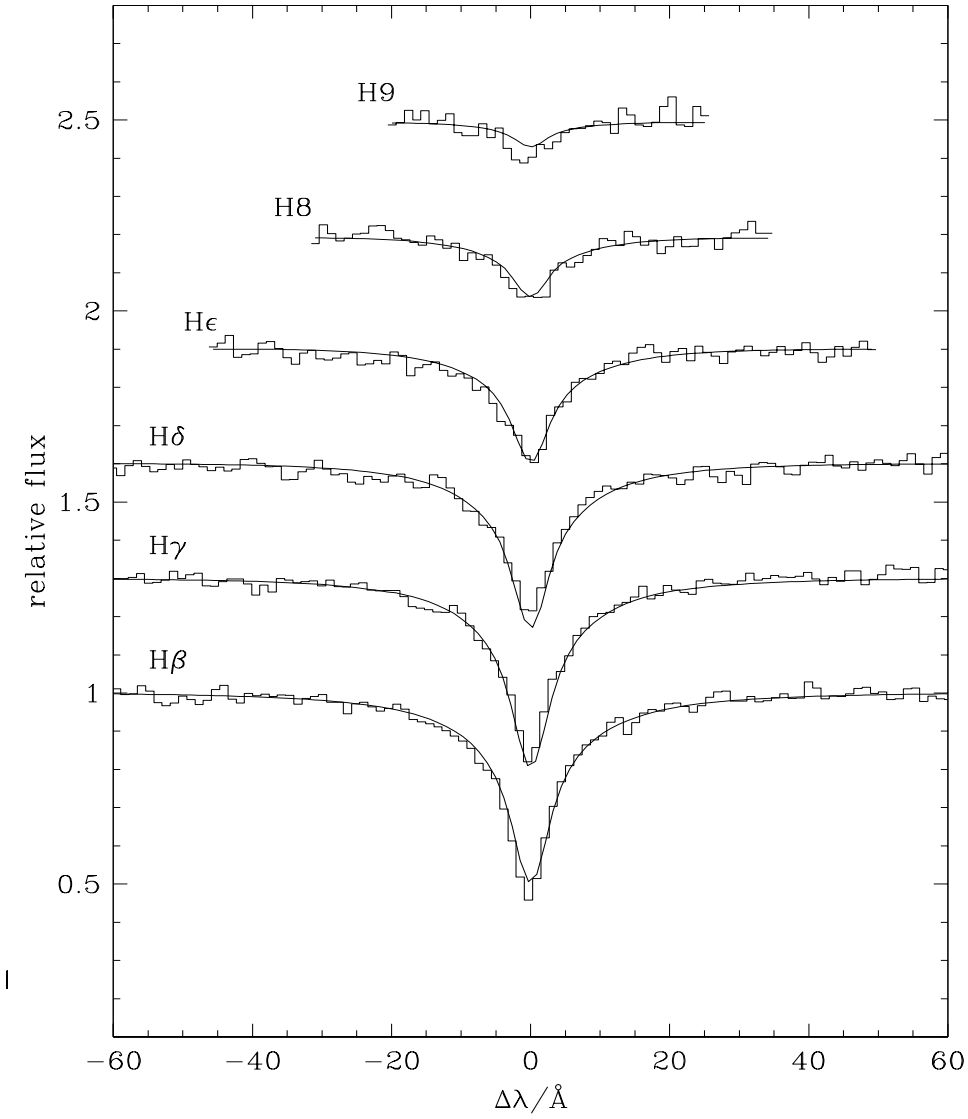

Figure 3.8: Model atmosphere fit to the Balmer lines of 2MASSJ0030 − 3740 giving best fit parameters of $T_{\rm eff}$ = 7600 K and log g=7.79. Observed and theoretical fluxes were normalised to the continuum. Line profiles are shifted for clarity.

3.3.3 A randomly aligned pair?

In order to determine if the new system is a bonafide UCD + WD binary, the likelihood that two such objects could be a line-of-sight association with photometry and proper motion consistent with binarity by random chance has been statistically assessed. To do this, firstly the UCD luminosity function of Cruz et al. (2007) was taken, which gives a number density of $(4.9 \pm 0.6) \times 10^{-3}$ UCDs per pc^3 for M7-M9.5 types. Then a volume associated with 1532 circular areas on the sky (one for each of the WD candidate sample), with radii of 89 arcsec (separation of the components) and a line-of-sight depth of 58 ± 17pc (approximate distance to the new M9 UCD, using relations from Dahn et al. 2002) were calculated. This volume equates to 58 ± 26 pc^{-3}, giving a total expected number of 0.28 UCDs to be within 89 arcsec of one of the WD candidates.

To factor in the probability that two objects might have a common proper motion at the same level as the measurements, a magnitude-limited sample ($R < 20$) was downloaded from the SuperCOSMOS Science Archive (SSA), applying the same minimum proper motion requirement that was used to create the WD candidate sample. A magnitude limited sample of 160 sources, selected from a large circular sky radius of 90 arcmin centred on the WD. A proper motion vector-point-diagram was constructed and sources counted that were found to be within the $2\,\sigma$ uncertainty circle of the measured UCD proper motion. Four of the 160 sources had proper motion consistent with the UCD, suggesting a probability of $2.4 \pm 1.2\%$ that such common proper motion could occur by random chance (where Poisson uncertainties associated with this and other samples were considered here).

An additional requirement fulfilled by the UCD + WD system is that the colour-magnitude information must be consistent with a common distance (see Fig. 3.3) and 53% (786 ± 28) of the WD candidate sample were found to be photometrically consistent with being at the same distance as the UCD.

Finally considered was the fraction of WD candidates that might be spurious and thus not able to contribute to non binary line-of-sight associations where the WD has been confirmed spectroscopically. In the magnitude range $R < 14$, where MS99 is thought to be essentially complete, it was find that 66% of our WD candidates are included in the MS99 catalogue. This suggests that, at least for brighter magnitudes, the WD candidates presented here are relatively free from contaminating objects, and that the selection techniques are robust. While it cannot be guaranteed that the same low-level of

contamination applies to the full magnitude range, a conservative approach was taken, by assuming that the full WD candidate sample could potentially contribute to non-binaries that appear to be UCD + WD pairs.

Taking into account all these factors, it is estimated that one would expect 0.0036 ± 0.0025 randomly aligned UCD + WD pairs with ≤ 89 arcsec separation, proper motion and photometry consistent with binarity at the level of the observations. The likelihood of the system being merely a line-of-sight association is thus vanishingly small, and it can thus be assumed that the UCD + WD pair is a gravitationally bound binary system.

3.3.4 Binary age

The age of the binary system can be constrained from the WD mass and cooling age. For the corrected fit, 2MASSJ0030 − 3740 has a mass of $0.48\,M_{\odot}$ and a cooling age of 0.94 Gyr. The IFMR determinations of Weidemann (2000), Dobbie et al. (2004), Dobbie et al. (2006), Ferrario et al. (2005), Catalán et al. (2008) and Kalirai et al. (2008) were assessed to estimate a likely, initial-mass constraint for the main-sequence progenitor star of $1 - 2\,M_{\odot}$. The main-sequence lifetime of a progenitor of this mass is likely >1 Gyr (probably several Gyr) and thus is not useful when trying to constrain the upper age limit of the system. Note that if the WD mass were higher, for example if the helium enrichment of the atmosphere is lower than typical (see §3.3.2) then the WD's log g could be as high as 8.1 dex, with a WD mass of $\sim 0.65\,M_{\odot}$ and cooling age of $\sim$1.5 Gyr. This would allow the progenitor mass to be constrained to a likely range of $> 2.7\,M_{\odot}$, giving a main-sequence progenitor lifetime of < 0.83 Gyr (Monteiro et al. 2006) and a binary age constraint of $1.5 - 2.3$ Gyr. This possibility is instructive at least in demonstrating the level of age constraints (with accompanying UCD constraints) that may be placed on benchmark binaries of this type. However, it is not possible to judge the helium content of the WDs atmosphere (if any) and thus only a lower limit can be confidently placed on the age of this binary from the best fit cooling age for the WD, combined with an estimate of the main-sequence lifetime of the progenitor, which is likely equal to or larger than the WD cooling age. The age of the binary is thus > 1.94 Gyr.

3.3.5 UCD properties

$T_{\rm eff}$, mass and log g have been estimated from the Lyon group DUSTY models (Chabrier et al. 2000c; Baraffe et al. 2002), using the minimum age of the system (1.94 Gyr) and an estimated M_J for 2MASSJ0030 − 3739. The models indicate that 2MASSJ0030 − 3739 has $T_{\rm eff} = 2000 - 2400$ K, mass=$0.07 - 0.08\,{\rm M}_{\odot}$ and log g=5.30 − 5.35, placing it close to the limit for hydrogen burning. Note that the estimated $T_{\rm eff}$ is consistent with the semi-empirical estimates of Golimowski et al. (2004) for an M9 ±1 dwarf, which use well measured luminosities and a model constraint on radius (which changes by <10% for ages of 1 − 5 Gyr) to determine $T_{\rm eff}$ values spanning a wide range of spectral type. The full list of properties for the binary are listed in Table 3.4.

3.4 Searching SDSS and UKIDSS

A search for widely separated binary systems from a selected sample of WDs and UCDs from SDSS and UKIDSS (as described in §2.1.2 and 2.2.2) was conducted using a similar method as was used for the 2MASS and SuperCOSMOS search (described in in §3.2).

3.4.1 Simulated numbers of WD + UCD binaries

The number of potential WD + UCD binary systems that could be detected in the full coverage of SDSS and UKIDSS was estimated by Pinfield et al. (2006), who suggest that 50^{+13}_{-10} benchmark systems (with ages known to 10%) could be found out to a limiting magnitude of J≥19.0. The number of non-benchmark systems (where the WD <$0.7{\rm M}_{\odot}$) that could also be identified is estimated at five times that number, suggesting that up to 300 WD + UCD systems could be identified by combining UKIDSS with SDSS. Corresponding photometric properties were also derived and are shown in Fig. 3.9. The level of contamination from other objects such as high velocity stars (e.g. halo objects or red giants) was estimated at ∼400, which is comparable to the number of real systems expected via photometric selection alone. However, measuring a common proper motion for the components of potential systems should remove the majority of the contamination.

Table 3.4: Parameters of the binary 2MASSJ0030 − 3739 + 2MASSJ0030 − 3740 and its components.

Parameter		Value
Separation on sky	.....	89 arcsec
Estimated distance	.....	41 − 59 pc
Estimated line-of-sight separation	.....	3650 − 5250 AU
Minimum age of system	.....	> 1.94 Gyr
Ultracool Dwarf		
RA	.....	00 30 06.26
DEC	.....	-37 39 48.2
2MASS designation	.....	2MASSJ0030 − 3739
Distance	.....	41 – 75pc
2MASS J	.....	15.2 ± 0.05
2MASS H	.....	14.4 ± 0.05
2MASS K_s	.....	13.8 ± 0.06
DENIS I	.....	18.4 ± 0.23
DENIS J	.....	15.06 ± 0.14
SuperCOSMOS I	.....	∼18.3
μ RA	.....	-130 ±30 mas yr^{-1}
μ DEC	.....	-70 ±20 mas yr^{-1}
Spectral Type	.....	M9 ±1
Mass	.....	0.07 − 0.08 M$_\odot$
$T_{\rm eff}$	.....	2000 − 2400 K
log g	.....	5.30 − 5.35 dex
White Dwarf		
RA	.....	00 30 11.9
DEC	.....	-37 40 47.2
2MASS designation	.....	2MASSJ0030 − 3740
Distance	.....	27 − 59 pc
2MASS J	.....	16.1 ± 0.11
2MASS H	.....	15.8 ± 0.15
DENIS I	.....	16.2 ± 0.07
DENIS J	.....	15.9 ± 0.22
SuperCOSMOS B	.....	∼16.77
SuperCOSMOS R	.....	∼16.35
SuperCOSMOS I	.....	∼15.97
μ RA	.....	-83 ±30 mas yr^{-1}
μ DEC	.....	-70 ±12 mas yr^{-1}
Spectral Type	.....	DA
$T_{\rm eff}$	.....	7600±175 K
log g	.....	7.79 − 8.09 dex
Mass	.....	0.48 − 0.65 M$_\odot$
WD cooling age	.....	0.94 − 1.5 Gyr
WD progenitor age	.....	> 1 Gyr

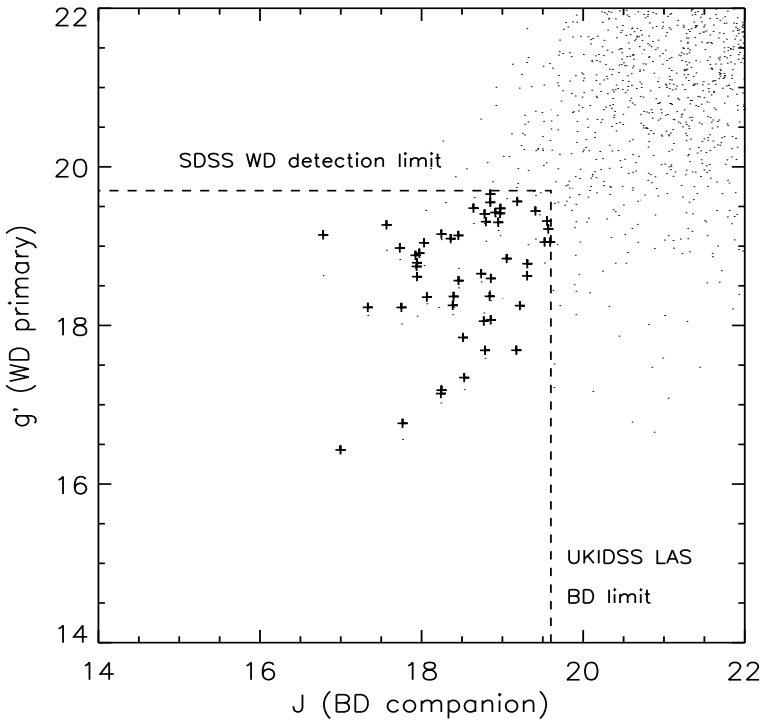

Figure 3.9: Simulated WD + UCD J- against g- magnitude diagram from Pinfield et al. (2006), showing a simulated population of WD + UCD binaries (dots) covering 10% of the sky for J≥16.0. Potential benchmark systems (WD $\geq 0.7 M_{\odot}$) are shown as plus symbols.

3.4.2 Binary selection

To select binary system candidates, firstly distance constraints were placed on the sample of WD candidates selected from SDSS using a CMD for WDs with known parallax from McCook & Sion (1999) in the SDSS colour system as shown in Fig. 3.10. In the same way as described in §3.2, this was used to estimate a lower distance for the WD candidate and thus a maximum separation based on a mass of $1.2 M_{\odot}$. UCD candidates were searched for out to an angular separation from each WD candidate corresponding to a projected separation of 20,000AU at this estimated distance. In order for a good UCD companion to be selected it must have a distance consistent with the WD it is paired with. This was assessed by placing the candidate UCD companion on a M_J against $J - H$ CMD, where M_J was calculated from the WD lower distance estimate and the UKIDSS J- band magnitude. The $J - H$ colour was chosen here, instead of the previously used $J - K$ colour (for L dwarf candidates in 2MASS), as T dwarfs have bluer NIR colour and can thus be very faint in the K- band. Selection regions were defined using known L and T dwarfs with measured parallax from DWARFARCHIVES.ORG. The regions defining these areas are shown as dotted (L) and dashed (T) line boxes, as illustrated in Fig. 3.11 and

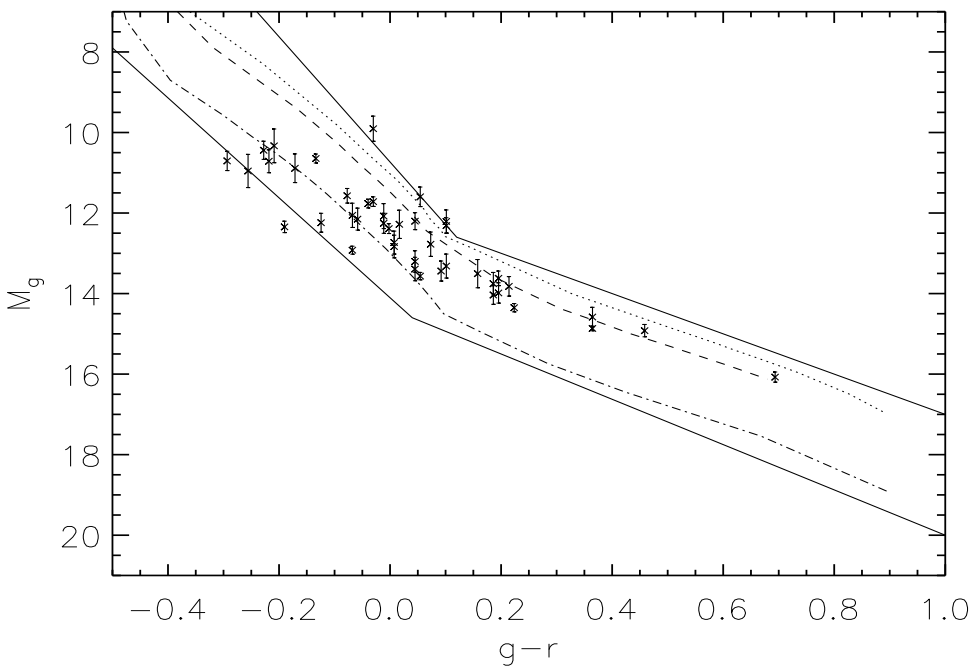

Figure 3.10: A WD colour-magnitude diagram for MS99 WDs with known parallax (crosses with error bars). Photometry is on the SDSS system. Overplotted are model cooling tracks (see §3.4.1) for WD masses of 0.5, 0.7 and 1.2 $M_\odot$ (dotted, dashed and dot-dashed lines respectively). The selected WD region in the CMD lies between the two solid lines.

were chosen to select objects with the most compelling UCD colours whilst minimising contamination from main-sequence stars. It is also noted that there is some cross over in the position of some late L and early T dwarfs, as is also shown by Knapp et al. (2004). The selection used here is flexible enough to account for this by allowing objects that have L dwarf $Y - J$ and $J - H$ colours, that also pass the T dwarf M_J, $J - H$ CMD criteria to be selected as possible L/T transition objects.

Candidate early/mid L dwarfs were selected if they occupy the L box in two-colour space (Fig. 2.5) and the corresponding L box in colour-magnitude space (Fig. 3.11). If an object is found in the L box in two-colour space and the T box in colour-magnitude space then is it selected as an L/T transition object, likewise a candidate T dwarf is selected if its position lies in the T box in both colour and colour-magnitude selections. The criteria for the three selections are outlined here:

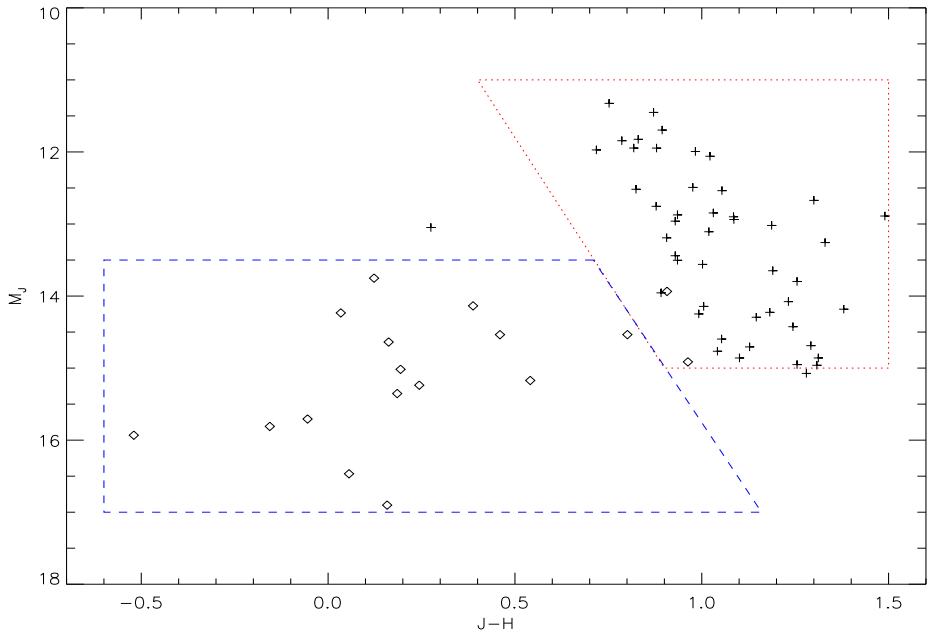

Figure 3.11: A UCD colour-magnitude diagram for L (plus symbols) and T (diamonds) dwarfs with known parallax from DWARFARCHIVES.ORG. The selection regions for L and T dwarfs are overplotted as dotted and dashed lines, respectively.

Early/Mid L dwarf colour and magnitude selection criteria:

$$0.4 < J - H < 1.2,\ 0.9 < Y - J < 1.5$$
$$\text{and}$$
$$11.0 < M_J < 15.0,\ M_J < 8.5(J - H) + 7.0$$

Late L/Early T dwarf (i.e. L/T transition objects) colour and magnitude selection criteria:

$$0.4 < J - H < 1.2,\ 0.9 < Y - J < 1.5$$
$$\text{and}$$
$$13.5 < M_J < 17.0,\ M_J > 8.5(J - H) + 7.0$$

Mid/Late T dwarf colour and magnitude selection criteria:

$$-0.5 < J - H < 0.4,\ 0.9 < Y - J < 1.25$$
$$\text{and}$$
$$13.5 < M_J < 17.0,\ M_J > 8.5(J - H) + 7.0$$

An IDL program was written to search for candidate pairs amongst the 22,087 WD and 24,293 UCD candidate objects using these selection criteria, which resulted in a sample of 517 candidate binary systems.

3.4.3 Candidate WD + UCD systems

As SDSS covers a large section of sky common to that of UKIDSS, the UCD candidates were cross matched with objects in the SDSS DR6 database, using the cross matching facility in a 2 arcsec radial search, which should detect any optical component for objects with a proper motion of less than $\sim$1 arcsec/yr. The UCD candidate sample was then split up into two categories; optical and non-optical detections. Properly assessing the optical non detections would require further follow-up beyond the scope of this thesis. For the optical detections additional colour cuts were used, based on the objects optical and optical-NIR colours.

Hawley et al. (2002) show that L and T dwarfs are separated quite well using $i-z$ and $z-J$ colours and suggest that $i-z>1.6$ would select M8 and later type dwarfs. Indeed Fan et al. (2001) and Chiu et al. (2006) select L and T dwarfs where $i-z>2.2$ and $z-J>2.0$. An $i-r$ colour could also be used, however many UCDs are very faint in the r- band and photometry can be unreliable. Following this approach, good L and T dwarf candidates were selected if they had i and z band SDSS counterparts with $\geq 5\sigma$ detections (corresponding to the approximate SDSS 5σ limits; $i<21.3$ and $z<20.8$), $i-z>1.75$, and $z-J>2.0$. Additionally a subset with $1.6<i-z<1.75$ and $z-J>2.0$ were also selected as candidate UCDs. Non $i-$ band detections or $'$drop outs$'$ were also considered, where the $z-J$ colour limits are consistent with being UCD like.

By including this optical selection the candidate list was reduced from 517 to 156. 68 have no optical counterpart within 2 arcsec of their NIR coordinates (implying $i>21.3$ and $z>20.8$) and are shown in Tables 3.11 and 3.12 as candidates named nBINx (where x is the identifying number). 18 are $i-$ band drop outs and are shown in Tables. 3.9 and 3.10 as candidates with name iBINx. 34 are good late M candidates, having $1.6<i-z<1.75$ and $z-J>2.0$ (Shown as candidates mBINx in Tables. 3.7 and 3.8). 36 are good L and T candidates based on their optical and optical-NIR colours ($i-z>1.75$ and $z-J>2.0$) and labelled as candidates bBINx in Tables. 3.5 and 3.6. These 156 candidates were also eyeballed in the UKIDSS/WFCAM images and the SDSS optical images to remove any spurious survey detection or non-star like objects. None of the candidates showed any

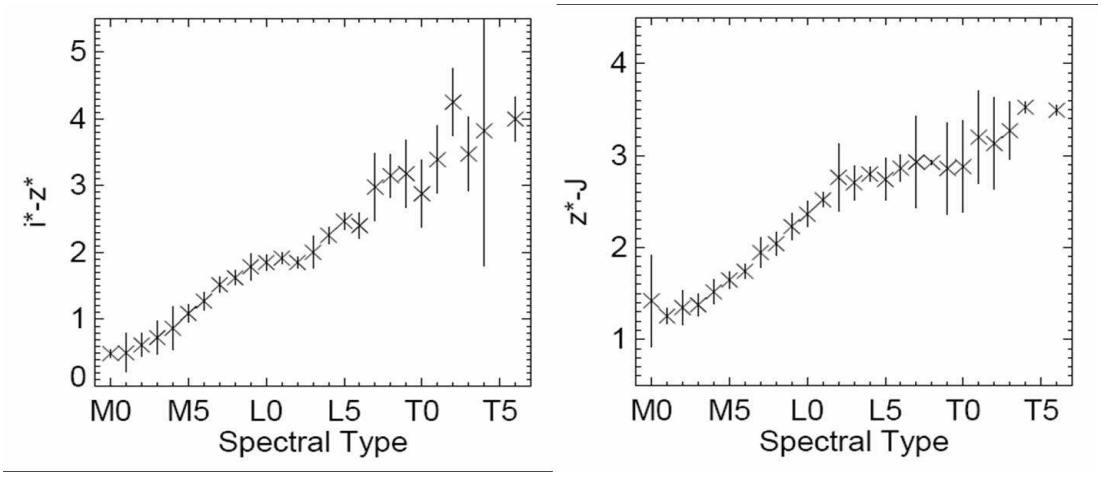

Figure 3.12: Left: $i - z$ against spectral type relation. Right: $z - J$ against spectral type relation from Hawley et al. (2002), showing means colours for each spectral type and the standard deviation of the measurements as error bars.

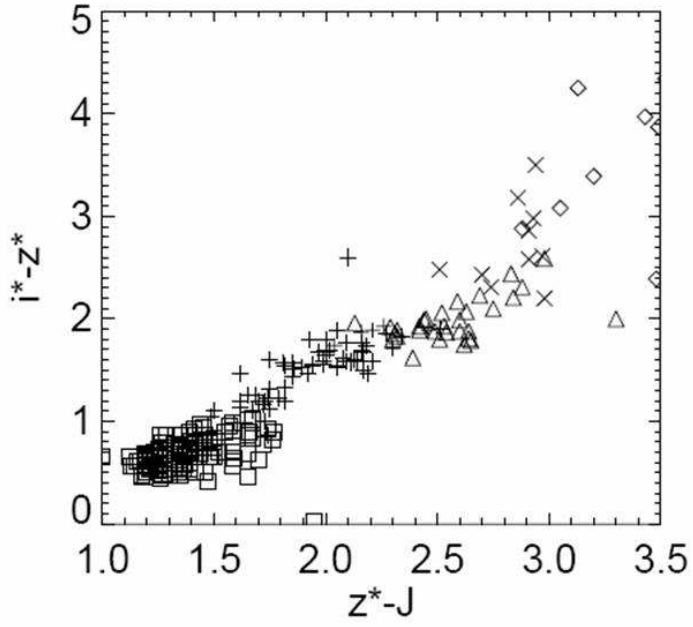

Figure 3.13: Colour-colour relations from Hawley et al. (2002). M dwarfs are shown as squares and plus signs, early L dwarfs as triangles, late Ls as crosses and Ts as diamonds.

sign of being spurious and are thus plotted in Figs. 3.14 and 3.15.

In addition the WD candidates were cross matched with the SDSS spectroscopic catalogue to check if any had spectra that could confirm them, or not as such. Of the 156 candidate WDs, 71 had spectra available from SDSS. Of these 36 are flagged as being WD (DA) targets and 35 are flagged as being $'$star$'$ like. This classification may not just contain main-sequence stars or late-type stars, but may include more unusual WD types (DB, DC, DO, DQ, DZ) as well as unresolved, spectroscopic binaries containing a WD member. Proper motion measurements were also checked for in the SDSS archive, which are measured by matching SDSS positions against the USNO-B1.0 catalogue (Monet et al. 2003). Details of all 156 candidate binary pairs are shown in Tables. 3.6 - 3.12.

3.4.4 Second epoch imaging and proper motion analysis of candidate UCDs

One of the candidate binary systems (bBIN1) has spectroscopically confirmed components as a DA WD and an L3 dwarf, however on inspection of the published proper motion of the WD (from SDSS) and the L dwarf (Jameson et al. 2008) they do not appear to share a common proper motion and this pair were thus ruled out as a potential binary system.

Additional pairs were prioritised from the list of candidates (where the WD component had a measured proper motion of >100mas/yr) for follow-up second epoch imaging on IRIS2/AAT during 2008 20-24 February. Nine candidates were imaged in the J-, H- and K- bands during poor weather time (seeing $>$ 2 arcsec). The images were reduced using the ORACDR package for IRIS2 and proper motions calculated using the IRAF routines GEOMAP and GEOXYTRAN using an average of 15 reference stars, as is described in §3.3.1. In the majority of cases the motion was less than a pixel and the baseline on average only $\sim$1 yr. Combined with high residuals of the transformations from the WFCAM/UKIDSS images onto the IRIS2/AAT images resulted in high uncertainties in the measurements. The proper motions of the nine UCD candidates, along with the measured proper motion of the WD counterpart are shown in Table. 3.13. Uncertainties were calculated from the residuals of the transformation combined with centroiding uncertainties of $\pm$0.5 pixels. Of the nine candidates measured two were deemed to be non-common proper motion and seven remain uncertain. In order to confirm the binary nature of these remaining seven candidate systems an additional epoch image is needed, ideally with a longer baseline.

Candidates bBIN17, bBIN26 and bBIN29 appear to have a sizeable proper motion,

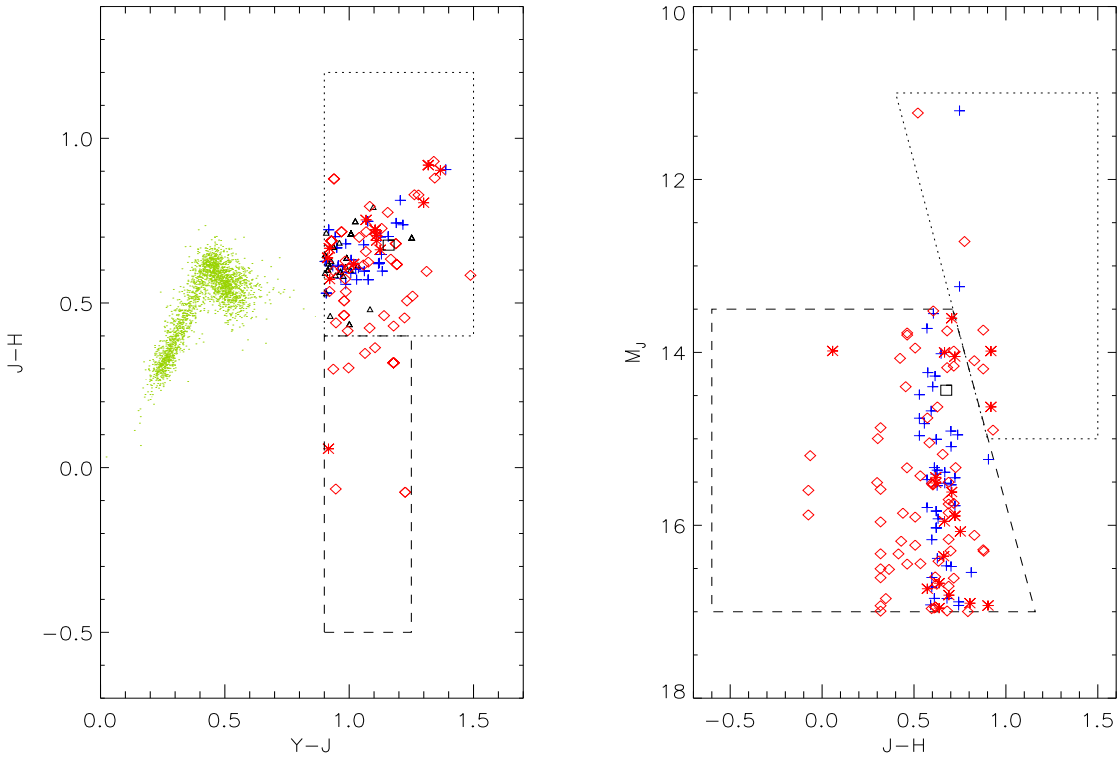

Figure 3.14: Left: A $Y-J$ against $J-H$ two-colour diagram. Right: An M_J against $J-H$ CMD of UCD candidate components of potential wide WD + UCD binaries. Blue plus symbols show L and T dwarf candidates with good optical colours, red asterisks are $i-$ band drop outs, red diamonds are non-optical detections and black triangles are UCD candidates with good optical colours, also overplotted are main-sequence stars as green dots. The open square shows the widely separated UCD candidate system from the spectroscopic WD + M dwarf (nBIN7; see §3.4.4). Also shown are the L and T dwarf selection regions (dotted and dashed boxes, respectively).

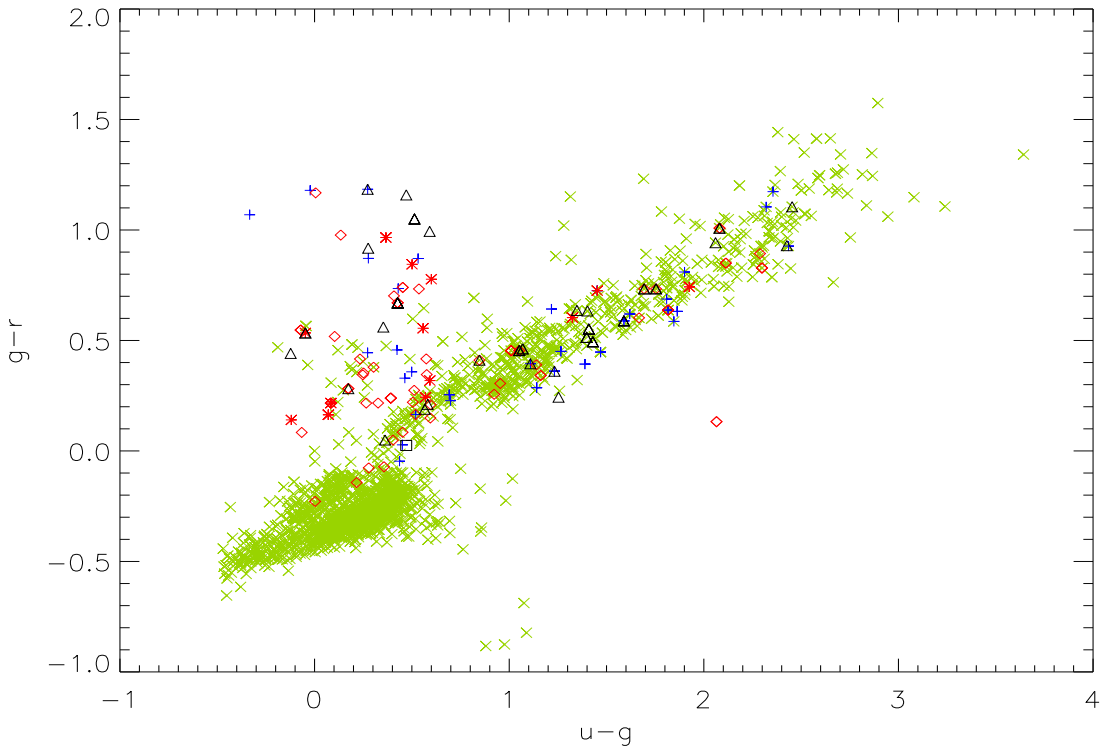

Figure 3.15: A $u-g$ against $g-r$ two colour diagram showing WD candidate components of potential wide WD + UCD binaries. Blue plus symbols show WD candidates whose L and T dwarf candidate counterparts have good quality optical colours, red asterisks are $i-$ band drop outs and red diamonds are optical non-detections, also overplotted are spectroscopically confirmed WDs as green crosses. The open square shows the widely separated WD candidate that appears to be an unresolved WD + M dwarf binary system (nBIN7; see §3.4.4).

Table 3.5: Parameters of the WD component of the WD + UCD binary candidates, where L and T dwarf candidates have optical colours $i - z > 1.75$ and $z - J > 2.0$.

ID	WD RA	WD DEC	g	$u-g$	$g-r$	M_g	D_{MIN} pc	SDSS[a] spectra?	WD?[b]	PM[c] mas/yr
bBIN1	221.61784	10.31341	18.27	0.27	0.87	19.09	6.87	y	y	8.0
bBIN2	0.82324	-0.69133	17.57	2.32	1.10	17.42	10.74	n	-	19.0
bBIN3	191.33584	12.09204	18.52	0.69	0.25	15.69	36.70	y	?	53.0
bBIN4	35.74638	1.149862	18.93	1.81	0.63	17.80	16.81	y	y	13.3
bBIN5	35.70941	1.087874	18.08	1.46	0.44	16.76	18.37	y	y	2.2
bBIN6	35.81944	1.097406	19.85	1.61	0.61	17.70	26.93	y	?	2.4
bBIN7	27.66100	-0.61713	20.82	2.35	1.17	20.75	10.32	n	-	10.6
bBIN8	136.03256	5.17269	14.14	1.14	0.28	13.77	11.85	n	-	27.6
bBIN9	136.03256	5.17269	14.14	1.14	0.28	13.33	14.52	n	-	27.6
bBIN10	134.14585	6.627492	15.23	1.58	0.58	14.84	12.00	n	-	23.1
bBIN11	33.16442	0.315815	19.20	0.46	0.32	16.11	41.59	n	-	25.1
bBIN12	230.69558	9.047541	15.37	1.86	0.63	15.05	11.55	n	-	36.0
bBIN13	45.41149	0.673927	21.03	0.42	0.73	18.34	34.58	n	-	15.6
bBIN14	131.02754	7.441029	18.86	0.53	0.87	19.08	9.03	y	y	5.1
bBIN15	341.88946	-0.33588	20.20	1.45	0.72	18.29	24.13	n	-	2.0
bBIN16	125.41386	2.323113	15.51	1.23	0.36	14.02	19.80	n	-	600.0
bBIN17	201.15371	8.965003	16.62	0.45	0.02	13.98	33.74	y	?	223.0
bBIN18	186.97874	14.29539	21.30	-0.02	1.17	20.78	12.72	y	?	20.6
bBIN19	36.15335	0.970674	20.40	0.42	0.45	16.81	52.15	n	-	32.6
bBIN20	237.54057	9.474614	14.76	1.21	0.64	15.11	8.51	n	-	4.8
bBIN21	50.82448	-0.64667	16.37	1.90	0.80	15.55	14.61	y	y	4.8
bBIN22	203.49940	0.28188	19.40	-0.33	1.06	17.24	27.01	y	y	387.3
bBIN23	226.95881	7.289019	21.19	0.27	1.18	20.81	11.90	n	-	13.3
bBIN24	227.62213	7.279871	14.71	1.38	0.39	14.13	13.07	n	-	28.0
bBIN25	337.61953	-0.39202	15.41	0.43	-0.04	13.21	27.51	y	y	29.0
bBIN26	226.50935	12.08509	19.58	0.69	0.22	15.55	64.20	y	?	142.0
bBIN27	342.45312	-1.01311	20.03	0.27	0.44	16.74	45.40	n	-	6.5
bBIN28	22.00966	-0.83069	17.52	2.43	0.92	15.95	20.63	n	-	11.2
bBIN29	203.42550	12.97313	18.09	1.10	0.39	16.47	21.15	y	y	273.0
bBIN30	190.70393	6.142031	14.27	1.80	0.68	15.13	6.70	n	-	263.0
bBIN31	125.41386	2.323113	15.51	1.23	0.36	14.02	19.80	n	-	n
bBIN32	204.74606	11.88798	18.20	0.49	0.35	16.27	24.42	y	y	5.4
bBIN33	50.22718	1.12256	20.22	1.84	0.58	17.52	34.63	n	-	4.6
bBIN34	188.44833	12.89613	17.28	0.51	0.16	15.20	26.01	y	?	n
bBIN35	224.16496	12.11607	15.16	1.26	0.45	14.33	14.65	n	-	21.4
bBIN36	341.88946	-0.33588	20.20	1.45	0.72	18.29	24.13	n	-	n

Notes: [a] A spectrum is available from SDSS. [b] SDSS target as WD or is classified as a WD.
? - SDSS classification is 'star' but may be a more unusual type of WD (i.e. DB, DC, DO, DQ, DZ).
[c] proper motion as measured by SDSS.

Table 3.6: Parameters of the UCD component of the WD + UCD binary candidates, where L and T dwarf candidates have optical colours $i-z$ >1.75 and $z-J$ >2.0.

ID	UCD RA	UCD DEC	J	$J-H$	$Y-J$	M_J	Separation	Separation	$i-z$	$z-J$
	degs	degs					arcsec	AU		
bBIN1	222.10729	10.53281	14.42	0.90	1.38	15.23	1930.96	13270.12	2.089	2.861
bBIN2	0.89488	-0.21635	16.70	0.81	1.20	16.54	1729.25	18575.69	1.774	2.655
bBIN3	191.31236	12.07832	16.06	0.74	1.07	13.23	97.89	3593.47	1.855	2.606
bBIN4	35.95639	1.06426	17.15	0.62	1.12	16.02	816.43	13725.35	1.883	2.596
bBIN5	35.95639	1.06426	17.15	0.62	1.12	15.83	893.17	16415.80	1.883	2.596
bBIN6	35.95639	1.06426	17.15	0.62	1.12	15.00	507.24	13660.48	1.883	2.596
bBIN7	27.92090	-0.86569	15.02	0.73	1.21	14.95	1294.66	13366.27	2.081	2.591
bBIN8	135.75381	5.27047	15.90	0.70	1.15	15.53	1063.43	12602.39	1.876	2.540
bBIN9	135.75381	5.27047	15.90	0.70	1.15	15.09	1063.43	15446.30	1.876	2.540
bBIN10	134.58187	6.72768	17.32	0.74	1.18	16.92	1610.58	19333.80	1.890	2.518
bBIN11	33.21045	0.40327	16.64	0.60	1.03	13.55	355.81	14801.71	1.974	2.493
bBIN12	230.63575	9.12049	17.02	0.59	1.06	16.71	339.64	3926.21	1.916	2.455
bBIN13	45.47679	0.53108	17.60	0.70	1.12	14.90	565.40	19554.30	1.922	2.451
bBIN14	130.62033	7.77405	16.62	0.67	0.98	16.84	1893.79	17107.54	1.810	2.440
bBIN15	341.70443	-0.43699	17.32	0.61	1.11	15.40	759.06	18323.32	1.822	2.419
bBIN16	125.40509	2.21258	17.27	0.57	1.07	15.79	399.16	7905.84	1.824	2.410
bBIN17	201.17509	9.03326	17.03	0.60	1.02	14.39	257.50	8689.43	2.025	2.361
bBIN18	187.17242	14.44828	16.99	0.70	0.94	16.47	888.31	11304.07	1.792	2.332
bBIN19	36.17794	1.00201	17.60	0.64	1.12	14.01	143.38	7478.02	2.034	2.299
bBIN20	237.48178	9.05534	15.16	0.66	0.95	15.51	1524.16	12971.55	1.818	2.295
bBIN21	50.68592	-0.69307	17.74	0.59	1.00	16.92	526.05	7686.51	1.859	2.274
bBIN22	203.32255	0.21910	16.83	0.59	0.97	14.67	675.58	18253.91	1.766	2.261
bBIN23	227.37811	7.47357	15.34	0.52	0.90	14.96	1649.21	19640.76	1.785	2.254
bBIN24	227.37811	7.47357	15.34	0.52	0.90	14.76	1121.59	14663.43	1.785	2.254
bBIN25	337.66729	-0.52167	16.47	0.61	0.95	14.27	497.39	13683.39	1.802	2.253
bBIN26	226.49679	12.13369	17.76	0.57	1.02	13.72	180.70	11601.16	2.291	2.243
bBIN27	342.53976	-1.05936	17.51	0.57	0.96	14.23	353.56	16052.41	1.889	2.238
bBIN28	21.93350	-0.81522	18.04	0.67	1.05	16.46	279.77	5771.85	1.919	2.233
bBIN29	203.17382	13.03917	18.01	0.62	0.90	16.38	936.72	19814.91	1.831	2.229
bBIN30	190.22282	6.04823	15.97	0.61	0.95	16.84	1764.60	11836.43	1.752	2.226
bBIN31	125.44366	2.49658	17.25	0.72	0.91	15.77	633.63	12549.84	1.779	2.221
bBIN32	204.64443	11.92594	17.86	0.63	1.00	15.92	390.54	9540.46	1.858	2.218
bBIN33	50.31347	1.22600	18.03	0.61	0.93	15.33	484.93	16793.86	1.864	2.217
bBIN34	188.37532	12.89610	16.90	0.55	0.98	14.82	262.84	6838.23	1.922	2.207
bBIN35	224.19619	11.89695	16.37	0.62	0.90	15.54	796.80	11679.44	1.817	2.205
bBIN36	342.01263	-0.35698	18.08	0.59	1.13	16.16	449.86	10859.40	2.011	2.201

Table 3.7: Parameters of the WD component of the WD + late M dwarf binary candidates selected from SDSS and UKIDSS.

ID	WD RA	WD DEC	g	$u-g$	$g-r$	M_g	D_{MIN} pc	SDSS[a] spectra?	WD?[b]	PM[c] mas/yr
mBIN1	194.49234	15.58729	20.17	0.47	1.15	20.67	7.96	y	y	2.7
mBIN2	37.526710	1.15889	18.68	2.45	1.10	17.42	17.89	y	?	9.0
mBIN3	130.48223	2.39738	18.98	0.56	0.18	15.33	53.71	y	?	76.0
mBIN4	171.00970	0.07283	19.21	0.84	0.41	16.56	33.93	y	y	1.7
mBIN5	170.94816	0.07170	16.45	1.05	0.45	16.79	8.53	y	y	6.8
mBIN6	170.90776	0.04772	19.97	2.08	1.00	16.22	56.05	y	?	4.7
mBIN7	171.02877	0.04855	14.81	1.06	0.46	14.36	12.26	y	y	1.1
mBIN8	170.92109	0.16004	16.97	1.69	0.73	15.29	21.71	y	y	16.0
mBIN9	170.86575	0.20482	16.91	1.75	0.73	15.29	21.09	y	y	1.1
mBIN10	170.94816	0.07170	16.45	1.05	0.45	14.34	26.43	y	y	6.8
mBIN11	22.95191	0.70853	20.13	2.42	0.92	19.40	13.96	n	-	19.9
mBIN12	22.97954	0.80239	16.10	2.06	0.94	16.00	10.48	n	-	12.3
mBIN13	22.52972	0.44318	18.71	0.59	0.99	16.86	23.43	n	-	n
mBIN14	132.22509	7.42600	20.50	0.42	0.67	17.98	31.95	y	?	11.6
mBIN15	21.12783	0.96516	14.30	1.43	0.49	14.47	9.21	n	-	22.6
mBIN16	209.07867	12.82209	19.40	0.58	0.21	15.46	61.47	y	y	63.0
mBIN17	128.19085	8.57491	19.75	0.27	0.91	19.34	12.03	y	y	4.0
mBIN18	128.15777	8.65947	15.26	1.40	0.55	14.67	13.12	n	-	24.0
mBIN19	6.95838	-0.17319	18.19	0.17	0.28	15.85	29.48	n	-	24.0
mBIN20	134.14585	6.62749	15.23	1.58	0.58	14.84	12.00	n	-	23.0
mBIN21	229.01525	9.07295	17.26	0.51	1.04	17.14	10.52	y	y	1.4
mBIN22	226.95881	7.28901	21.19	0.27	1.18	20.81	11.90	n	-	13.3
mBIN23	173.14897	0.51127	19.26	1.34	0.63	17.79	19.66	y	?	0.6
mBIN24	173.17076	0.48829	18.60	1.40	0.63	17.78	14.57	y	y	1.9
mBIN25	28.39781	0.26082	15.42	1.39	0.51	14.54	15.00	n	-	20.9
mBIN26	358.90307	0.19146	17.22	1.25	0.24	15.63	20.75	n	-	20.2
mBIN27	144.65409	7.24863	18.32	-0.04	0.53	17.23	16.47	n	-	27.0
mBIN28	52.55113	-0.54926	20.87	-0.12	0.44	16.72	67.40	n	-	n
mBIN29	144.65409	7.24863	18.32	-0.04	0.53	17.23	16.47	n	-	27.0
mBIN30	150.78918	7.63968	20.02	0.35	0.56	17.38	33.71	n	-	5.7
mBIN31	125.41386	2.32311	15.51	1.23	0.36	14.02	19.80	n	-	600.0
mBIN32	154.50003	8.63896	16.45	0.36	0.04	14.57	23.78	y	y	235.0
mBIN33	203.42550	12.97313	18.09	1.10	0.39	16.47	21.15	y	y	273.0
mBIN34	336.27880	0.14624	20.89	0.51	0.52	17.18	55.37	n	-	5.0

Notes: [a] A spectrum is available from SDSS. [b] SDSS target as WD or is classified as a WD.
? - SDSS classification is ′star′ but may be a more unusual type of WD (i.e. DB, DC, DO, DQ, DZ).
[c] proper motion as measured by SDSS.

Table 3.8: Parameters of the UCD component of the WD + late M dwarf binary candidates selected from SDSS and UKIDSS.

ID	UCD RA	UCD DEC	J	$J-H$	$Y-J$	M_J	Separation	Separation	$i-z$	$z-J$
	degs	degs					arcsec	AU		
mBIN1	194.19093	15.24543	16.04	0.60	1.00	16.53	1640.71	13068.13	1.68	2.50
mBIN2	37.58208	0.94662	17.21	0.61	1.03	15.94	789.73	14131.52	1.63	2.49
mBIN3	130.56904	2.40514	17.94	0.79	1.09	14.29	313.75	16851.89	1.62	2.46
mBIN4	170.93093	0.02568	16.27	0.71	1.00	13.61	330.49	11215.10	1.66	2.45
mBIN5	170.93093	0.02568	16.27	0.71	1.00	16.61	176.91	1510.71	1.66	2.45
mBIN6	170.93093	0.02568	16.27	0.71	1.00	12.52	115.14	6454.82	1.66	2.45
mBIN7	170.93093	0.02568	16.27	0.71	1.00	15.82	361.72	4436.00	1.66	2.45
mBIN8	170.93093	0.02568	16.27	0.71	1.00	14.58	485.00	10531.28	1.66	2.45
mBIN9	170.93093	0.02568	16.27	0.71	1.00	14.64	686.27	14480.38	1.66	2.45
mBIN10	170.93093	0.02568	16.27	0.71	1.00	14.15	176.91	4676.85	1.66	2.45
mBIN11	22.75033	0.43376	16.78	0.63	0.99	16.06	1226.81	17130.81	1.68	2.43
mBIN12	22.75033	0.43376	16.78	0.63	0.99	16.68	1562.67	16378.20	1.68	2.43
mBIN13	22.75033	0.43376	16.78	0.63	0.99	14.93	794.91	18626.26	1.68	2.43
mBIN14	132.24311	7.45873	17.99	0.69	1.25	15.47	134.52	4298.55	1.63	2.43
mBIN15	20.61140	0.97410	16.13	0.60	0.91	16.30	1859.43	17143.30	1.61	2.40
mBIN16	209.11651	12.85143	17.62	0.62	0.92	13.67	172.37	10597.37	1.69	2.36
mBIN17	127.82177	8.69213	17.16	0.59	0.96	16.76	1394.08	16784.49	1.70	2.36
mBIN18	127.82177	8.69213	17.16	0.59	0.96	16.57	1215.29	15946.19	1.70	2.36
mBIN19	7.02843	-0.26478	17.11	0.58	0.94	14.76	415.08	12237.70	1.61	2.32
mBIN20	134.17875	6.92316	17.30	0.74	1.02	16.90	1070.99	12856.52	1.63	2.32
mBIN21	229.18598	9.09350	16.85	0.66	0.93	16.74	619.06	6516.30	1.68	2.31
mBIN22	227.37811	7.47357	15.34	0.52	0.90	14.96	1649.21	19640.76	1.78	2.25
mBIN23	173.03959	0.36443	17.69	0.43	1.00	16.22	659.13	12962.98	1.66	2.25
mBIN24	173.03959	0.36443	17.69	0.43	1.00	16.87	649.44	9467.64	1.66	2.25
mBIN25	28.34825	0.29048	17.29	0.64	0.90	16.41	207.95	3119.87	1.61	2.23
mBIN26	359.05133	0.24332	17.57	0.58	0.97	15.98	565.43	11735.12	1.81	2.13
mBIN27	144.64984	7.54040	16.95	0.71	0.90	15.87	1050.45	17311.34	1.74	2.12
mBIN28	52.57260	-0.52133	18.03	0.59	0.90	13.88	126.83	8549.54	1.80	2.11
mBIN29	144.53628	7.37010	17.62	0.61	0.92	16.54	609.18	10039.17	1.73	2.07
mBIN30	150.78230	7.53372	18.04	0.46	0.92	15.40	382.26	12888.46	1.74	2.07
mBIN31	125.39768	2.05674	17.18	0.68	0.96	15.69	960.72	19028.31	1.71	2.06
mBIN32	154.51393	8.44871	17.41	0.62	0.91	15.53	686.72	16332.18	1.73	2.06
mBIN33	203.66122	12.86231	18.20	0.48	1.08	16.57	937.68	19835.23	1.95	2.05
mBIN34	336.23196	0.20562	17.84	0.61	0.98	14.13	272.27	15076.59	2.13	2.00

Table 3.9: Parameters of the WD component of the WD + UCD i- band drop out binary candidates selected from SDSS and UKIDSS.

ID	WD RA	WD DEC	g	$u-g$	$g-r$	M_g	D_{MIN} pc	SDSS[a] spectra?	WD?[b]	PM[c] mas/yr
iBIN1	341.88946	-0.33588	20.20	1.45	0.72	18.29	24.13	n	-	2.0
iBIN2	8.56741	-0.14720	17.62	0.07	0.16	15.20	30.54	y	?	4.5
iBIN3	52.88388	-0.91481	18.03	0.08	0.21	15.49	32.28	n	-	6.5
iBIN4	39.51829	-0.09603	19.19	0.55	0.55	17.35	23.32	n	-	5.0
iBIN5	144.65409	7.24863	18.32	-0.04	0.53	17.23	16.47	y	?	27.0
iBIN6	142.45962	10.84892	19.98	0.59	0.77	18.57	19.15	y	y	4.8
iBIN7	202.82298	9.15858	19.98	0.50	0.84	18.94	16.12	y	y	6.0
iBIN8	17.67502	-1.14424	15.49	-0.11	0.14	15.07	12.15	n	-	31.9
iBIN9	162.30271	-0.14858	18.43	0.56	0.24	15.63	36.19	y	?	n
iBIN10	338.48321	0.68342	20.48	0.59	0.31	16.05	76.99	n	-	0.5
iBIN11	210.52662	9.05355	19.42	0.36	0.96	16.08	46.49	y	y	7.6
iBIN12	353.90286	-0.42604	16.89	1.92	0.74	15.32	20.57	n	-	8.3
iBIN13	0.65565	0.45206	17.48	1.32	0.60	14.85	33.58	n	-	n
iBIN14	8.56741	-0.14720	17.62	0.07	0.16	13.35	71.39	y	?	n
iBIN15	162.30271	-0.14858	18.43	0.56	0.24	13.62	91.36	n	-	n
iBIN16	210.52662	9.05355	19.42	0.36	0.96	16.72	34.53	n	-	n
iBIN17	353.90286	-0.42604	16.89	1.92	0.74	15.61	18.01	n	-	n
iBIN18	0.65565	0.45206	17.48	1.32	0.60	14.91	32.59	n	-	n

Notes: [a] A spectrum is available from SDSS. [b] SDSS target as WD or is classified as a WD.
? - SDSS classification is 'star' but may be a more unusual type of WD (i.e. DB, DC, DO, DQ, DZ).
[c] proper motion as measured by SDSS.

Table 3.10: Parameters of the UCD component of the WD + UCD i- band drop out binary candidates selected from SDSS and UKIDSS.

ID	UCD RA	UCD DEC	J	$J-H$	$Y-J$	M_J	Separation	Separation	$z-J$
	degs	degs					arcsec	AU	
iBIN1	342.03421	-0.44069	18.27	0.66	1.12	16.35	643.34	15529.92	2.30
iBIN2	8.58669	-0.18066	18.31	0.72	1.10	15.89	139.03	4246.37	2.08
iBIN3	52.91433	-0.95821	18.49	0.66	0.92	15.95	190.85	6160.86	2.19
iBIN4	39.69617	-0.11760	17.91	0.75	1.06	16.07	645.07	15048.76	2.23
iBIN5	144.43609	7.31759	17.89	0.68	1.11	16.80	823.13	13565.03	2.32
iBIN6	142.58247	10.82616	18.14	0.57	0.92	16.73	449.78	8616.71	2.41
iBIN7	202.55589	9.15752	17.96	0.90	1.36	16.92	961.53	15506.40	2.64
iBIN8	17.96622	-1.09284	17.32	0.80	1.29	16.90	1064.51	12933.86	2.63
iBIN9	162.27127	-0.11369	18.40	0.70	1.10	15.61	169.10	6120.48	2.15
iBIN10	338.47644	0.64254	18.41	0.05	0.91	13.98	149.15	11483.85	2.03
iBIN11	210.46849	9.12587	17.32	0.91	1.31	13.98	334.05	15530.08	2.87
iBIN12	353.84167	-0.56285	18.23	0.63	0.91	16.67	539.50	11098.40	2.27
iBIN13	0.57525	0.44684	18.07	0.61	1.01	15.44	290.06	9743.06	2.51
iBIN14	8.58669	-0.18066	18.31	0.72	1.10	14.04	139.03	9926.62	2.08
iBIN15	162.27127	-0.11369	18.40	0.70	1.10	13.60	169.10	15449.88	2.15
iBIN16	210.46849	9.12587	17.32	0.91	1.31	14.63	334.05	11537.17	2.87
iBIN17	353.84167	-0.56285	18.23	0.63	0.91	16.95	539.50	9719.66	2.27
iBIN18	0.57525	0.44684	18.07	0.61	1.01	15.51	290.06	9454.11	2.51

Table 3.11: Parameters of the WD component of the WD + UCD non-optical detection binary candidates selected from SDSS and UKIDSS.

ID	WD RA	WD DEC	g	$u-g$	$g-r$	M_g	D_{MIN} pc	SDSS[a] spectra?	WD?[b]	PM[c] mas/yr
nBIN1	190.92890	14.83213	19.05	0.51	0.27	15.80	44.65	y	?	2.9
nBIN2	44.97204	-0.33116	20.60	0.40	0.70	18.16	30.76	n	-	16.0
nBIN3	154.05058	1.19911	18.90	0.35	-0.07	12.95	154.50	y	y	29.0
nBIN4	8.12547	0.19404	18.68	0.00	-0.22	11.32	296.23	y	y	15.0
nBIN5	154.52101	1.18986	16.27	0.21	-0.14	12.21	64.85	y	y	55.9
nBIN6	144.42053	8.22248	15.16	0.27	-0.07	12.90	28.40	y	y	5.2
nBIN7	194.93582	15.74895	18.15	0.47	0.02	13.95	69.23	y	?	100.3
nBIN8	217.80447	0.50087	19.47	0.30	0.37	16.38	41.52	y	?	7.0
nBIN9	35.74638	1.14986	18.93	1.81	0.63	17.80	16.81	y	?	13.0
nBIN10	33.75454	1.15135	17.58	0.95	0.30	15.97	20.95	y	?	12.5
nBIN11	50.85178	0.95288	20.08	2.29	0.82	18.85	17.58	y	?	2.2
nBIN12	53.14430	0.10522	19.90	1.66	0.60	17.61	28.66	y	y	19.6
nBIN13	5.87887	0.43965	19.22	0.92	0.25	15.71	50.38	n	-	5.7
nBIN14	238.93653	6.79168	18.97	1.01	0.45	16.79	27.30	y	y	224.0
nBIN15	238.93653	6.79168	18.97	1.01	0.45	16.79	27.30	n	-	n
nBIN16	220.68412	0.45411	18.02	0.40	0.04	14.57	49.01	y	y	92.9
nBIN17	141.21513	-0.29346	18.54	0.25	0.35	16.24	28.84	y	?	26.6
nBIN18	149.49652	-1.11873	17.71	0.45	0.08	14.76	38.94	n	-	133.9
nBIN19	6.95838	-0.17319	18.19	0.17	0.28	15.85	29.48	n	-	n
nBIN20	340.93621	1.15132	20.25	0.32	0.21	15.49	89.55	n	-	11.9
nBIN21	47.27010	-1.01693	20.23	0.53	0.73	18.33	23.98	y	?	24.8
nBIN22	52.88388	-0.91481	18.03	0.08	0.21	15.49	32.28	n	-	6.5
nBIN23	52.88388	-0.91481	18.03	0.08	0.21	15.49	32.28	n	-	6.5
nBIN24	147.51446	6.25106	19.28	0.57	0.41	16.59	34.58	y	?	2.7
nBIN25	131.50904	5.59424	19.46	0.10	0.51	17.15	28.96	y	?	n
nBIN26	137.86399	8.69466	19.70	-0.07	0.54	17.30	30.12	y	?	2.8
nBIN27	147.83970	10.12002	18.84	0.39	0.23	15.61	44.19	y	?	5.7
nBIN28	147.83970	10.12002	18.84	0.39	0.23	15.61	44.19	y	?	3.5
nBIN29	132.22509	7.42600	20.50	0.42	0.67	17.98	31.95	y	?	3.5
nBIN30	132.22509	7.42600	20.50	0.42	0.67	17.98	31.95	y	?	11.6
nBIN31	354.52755	0.10868	20.29	0.57	0.34	16.20	65.87	n	-	11.6
nBIN32	56.72113	0.14430	20.80	0.24	0.34	16.19	83.66	n	-	5.4

nBIN33	233.67401	7.81499	18.32	0.59	0.20	15.45	37.49	y	y	n
nBIN34	188.44833	12.89613	17.28	0.51	0.16	15.20	26.01	y	?	35.0
nBIN35	201.11300	8.07370	19.01	0.23	0.41	16.58	30.50	y	?	n
nBIN36	186.68428	6.64811	17.38	0.26	0.21	15.49	23.90	y	?	35.0
nBIN37	170.97576	0.24442	17.03	2.06	0.13	15.02	25.20	n	-	1.5
nBIN38	171.00970	0.07283	19.21	0.84	0.41	16.56	33.93	n	-	28.0
nBIN39	215.32078	0.46377	18.06	1.13	0.39	16.44	21.11	y	y	1.7
nBIN40	44.57451	1.16275	18.16	-0.06	0.08	14.76	47.84	y	?	5.1
nBIN41	144.26768	6.77433	18.67	0.59	0.14	15.12	51.37	y	y	4.7
nBIN42	189.20321	10.69730	19.33	0.50	0.22	15.51	58.04	y	y	46.7
nBIN43	170.97576	0.24442	17.03	2.06	0.13	15.02	25.20	y	?	60.6
nBIN44	6.95838	-0.17319	18.19	0.17	0.28	13.75	77.25	n	-	n
nBIN45	50.85178	0.95288	20.08	2.29	0.82	15.61	78.16	n	-	n
nBIN46	33.69876	1.25501	17.34	2.11	0.85	15.69	21.45	n	-	n
nBIN47	33.77895	1.14763	16.49	2.28	0.89	15.83	13.52	n	-	n
nBIN48	33.83406	1.18117	15.46	1.16	0.34	13.96	20.00	n	-	n
nBIN49	238.93653	6.79168	18.97	1.01	0.45	14.34	84.47	n	-	n
nBIN50	52.88388	-0.91481	18.03	0.08	0.21	13.53	79.42	n	-	n
nBIN51	137.86399	8.69466	19.70	-0.07	0.54	14.66	102.01	n	-	n
nBIN52	147.83970	10.12002	18.84	0.39	0.23	13.61	111.13	n	-	n
nBIN53	170.92109	0.16004	16.97	1.69	0.73	15.29	21.71	n	-	n
nBIN54	170.90776	0.04772	19.97	2.08	1.00	16.22	56.05	n	-	n
nBIN55	170.86575	0.20482	16.91	1.75	0.73	15.29	21.09	n	-	n
nBIN56	170.94816	0.07170	16.45	1.05	0.45	14.34	26.43	n	-	n
nBIN57	143.11360	7.83997	18.67	0.45	0.74	15.31	46.95	n	-	n
nBIN58	6.95838	-0.17319	18.19	0.17	0.28	13.30	95.00	n	-	n
nBIN59	143.90414	0.40610	20.12	0.13	0.97	16.78	46.64	n	-	n
nBIN60	50.85178	0.95288	20.08	2.29	0.82	16.04	64.27	n	-	n
nBIN61	33.69876	1.25501	17.34	2.11	0.85	16.15	17.35	n	-	n
nBIN62	33.83406	1.18117	15.46	1.16	0.34	13.60	23.54	n	-	n
nBIN63	238.93653	6.79168	18.97	1.01	0.45	14.16	91.52	n	-	n
nBIN64	137.86399	8.69466	19.70	-0.07	0.54	14.63	103.17	n	-	n
nBIN65	237.44277	6.14746	19.12	0.00	1.16	17.74	18.94	n	-	n
nBIN66	170.90776	0.04772	19.97	2.08	1.00	16.94	40.35	n	-	n
nBIN67	170.94816	0.07170	16.45	1.05	0.45	14.17	28.63	n	-	n
nBIN68	143.11360	7.83997	18.67	0.45	0.74	15.60	41.19	y	-	n

Notes: [a] A spectrum is available from SDSS. [b] SDSS target as WD or is classified as a WD.
? - SDSS classification is ′star′ but may be a more unusual type of WD
(i.e. DB, DC, DO, DQ, DZ). [c] proper motion as measured by SDSS.

Table 3.12: Parameters of the UCD component of the WD + UCD non-optical detection binary candidates selected from SDSS and UKIDSS.

ID	UCD RA	UCD DEC	J	$J-H$	$Y-J$	M_J	Separation	Separation
	degs	degs					arcsec	AU
nBIN1	190.95509	14.73274	18.29	0.58	1.48	15.04	370.00	16522.46
nBIN2	44.83241	-0.44363	18.95	0.36	1.10	16.51	645.48	19859.01
nBIN3	154.03607	1.17467	18.66	0.77	1.15	12.71	102.31	15807.88
nBIN4	8.13368	0.18884	18.58	0.52	1.25	11.23	34.97	10361.71
nBIN5	154.49481	1.19028	18.45	0.45	1.22	14.39	94.32	6117.91
nBIN6	144.35075	8.17548	18.45	0.43	1.17	16.18	302.86	8601.62
nBIN7	195.00953	15.72255	18.63	0.67	1.15	14.43	281.87	19516.62
nBIN8	217.77197	0.44333	18.62	0.60	0.96	15.53	237.90	9878.43
nBIN9	35.44890	1.27798	18.07	0.61	1.19	16.94	1166.02	19602.27
nBIN10	33.90968	1.31790	17.36	0.68	0.92	15.75	819.38	17169.04
nBIN11	50.83811	0.97248	18.21	0.68	1.18	16.99	86.02	1512.91
nBIN12	53.18057	-0.03293	18.96	0.62	1.07	16.68	514.23	14739.90
nBIN13	5.98596	0.42717	18.84	0.46	1.14	15.33	388.16	19556.24
nBIN14	238.94378	6.96888	18.51	0.41	0.99	16.33	638.43	17430.13
nBIN15	238.90513	6.79960	18.79	0.71	0.96	16.61	116.58	3182.94
nBIN16	220.76733	0.37788	18.63	0.65	1.06	15.17	406.23	19911.28
nBIN17	141.19961	-0.42033	18.53	0.50	1.23	16.23	460.13	13273.04
nBIN18	149.48941	-1.04838	18.37	0.53	0.98	15.42	254.55	9912.93
nBIN19	6.95321	-0.19272	18.63	0.87	0.93	16.28	72.74	2144.59
nBIN20	340.94342	1.09947	18.82	0.42	1.08	14.06	188.46	16878.51
nBIN21	47.08124	-0.96090	18.49	0.61	1.05	16.59	709.17	17011.82
nBIN22	52.93743	-1.07142	18.40	0.43	0.94	15.86	595.85	19234.24
nBIN23	52.89353	-0.86081	18.44	0.50	0.97	15.90	197.47	6374.37
nBIN24	147.50981	6.24843	18.44	0.71	1.06	15.74	19.24	665.73
nBIN25	131.64880	5.50063	18.75	0.53	0.92	16.44	605.54	17540.05
nBIN26	137.91061	8.68861	18.84	0.46	0.97	16.44	169.22	5097.25
nBIN27	147.89102	10.22367	18.55	0.72	1.13	15.33	416.36	18402.11
nBIN28	147.86074	10.13511	18.75	0.60	0.99	15.52	93.21	4120.02
nBIN29	132.20715	7.25334	18.04	0.59	0.93	15.51	624.92	19968.26
nBIN30	132.17518	7.53208	18.82	0.87	1.34	16.29	422.05	13486.08
nBIN31	354.46313	0.06112	18.85	0.57	0.98	14.75	288.27	18990.13
nBIN32	56.71809	0.19229	18.70	0.82	1.27	14.09	173.11	14483.16

nBIN33	233.70870	7.67471	18.98	0.82	1.26	16.11	520.20	19506.16
nBIN34	188.32243	12.88448	18.49	0.63	1.16	16.41	455.17	11841.78
nBIN35	201.09075	7.96770	18.71	0.69	1.04	16.29	389.91	11893.51
nBIN36	186.77626	6.48453	18.89	0.79	1.08	16.99	675.58	16148.58
nBIN37	170.79554	0.22210	18.97	0.59	1.31	16.96	653.75	16475.41
nBIN38	170.94703	0.04352	18.61	0.31	1.17	15.96	249.06	8451.83
nBIN39	215.42668	0.25190	18.47	0.34	1.06	16.84	852.69	18003.46
nBIN40	44.54674	1.26255	18.90	0.29	0.93	15.50	372.92	17841.59
nBIN41	144.25012	6.84019	18.74	-0.06	0.94	15.19	245.39	12606.73
nBIN42	189.13908	10.76618	18.81	0.30	0.99	14.99	338.80	19665.04
nBIN43	170.94703	0.04352	18.61	0.31	1.17	16.60	730.58	18411.68
nBIN44	6.95321	-0.19272	18.63	0.87	0.93	14.19	72.74	5619.87
nBIN45	50.83811	0.97248	18.21	0.68	1.18	13.75	86.02	6723.63
nBIN46	33.90968	1.31790	17.36	0.68	0.92	15.70	792.31	16999.11
nBIN47	33.90968	1.31790	17.36	0.68	0.92	16.70	772.78	10453.87
nBIN48	33.90968	1.31790	17.36	0.68	0.92	15.85	562.49	11253.94
nBIN49	238.90513	6.79960	18.79	0.71	0.96	14.15	116.58	9848.31
nBIN50	52.89353	-0.86081	18.44	0.50	0.97	13.94	197.47	15683.65
nBIN51	137.91061	8.68861	18.84	0.46	0.97	13.79	169.22	17263.90
nBIN52	147.86074	10.13511	18.75	0.60	0.99	13.52	93.21	10360.19
nBIN53	170.94703	0.04352	18.61	0.31	1.17	16.93	429.73	9331.15
nBIN54	170.94703	0.04352	18.61	0.31	1.17	14.87	142.19	7971.13
nBIN55	170.94703	0.04352	18.61	0.31	1.17	16.99	650.23	13719.71
nBIN56	170.94703	0.04352	18.61	0.31	1.17	16.50	101.52	2683.90
nBIN57	143.17445	7.77017	18.95	-0.07	1.22	15.59	333.36	15652.33
nBIN58	6.95321	-0.19272	18.63	0.87	0.93	13.74	72.74	6910.84
nBIN59	143.98204	0.48404	18.24	0.92	1.34	14.89	396.69	18503.12
nBIN60	50.83811	0.97248	18.21	0.68	1.18	14.17	86.02	5528.68
nBIN61	33.90968	1.31790	17.36	0.68	0.92	16.16	792.31	13754.01
nBIN62	33.90968	1.31790	17.36	0.68	0.92	15.50	562.49	13241.64
nBIN63	238.90513	6.79960	18.79	0.71	0.96	13.98	116.58	10670.73
nBIN64	137.91061	8.68861	18.84	0.46	0.97	13.77	169.22	17460.28
nBIN65	237.53698	5.93561	16.01	0.62	0.98	14.63	834.65	15811.03
nBIN66	170.94703	0.04352	18.61	0.31	1.17	15.58	142.19	5739.07
nBIN67	170.94703	0.04352	18.61	0.31	1.17	16.32	101.52	2906.80
nBIN68	143.17445	7.77017	18.95	-0.07	1.22	15.87	333.36	13733.22

Table 3.13: Proper motion analysis for followed up candidate WD + UCD binary pairs from SDSS and UKIDSS

Candidate UCD	PM RA (WD) mas/yr	PM DEC (WD) mas/yr	Baseline yr	PM RA[a] mas/yr	Pixel Motion (RA)	PM DEC[a] mas/yr	Pixel Motion (DEC)	CPM ?
bBIN1[b]	9	-80	-	-99	-	253	-	No
bBIN17	100	-199	1.01	307.7±226	0.69	-54.0±226	0.11	?
mBIN32	-117	-205	2.09	-279.5±141	1.46	21.7±135	0.11	?
bBIN26	-20	-143	1.02	-406.0±231	1.04	86.6±236	0.22	No
bBIN30	-150	-216	1.08	81.3±221	0.40	-114.2±224	0.49	?
bBIN29	241	-131	0.70	421.0±333	0.66	108.0±331	1.53	?
bBIN22	250	-328	2.69	33.1±88	0.19	2.0±85	0.01	No
mBIN33	241	-131	0.80	214.5±309	0.38	-59.0±285	0.10	?
nBIN7	-78	-64	1.08	165.6±219	0.40	48.6±216	0.11	?
nBIN16	24	-89	1.70	68.3±138	0.26	-69.8±135	0.27	?

Notes - ? Indicates uncertainty, due to high uncertainties and small measured motions

[a] - uncertainties on the proper motion from fit to the residuals of the transformation only.

[b] - UCD PM measurement from Jameson et al. (2008).

typically at least 100mas/yr if being conservative with the associated errors and taking them at their largest values. This would indicate that these objects, despite two of them being non-common proper motion with their paired WD may still be UCDs, as their sizable motion is indicative of a close by object. There may however still be some contamination from high proper motion halo objects. Spectroscopic follow-up would be required to confirm these as UCDs.

3.4.5 A candidate wide L dwarf companion to a spectroscopic WD + M dwarf binary

Of the nine candidates that were followed-up seven had spectra in SDSS, five of which were flagged as WDs, one flagged as being unknown and one has a spectra that appears to show that it is an unresolved WD + M dwarf binary. This candidate is the counterpart to the UCD candidate nBIN7 (from Tables. 3.12 and 3.13, which is an L dwarf candidate at a projected separation of 19,500AU). The SDSS spectrum is shown in Fig. 3.16, where

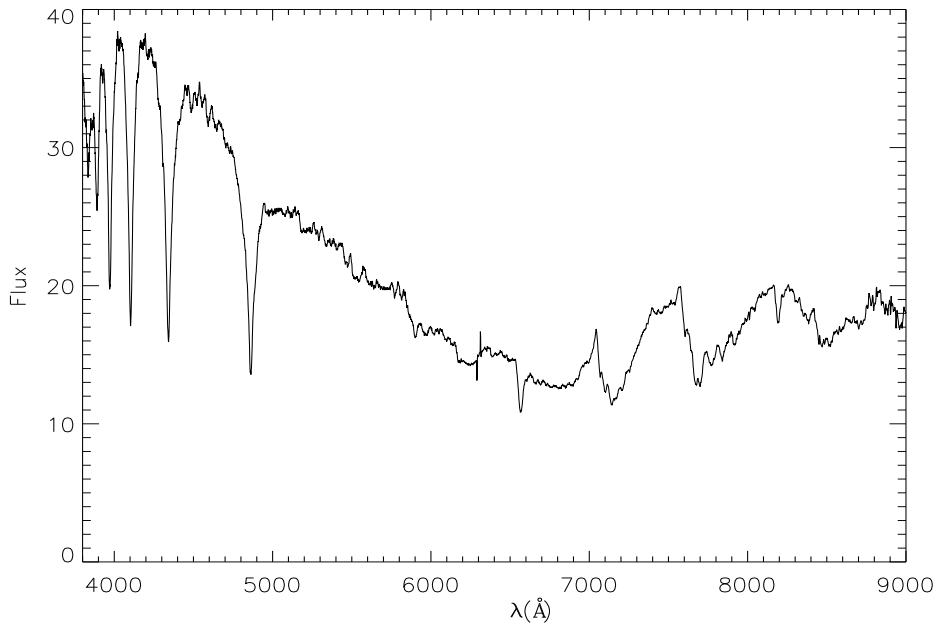

Figure 3.16: SDSS spectra of the WD candidate nBIN7.

the hydrogen Balmer lines of a DA WD are clearly visible at the blue end and features of a cooler M dwarf, such as the VO feature at 7500Å , NaI at 8200Å and CaH at 7050Å can be seen at the red end of the spectrum.

Estimating spectral types of the WD and M dwarf

In order to establish the WD and M dwarf contribution to the spectra, convolved spectral models were constructed. Template WD spectra were taken from the SDSS DR1 WD spectroscopic catalogue of Kleinman et al. (2004) and template M dwarf spectra were taken from Bochanski et al. (2007), who have co-added many spectra of the same spectral type to create template spectra for M0-L0 covering the SDSS wavelength range (3800-9100Å).

The WD and M dwarf spectra were both rebinned to the same dispersion and wavelength range as the original SDSS spectra. The WD and M dwarf components were then individually scaled to the peak of the flux of the WD and M dwarf, respectively. The WD was firstly normalised to the flux peak in the SDSS reference spectrum at 4000Å the M dwarf spectrum was then scaled to the peak of the flux of the M dwarf component at 8080Å in the SDSS reference spectrum. Both components were then smoothed to the same resolution as the SDSS reference spectra and finally combined together, by adding the WD and M dwarf components. This was repeated for different combinations of DA WD and UCD (M0-L0) and overplotted onto the original SDSS spectra for visual comparison.

The best fit to the SDSS spectra was found by visually inspecting the fit to the model spectra. On first inspection the best fit to the WD comes from a DA4/5. The WD + M dwarf spectra for a DA4 and DA5 are shown in Figs. 3.17 and 3.18. On closer inspection to the depth and width of the Balmer lines and the depth of the features in the M dwarf combined with the overall fit, the best fitting spectral combination is provided by a DA4 + M4, as shown in Fig. 3.19.

To verify the spectral type of the M dwarf and check for any possible spectroscopic peculiarities, the model DA4 was deducted from the original SDSS spectrum and spectral ratios covering the wavelength range 3800-9000Å were assessed, including the pseudo-continuum (PC) ratios from Martín, Rebolo & Zapatero-Osorio (1996) and Martín et al. (1999). The PC ratios use points in the spectrum that are less affected by molecular opacity that cause the true stellar continuum to be suppressed, causing a pseudocontinuum.

The PC1, PC2 and PC3 ratios were used over this wavelength range (3800-9100Å). The PC1 ratio (the mean flux in the ranges 7030-7050Å/6525-6550Å) gave a ratio of 1.406, which corresponds to a spectral type of an M4/5 from table 3 of Martín, Rebolo & Zapatero-Osorio (1996). The PC2 ratio (7540-7580Å/7030-7050Å) was measured as 1.677, indicating an M5 type. The PC3 ratio was also assessed, which is used as the primary index for spectral typing by Martín et al. (1999). The ratio (8230-8270Å/7540-7580Å) was measured as 1.148; indicating an M4 type. This verifies the M4 type that was initially estimated from the model comparison with the convolved spectra. The M4 spectra with the DA4 model removed is shown in Fig. 3.20, with the model M4 spectra overplotted for comparison.

An age estimate for the WD + M4 system

The spectrum of the M4 (with the WD component removed) can also be used to place a crude age estimate on the age of the system. West et al. (2008) calculated an age-activity relation for M dwarfs based on their Hα emission. Activity in M dwarfs has been shown to decrease over time and suggests that it is thus limited to a finite age (Fleming, Schmitt & Giampapa 1995; Gizis, Reid & Hawley 2002). If stars are still active they should show prominent Hα emission at 6562Å . The M dwarf spectra here (shown in Fig. 3.20), was compared to the template spectra of active and non-active M dwarfs from Bochanski et al. (2007) and shows no evidence of Hα emission. West et al. (2008) calculate an activity lifetime of $4.5^{+0.5}_{-1.0}$ Gyr for an M4 dwarf, which suggests that this system is ≥ 3.5 Gyr.

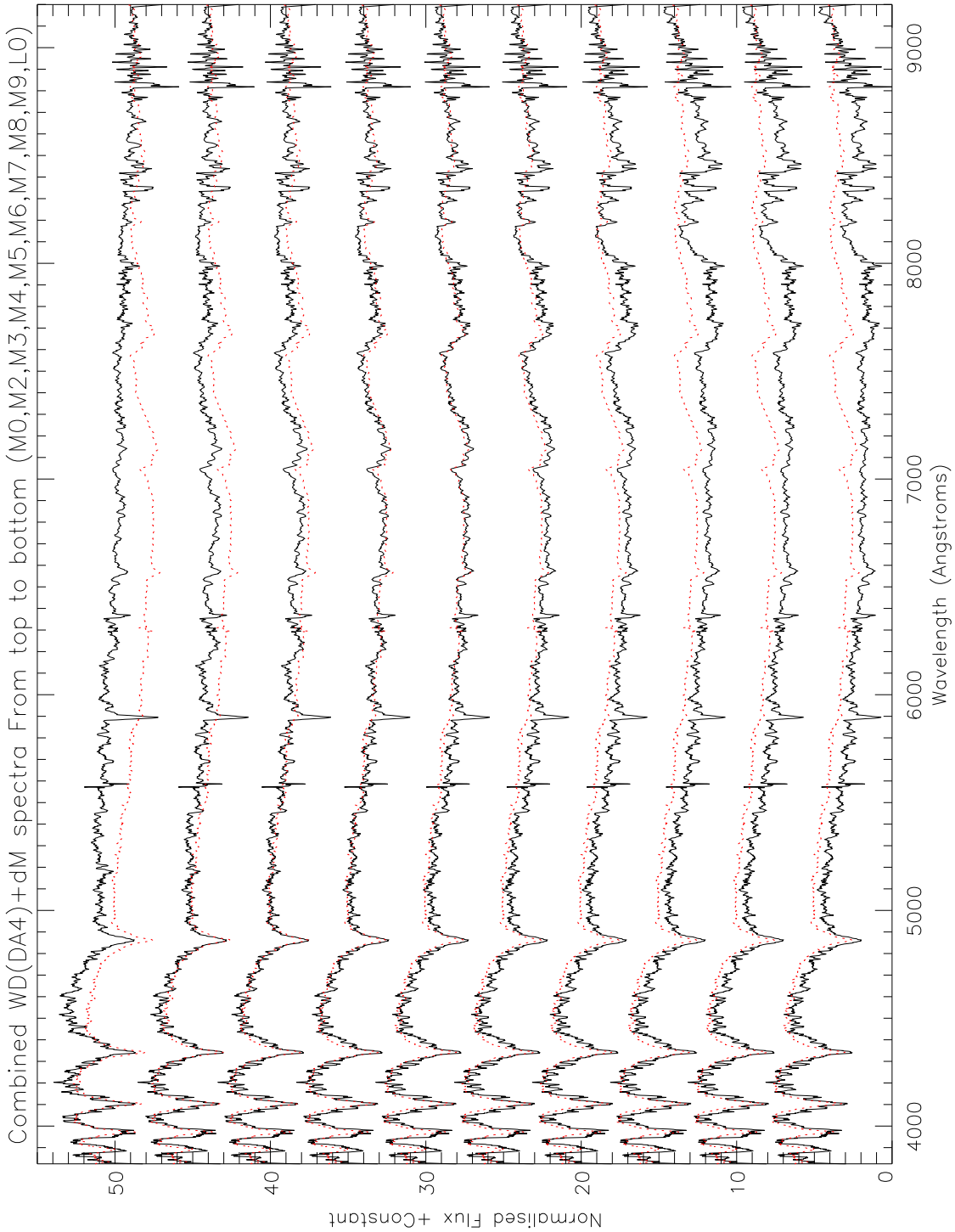

Figure 3.17: Model DA4 WD spectra combined with M0-L0 (top to bottom) spectra (solid lines) overplotted with the original SDSS spectra (red dotted lines) over the wavelength range (3800-9100Å).

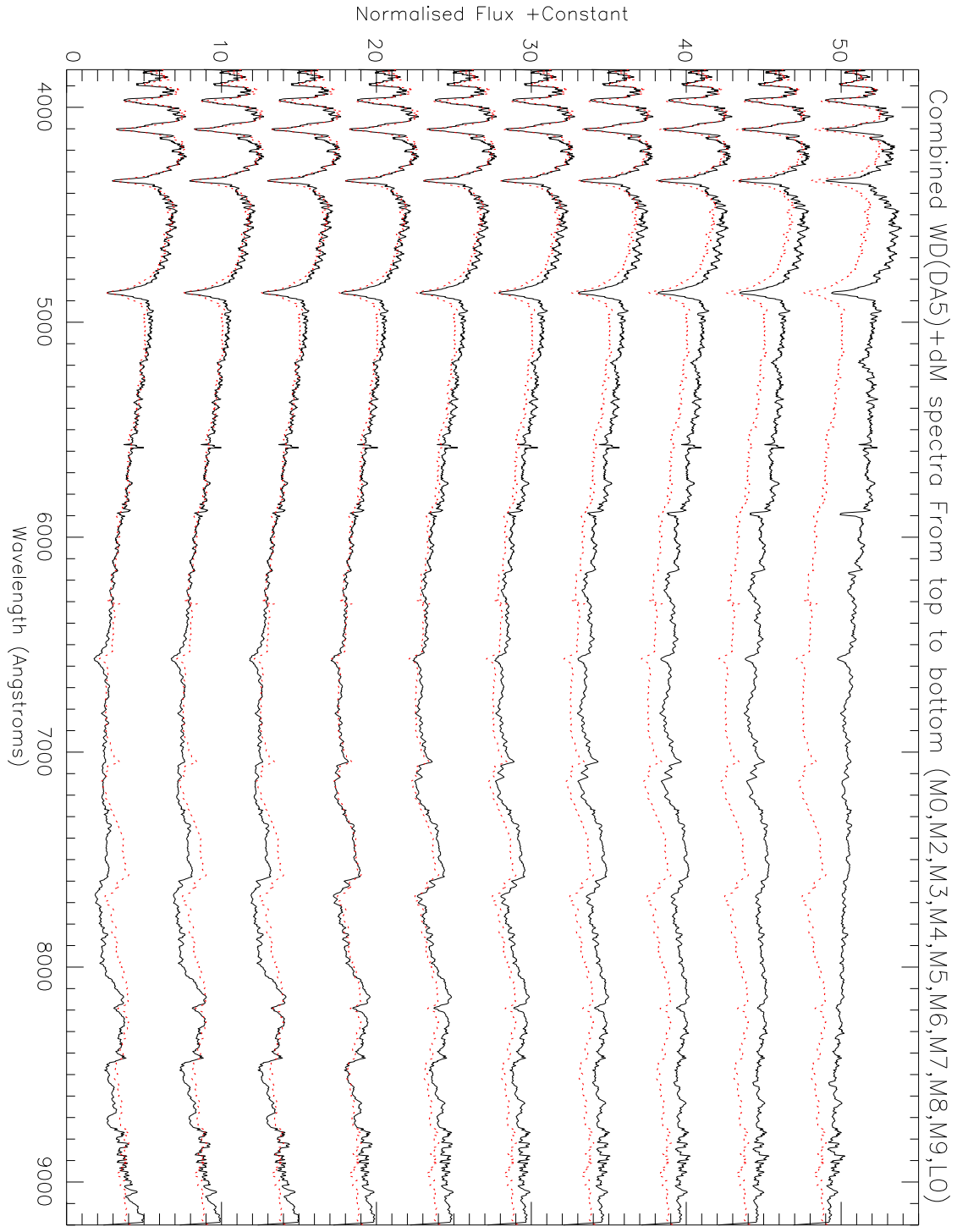

Figure 3.18: Model DA5 WD spectra combined with M0-L0 (top to bottom) spectra (solid lines) overplotted with the original SDSS spectra (red dotted line) over the wavelength range (3800-9100Å).

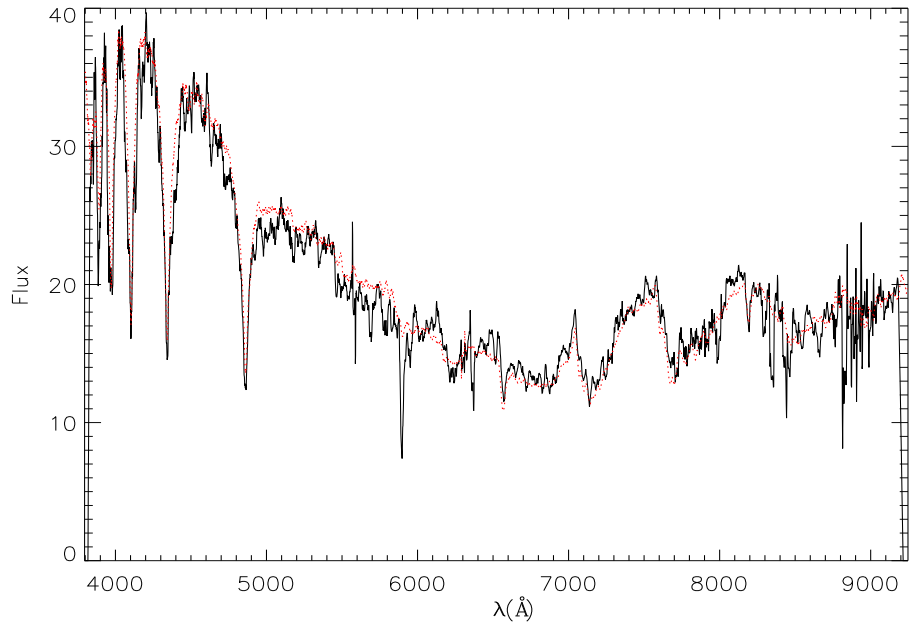

Figure 3.19: Model DA4 WD combined with an M4 spectra (solid line), overplotted with the original SDSS spectra (red dotted line) over the wavelength range (3800-9100Å).

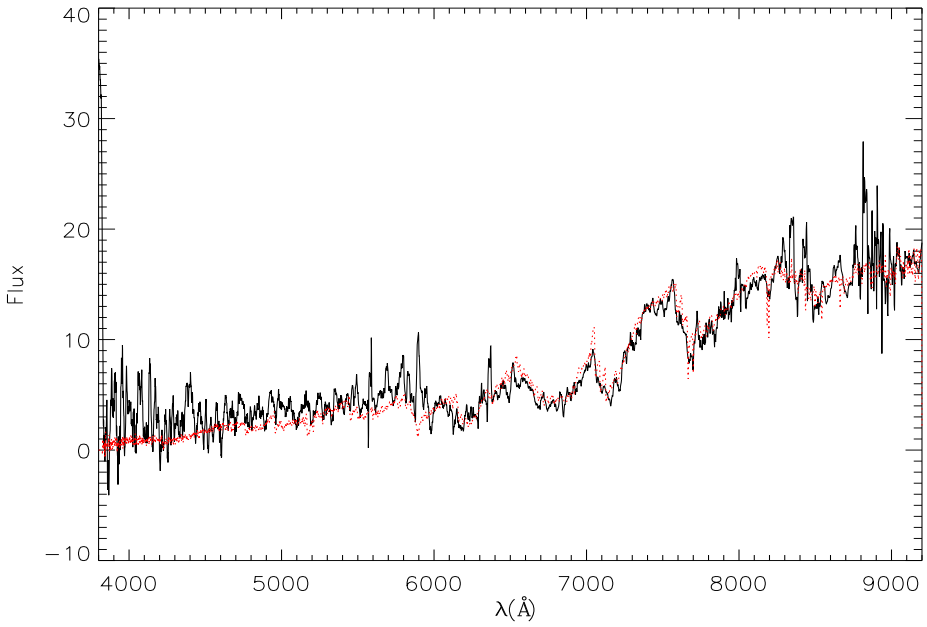

Figure 3.20: M4 component of the convolved spectra (solid line), created from the original SDSS spectra - model DA4 spectra, overplotted with the M4 model spectra (red dotted line).

Thus if the UCD wide binary candidate is confirmed as so, through proper motion and spectral analysis, it will have at least an independent minimum age constraint.

3.5 Summary of chapter

This chapter has presented the search for UCD companions to WDs using archival data from SuperCOSMOS and 2MASS, including the discovery of the widest separated UCD + WD binary system. Also presented were a large number of candidate UCD + WD systems from SDSS (DR6) and UKIDSS (DR3). Of these 156 candidate binaries, 10 UCD components have been followed-up with second epoch imaging to assess their proper motion. Three were found to be non-common and thus not UCD + WD binary systems. The other seven remain uncertain due to high uncertainties associated with their measurements arising from a combination of a short baseline and a small motion of the object. One of these uncertain systems however has a spectroscopic WD + M4 primary, which has a minimum age constraint of 3.5 Gyr, based on the non-presence of Hα in the M dwarf spectrum and the age-activity relations from West et al. (2008). Thus if this UCD is confirmed as such it will be add to the complement of UCDs with known ages and be able to provide useful information for trends in properties with age. Further studies of the WD will also allow an additional verification of the age of the system. Indeed if the WD proves to have a high mass, it is likely to yield an age constraint to within 10% accuracy, which would make it an ideal benchmark system.

The other candidates, along with the four systems (UCD5, 6, 7 & 8) remain uncertain from the search of SuperCOSMOS and 2MASS. All require additional epoch imaging to properly assess if their motion is common to their paired WD. Subsequent spectroscopy of any confirmed common proper motion systems would also be needed to confirm their nature as UCDs. The sample however looks promising for potentially finding a large number of UCD companions to WDs at wide separations. If confirmed these will greatly increase the number of such systems known as well as providing useful age constraints.

Chapter 4

Ultracool companions to Subgiants

Presented in this chapter is a search for widely separated UCD companions to subgiant stars in the southern hemisphere through a NIR imaging survey. The observational strategy, calibration and analysis is described that allows the selection of good candidate binary systems. In addition, the followup methods, subsequent analysis and the findings so far are summarised in the following sections.

4.1 A pilot survey of southern Hipparcos subgiants

A pilot survey was carried out to search for UCD companions to Hipparcos subgiants via NIR imaging, using the 3.9m Anglo-Australian Telescope (AAT) and the IRIS2 instrument (in wide field imaging mode) over an eight night run in 2005 December. The FOV allows for wide separations to be probed with relatively short integration times, enabling a subgiant to be efficiently imaged in three NIR filters over approximately 20 minutes per target.

4.1.1 Selection of subgiants

The subgiant sample were selected from the Hipparcos catalogue (Perryman et al. 1997) and as described in Pinfield et al. (2006), a publication on which I collaborated. Selected subgiants have well measured magnitudes, parallax distances and a large number have a constrained mass, age and metallicity from Feltzing, Holmberg & Hurley (2001) and from Nordstrom et al. (2004), who both derive metallicity from Strömgren photometry and then

use stellar evolution models to infer a corresponding age. Subgiants were selected based on their position on a M_V against $B-V$ CMD for stars with $V < 13.0$ and $B-V > 0.6$. A parallax measurement constraint was also imposed such that $\pi/\sigma \geq 4$, leading to an uncertainty in the parallax of $\leq$25%. A range in M_V of 2.0-4.5 was also chosen to avoid the brightest subgiants, for which glare may become as issue when trying to image faint, closely separated UCD companions, whose signal may be hidden by the PSF wings of very bright subgiants, which can extend for several arcsec.

The colour cuts were defined to select against dwarfs and giant stars, as shown by the selection boxes in Fig. 4.1, using solar metallicity isochrones from Girardi et al. (2000) as a guide. Note that these isochrones become bluer and brighter for lower metallicity and it is therefore possible that some contamination may arise from sub-solar metallicity giants in the top right of the selection region. To help minimise this contamination any objects spectroscopically flagged as giants in the Hipparcos database were removed from the sample. Another issue considered was interstellar reddening, that could make it difficult to separate L dwarfs photometrically from reddened background objects. Therefore subgiants in reddened regions where galactic extinction was higher than $A_V > 0.3 (E_{J-K} < 0.05)$ (derived from the reddening maps of Burstein & Heiles 1982) were removed from the sample. Areas of overcrowding were also avoided as blended point source profiles may become problematic when extracting photometry. These areas included the galactic plane, LMC, SMC and some areas where the nearest neighbouring object was <10 arcsec away. Subgiants with small proper motions ($< 40 mas/yr$) were also removed, as confirmation of UCD companions will be based partially on subsequent proper motion measurements. If a subgiant has a small proper motion it will be difficult to confirmation a UCD companion through common proper motion over a short baseline. Finally a distance constraint of 160pc was imposed, as L and T dwarfs at distances greater than this would have apparent brightnesses that are too faint to be detected in the exposure times that were used. This set of selection criteria gave a target sample of 918 subgiants.

4.1.2 Simulated populations

Simulations of the expected number of UCD companions to subgiants that could be discovered with imaging observations was presented in Pinfield et al. (2006). This was based on a simulated disk population of subgiants. A Salpeter mass function was assumed, with a birth rate history from Rocha-Pinto et al. (2000) and a disc scale height-age

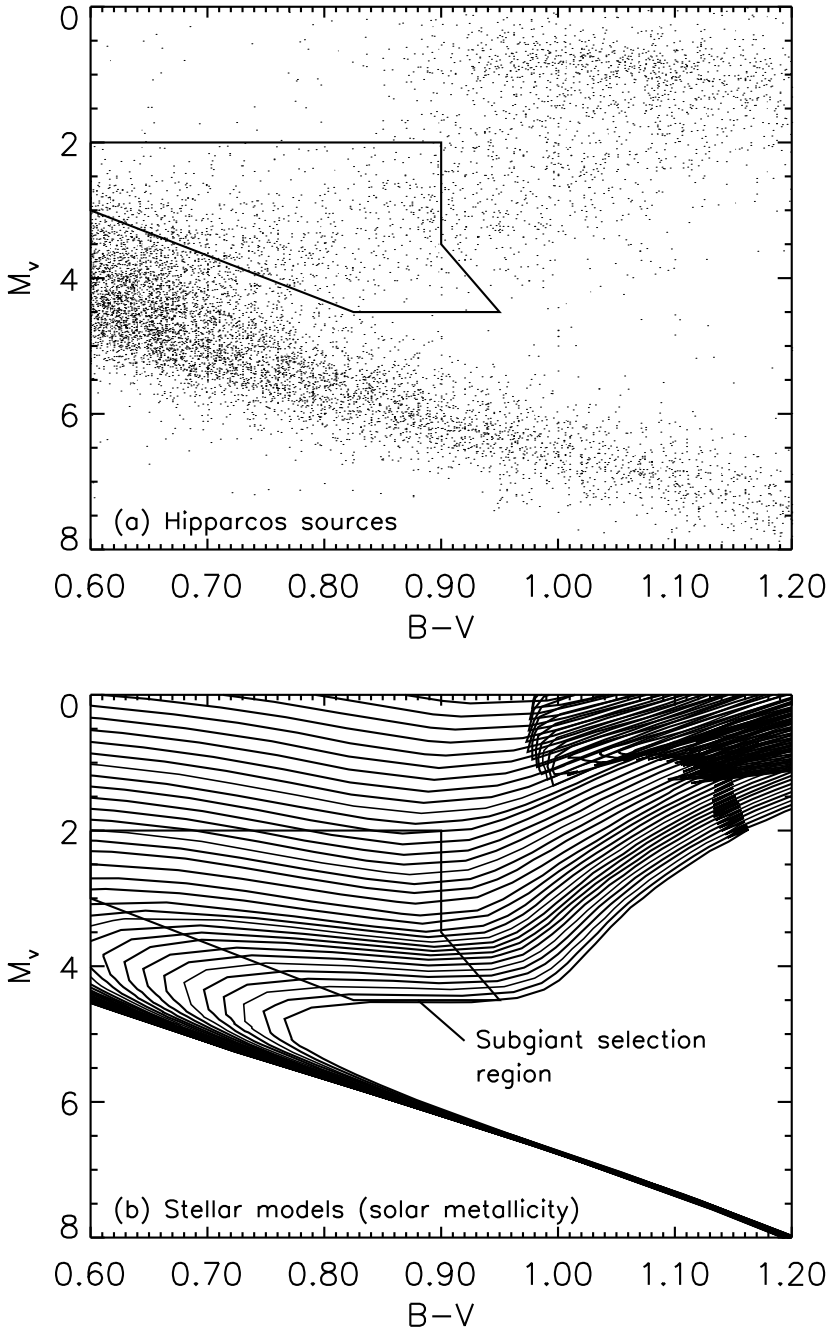

Figure 4.1: Subgiant selection. (a) An M_V against $B-V$ diagram of Hipparcos stars with $V < 13.0$ and $\pi/\sigma \geq 4$. (b) Theoretical isochrones from Girardi et al. (2000) for solar metallicity. Overplotted as boxed areas in both plots is the subgiant selection region.

relation from Just (2003). A metallicity distribution was taken from Edvardsson et al. (1993) and UCD companions were randomly added to the simulation around 34% of the subgiant sample (the wide binary fraction from Pinfield et al. 2006, although uncertainties associated with this fraction were also taken into account), with separations uniformally distributed between 1000-5000AU. An age distribution for the UCDs was derived for the subgiant sample and a UCD mass function of a power law where α=1 (following Gizis et al. 2001) was imposed. Lyon group models were used to derive $T_{\rm eff}$, log g and M_J from UCD mass and age, and a J- band magnitude was calculated for the distance of the subgiants. This simulated distance-magnitude and separation-distance distribution is shown in Fig. 4.2 and 4.3, respectively. Also shown in 4.3 is the glare limit, which corresponds to the minimum separation that could be imaged around a star. This was calculated from the brightness of the object. The brighter the object the larger the PSF wings (glare), however brighter objects are also generally closer and so separations of a few arcsec, correspond to only a few AU at these distances. This effectively causes the two effects to cancel each other out, creating a nearly vertical glare limit. A photometric limit of $J \leq$20 was also imposed on the selection of simulated UCD companions, such that UCD candidates could be spectroscopically followed up on an 8m class telescope. The simulation predicts that $\sim 80^{+21}_{-14}$ L and T dwarfs with $J \leq 20$ might be detectable around a sample of 918 subgiants within a distance of 160pc, across the whole sky. Note that this value, obtained from simulations is indicative rather than rigorously quantitative.

4.2 The pilot survey

Imaging of a subset of the sample was taken during 2005 December 05-12 on IRIS2/AAT in the J-, H- and Z- bands. The IRIS2 Z- band is actually very similar to the Y_{MKO} filter used by UKIDSS, thus UCD companions were selected via their colours based on previously described (see §2.2.2). Subgiants for this subset were selected so that they were visible at >30° (airmass <2) for at least an hour during the observing time allocation. Out of the sample of 918 subgiants, 384 were visible from the AAT during the scheduled observing time. Targets were then prioritised according to distance, so that the closest subgiants were higher priority, along with those that already had a well constrained mass, age and/or metallicity.

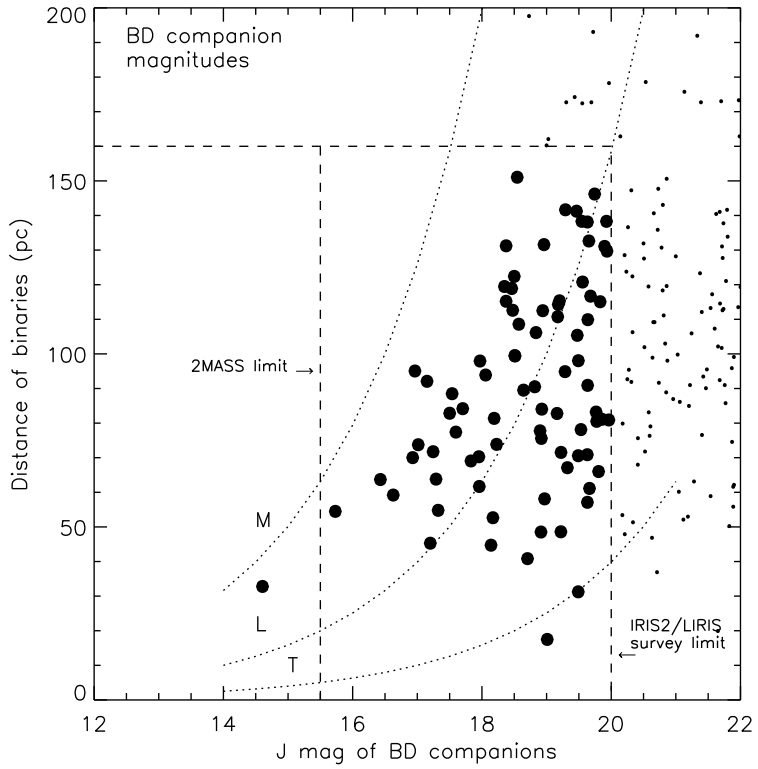

Figure 4.2: Simulated distance - magnitude distribution of UCD companions to Hipparcos subgiants from Pinfield at al. (2006). Dotted lines show the positions of the M/L, L/T and T/Y dwarf transition. The dashed lines show the photometric limits that were employed to simulate potential survey and followup limitations. The 2MASS photometric limit is also shown for comparison. The simulated UCD companions are overplotted as large filled circles.

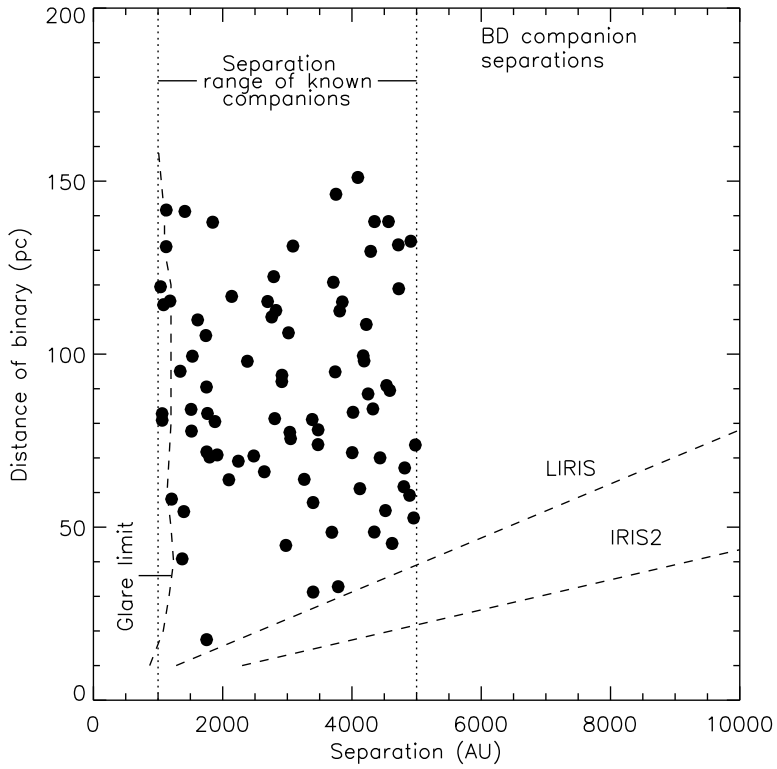

Figure 4.3: Predicted separation-distance distribution of subgiant + UCD binaries from Pinfield et al. (2006). The vertical dashed line shows the separation at which the subgiants PSF wings are expected to extend for the sky background to be doubled in the Z- band, thus indicating the lower limit above which the PSF wings will not significantly affect the detection of faint companions. The other dashed lines indicate the maximum separation covered by the IRIS2/AAT and LIRIS/WHT imagers. The dotted lines show the expected separation range for wide binary systems to main sequence stars (1000-5000AU), including subgiants. Overplotted as filled circles are the simulated UCD companions.

4.2.1 Observing strategy

The observing strategy adopted was to image around each of the subgiants by observing two fields, one to the north of the subgiants position and one to the south, so that the subgiant was just off the FOV. Observations made in this way also allow for wider separations around the subgiant to be searched. A separation of 1000AU at a distance of 50-150pc corresponds to an angular separation of 7-20 arcsec. It is estimated that ∼95% of the potential companion region around each subgiant are included when imaging in this way. The offset amount (between the edge of the array and the position of the subgiant) required was determined from the distance of the subgiant. The offset (in the DEC direction) was calculated as $\pm 231 + \frac{1}{2}(\frac{1000AU}{Distance})$ arcsec (where $231'' =$ half the FOV of IRIS2). The position of the IRIS2 observing field, with respect to the subgiant is shown in Fig. 4.4.

Over the eight night observing period 71 subgiants were imaged in the J-, H- and Z-bands, using total exposure times of 1, 2 and 5 minutes respectively. A five point dither pattern was used with 12s (J- and H-) and 60s (Z-) exposures at each position. The sensitivity reached using these exposure times, with the observing conditions (average seeing ∼1 arcsec) was J =19.0 to a 5σ detection limit.

4.2.2 Extraction and calibration of photometry

The images were reduced with the standard ORACDR package for IRIS2, as described in §3.2.1. Photometry was then extracted using the following IRAF routines. The DAOFIND routine was used to identify stars within the image that were above a minimum detection value of 5σ above the background value, and extended over a greater area than the full width half maximum (FWHM) of faint stars in the image to avoid selecting cosmic rays. This was measured by inspecting individual images using IMEXAMINE and taking the standard deviation of the background and measuring the average FWHM for fainter stars in individual images. A saturation limit of 25,000 counts was also imposed to avoid very bright, saturated objects in any image.

The process of detecting objects was checked by overlaying their coordinates onto the original image using the TVMARK command. The detection limit had to be changed on one or two occasions to strike the best balance between detection of faint stars whilst avoiding noisy background regions. The PHOT routine was then used to extract photometry of the

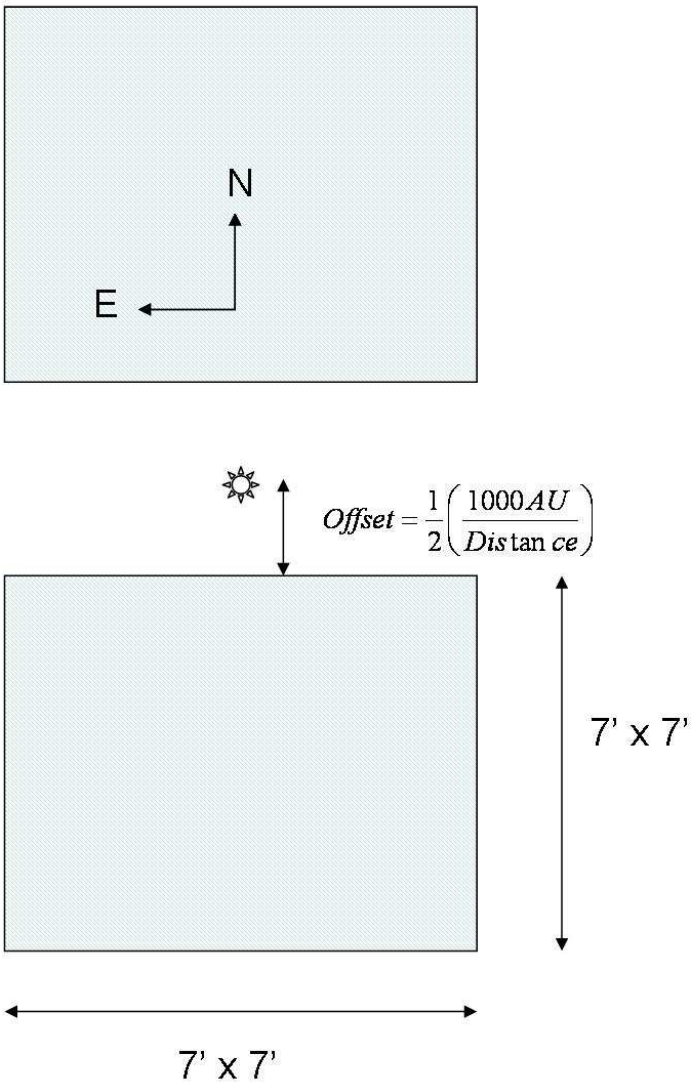

Figure 4.4: A diagram showing the imaging strategy used. The 7 X 7 arcmin FOV of IRIS2 was placed to the north and the south of each target subgiant, and offset in the ±DEC direction by an amount dependent on the subgiant distance (§4.2) (NOT TO SCALE).

objects using an aperture size of twice the FWHM (in pixels) and where the measured photometric uncertainty was $<5\sigma$ for each filter. Objects in all three filter images were cross matched by their pixel coordinates using the TMATCH routine, with a matching radius of three pixels.

Calibrating with standard stars

To calibrate the photometry, firstly the extracted magnitudes were normalised to 1 second exposures. This was done by adding a magnitude correction (MC), defined by the exposure time, such that MC=-2.5log(exposuretime). An airmass curve was then derived to determine a zero-point (ZP) as a function of the zenith distance. A0 standard stars were observed throughout the night at different airmasses and a ZP was calculated from the instrumental magnitude (and airmass). The STARLINK software GAIA was used to extract the flux (normalised to a 1 second exposure) and convert it to an instrumental magnitude, ZP where ZP=-2.5log(flux). The corresponding airmass was calculated from the zenith distance (obtained from the fits header) such that airmass=$\frac{1}{cos(ZD)}$. The ZP was then plotted for observations at different airmass to create an airmass curve by using a least squares fit to the observed data points. An example of this shown in Fig. 4.5. This was used to calculate a corresponding ZP for a said airmass.

An aperture correction was calculated using the true magnitude of the standard star, as measured by the 2MASS science archive. The aperture correction, being the difference between the true (2MASS) magnitude and the instrumental (IRIS2) magnitude. The 2MASS science archive provides magnitudes in the J- and H- bands. For the Z- band the knowledge that A0 stars have zero colour was used to assume the Z- band magnitude to be the same as the J- band magnitude. In addition the 2MASS magnitudes were converted into the MKO filter system (see §2.2.2) used by IRIS2, which were calculated from the colour relations of Carpenter (2001). For A0 stars ($J-H$=0), this correction was small (+0.002 mags). The calibrated magnitudes were then calculated as Mag_{cal}=ZP-Mag_{inst}-Aperture correction. This was repeated for each of the J-, H- and Z- bands, for each night of observation.

Calibrating with 2MASS objects

For the nights where no standard star observations were made or only one measurement was taken, due to bad weather causing short observing windows or the early closure of

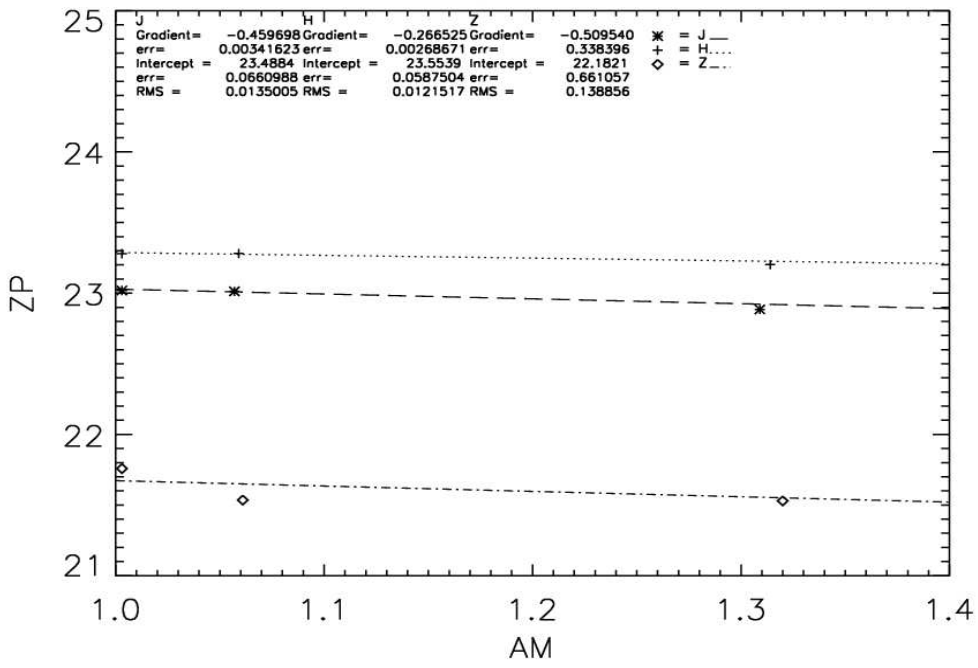

Figure 4.5: An airmass curve for standard star observations taken on the first night of observations (see §4.2.2).

the telescope, 2MASS objects in the images were used as secondary calibrators. The large FOV allowed enough reference stars to be identified from 2MASS for the purposes of a photometric calibration based on their $J-H$ colour. J- and H- band images were downloaded from the 2MASS infrared data archive for the same area of sky as the observations. The STARLINK package ASTROM was then used to convert 2MASS coordinates into pixel coordinates on the IRIS2 image, using a set of ∼10 stars for reference. The 2MASS objects were then matched with objects in the IRIS2 image using TMATCH in IRAF, as described previously. A calibration was determined by converting 2MASS magnitudes into IRIS2 magnitudes for the J- and H- bands and using the difference in magnitude (e.g. $J_{IRIS2} - J_{2MASS}$), which was calculated by plotting Δ magnitude as a function of J_{IRIS2}. Using a least squares fit to the data it was possible to interpolate for fainter objects visible in the IRIS2 images, that were not present in the 2MASS images. For the Z band, Z_{IRIS2}-J_{2MASS} was used and plotted against $J - H_{(2MASS)}$. A least squares fit was made to the data points and the difference in the magnitude at $J-H$=0 (the equivalent of an A0 star) was calculated and applied to the instrumental magnitude, along with the small (+0.002) correction to account for the differences in the filter systems. An example of the 2MASS calibration plot is shown in Fig. 4.6.

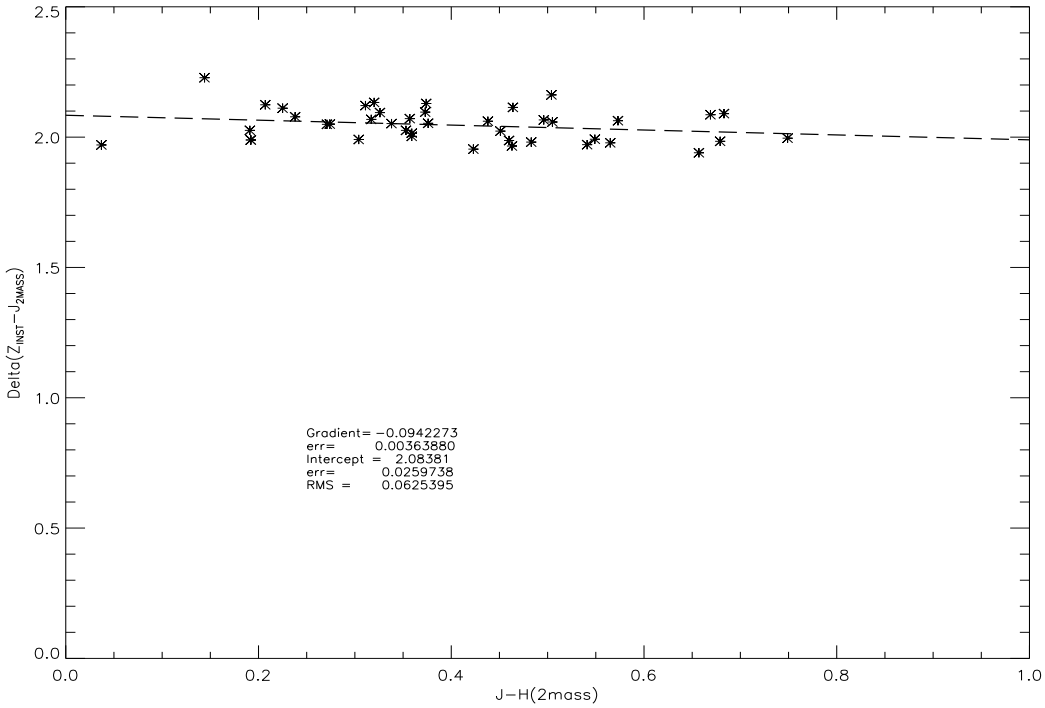

Figure 4.6: A $J - H$ against Δ magnitude plot showing the ZP calibration using 2MASS objects for the Z- band for one IRIS2 imaging field.

Calculating uncertainties on the magnitudes

The uncertainties associated with the calibrated magnitudes were calculated from the errors on the instrumental magnitude, which were taken from the uncertainties measured by IRAF when using the PHOT routine, as measured from the flux and background values of the images. The uncertainties on the ZP were taken from the RMS fit of the airmass curve and were typically $\pm$0.02-0.03 mags. Finally the uncertainty in the aperture correction must also be taken into account. This was also taken from the RMS of the aperture correction fit. These were all added in quadrature to give the final uncertainties on the calibrated magnitudes.

4.2.3 Selection of good candidate systems

In order to select star-like or point source objects and avoid contamination from extended sources (i.e. galaxies) an analysis of the shape of the objects in the images was made. Photometry was extracted for two aperture sizes; using a radius of one pixel, and of twice the FWHM (in pixels). For extended sources the difference in average flux between the two apertures should be greater than for point sources. This difference (in magnitude)

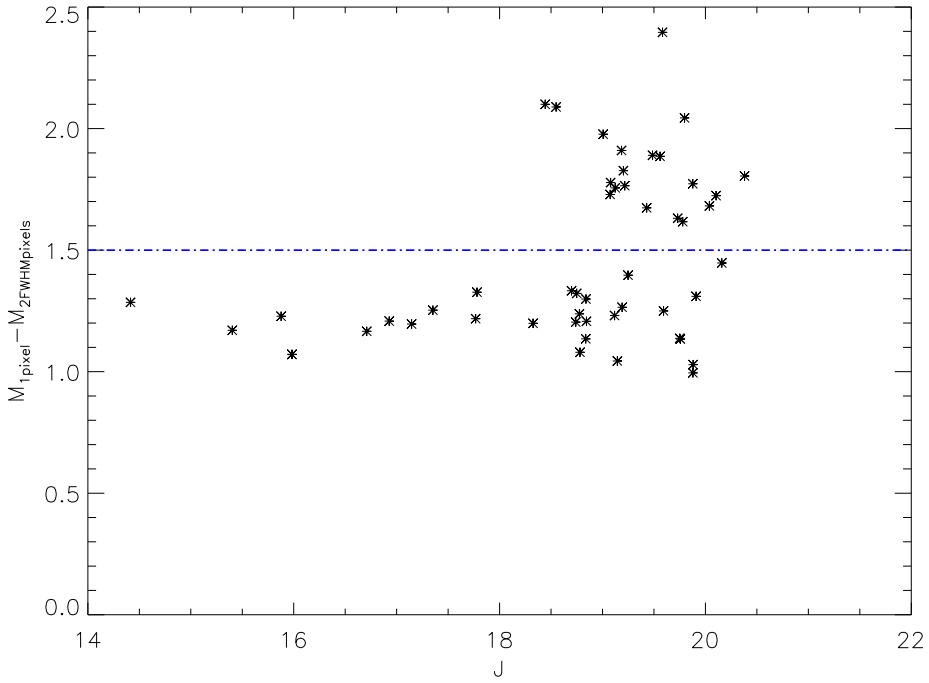

Figure 4.7: A plot of magnitude against the difference in flux between two aperture sizes in the J- band for objects in one image. Overplotted is the selection line (dot-dash), where point like objects were selected if they lay below this.

was plotted against instrumental magnitude for each band (e.g. Fig. 4.7) and shows that point and extended source objects are well separated, although it is noted that there is some scatter at fainter magnitudes. A selection line was chosen to encompass some of this spread but also remove objects that were clearly not point source like. Sources consistent with being star-like are selected if they lie below this selection line.

Colour and magnitude selection

Candidate L and T dwarfs were selected from their position on a two colour diagram and a CMD, based on previously described selections presented in §2.2.2 and §3.4, where M_J was calculated from the measured parallax distance of the subgiant. As the Z- filter of IRIS2 is similar to that of the Y- band filter used on WFCAM/UKIDSS, a similar two-colour selection space was used, with an expansion to allow for slight differences in the filter systems and errors on the colours. The expanded two-colour region is shown in Fig. 4.8 and overlaps with the colour selection used previously. The colour-magnitude space as presented in §3.4 was also adopted here and candidate UCDs were selected if they met the following photometric criteria.

L dwarf colour and magnitude selection criteria:

$$0.5 \leq J - H \leq 1.2,\ 0.9 \leq Z - J \leq 2.0$$
$$\text{and}$$
$$11.0 \leq M_J \leq 15.0,\ M_J \leq 8.5(J - H) + 7.0$$

L/T dwarf colour and magnitude selection criteria:

$$0.5 \leq J - H \leq 1.2,\ 0.9 \leq Z - J \leq 1.5$$
$$\text{and}$$
$$J - H \leq 1.25(Z - J) - 0.65 \text{ and } M_J \geq 8.5(J - H) + 7 \text{ and } M_J \geq 13.5$$

T dwarf colour and magnitude selection criteria:

$$0.5 \geq (J - H) \geq 0 \text{ and } Z - J \geq 0.5$$
$$J - H \leq 1.25(Z - J) - 0.65 \text{ and } M_J \geq 8.5(J - H) + 7 \text{ and } M_J \geq 13.5$$
$$\text{or}$$
$$0 \geq (J - H) \geq -0.5 \text{ and } Z - J \geq 0.5$$
$$J - H \leq 1.25(Z - J) - 0.65 \text{ and } M_J \geq 8.5(J - H) + 7 \text{ and } M_J \geq 13.5$$

Objects from each field imaged were plotted onto a two-colour diagram and a CMD and the position of candidate UCDs, with respect to MS stars (the bulk of the objects in the image) was inspected. Sources that sat close to the MS were rejected as they were deemed likely contaminant M dwarfs.

Whilst the selection and calibration was carried out meticulously there could still be some sources of contamination. One source may come from cosmetic effects such as cross talk, or from contaminant red giant stars, which exhibit similar colours to L dwarfs. In order to minimise this all candidates were eyeballed in the J-, H- and Z- band images to make sure they were good detections. Objects were also cross matched with the SuperCOSMOS science archive data where I- and R- band images were inspected to check for optical counterparts. The quoted limiting magnitude for detection in the SuperCOSMOS SSA I band is $\sim$18.5, but objects around a magnitude fainter can still be seen in the images. Objects with an R- and/or I- band counterpart such that $I - J \leq$3.0 were deemed not consistent with being UCD like, following the optical plus NIR colours of late M, L and T dwarfs from Hawley et al. (2002). If an object was not detected in

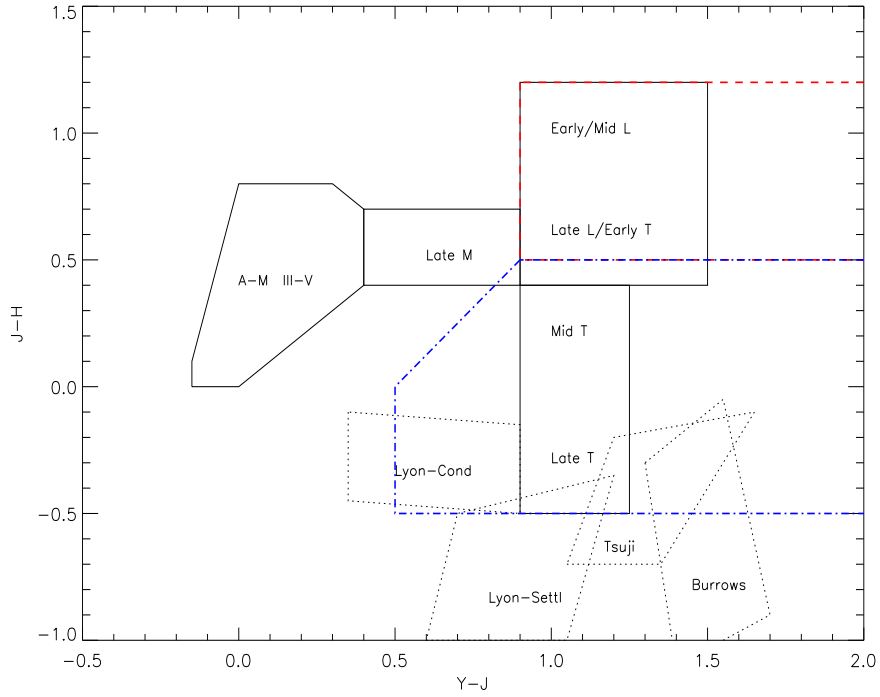

Figure 4.8: A $J-H$ against $Y-J$ two-colour diagram, showing the position of main sequence stars, M, L and T dwarfs, along with the predicted colours of very cool dwarfs ($T_{eff} < 700K$), as described in §2.2.2 and §3.4. Overplotted are the IRIS2 L and T dwarf selection area for subgiant companions as red dashed and blue dot-dashed lines, respectively.

the archive but was visible in the I- or R- band image, it was assumed that the I- band magnitude was $18.5 \geq I \geq 19.5$ and thus the $I-J$ colour assessed from this. If there was no I- and R- band detection then these remained good candidate UCDs.

This selection yielded 30 candidate subgiant + UCD wide binary systems, for which the UCD candidate components consisted of 2 L dwarf, 3 L/T and 25 potential T dwarf candidates. The details of the potential systems are shown in Fig. 4.9, where L dwarfs are shown as red plus signs, L/T candidates as orange asterisks and T dwarfs as blue diamonds, and are referenced in Table. 4.1.

4.3 Follow-up Observations

A follow-up program was undertaken to confirm the status of the candidate binary pairs and the nature of the UCD candidate components. In order to confirm companions the approach was taken to measure proper motion. The subgiants all have accurately measured proper motions and taking second epoch images will allow the proper motion of the UCD candidates to be calculated. Common proper motion pairs can then be searched

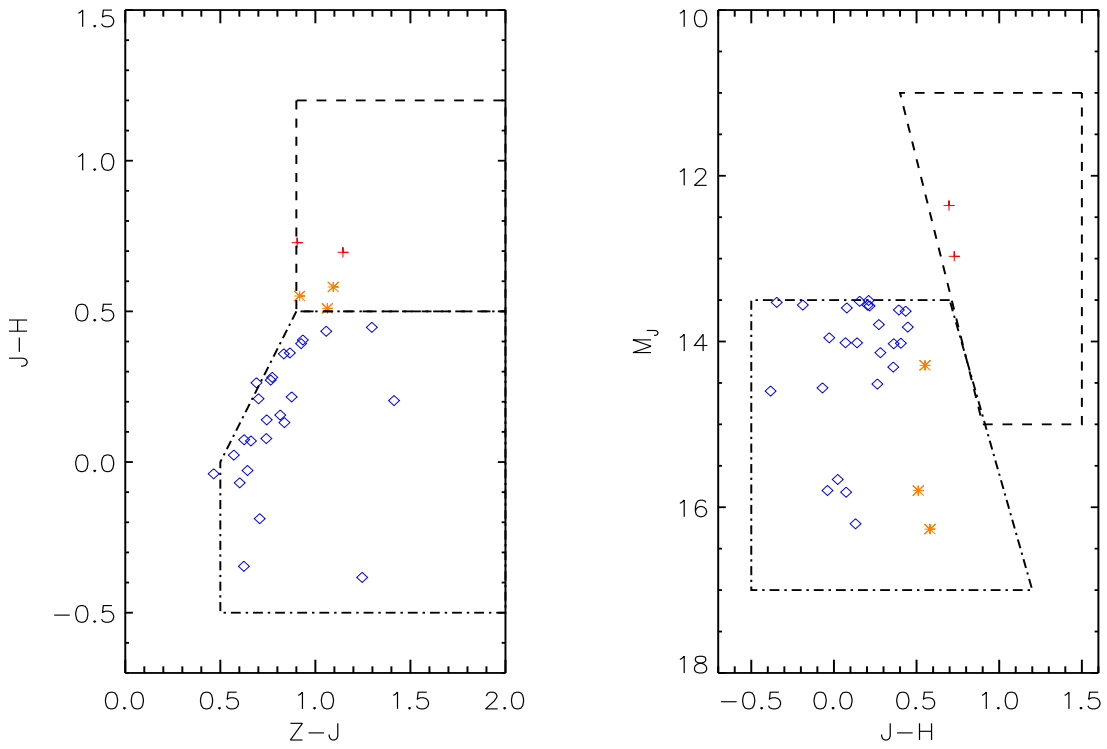

Figure 4.9: Left: A $J-H$ against $Z-J$ two-colour diagram, showing candidate L dwarfs (red plus symbols), L/T candidates (orange asterisks) and T dwarfs (blue diamonds), overplotted with the selection regions, as defined in §4.2.3 Right: A M_J against $J-H$ CMD of L and T dwarf candidates, symbols the same as plot on the left and overplotted with the corresponding selection regions.

Table 4.1: Candidate subgiant + UCD binary systems.

Name	RA	DEC	Subgiant Hip No	Distance pc	Sep arcsec	J-	J_{err}	$J-H$	$Z-J$	M_J
Cand T1	00 37 32.08	-37 24 27.04	2944	44.9	455.5	17.85	0.09	-0.38	1.24	14.59
Cand T2	00 37 39.53	-37 20 26.79	2944	44.9	322.9	17.27	0.05	0.07	0.66	14.01
Cand T3	00 37 42.60	-37 21 10.73	2944	44.9	386.1	17.27	0.06	0.14	0.74	14.01
Cand T4	01 59 46.33	-48 40 36.85	9316	76.9	241.5	18.38	0.12	-0.02	0.64	13.95
Cand T5	02 39 04.66	-09 02 00.67	12350	53.0	385.4	17.64	0.07	0.36	0.86	14.02
Cand T6	03 48 45.37	-04 24 45.93	17801	52.7	115.9	18.12	0.08	0.26	0.69	14.51
Cand T7	04 02 02.51	-34 25 38.73	18824	52.2	197.1	17.10	0.05	0.15	0.81	13.51
Cand T8	04 09 18.53	-07 56 32.58	19431	56.2	379.1	18.30	0.08	-0.06	0.60	14.56
Cand T9	04 09 50.92	-07 51 38.84	19431	56.2	190.3	18.05	0.08	0.35	0.83	14.30
Cand L1	04 28 09.41	-37 35 00.94	20879	82.9	295.3	16.94	0.06	0.69	1.14	12.35
Cand T10	04 28 26.03	-37 35 27.15	20879	82.9	83.2	18.18	0.12	0.07	0.74	13.59
Cand T11	04 28 32.09	-37 39 05.34	20879	82.9	153.4	18.09	0.09	0.21	0.70	13.50
Cand T12	05 35 25.31	-27 35 14.41	26273	84.0	264.4	18.14	0.09	-0.34	0.62	13.52
Cand T13	05 35 56.85	-27 38 23.76	26273	84.0	247.0	18.64	0.11	0.40	0.93	14.02
Cand LT1	05 35 42.16	-27 39 42.74	26273	84.0	150.5	18.90	0.12	0.55	0.91	14.28
Cand L2	05 44 07.07	-19 43 02.53	27014	79.9	369.5	17.48	0.08	0.72	0.90	12.97
Cand T14	06 39 41.39	-48 38 12.88	31895	87.4	457.7	18.26	0.09	-0.18	0.70	13.56
Cand T15	07 17 17.24	-40 35 59.85	35279	63.7	205.0	17.65	0.07	0.43	1.05	13.63
Cand T16	08 38 57.23	-22 43 16.20	42430	19.9	265.3	17.30	0.06	0.07	0.62	15.81
Cand LT2	08 38 58.62	-22 37 10.95	42430	19.9	210.4	17.75	0.08	0.58	1.09	16.26
Cand T17	08 39 10.37	-22 45 51.03	42430	19.9	366.1	17.69	0.09	0.13	0.83	16.20
Cand T18	09 06 32.40	-02 35 12.22	44696	78.1	61.0	18.08	0.09	0.39	0.92	13.61
Cand T19	09 06 41.65	-02 29 07.74	44696	78.1	448.1	18.03	0.10	0.21	0.87	13.57
Cand T20	09 16 20.58	-30 04 33.00	45514	83.8	256.7	18.41	0.10	0.27	0.76	13.79
Cand T21	09 16 36.90	-30 03 44.24	45514	83.8	260.1	18.17	0.08	0.20	1.41	13.56
Cand T22	09 27 48.24	-05 58 46.75	46404	31.2	329.5	18.26	0.07	-0.03	0.46	15.79
Cand LT3	09 28 00.02	-06 10 56.39	46404	31.2	446.2	18.26	0.09	0.51	1.06	15.79
Cand T23	09 48 34.82	-26 28 08.43	48125	38.8	230.8	18.60	0.10	0.02	0.57	15.66
Cand T24	10 55 58.40	-35 10 52.23	53437	54.7	249.9	17.82	0.09	0.28	0.77	14.13
Cand T25	10 56 13.63	-35 08 16.20	53437	54.7	306.7	17.51	0.09	0.44	1.29	13.82

Notes: Name- Indicates the estimated type of UCD (L, L/T or T).
M_J is estimated from the distance of the subgiant.

for, in the same way as 2MASSJ0030 − 3739 and 2MASSJ0030 − 3740 were confirmed as a WD + M9 wide binary system (see §3.3). For the T dwarf candidates the follow-up was performed with methane filters, to assess the strength of any methane absorption, which would indicate a T dwarf.

4.3.1 Second epoch imaging

L and early T dwarf candidates were followed-up with second epoch imaging using WFCAM on UKIRT, EMMI on the New Technology Telescope (NTT) and with IRIS2 on the AAT.

WFCAM

Observations of Cand T9 and Cand T5 were taken using WFCAM/UKIRT (described in §3.2.1). Cand T9 was imaged for a total integration time of 75 seconds, composed of three cycles of five second exposures using a five point jitter pattern and Cand T5 for 50 seconds (10 second individual exposures) in the *J*- band on 2007 September 24.

The images were reduced and calibrated using the WFCAM/UKIDSS standard pipeline (Irwin et al. 2008) and proper motions were calculated as described in §3.2.1. Cand T5 is a potential T dwarf companion to the subgiant Hip12350, which has a proper motion of 277.8 mas/yr (PMRA: 272.9 mas/yr, PMDEC: -51.8 mas/yr). Using 18 reference stars over a baseline of 1.78yr the proper motion measured for Cand T5 was 217±111 mas/yr, where the quoted errors are from the residuals of the coordinate transformation and from centroiding errors, which were conservatively taken as 0.5 pixels. At first glance the motion seems common, however when the direction of motion is analysed into the RA and DEC components (PMRA: -168±141 mas/yr and PMDEC: 137.±153 mas/yr) which showed the pair do not share a common proper motion, even when taking into account their large uncertainties, thus this system is rejected as a real binary system.

Cand T9, is paired with subgiant Hip19431 (PM: 107.2 mas/yr, PMRA: 34.5 mas/yr, PMDEC: 101.5 mas/yr), using 19 reference stars over the same baseline as T5, the proper motion measured was 118.7 mas/yr (PMRA: -109±142 mas/yr, PMDEC: -45±139 mas/yr), which showed the motion appeared not to be common. However as the movement is small and the baseline short so it was not ruled out as a candidate system at this time.

EMMI

The red arm optical filter on the wide field imager of EMMI, housed on the 3.6m New Technology Telescope (NTT) located in La Silla, Chile was used to image Cand L1, Cand T6, Cand T10, Cand T1, Cand T12 and Cand T13 in the I- band during 2007 November 16-18. Exposure times of 900 seconds (a combination of 3 x 300 second integrations) were taken for each candidate.

Basic data reduction, including the background, dark and bias subtraction were done by Dr Ben Burningham. The individual (300 second) images were then cropped to remove most of the vignetting pattern on the the chip. Cropping was done using the STARLINK FIGARO routine ISUBSET to select the fully illuminated part of the image. The set of three images were then lined up using CCDPACK. Firstly the PAIRNDF routine was used to interactively overlay one image on top of another via the $'$drag and drop$'$ facility, where bright stars in the images were used as a positioning reference. This allows the offset of each image to be calculated using the REGISTER routine, which creates a transformation function to determine any shift, rotation or magnification in the images, with respect to each other. The images were then transformed to the same scale, orientation and offset using TRANNDF and finally median combined using MAKEMOS.

EMMI has a FOV of $9.1'$ x $9.9'$, with a pixel scale of 0.1665 arcsec/pixel. Proper motions were calculated as previously described, transforming from the IRIS2/AAT co-ordinate system into the EMMI/NTT system and vice versa to verify the proper motions over the baseline of 1.92 yr, using an average of 18 reference stars. The proper motion measurements of all six candidates are shown in Table. 4.2. All but one of the candidates (Cand T13) had high associated residuals and a short baseline, leaving high uncertainties on these measurements. For Cand T13 the motion, even considering the large associated uncertainties appears not to be common when assessing the direction and high proper motion of the possible subgiant companions.

IRIS2

Cand LT2 and Cand LT3 were imaged in the J- band using IRIS2/AAT during 2008 February 20-24 in seeing of 1.5-2.0 arcsec. The data were reduced using the standard ORACDR pipeline for IRIS2 and their proper motions calculated as previously described. 19 and 23 reference stars respectively were used to derive transformations over a baseline

Table 4.2: Proper motion measurements of candidate L and early T dwarfs.

Candidate	SG PM RA	SG PM DEC	2nd epoch instrument	Baseline yr	UCD PM[a] RA	UCD PM [a] DEC	CPM?
Cand T5	272.9	-51.8	WFCAM	1.78	-168±141	137±153	No
Cand T9	34.5	101.5	WFCAM	1.78	-109±142	-45±139	?
Cand T10	51.6	-117.0	EMMI	1.92	18±130	28±125	?
Cand L1	54.6	-117.0	EMMI	1.92	-92±127	2±123	?
Cand T6	42.2	-20.6	EMMI	1.92	-37±120	-36±120	?
Cand T11	51.6	-117.0	EMMI	1.92	37±119	22±127	?
Cand T13	23.5	-217.9	EMMI	1.92	-94±121	148±122	No
Cand T12	23.5	-217.9	EMMI	1.92	-52±122	-64±124	?
Cand LT2	-268.3	424.1	IRIS2	2.2	-37±106	-1±104	No
Cand LT3	-232.8	-65.2	IRIS2	2.2	-15±107	-19±106	No

Notes: SG - Subgiant.

? Indicates uncertainty, due to large errors and small measured motions

[a] - uncertainties on the proper motion from fit to the residuals of the transformation.

of 2.2yr. Cand LT2 had a measured proper motion of PMRA: -37±120 mas/yr and PMDEC: -1±104 mas/yr, which is consistent with a zero motion and not consistent with the proper motion of its possible subgiant companion Hip42430, which has a sizable measured proper motion of PMRA: -268.3.8 mas/yr and PMDEC: 424.1 mas/yr. Cand LT3 also has a small motion of PMRA: -15 ±107 mas/yr, PMDEC: -19±106 mas/yr, which is much smaller than the motion measured for its possible subgiant companion (Hip46404, which has a proper motion of PMRA: -232.8 mas/yr and PMDEC: -65.2 mas/yr). These two candidates were considered non-common proper motion objects and thus not binary systems.

The proper motion of all candidates followed-up are summarised in Table. 4.2.

4.3.2 Methane imaging

The T dwarf spectral type is defined (and classified) by the presence of strong methane absorption in their spectra. This shows up strongly in the NIR and is most prevalent in the H- band over the wavelength range 1.5-1.8μm. The strength of the methane absorption becomes stronger with later spectral type (Burgasser et al. 2003a). The

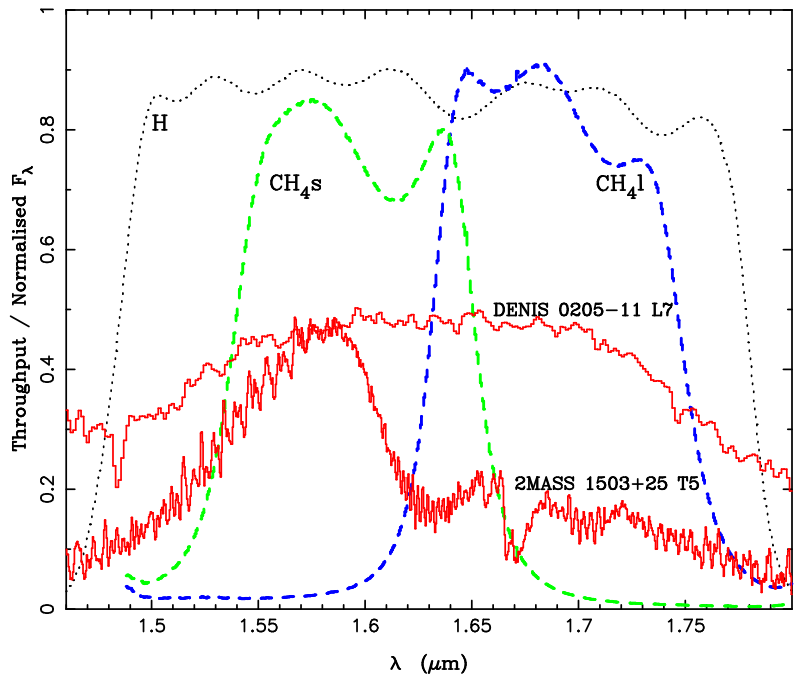

Figure 4.10: Plot from Tinney et al. (2005) showing the position of the methane filters; CH_4s and CH_4l as dashed green and blue lines respectively, with comparison to the H- band of IRIS2 (dotted line). Also overplotted are the spectra from an L7 and a T5 dwarf (red solid lines, normalised for clarity) from Burgasser et al. (2004) and Leggett et al. (2001).

strong methane absorption is unique to T dwarfs and thus serves as a tool to distinguish them from other stars. Differential imaging in and out of the methane absorption was chosen for this reason, to test if the T dwarf candidates were genuine T dwarfs. A set of filters based on the position of the main methane feature in the H- band were used, following the method of Tinney et al. (2005). The two filters used are CH_4s centred on 1.57μm, where there is no methane absorption and CH_4l, centred on 1.69μm where the methane absorption is strong. The position of the filters, with respect to the H- band filter of IRIS2 and the spectra of a mid T and a late L dwarf are shown in Fig. 4.10. The difference in flux between the two filters i.e. the $CH_4s - CH_4l$ colour are measured and compared to the that for main-sequence stars and known T dwarfs. Mid to late T dwarfs have $CH_4s - CH_4l < -0.5$, whereas main-sequence stars have neutral colours. The $CH_4s - CH_4l$ colour for main-sequence stars and L and T dwarfs are shown in Fig. 4.11. Also seen is a slight reddening of the methane colour for late M and L dwarfs and a sharp blue-ward turn for mid T dwarfs.

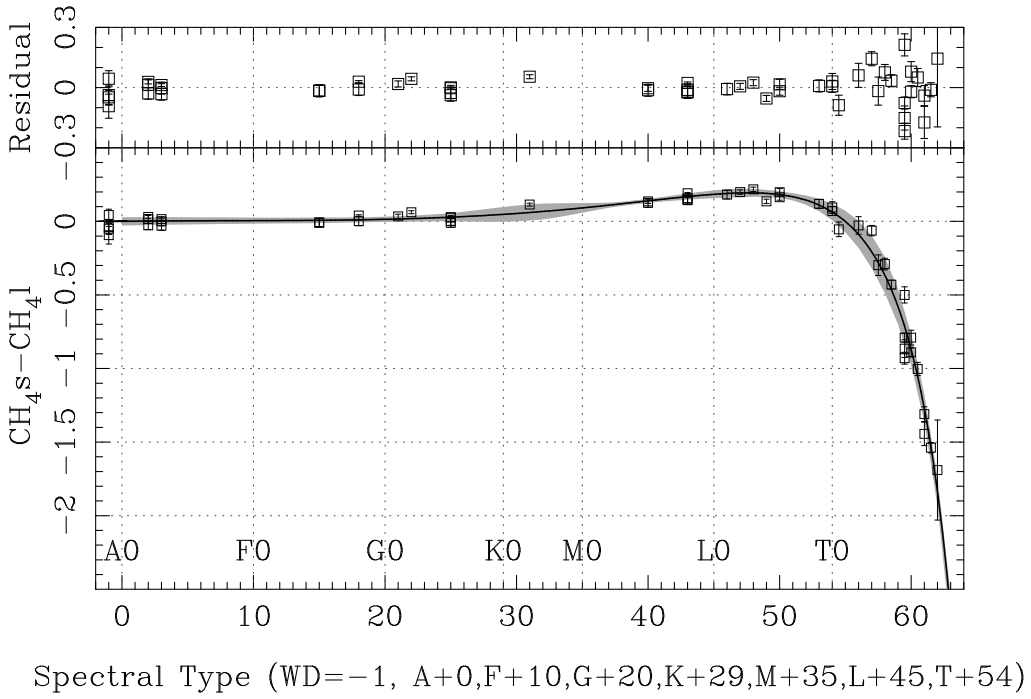

Figure 4.11: A $CH_4s - CH_4l$ colour against spectral type plot from Tinney et al. (2005). Showing the position of main-sequence stars and T dwarfs.

Observations of Cand T10, T11, T12, T14, T18, T19, T20, T22, T24 and T25 were taken on 2008 February 20-24, with IRIS2/AAT; the observing conditions were reasonable where the seeing was typically ∼1 arcsec. Integrations of 30 minutes in each of the CH_4s and CH_4l filters were taken for targets with $17.0 < H < 18.0$ and 60 minutes for targets with $18.0 \geq H \geq 18.5$. As with previous observations a five point jitter pattern was used. The images were reduced using the ORACDR pipeline (described previously). Photometry was extracted, calibrated and the $CH_4s - CH_4l$ colour calculated using a custom built PERL pipeline written by Chris Tinney and described in Tinney et al. (2005). Firstly objects in the reduced images were extracted using the STARLINK package SEXTRACTOR, and J-, H- and K- band photometry for objects contained in the image area were downloaded from the 2MASS infrared science archive. These were cross matched with objects in the image and used to calibrate $CH_4s - CH_4l$ from standard A, F and G stars over the colour range -0.05< $(J - H)$ <0.5 and 0.6< $(J - H)$ <1.1, where uncertainties in 2MASS magnitudes were <0.1. Derived relation for $CH_4s - CH_4l$ with $J - H$ from Tinney et al. (2005) were used to calculate a $CH_4s - CH_4l$ zero point based on their $J - H$ colour. The $CH_4s - CH_4l$ colour for all objects from the image were then plotted as a function of spectral type.

T dwarfs should have colours $CH_4s - CH_4l < -0.2$ (Tinney et al. 2005), however there is a large amount of scatter for magnitudes fainter than $CH_4s > 18.0$, as can be seen in Fig. 4.12. Thus a confident detection of a T dwarf should exhibit colours $CH_4s - CH_4l < -0.2$ and sit outside of the region of scatter. Cand T18, Cand T19, Cand T24 and Cand T25 all showed $CH_4s - CH_4l > 0.1$, which is consistent with the colours of main-sequence stars. The differential methane imaging ($CH_4s - CH_4l$ against CH_4s) colour-magnitude diagram for Cand T18 is shown in Fig. 4.12, as an example. Overplotted are other objects in the image for comparison, where it can be seen that the candidate is likely a contaminant main-sequence object and is thus considered not to be a T dwarf. Additionally in the FOV of Cand T18, two objects showed extreme $CH_4s - CH_4l$ colours (<-0.5) and would be typed as T7 and T8 by the pipeline. However on closer inspection of the images one of these objects sits in an area affected by cross talk and the other at the same location as a bad pixel in the CH_4s image. Their colours were thus deemed unreliable.

Solutions were not possible for Cand T10, T11, T12 and T20, due to one or more of the following factors; the target could not be resolved due to an insufficient signal-to-noise or the images were affected by cloud causing diffraction rings, thus creating an uneven background level that made it impossible to extract reliable photometry. The T dwarf candidate in these images was visually inspected to see if a noticeable change in brightness in the CH_4s band compared with the CH_4l could be seen, indicating the presence of strong methane, however none of the candidates showed a convincing difference in brightness and are considered likely not to be T dwarfs, but can not be ruled out by this crude estimation.

There were two objects, Cand T14 and Cand T22, that were typed as early T dwarfs, T0.9±1.4 and T0.5±1.5 respectively. While their $CH_4s - CH_4l$ colours (-0.01±0.07 and -0.01±0.14) are not convincingly strong detections of methane (compared to main-sequence stars) they can not be ruled out with this data, since their colours lie in the range $0.1 < CH_4s - CH_4l < -0.2$ and might yet be shown to be T dwarfs. It is likely that they are not T dwarfs but require additional follow-up to confirm their nature.

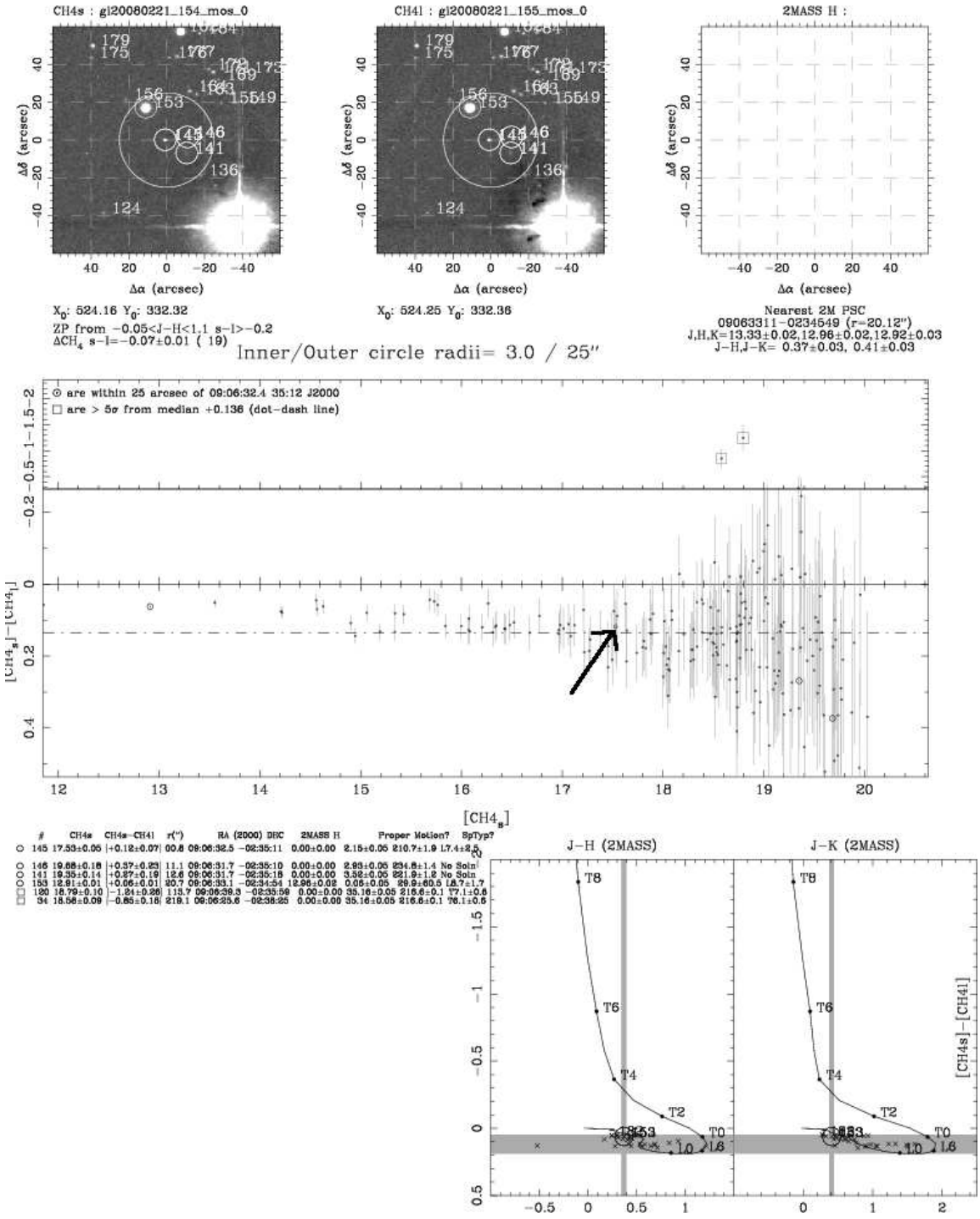

Figure 4.12: A $CH_4s - CH_4l$ against CH_4s CMD for Cand T18 (indicated with an arrow), and an estimated spectral type that the program calculates based on the $CH_4s - CH_4l$ verses spectral type relation from Tinney et al. (2005) (shown in the insert at the bottom right of the figure). Also shown are all other stars in the 7.7′ x 7.7′ FOV imaged by IRIS2, providing a comparison to the position of the main-sequence. Two objects with ′extreme′ $CH_4s - CH_4l$ colours are also shown as squares (see §4.3.2).

4.4 Discussion

Of the 30 subgiant + UCD candidate binary systems from this pilot survey, ten were followed-up with second epoch imaging. Four of the ten systems were rejected as non common proper motion binaries and six remain uncertain due to small motions and large associated uncertainties on those motions (on average ∼120 mas/yr). What is needed in order to better evaluate their binary nature is an additional epoch, over a longer baseline or with a smaller spatial resolution and higher signal-to-noise measurement. Ten candidate systems were also followed-up with methane imaging. Four of these were confirmed as not being T dwarfs and were rejected as subgiant + T dwarf binary systems and six remain uncertain due to low signal-to-noise data. For these six additional methane imaging or spectral follow-up on an 8m class telescope is required to determine if they are real subgiant + UCD binary systems.

There are two candidates that, despite their non-common proper motion status still showed a potentially significant motion (Cand T5 and Cand T13). If their motion is real (or is of low significance when compared to the large 1σ uncertainties), then they are either close by T dwarfs or background M dwarfs (with scattered colours) with a space velocity of ∼200km/s. It is likely however, that the latter is the case. The expected number of field T dwarfs (not binary companions) in the IRIS2 survey area was assessed using identified mid-late T dwarfs (≥T4) from the UKIDSS LAS DR1 and DR2 coverage. Pinfield et al. (2008) analysed the number of ≥T4 dwarfs in the UKIDSS LAS DR2 coverage, which is effectively complete down to J≤19. This was compared to the subgiant survey area, which probes out to similar magnitude limits. They find 17±4 mid-late T dwarfs in the 280 degree^2 coverage of UKIDSS DR2. This suggests that a T dwarf should be found in every $16.5^{+4.5}_{-3.2}$ degree^2 of sky. The sky coverage for each subgiant was calculated as 0.0335 degree^2 (15.73 x 7.7 arcmin around each subgiant), thus for the pilot survey of 71 subgiants this equates to 2.4 degree^2 of sky. One would therefore expect to find $0.15^{+0.03}_{-0.04}$ ≥T4 field dwarfs in the sky coverage of the pilot survey. This suggests that a field T dwarf should only be found once for every ∼490 subgiants imaged. Thus the chance of finding a mid-late T dwarf that is not a companion in the imaging survey is very small, Cand T5 and Cand T13 are hence more likely to be background objects.

The remaining ten candidates were unable to be followed-up due to their observability during the follow-up time awarded. The best candidate is T1, which has the bluest $J-H$ colour and the reddest $Z-J$ colour of the sample. This object has been prioritised

for near future methane and second epoch imaging. A table summerising the results of the follow-up program are shown in Table. 4.3.

The number of subgiants with UCD companions predicted by Pinfield et al. (2006) over the whole sky is 80^{+21}_{-14} systems. Evaluating the clean sample of 918 subgiants suggests that one in eleven should have a UCD companion. For the 71 subgiants observed during this pilot survey, which represents 7% of the total sample, the Pinfield et al. (2006) simulations, suggest that six systems could be found. As a large number of the candidate systems (22 out of the 30) are uncertain it is not possible to support nor confirm the simulated predictions, but it seems likely that several of the remaining candidates could prove to be genuine in the future.

Table 4.3: The status of UCD candidates (confirmed or not).

Candidate	Followup type	Confirmation of UCD?
Cand T1	No	?
Cand T2	No	?
Cand T3	No	?
Cand T4	No	?
Cand T5	PM	No
Cand T6	PM	?
Cand T7	No	?
Cand T8	No	?
Cand T9	PM	?
Cand L1	PM	?
Cand T10	Met Imaging/PM	?
Cand T11	Met Imaging/PM	?
Cand T12	Met Imaging/PM	?
Cand T13	PM	No
Cand LT1	No	?
Cand L2	No	?
Cand T14	Met Imaging	?
Cand T15	No	?
Cand T16	No	?
Cand LT2	PM	No
Cand T17	No	?
Cand T18	Met Imaging	No
Cand T19	Met Imaging	No
Cand T20	Met Imaging	?
Cand T21	No	?
Cand T22	Met Imaging	?
Cand LT3	PM	No
Cand T23	No	?
Cand T24	Met Imaging	No
Cand T25	Met Imaging	No

Notes - ? Indicates uncertainty, due to a non measurement or large uncertainties on the measurements.

Chapter 5

Ultracool companions to main-sequence stars

A search for UCD companions to main-sequence stars was carried out and presented in Pinfield et al. (2006). Two of these new systems identified were subsequently followed-up with spectroscopy to confirm the nature of the UCD component here, and confirm their usefulness as benchmark objects. Section 5.1 summarises the selection of common proper motion binary systems from Pinfield et al. (2006) (in which I collaborated), and sections 5.2-5.4 present the new spectroscopic analysis of two of the candidates.

5.1 Selection of Hipparcos main-sequence + UCD wide binary systems

Main-sequence stars within 50pc were selected from the Hipparcos catalogue covering areas across the whole sky, omitting the galactic plane ($|b| < 30$). They include stars in the range $0<M_V<10$ and $-1.4<V<13.25$ for early A to early M spectral types, totalling to a sample of $\sim$40,000 Hipparcos stars. These stars were then cross matched with the 2MASS infrared data archive and UCD companions were searched for using a cone search with a radius equal to a separation of 5000 AU, at the parallax distances of the stars, out to a maximum of 300 arcsec separation (the Gator search limit). The search is thus incomplete (out to separations of 5,000 AU) for distances < 16.67 pc. Colour and magnitude constraints were also imposed, selecting UCD candidates if they had $J - K \geq 1.1$, $J \leq 16.1$ and where either no optical counterpart exists in the USNO catalogue

(where 2MASS can cross reference the USNO data) or if the optical constraint yielded $R-K \geq 5.5$ (as described in §2.2.1). Objects were then visually inspected in images from 2MASS, SuperCOSMOS (I- and R- bands) and SDSS (DR4) where available, to ensure there was no contamination from image artifacts.

An absolute magnitude (M_J) was calculated for the candidate UCDs by assuming they are at the same distance as their paired Hipparcos primary. This was used to plot candidates on a $J-H$ against M_J CMD, where a selection region was defined using known L dwarfs as described in §3.2. Sixteen candidate systems were identified in this way and are shown in Table. 5.1 and Fig. 5.1 as filled circles. Five of these were previously identified by Kirkpatrick et al. (2001) and Wilson et al. (2001) (Cand 3, 4, 5, 12 and 14) and are also shown as overplotted circles on Fig. 5.1. For the remaining candidates, five have SDSS measurements (Cand 2, 6, 8, 9 and 10), and Cand 13 and Cand 16 have SuperCOSMOS measurements. All showed colours consistent with L dwarfs when compared to the colours presented in Fan et al. (2001) and Hawley et al. (2002).

Proper motions were calculated where possible by measuring the motion between the 2MASS first epoch and SDSS or SuperCOSMOS second epoch images. For one of the candidate systems (Cand 2) the baseline was only ∼0.27yr, which is too short for an accurate proper motion to be calculated. Cands 8, 10, 13 and 16 however have longer baselines of 2.0, 6.1, 5.7 and 14.9 yr, respectively so their motions were measurable. Proper motions were thus calculated using the GEOMAP and GEOXYTRAN routines in IRAF, as previously described in §3.2.1 using an average of 10-15 reference stars. Residuals of the transformations were typically 0.2-0.3 arcsec and centroiding accuracies were typically ±0.1-0.3 arcsec. Proper motions were derived using the full range of epochs available (first epoch J-, H- and K- band and second epoch r-, i- and z- bands), giving an overall uncertainty of 0.2-0.4 arcsec. The corresponding proper motions are shown on a vector point diagram in Fig. 5.2. Cand 8, which has a relatively short baseline (2yr) has large associated uncertainties, however Cands 10, 13 and 16 show a consistent motion with their primaries and were thus identified as common proper motion binary systems.

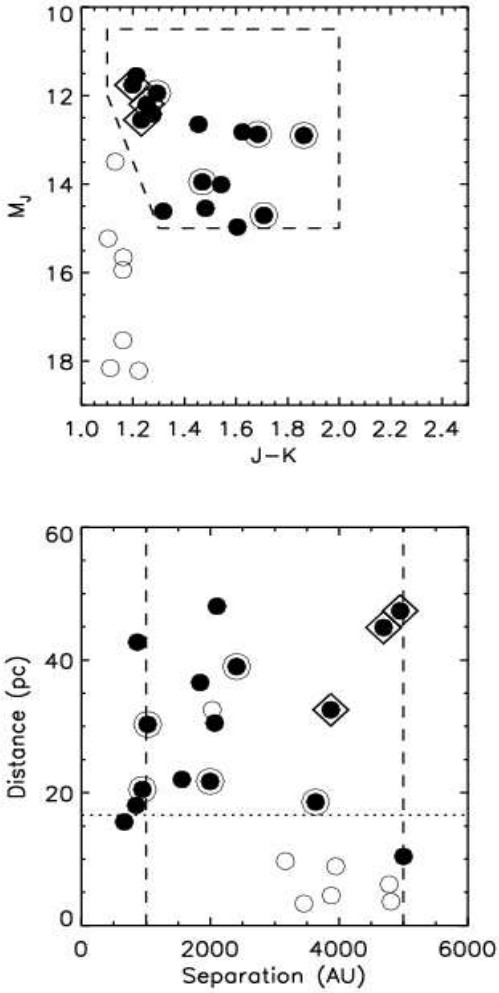

Figure 5.1: Top: M_J against $J-K$ CMD for candidate L dwarf companions to Hipparcos stars, where M_J is estimated using the distance of the Hipparcos primary star. Bottom: A distance - separation plot for the candidate main sequence + L dwarf binary systems. Filled circles are objects that pass the photometric criteria defined for L dwarfs as described in §5.1. Overplotted with circles and diamonds are previously confirmed systems and systems with a measured common proper motion, respectively. Also overplotted is the L dwarf separation range 1000-5000 AU (dashed lines).

Table 5.1: Widely separated main sequence + L dwarf candidate systems.

Cand	Primary name	Primary SpT	L cand 2MASS ID	J	$J-K$	M_J	D pc	Sep AU
Cand 1	Gl 87	M1.5	2MASS J02124236+0341004	14.70±0.03	1.32	14.62	10.4	5000
Cand 2	HD 74150	K0III-IV	2MASS J08444996+5532121	14.70±0.04	1.21	11.55	42.7	865
Cand 3	Gl 337AB	G9V/G9V	2MASS J09121469+1459396	15.51±0.08	1.47	13.95	20.5	946
Cand 4	HD 89744	F7IV-V	2MASS J10221489+4114266	14.90±0.04	1.29	11.95	39.0	2409
Cand 5	Gl 417	G0V	2MASS J11122567+3548131	14.58±0.03	1.86	12.90	21.7	1997
Cand 6	HD 102124	A4V	2MASS J11451802+0814414	15.47⋆	1.45	12.65	36.6	1842
Cand 7	HD 107325[a]	K2III-IV	2MASS J12201925+2636278	15.83±0.16	1.28	12.42	48.1	2102
Cand 8	HD 116012	K2V	2MASS J13204427+0409045	15.25±0.05	1.62	12.82	30.5	2069
Cand 9	Gl 512.1	G5V	2MASS J13282546+1346023	15.84±0.16	1.48	14.55	18.1	848
Cand 10	HD 120005[b]	F5	2MASS J13460815+3055038	15.46±0.06	1.25	12.20	44.9	4691
Cand 11	Gl 527A[a]	F6IV	2MASS J13471545+1726426	15.94±0.20	1.61	14.97	15.6	664
Cand 12	Gl 584AB	G0V/G3V	2MASS J15232263+3014562	16.06±0.10	1.71	14.71	18.6	3635
Cand 13	Gl 605	M0	2MASS J15575569+5914232	14.32±0.03	1.20	11.76	32.5	3871
Cand 14	Gl 618.1[a]	M0V	2MASS J16202614-0416315	15.28±0.05	1.69	12.88	30.3	1027
Cand 15	Gl 694.1A	F5IV-V	2MASS J17420515+7208002	15.73⋆	1.54	14.01	22.0	1558
Cand 16	HD 216405[c]	K1/K2V	2MASS J22530539-3751335	15.93±0.08	1.23	12.55	47.4	4950

[a]Variable star. [b]Spectroscopic binary. [c]Double/multiple star.

⋆: 95% confidence upper limit.

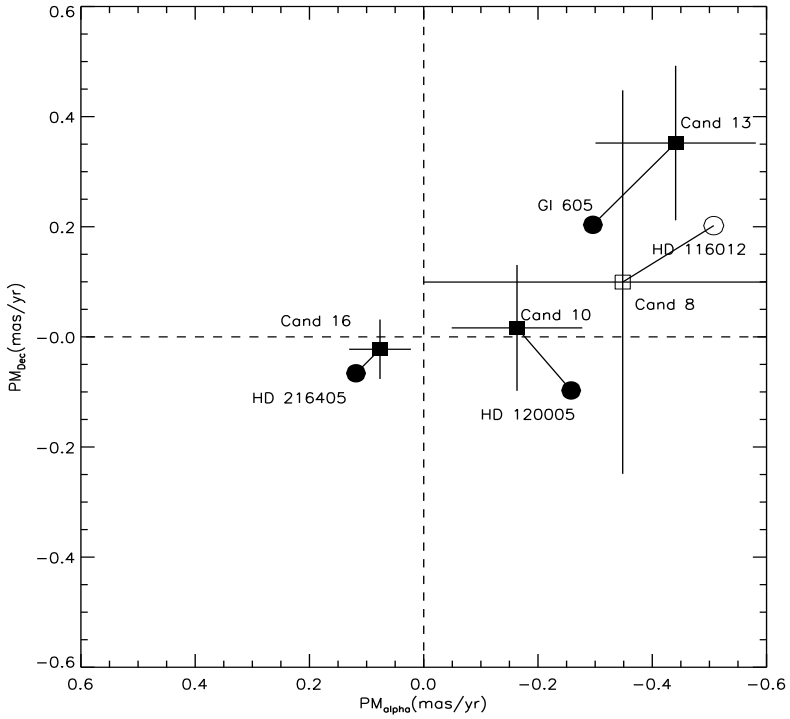

Figure 5.2: A vector point diagram of the four candidate main-sequence + L dwarf common proper motion systems. The primary (Hipparcos) stars are shown as filled circles and the L dwarf candidates are shown as filled squares. Cand 8, with its large uncertanties is plotted as open symbols. Each pair are joined with a line for clarity.

5.2 Spectroscopic follow-up observations

Spectra were taken of Cand 10 and 13 with the Long-slit Intermediate Resolution Infrared Spectrograph (LIRIS) on the 4.2m William Herschel Telescope (WHT), part of the Isaac Newton Group of telescopes on La Palma during 2006 January 18-19. The wavelength range of 0.9-2.3μm was measured, which covers the Z- to K- bands, however it is split into two ranges, corresponding to the ZJ (0.9-1.5μm) and HK (1.4-2.4μm) grisms. For Cand 13 a total exposure time of 10 minutes in ZJ and 40 minutes in HK were obtained by nodding along the slit in an "ABBA" pattern. Cand 10 was observed with the HK grism only with a total exposure time of 30 minutes.

5.2.1 Reduction and extraction of data

The spectra were reduced and extracted in the same way as described in §3.3.1, including flatfielding, using dome flats and the removal of bad pixels. The A and B position data were median combined to create a single A and B pair and were differenced to create a positive (A-B) and negative (B-A) spectrum. They were extracted using the APALL routine

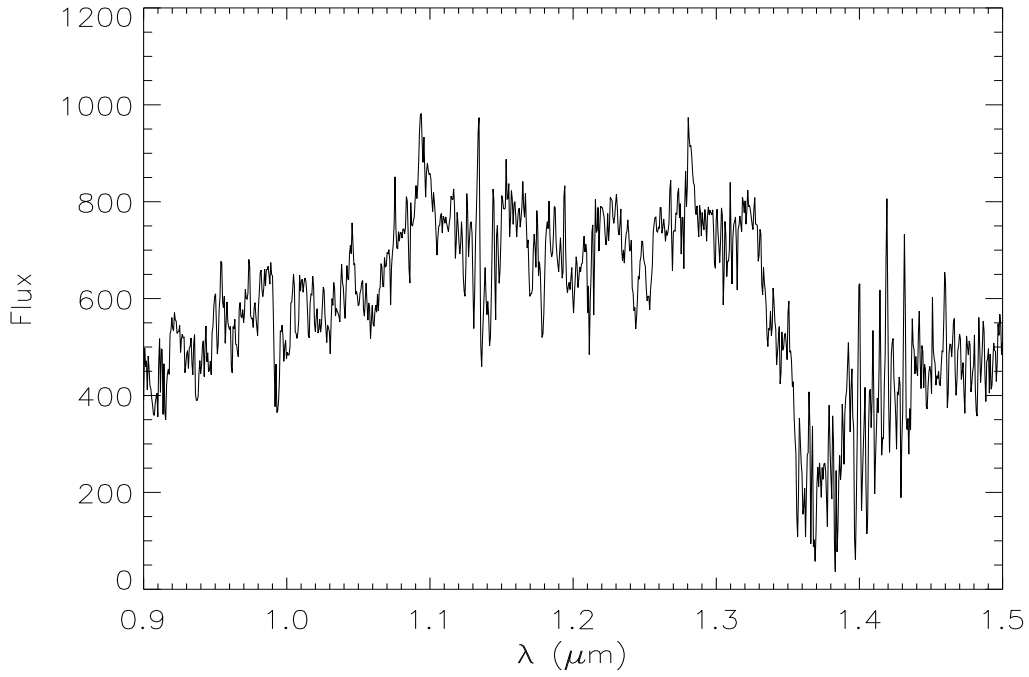

Figure 5.3: The ZJ spectrum of Cand 13.

in IRAF and wavelength calibrated using a Xenon arc lamp for the ZJ spectra, and both a Xenon and Argon lamp for the HK spectrum. The reference wavelength of the features in each spectrum were taken from the LIRIS/WHT web pages (www.iac.es/project/LIRIS). The spectra were flux calibrated using an F0V star for Cand 13 and an F2V star for Cand 10. The flux standard spectra were normalised to $\sim$1 and divided into the spectrum, which was then multiplied by a smoothed blackbody spectrum with the same temperature as the flux standard (7020K and 6750K for an F0V and an F2V, respectively). The positive and negative extracted and calibrated spectra were then median combined. The resulting spectra for Cand 13 are shown in Figs. 5.3 and 5.4 and Cand 10 in Fig. 5.5.

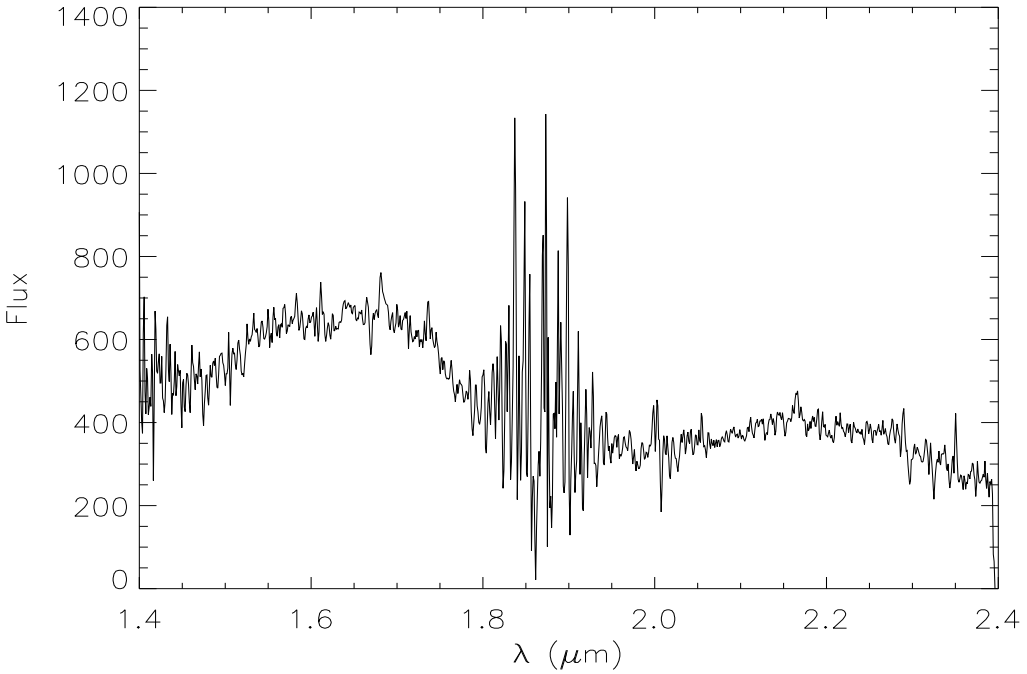

Figure 5.4: The HK spectrum of Cand 13.

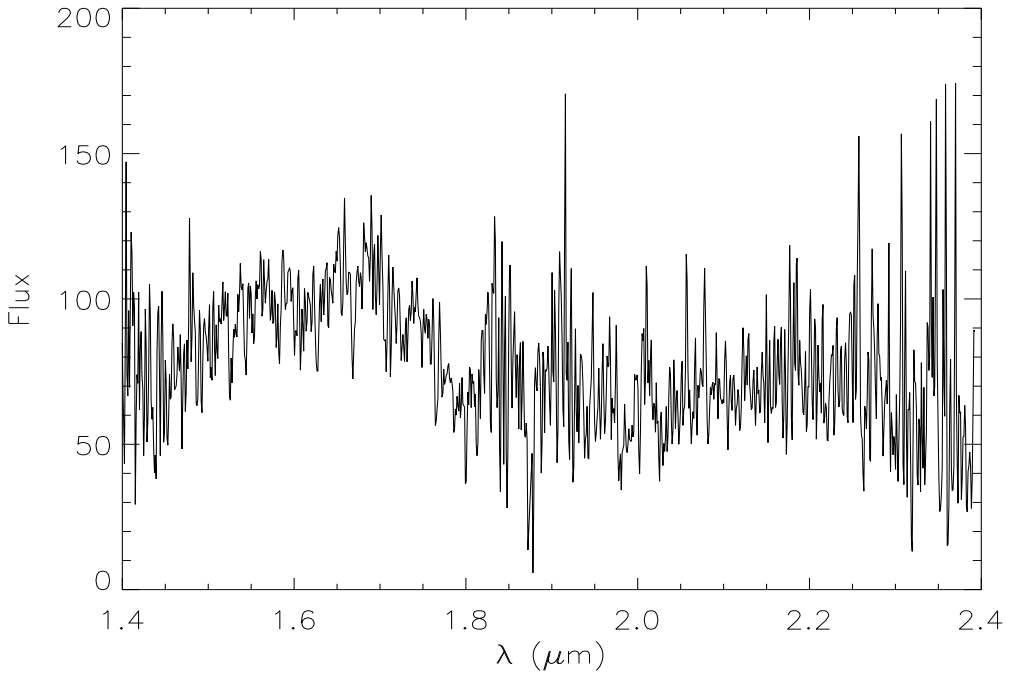

Figure 5.5: The HK spectrum of Cand 10.

5.3 Spectral classifications

The spectral type of Cand 10 and 13 were calculated using spectral ratios, equivalent widths of the KI lines (in ZJ) and by comparison to template spectra of late M and early L dwarfs.

5.3.1 Cand 13

Spectral ratios

Cand 13 has full spectral coverage from 0.9 to 2.3μm and was analysed using spectral ratios available from the literature covering this wavelength range. For the ZJ spectra the J-FeH and H_2O_A ratios from McLean et al. (2003), the FeH and H_2OI ratios from Slesnick, Hillenbrand & Carpenter (2004) and the H_2OA ratio from Reid et al. (2001a) were used to calculate a spectral type for Cand 13 in the range M8-L2. In the HK spectra the H_2OB and H_2OD ratios from McLean et al. (2003) and Reid et al. (2001a) were considered as well as the H_2O2 ratio from Slesnick, Hillenbrand & Carpenter (2004). These ratios are also consistent with the spectral type range indicated by the ZJ spectra. The parameters of each of the ratios used, including their wavelength, bandwidth, their calculated values and corresponding spectral types are shown in Table. 5.2 and indicate a spectral type of L0$\pm$2.

Equivalent widths

Equivalent widths of the KI lines in the ZJ band were calculated as described in §3.3.1, where the FEATURE program in IDL was used to interactively determine the width of the feature by selecting points in the pseudocontinuum at either side of the KI line along with the maximum depth of the feature. This method was repeated $\sim$30 times for each line, by measuring the width at different points along the continuum. The equivalent width was calculated from the median value of the measurements and the error from the standard deviation. For KI lines at 1.168, 1.177, 1.243 and 1.254μm these were calculated and compared to the relation between equivalent width and spectral type from McLean et al. (2003). For the KI features at 1.168, 1.177 and 1.254μm these were all consistent with a spectral type of M8/9 and the width of the KI feature at 1.243μm is consistent with an M9/L0 type. The measurements, standard deviation and corresponding spectral type for each line are shown in Table. 5.3.

Table 5.2: Spectral ratios for Cand 13

Spectral feature	Ratio	Reference	Bandwidth μm	Value	SpT
J-FeH	1.200/1.185	McLean ′03	0.004	0.865	M8-L2
H_2O_A	1.343/1.313	McLean ′03	0.004	0.685	L0±0.6
FeH	1.200/1.230	Slesnick ′04	0.013	0.854	M9.3±0.6
H_2O_I	1.340/1.300	Slesnick ′04	0.010	0.703	M8.8±1
H_2OA	1.340/1.290	Reid ′01	0.004	0.698	L0±1
H_2OB	1.456/1.570	McLean ′03	0.004	0.732	M9
H_2OC	1.788/1.722	McLean ′03	0.004	0.659	L2.9±1.8
H_2OD	1.964/2.075	McLean ′03	0.004	1.020	M9±0.8
H_2OB	1.480/1.600	Reid ′01	0.020	0.782	L1.2±1
H_2OD	2.000/2.160	Reid ′01	0.020	0.830	M8/9
H_2O2	2.040/2.150	Slesnick ′04	0.010	0.883	L0±0.5

Table 5.3: Equivalent widths for Cand 13

Equivalent width wavelength	Median value	Standard deviation	SpT
1.168	4.747	0.668	M8/9
1.177	7.438	0.949	M8/9
1.234	7.025	1.680	M9/L0
1.254	5.254	1.646	M8/9

Comparison to template spectra

Template spectra of late M and early L dwarfs were used as a visual comparison to the spectra of Cand 13 in the ZJ and HK spectra. Template spectra of an M7 (VB8), M8 (VB10), M9 (LHS2924), L0.5 (2MASSJ0746), L1 (2MASSJ1439) and L2 (KELU 1) were obtained from the Infrared Telescope Facility SpeX spectral library (http://irtfweb.ifa.hawaii.edu/ spex/WebLibrary/) from Cushing, Rayner & Vacca (2005). The template spectra were broadened to the instrumental resolution of the observed spectra and re-binned to the same dispersion. Finally the spectra were normalised to $\sim$1 at 1.26μm in ZJ and at 1.64μm in HK. The spectra were then overplotted for direct comparison. The ZJ spectra is plotted in Fig. 5.6 and the best fit comes from an M8/M9. The HK spectra (shown in Fig. 5.7) is best fit by an M9/L0 type, both of which are consistent with the spectral ratio and equivalent width measurements. In addition M_J was calculated as M_J=11.76 from the distance of the primary star, which is in agreement with a spectral type of M9/L0 type (using the spectral type-M_J relation from Dahn et al. 2002) and is also consistent with the spectral types calculated from the other methods considered here. Thus the estimated spectral type for Cand 13 or Gl 605B (as is here confirmed) is L0$\pm$2.

5.3.2 Cand 10

Spectral ratios

The wavelength range covered for Cand 10 is only 1.4-2.3μm (HK). The spectral ratios used to estimate Cand 13 in this range were also used here. The H_2O ratios from McLean et al. (2003) were calculated as 0.677 for the H_2OB ratio, indicating an L4 type. H_2OC gave a ratio of 0.605 and a corresponding spectral type of L5 and H_2OD gives a ratio of 1.021, suggesting an M8$\pm$0.8 type. The H_2OB and H_2OD ratios from Reid et al. (2001a) were calculated as 0.865 and 0.934 with spectral types M9$\pm$1 and M8, respectively. The final spectral ratio considered, the H_2O2 from Slesnick, Hillenbrand & Carpenter (2004), gave a ratio of 0.887 which corresponds to an L0$\pm$0.5 type. All the estimated spectral ratios of Cand 10 are shown in Table. 5.4.

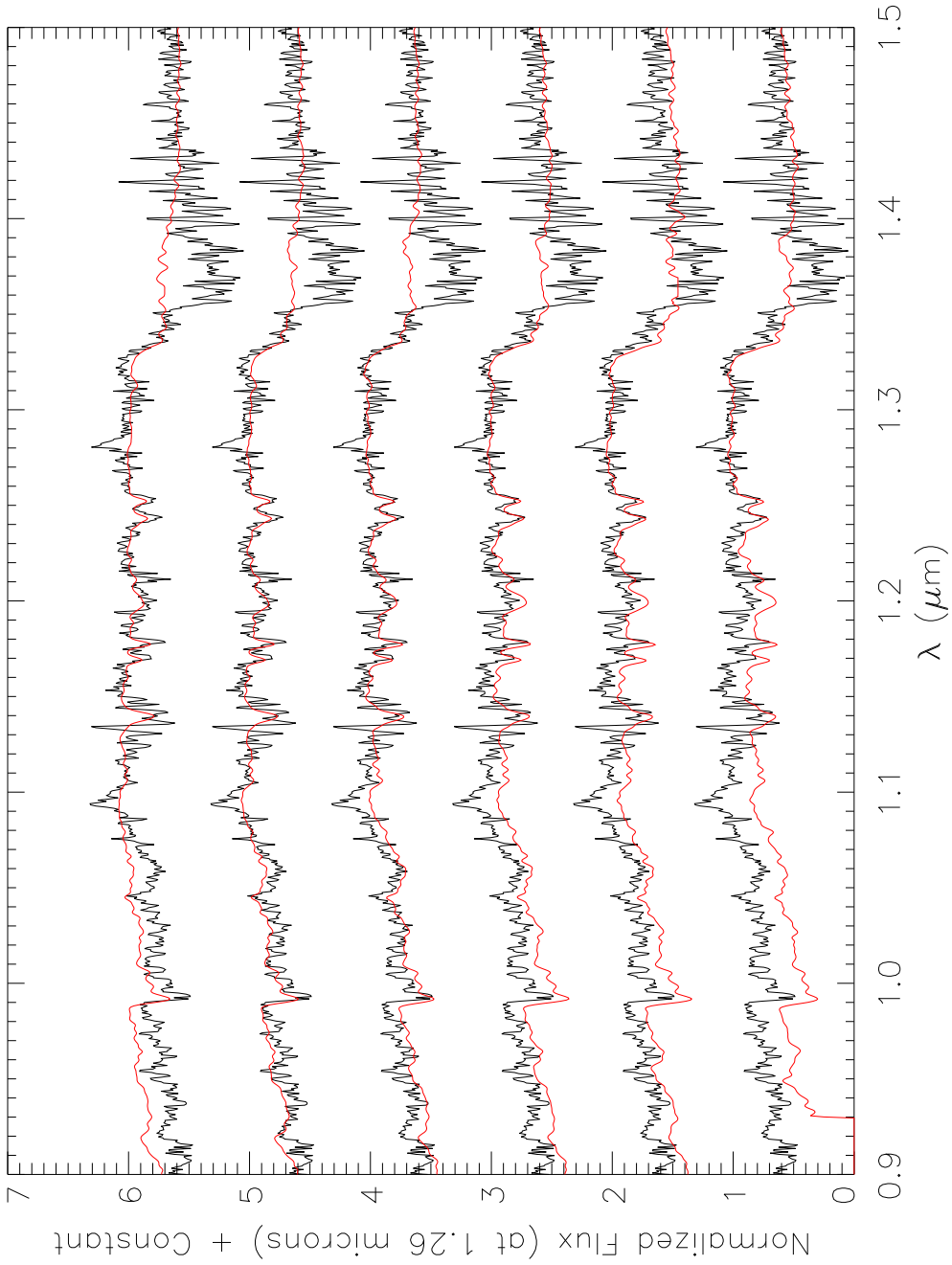

Figure 5.6: The ZJ spectrum of Cand 13 (Black), overplotted (in red) by template spectra (from top to bottom) of an M7, M8, M9, L0.5, L1 and L2 type from Cushing, Rayner & Vacca (2005).

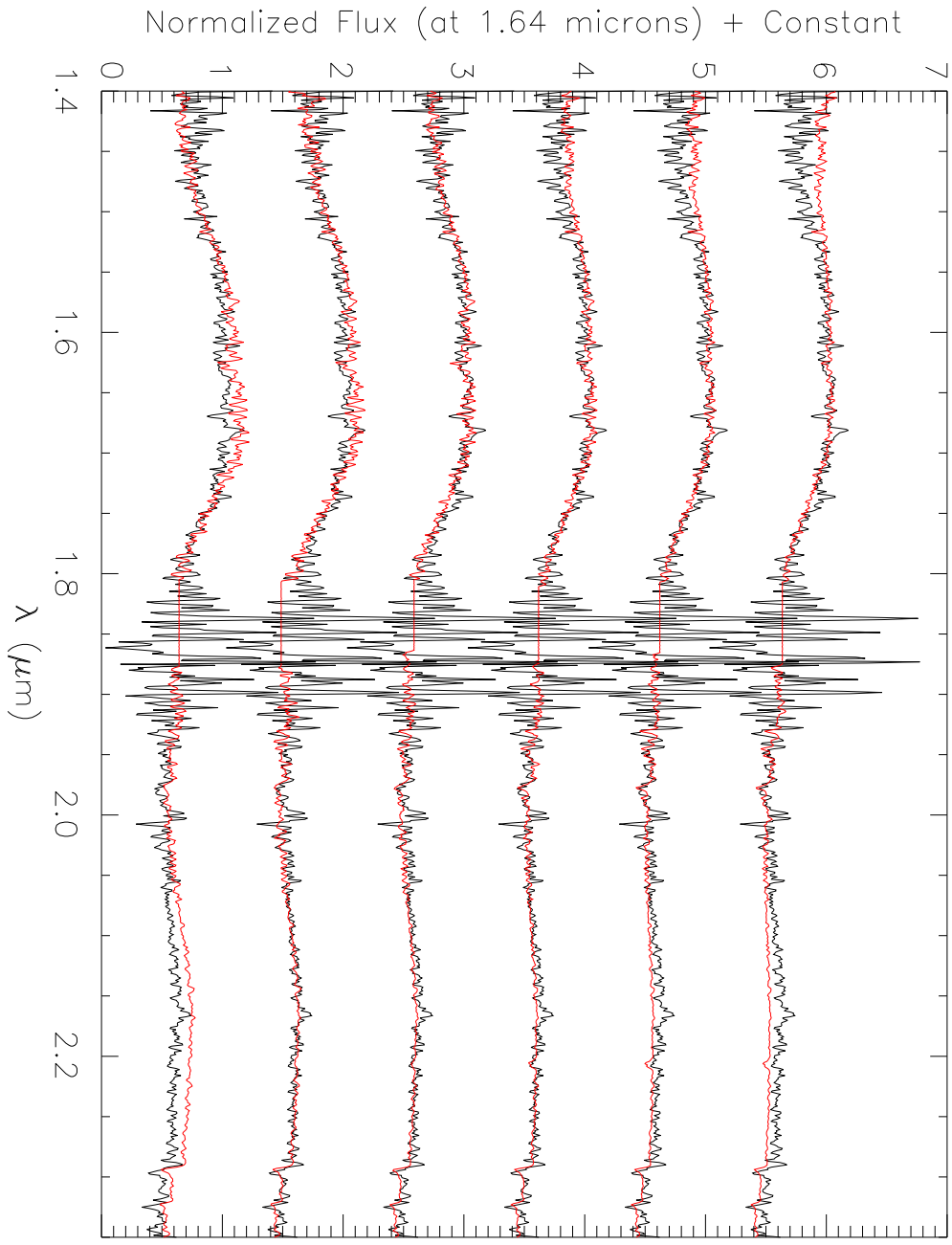

Figure 5.7: The HK spectrum of Cand 13 (Black), overplotted (in red) by template spectra (from top to bottom) of an M7, M8, M9, L0.5, L1 and L2 type from Cushing, Rayner & Vacca (2005).

Table 5.4: Spectral ratios for Cand 10

Spectral feature	Ratio	Reference	Bandwidth μm	Value	SpT
H_2OB	1.456/1.570	McLean '03	0.004	0.677	L4
H_2OC	1.788/1.722	McLean '03	0.004	0.605	L5
H_2OD	1.964/2.075	McLean '03	0.004	1.021	M8±0.8
H_2OB	1.480/1.600	Reid '01	0.020	0.865	M9±1
H_2OD	2.000/2.160	Reid '01	0.020	0.934	M8
H_2O2	2.040/2.150	Slesnick '04	0.010	0.887	L0±0.5

Comparison to template spectra

The HK spectrum of Cand 10 was also compared directly with the template spectra. This was again done by broadening and re-binning to the dispersion of the observed spectra, then normalising to ∼1 at 1.64μm. The best fit comes from an L1-L2 type, as shown in Fig. 5.8. It should be noted that the spectra for Cand 10 is quite noisy and the estimation of types L4 and L5 and should be taken with caution. Indeed for an L4/L5 type the UCD would have to be much closer, at nearly half the distance of the primary (calculated from the spectral type, absolute magnitude relations of Dahn et al. 2002) . Tentatively the spectral type of Cand 10 is estimated as L0±2. In addition M_J was calculated as M_J=12.2 and is in agreement with a spectral type of L1 (as calculated from the distance of the primary star). Thus Cand 10 or HD120005C is spectroscopically typed as an L0±2 UCD.

5.4 Parameters of the systems

5.4.1 Gl605

The primary star for Gl605 has a spectral type of M0V, however no information about the age or metallicity is available from the literature. A spectrum is also unavailable and thus any limits on the age of the system can not be placed. If a spectrum were available then the presence of the Hα emission feature at 6562Å could be assessed in relation to age. West et al. (2008) presented an activity-age relation for M dwarfs and suggest that for an M0, the activity lifetime is 0.8±0.6 Gyr. Over this activity lifetime Hα should appear as a strong emission feature. While this would not represent a particularly

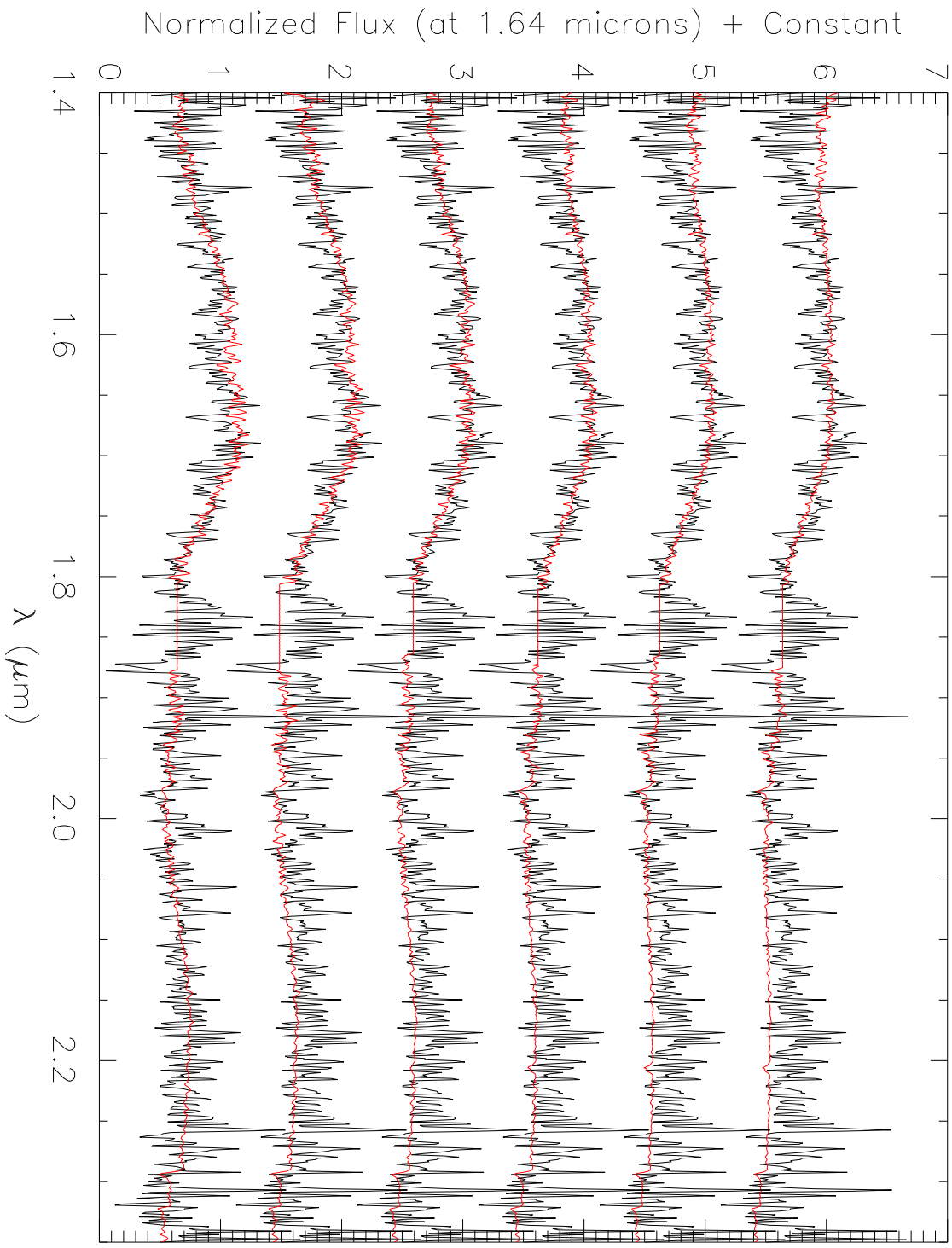

Figure 5.8: The HK band spectrum of candidate 10 (Black), overplotted (in red) by template spectra (from top to bottom) of an M7, M8, M9, L0.5, L1 and L2 type from Cushing, Rayner & Vacca (2005).

accurate constraint on the age it would give an indication if the pair were older or not than $\sim$ 1Gyr. If the M0V primary were indeed >1 Gyr the Lyon group DUSTY and COND models suggest a $T_{\rm eff}$<2200K, log g $\sim$5.3 dex and mass $\sim$0.072$M_{\odot}$. It is also possible to calculate a metallicity value for the M dwarf primary using the relations of Bonfils et al. (2005), who find that metallicity in M dwarfs can be well defined from the relation between M_K and $V-K$, where M_K is between 4.0 and 7.5 and $V-K$ is between 2.5 and 6.0. The V and K magnitudes along with a parallax distance have been measured for Gl605A from the TYCHO2 and 2MASS catalogues and the distance was measured by Perryman et al. (1997). They give an M_K=4.58 and $V-K$=3.26, which indicates an Fe/H = -0.25$\pm$0.2 dex. If the M dwarf were metal poor, then it would be an indication of an older disk population, however for this M dwarf no such age constraint can be placed, thus this UCD does not make an ideal benchmark object.

5.4.2 HD120005

The primary component of the binary system containing HD120005C is a spectroscopic binary F5V star system and has been included in various attempts to calculate age and metallicity constraints for main sequence F type stars. Feltzing, Holmberg & Hurley (2001) calculate a metallicity of 0.11$\pm$0.16 dex, based on Strömgren photometry and derive an age of 2.345$\pm$0.808 Gyr, which they calculate based on the rapid stellar evolution algorithms of Hurley, Pols & Tout (2000).

Metallicity constraints have also been derived by Nordstrom et al. (2004), who calculate [Fe/H] =-0.06$\pm$0.12 dex, where they too use Strömgren photometry from Edvardsson et al. (1993) and relations of Schuster & Nissen (1989) to calculate [Fe/H]. Marsakov & Shevelev (1995) also derive a metallicity of 0.05 dex, from the Strömgren photometry of Hauck & Mermilliod (1985), which is consistent with the value of Nordstrom et al. (2004) to within their quoted uncertainties (0.12 dex). This suggests that HD 120005 is around solar metallicity. However they also derive an age of 2.78 Gyr from the Yale isochrones (Green, Demarque & King 1987), which is consistent with that of Feltzing, Holmberg & Hurley (2001). There is an additional derived age and metallicity available from the catalogue of age-metallicity relations for nearby stars from Ibukiyama & Arimoto (2002), who derive an age of 4.03 Gyr using newer Yonsei-Yale isochrones from Yi et al. (2001) and a derived [Fe/H] of -0.09 dex from the Strömgren photometry of Hauck & Mermilliod (1998). Conservatively, it can be estimated that the age of HD120005C is thus 2-4 Gyr.

The Lyon DUSTY (Chabrier et al. 2000c; Baraffe et al. 2002) and COND (dust-free Allard et al. 2001; Baraffe et al. 2003) models (with solar metallicity) were used to calculate a corresponding mass, $T_{\rm eff}$ and log g for HD120005C, taking an age estimate of 2-4 Gyr. Although L dwarfs have dusty atmospheres, using the dust-free COND models provides an indication of the uncertainties that may be expected to result from different treatments of dust. The DUSTY models suggest that for an age of 2 Gyr and M_J=12.2 (as calculated from the apparent J- band magnitude and the parallax distance of the primary) that the UCD has $T_{\rm eff}$=2090K, mass=0.073$M_{\odot}$ and log g=5.33 dex. For an age of 4 Gyr the DUSTY models suggest similar values of $T_{\rm eff}$=2107K, mass=0.075$M_{\odot}$ and log g=5.35dex. In comparison the COND models suggest (for 2 Gyr) $T_{\rm eff}$ of 1972K, mass=0.068$M_{\odot}$ and log g=5.33 dex. For 4 Gyr these values vary by small amounts and give $T_{\rm eff}$ as 1994K, mass=0.072$M_{\odot}$ and log g=5.38 dex. In general the DUSTY models predict hotter temperatures and slightly higher masses than the COND models for these parameters. The mean of the $T_{\rm eff}$ values are 2041K with a standard deviation of 67K. They suggest that Cand 10 has a log g=5.3-5.4 and a mass of 0.072$\pm$0.003$M_{\odot}$ (also calculated as the mean and standard deviation of the results from the models with the age range). A further observation of a higher signal-to-noise spectrum would help tighten the constraints on the spectral type here. Nonetheless HD120005C has a constrained age and distance. The full set of parameters for the HD120005C system are shown in Table. 5.5.

5.5 Discussion

Of the 16 candidate UCD + main-sequence binary systems, five (Cand 3, 4, 5, 12 &14) have been previously identified as such (Kirkpatrick et al. 2001; Wilson et al. 2001), four (Cand 1, 7, 11 & 15) have colours inconsistent with those of known L dwarfs. The remaining seven were analysed for common proper motion. Cand 2 had a small baseline and a proper motion could not be measured, two (Cand 6 & 9) are ruled out as companions and four (Cand 8, 10, 13 & 16) are common proper motion companions. Of these, two (Cand 10 & 13) are confirmed as UCDs through spectroscopy. The chance of finding a randomly aligned UCD to a star with a common proper motion is small. As previously discussed in §3.3.3 the chance of finding a randomly aligned WD + UCD with a common proper motion at a separation of 89 arcsec is 0.0036. Taking into account the relative number of main-sequence stars in the sample (25 times the number of WDS; 1532 compared to 40,000), it suggests that the chance of a randomly aligned main-sequence

Table 5.5: Parameters of the system HD12005

Parameter		Value
Separation	.....	4691 AU
Distance	.....	44.9 pc
Age of system	.....	2-4 Gyr
Fe/H	.....	0.0 dex
HD120005AB		
RA	.....	15 57 49.62
DEC	.....	+59 16 15.69
SpT	.....	F5
V	.....	6.51
M_V	.....	3.25
B-V	.....	0.49
HD120005C		
RA	.....	13 46 08.15
DEC	.....	+30 55 03.8
J	.....	15.46±0.06
J-K	.....	1.25
M_J	.....	12.20
SpT	.....	L0±2
$T_{\rm eff}$	.....	2041±67 K
mass	.....	0.072±0.003 $M_\odot$
log g	.....	5.3-5.4 dex

+ UCD system at the level of the proper motions (104 and 119 arcsec for Cand10 and Cand13, respectively) is 0.09 and thus these two systems, verified through spectroscopy can be assumed to be bonafide UCD + main-sequence binaries.

In order to confirm the remaining two common proper motion UCD + main-sequence systems, follow-up spectroscopy is required to confirm their cool nature. An additional epoch measurement would also be required to analyse the proper motion of Cand 2, confirming it, or not as a common proper motion companion.

Chapter 6

Further discussion and conclusions

In this chapter the findings presented throughout this thesis are brought together and the contribution made to the number of known systems with an age constraint is reviewed. Other UCDs with constrained ages come from studies of the primary member of a binary system, from a member of an open cluster or moving group, or from the few instances of young isolated field UCDs where the detection of lithium can be used as an age indicator. These UCDs with constrained ages are here referred to as benchmarks. The benefit these UCDs could have to current models and the understanding of ultracool atmospheres is also discussed, along with a comparison to simulations of the distribution in mass-age space of such benchmarks. In the following sections benchmark UCDs from the literature are reviewed and suggestions on how they can be studied to help refine models are made. Correlations between the available broadband NIR colours and properties ($T_{\rm eff}$, log g and [Fe/H]) of these UCDs are also investigated. Finally recommendations for the expansion of this work are made.

6.1 The ultracool mass-age distribution

As well as substantial candidate samples this work has presented the confirmed discovery of three UCDs in binary systems with main-sequence (F and M) and WD stars. The properties (age and distance) of the UCDs were constrained from the primary stars and UCD mass, $T_{\rm eff}$ and log g estimated using the Lyon group models assuming both dusty (DUSTY) and dust-free (COND) atmospheres. Whilst neither model is perfect the use of these two types provides a good indication of the uncertainties in the derived atmospheric

properties. These systems are thus benchmark UCDs with derived properties for ages >1Gyr.

An indication of the expected distribution of benchmark objects was presented in Pinfield et al. (2006), who simulated a local disk population of UCDs assuming a uniform spatial distribution with an IMF (α=1) and a formation history identical to the local stellar population as described by Rocha-Pinto et al. (2000). The spread in scale height with age in the disk (which causes older populations to become more vertically dispersed, causing lower densities in the plane) was also taken into account by normalising each UCD using the relations from Just (2003). Two populations, corresponding to the detection limits of 2MASS (J$\leq$16 and $|b| > 15$) and the UKIDSS LAS (J$\leq$ 19.5 and $|b| > 57$, assuming the full expected 4000 degree^2 coverage) were simulated. For 2MASS one could expect to probe L dwarfs out to $\sim$20pc (where M_J $\sim$14.5) and the UKIDSS LAS should be sensitive to late T dwarfs out to $\sim$50pc (M_J $\sim$15.5). These populations are shown in Fig. 6.1

As well as simulations of the mass-age distribution for UCDs expected to be detected from surveys, a simulation of the number of expected benchmark UCD companions to subgiants and WDs was also made, and are shown as filled circles and open squares, respectively in Fig. 6.2. They show a large amount of overlap in mass-age space, but in general show that subgiant companions are more sensitive to late T dwarfs and cover age ranges 2-10 Gyr, while the WD companions should better probe the intermediate age range (2-4 Gyr). Young benchmarks (not the focus of this thesis) can be found in clusters and moving groups, indicated as a boxed region in Fig. 6.2.

6.2 The current benchmark population

A search of the literature was conducted to search for all known UCDs with some form of age and mass constraints. These include UCDs as members of wide binary systems, field UCDs that could have a robust age indicator and members of open clusters or moving groups. An age constraint of 0.1-10Gyr was also placed on the population considered, as UCDs in very young clusters ($\leq$10Myr) such as Orion (Hillenbrand 1997; Muench et al. 2002; Slesnick, Hillenbrand & Carpenter 2004), IC348 (Luhman et al. 2003b; Muench et al. 2003), Taurus (Briceño et al. 2002;Guieu et al. 2006), ρOphiuchus (Luhman & Rieke 1999; Wilking et al. 2005), Chameleon (Comerón et al. 2004; Luhman 2004) and Upper Sco (Lodieu, Hambly & Jameson 2006; Lodieu et al. 2008) were not included here

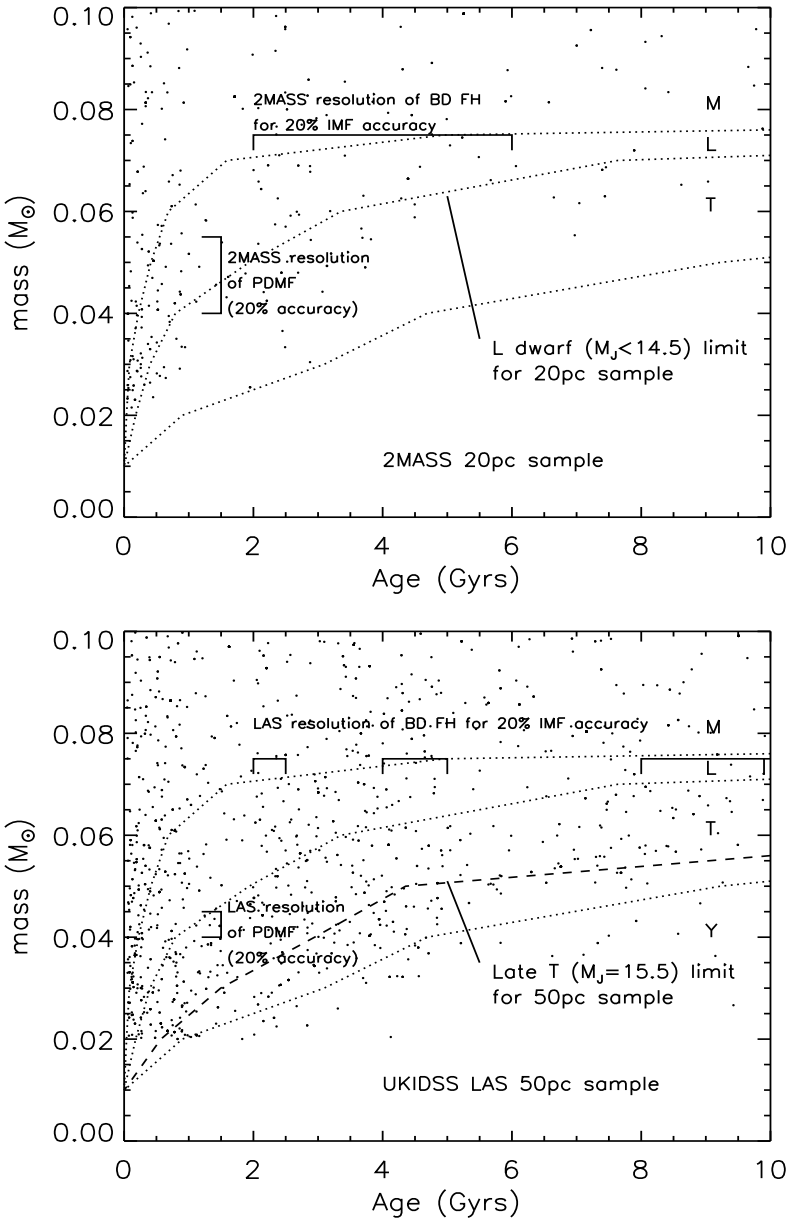

Figure 6.1: Simulations of the UCD mass-age population from Pinfield et al. (2006). Top: For 2MASS, where J≤16.0 and $|b| > 15$. Bottom: for UKIDSS LAS, where J≤ 19.5 and $|b| > 57$ for the full expected 4000degree^2 coverage. Overplotted are estimated spectral divisions for M, L and T dwarfs. Also indicated are the detection limits of 20pc and 50pc for 2MASS and UKIDSS LAS, respectively and the resolution (for 20% Poisson uncertainties) of the UCD formation history (FH) and the present day mass function (PDMF).

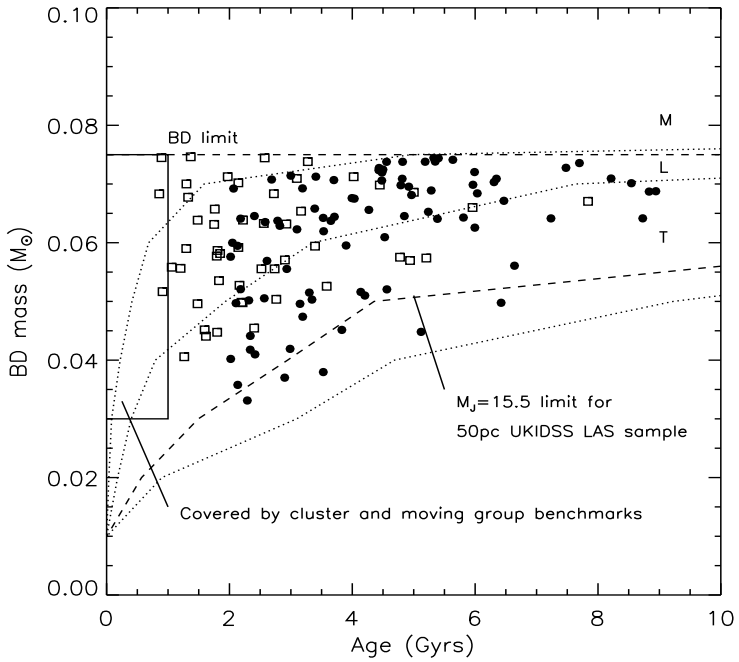

Figure 6.2: Simulations of the UCD mass-age population from Pinfield et al. (2006) for UCD companions to WDs (open squares) and subgiants (filled circles). Overplotted are estimated spectral type divisions for M, L and T dwarfs and the UKIDSS LAS detection limit of 50pc. Also shown is a boxed region where the young benchmark UCDs (members of clusters and moving groups) are expected.

as the formation of UCDs is not, as yet fully understood and the models of such youthful objects remain unreliable.

As benchmark UCDs will ultimately be used to test models via their photometric and spectroscopic properties, then UCDs as members of eclipsing binaries and unresolved companions are not likely to be useful for these kinds of studies. Despite the potential to provide a mass and radius constraint, which could be otherwise used to compare structure models. Such systems include the eclipsing binary system GJ 802, a companion to an M5 star, with a period 19 hrs. Discovered by Pravdo, Shaklan & Lloyd (2005) and typed as an L5-L7 (Knapp et al. 2004), GJ 802 has a measured dynamical mass of 65±5M$_{Jup}$, with an orbit of 3.14±0.03 yr (Ireland et al. 2008). The age of the UCD, inferred from the M5 primary is based on activity (Pravdo, Shaklan & Lloyd 2005), having both Hα and X-ray emission, indicating an age of ∼6 Gyr. However its measured kinematics place it in the thick disk population at an age of ∼10 Gyr (but indicate it should be at least 3 Gyr). Ireland et al. (2008) also compared the measured ages with those suggested from the Lyon group models, which indicate an age of ∼2 Gyr. They thus place the age range for the system of 2-10 Gyr, which is a large uncertainty for use as a benchmark object.

One of the most recently discovered benchmarks in terms of mass comes from the binary system 2M15344-2952AB, which comprises of two T dwarfs (T5.0+T5.5). The system was discovered as a single object by Burgasser et al. (2002) and later resolved into its 15.1 yr orbital period system with adaptive optic (AO) observations of Liu, Dupuy & Ireland (2008) to a separation of ∼2 AU. They estimate the age of the system at 0.78±0.09 Gyr with dynamical masses of 30.1±1.7 and 28.2±1.7 by mapping the orbit through repeated AO observations. Measurements of log g were calculated using evolutionary tracks from the Tucson group models (Burrows et al. 1997b) and the Lyon COND models, with the measured bolometric luminosity and mass of the system, such that they estimate log g as 4.91±0.04 and 4.87±0.04, for the T5 and T5.5, respectively.

The system GD1400 is a spectroscopic WD + L6/7 binary, discovered by Farihi & Christopher (2004) (separation unknown) and has an age estimate from the WD cooling age. The cooling age of the WD was derived from models, then added to the main-sequence age, which was estimated using predicted masses from initial-final-mass relations, suggesting an age of 1-1.5 Gyr. The kinematics of the system are also consistent with a young disk object and are in agreement with the age derived from the WD models. A likely mass and $T_{\rm eff}$ are also suggested as ∼1650K and ∼60M_{Jup}, based on models the of Chabrier et al. (2000c).

The WD 0137-349 is also a close binary system containing a WD + L8. The system, which was discovered by Maxted et al. (2006) via radial velocity measurements and then confirmed by Burleigh et al. (2006a) by spectroscopy has a separation of a = 0.65 $R_{\odot}$ (0.003 AU). The mass of the system was derived from the mass ratio and radial velocity measurements to infer a mass of 55±6M_{Jup}. For the L8 Burleigh et al. (2006a) estimated a $T_{\rm eff}$ of 1300-1400K from the models of Burrows et al. (1997b) and the Lyon group COND models, which suggest an age of ∼1 Gyr. They note however that the system may be older than this due to possible interaction between the two components, thus this gives only a minimum age for the system.

None of these four systems, while having some constraints will prove useful for subsequent analysis of their spectroscopic and photometric properties and were not considered good benchmarks objects in this context.

In addition to the systems confirmed in this work, the candidate systems from searches of UCD companions to subgiants and main-sequence stars (described in Chapters 4 and 5) with a measured age (Nordstrom et al. 2004; Feltzing, Holmberg & Hurley 2001) and distance were also included. For these candidates, masses were estimated from the

Lyon group DUSTY and COND models using the age of the primary and interpolating between two appropriate age intervals in the model grids. The quoted masses are the mean of the model derived values and errors are the standard deviation. The properties (assuming the candidates are genuine), including the mass, age, $T_{\rm eff}$ and log g are shown in Table. 6.1 (subgiant + UCD candidates) and 6.2 (MS + UCD candidates) and are plotted as large open orange diamonds and small open blue diamonds, respectively in Fig. 6.3 - 6.5.

6.2.1 Open clusters and moving groups

Young (<1Gyr) benchmark UCDs can be identified as members of open clusters from their measured distances, proper motions and their position on a colour-magnitude diagram, or from members of moving groups via their kinematics, which can be traced back to the originating cluster position, confirming their membership. This kinematic signature should still be intact until an age ∼1 Gyr before the stars are dispersed by disk heating (De Simone, Wu & Tremaine 2004). Included here are confirmed cluster and moving group members with ages 0.15 <Gyr< 1 from the Hyades, Praesepe, Pleiades and TWA Hydra clusters and the Castor moving group.

Hyades

The Hyades is the closest cluster at 46.3pc and is dated at 0.625±0.05 Gyr with a measured metallicity of [Fe/H]=0.14±0.05 (Perryman et al. 1998). There have been various searches for UCD members of the Hyades, but not until recently, with the aid of deep NIR imaging surveys have any been identified. Hogan et al. (2008) presented 12 L dwarfs, discovered through photometric and proper motion analysis from UKIDSS and 2MASS data; and Bouvier et al. (2008) present the first T dwarfs from their survey using the Canada-France-Hawaii Telescope (CFHT).

M_J measurements and age (inferred from cluster membership) were used to derive mass, $T_{\rm eff}$ and log g estimates for the L dwarfs from Hogan et al. (2008). Using the Lyon group COND and DUSTY models masses were derived by interpolating between the 500 Myr and 1 Gyr simulations. These values are shown in Table. 6.3, along with the published values for mass of the two T dwarfs confirmed from Bouvier et al. (2008), who use the DUSTY models but also consider the grainless NextGen models (Baraffe et al.

Table 6.1: Subgiant + UCD candidates with age and mass constraints estimated from the Lyon group DUSTY and COND models, assuming they are genuine companions.

Candidate UCD	Subgiant	D pc	Age[a] Gyr	Fe/H[a] dex	Mass M_{Jup}	$T_{\rm eff}$ K	log g dex
Cand T11	2944	44.9	$9.2^{+1.4}_{-1.1}$	-0.48	69.2±2.1	1447±238	5.44±0.04
Cand T2	2944	44.9	9.2±1.4	-0.48	70.7±1.2	1552±185	5.44±0.04
Cand T3	2944	44.9	$9.2^{+1.4}_{-1.1}$	-0.48	70.7±1.2	1552±185	5.44±0.04
Cand T4	9316	76.9	$5.8^{+1.3}_{-1.0}$	-0.01	68.0±2.8	1558±186	5.40±0.04
Cand T6	17801	52.7	$12.7^{+0.0}_{-2.0}$	-0.38	70.1±1.4	1460±284	5.45±0.04
Cand T7	18824	52.2	$4.5^{+0.8}_{+0.7}$	-0.21	68.8±4.0	1664±158	5.38±0.01
Cand T8	19431	56.2	5.5±1.2	-0.50	65.4±5.8	1444±245	5.39±0.04
Cand T9	19431	56.2	5.5±1.2	-0.50	66.4±5.1	1492±220	5.39±0.04
Cand T12	26273	84.0	8.1±2.3	-0.50	71.7±1.0	1656±147	5.43±0.04
Cand LT1	26273	84.0	8.1±2.3	-0.50	69.5±2.7	1501±214	5.43±0.04
Cand L2	27014	79.9	3.3±0.6[b]	-	67.8±4.5	1797±133	5.44±0.04
Cand T14	31895	87.4	4.8±1.0	0.17	68.0±5.0	1636±160	5.38±0.05
Cand T15	35279	63.7	6.5±0.8[b]	-	70.9±1.4	1626±183	5.42±0.04
Cand T16	42430	19.9	$7.1^{+1.0}_{-0.9}$	0.30	62.3±7.9	1249±323	5.38±0.02
Cand T17	42430	19.9	7.1±1.0	0.30	60.2±9.4	1195±339	5.36±0.04
Cand T20	45514	83.8	$13.7^{+0.0}_{-3.2}$	-0.30	71.5±0.4	1595±197	5.44±0.04
Cand T21	45514	83.8	$13.7^{+0.0}_{-3.2}$	-0.30	72.0±0.4	1649±182	5.43±0.06
Cand T22	46404	31.2	3.3±0.4	-0.34	51.2±12.7	1225±338	5.19±0.13
Cand T23	48125	38.8	1.0±0.5	-0.01	46.4±15.9	1215±424	5.10±0.22

[a]: Nordstrom et al.(2004), [b]: Feltzing et al.(2001).

Uncertainties for [Fe/H] are not published but from comparisons with other work by Jenkins et al. (2008) would indicate uncertainties on the order of 0.1dex.

Candidates are ordered in RA and distances are calculated from Hipparcos parallaxes.

Table 6.2: Main-sequence + UCD Candidates with known ages and masses derived from the Lyon group DUSTY and COND models.

Candidate UCD	MS ID	D pc	Separation AU	Age[a] Gyr	Fe/H[a] dex	Mass M_{Jup}	$T_{\rm eff}$ K	log g dex
Cand 4	HD 89744	39.0	2409	2.2±0.2	0.17	73.5±2.0	2124±46	5.33±0.01
Cand 5	Gl 417	21.7	1997	7.7±4.7	-0.01	73.6±0.6	1840±105	5.41±0.04
Cand 9	Gl 512.1	18.1	848	$7.4^{+0.5}_{-0.7}$	-0.09	68.3±3.0	1454±238	5.43±0.03
Cand 11	Gl 527A[a]	15.6	664	$2.4^{+0.7b}_{-1.1}$	0.09	50.3±13.3	1334±307	5.19±0.13
Cand 12	Gl 584AB	18.6	3635	$6.5^{+1.0}_{-0.9}$	-0.08	67.2±4.0	1424±252	5.42±0.02
Cand 15	Gl 694.1A	22.0	1558	$2.4^{+0.2}_{-0.3}$	-0.24	56.8±8.8	1512±224	5.26±0.05

[a]: Nordstrom et al.(2004), [b]: Feltzing et al.(2001)
Uncertainties for [Fe/H] are not published but from comparisons with other work by Jenkins et al. (2008) would indicate uncertainties on the order of 0.1dex.
Distances are calculated from Hipparcos parallaxes.

1998), which are generally only useful for T_{eff} >1700K. These Hyades UCDs are plotted as pink asterisks in Fig. 6.3- 6.5.

Praesepe

The Praesepe open cluster has a similar age to the Hyades, an intermediate-age of 0.9±0.5 Gyr and lies at a distance of ∼170pc with a near solar-metallicity (Hambly, Digby & Oppenheimer 2005). Magazzu et al. (1998) spectroscopically confirmed the first (an M8.9) UCD in Praesepe, RPr1. Chappelle et al. (2005) also identified a number of candidate low mass objects through colour and proper motion measurements and calculated their corresponding masses using the DUSTY and NextGen models from their M_J measurements. In this way they identified six UCD mass candidates. These are overplotted on Fig. 6.3 - 6.5 as blue filled squares and their corresponding properties are shown in Table. 6.3.

Pleiades

One of the first bonafide BDs discovered Tiede1 (Rebolo, Zapatero-Osorio & Martin 1995), an M8 dwarf, is a member of the Pleiades cluster (age 0.08-0.125 Gyr; Schwartz & Becklin 2005, [Fe/H]=0.02±0.14; Funayama et al. 2008). Since then a handful of other late M UCDs have been spectroscopically confirmed including Calar3 (Martín et al. 1998), PIZ1 (Cossburn et al. 1997) and Roque 4 and 11 (Zapatero Osorio et al. 1998). Only one spectroscopically confirmed L dwarf has been confirmed, Roque25, an L0 of mass $57\pm15 M_{Jup}$ (Martín et al. 1998). Other searches for L dwarf members have also been presented by Bouvier et al. (1998) and Moraux et al. (2003), but only the searches by Bihain et al. (2006) and Casewell et al. (2007) have confirmed L dwarf members through proper motion. Bihain et al. (2006) confirm 6 new members and Casewell et al. (2007) confirm 9 new likely L and T members. For these, like the Hyades objects their mass, $T_{\rm eff}$ and log g values were calculated using the Lyon group COND and DUSTY models and are shown in Table. 6.4.

TWA Hydra

Also included in the list of open cluster benchmarks, despite it's young age is the UCD binary system 2MASS 1207-3932AB. This binary is a pair of young UCDs with spectral types M8 and mid-late L (where the late type UCD has a planetary mass of $\sim 8 M_{Jup}$). They were confirmed as a member of the TWA Hydrae association by Mohanty, Jayawardhana & Basri (2005) and Mohanty et al. (2007), whose very young age of ∼8Myr and distance of only ∼50pc allows the very low mass end of the UCD sequence to potentially be explored. Mohanty et al. (2007) detect Hα and X-ray emission from the sources, also confirming their youth and suggest that there may be evidence for a disk around 2MASS1207, with possible accretion in the late M companion (Gizis & Bharat 2004). They also show evidence for fluctuations in the Hα emission, suggestive of variations in the accretion rate (Mohanty, Jayawardhana & Basri 2005; Scholz, Jayawardhana & Brandeker 2005; Scholz & Jayawardhana 2006).

Castor moving group

The Castor moving group has an estimated age of 320±80 Myr, with roughly solar metallicity (Ribas 2003). LP 944-20 was confirmed as a BD by spectroscopic observations of Tinney (1998), who showed the detection of Lithium (Li) in its spectrum. Li is destroyed in stars above $0.6M_{\odot}$ and the rate at which this occurs is dependent on mass and luminosity (Basri 1998), such that more massive stars burn lithium quicker, hence for a UCD Li should take longer to be depleted, on the order of a few Myr. This is the basis of the Lithium test which was used by Tinney (1998) to estimate an age for LP 944-20 and a mass was constrained using the models of Chabrier, Baraffe & Plez (1996). In addition Ribas (2003) confirmed, through kinematics that LP 944-20 was a member of the Castor moving group (age ∼320 Myr) with roughly solar metallicity and in general agreement with the age estimates made by Tinney (1998) from the Li test.

The parameters for these UCDs are shown in Table. 6.3 and plotted in Fig. 6.3 - 6.5 as grey filled triangles.

Table 6.3: Cluster and Moving Group UCDs.

Candidate UCD	SpT	Cluster/MG	D pc	Age Gyr	Mass M_{Jup}	$T_{\rm eff}$ K	log g dex	J 2MASS	$J-H$ 2MASS	$J-K$ 2MASS	Reference
CFHT-Hy20	T2	Hyades	$\sim$46.3[a]	0.625±0.05	47±7	-	-	-	-	-	1
CFHT-Hy21	T1	Hyades	$\sim$46.3[a]	0.625±0.05	44±7	-	-	-	-	-	1
HY1	late M/ early L	Hyades	36.2 ± 1.63	0.625±0.05	48.42±15.8	1993±109	4.95±0.32	14.60	0.75	1.18	2
HY2	late M/ early L	Hyades	52.8 ± 3.08	0.625±0.05	41.29±13.7	1866±29	4.83±0.38	15.94	1.13	1.68	2
HY3	late M/ early L	Hyades	54.6 ± 3.72	0.625±0.05	32.70±14.9	1935±73	4.90±0.34	15.75	0.97	1.58	2
HY4	late M/ early L	Hyades	54.4 ± 4.46	0.625±0.05	46.69±15.2	1950±95	4.92±0.33	15.60	0.63	1.37	2
HY5	late M/ early L	Hyades	46.6 ± 2.56	0.625±0.05	40.14±12.7	1824±45	4.82±0.37	15.81	1.09	1.76	2
HY6	late M/ early L	Hyades	50.9 ± 3.49	0.625±0.05	46.10±15.0	1943±84	4.91±0.34	15.50	0.69	1.25	2
HY7	late M/ early L	Hyades	53.0 ± 4.06	0.625±0.05	40.96±11.6	1854±33	4.83±0.38	15.99	0.96	1.63	2
HY8	late M/ early L	Hyades	44.8 ± 3.68	0.625±0.05	41.13±13.5	1859±31	4.83±0.38	15.60	1.05	1.58	2
HY9	late M/ early L	Hyades	57.8 ± 5.36	0.625±0.05	36.01±10.6	1707±100	4.78±0.36	16.68	1.39	2.16	2
HY10	late M/ early L	Hyades	47.8 ± 2.98	0.625±0.05	34.00±9.1	1640±132	4.77±0.34	16.54	1.11	1.70	2
HY11	late M/ early L	Hyades	37.6 ± 1.56	0.625±0.05	33.48±8.7	1618±142	4.76±0.33	16.11	1.06	1.83	2
HY12	late M/ early L	Hyades	41.4 ± 2.56	0.625±0.05	47.22±16.7	1988±115	4.92±0.33	16.73	0.96	1.93	2
LP 944-20	M9	Castor	5.0	0.320±0.08	61±5	2026±52	-	-	-	-	3
WFC81	late M/ early	Praesepe	$\sim$170	0.9±0.5	75±6	-	-	17.47	0.67	1.17	4
WFC76	late M/ early	Praesepe	$\sim$170	0.9±0.5	73±7	-	-	17.58	0.75	1.12	4
WFC53	late M/ early	Praesepe	$\sim$170	0.9±0.5	71±8	-	-	17.83	0.65	1.19	4
WFC24	late M/ early	Praesepe	$\sim$170	0.9±0.5	68±8	-	-	17.99	0.68	1.96	4
WFC11	late M/ early	Praesepe	$\sim$170	0.9±0.5	65±9	-	-	18.37	0.85	1.17	4
RPr1	M8.5	Praesepe	$\sim$170	0.9±0.5	74±7	-	-	17.7	-	1.26	4,5
2MAS1207A	M8	TWA	$\sim$50	$\sim$0.008	24±6	2550±150	3.5-4.5	13.0	0.61	1.05	6
2MAS1207B	Mid-Late L	TWA	$\sim$50	$\sim$0.008	8±2	1600±100	3.5-4.5	20.0	1.91	3.07	6

Table 6.4: Pleiades cluster UCDs.

Tiede1	M8	Pleiades	135±2	∼120Myr	57±15	-	-	-	-	-	7
Calar3	M8	Pleiades	135±2	∼120Myr	57±15	-	-	-	-	-	8
Roque4	M9	Pleiades	135±2	∼120Myr	57±15	2285^{+150}_{-215}	-	-	-	-	9
Roque11	M8	Pleiades	135±2	∼120Myr	57±15	2485 ±250	-	-	-	-	9
PIZ1	M9	Pleiades	135±2	∼120Myr	57±15	∼2300	-	-	-	-	10
Roque25	L0	Pleiades	135±2	∼120Myr	55±15	1900-2200	-	-	-	-	11
BRB18	late M/ early L	Pleiades	135±2	∼120Myr	30.9±3.5	1543±425	4.72±0.05	17.61	0.87	1.53	12
BRB20	late M/ early L	Pleiades	135±2	∼120Myr	27.3±4.3	1753±110	4.67±0.05	18.06	0.73	1.50	12
BRB21	late M/ early L	Pleiades	135±2	∼120Myr	26.9±4.6	1732±120	4.66±0.05	18.14	1.09	1.75	12
BRB22	late M/ early L	Pleiades	135±2	∼120Myr	25.8±5.2	1689±140	4.64±0.07	18.31	0.94	1.62	12
BRB28	late M/ early L	Pleiades	135±2	∼120Myr	20.9±7.9	1521±215	4.50±0.18	19.02	1.13	2.02	12
BRB29	late M/ early L	Pleiades	135±2	∼120Myr	20.9±7.9	1515±215	4.50±0.18	19.05	1.29	2.17	12
PLZJ56	late M/ early L	Pleiades	135±2	∼120Myr	76.3±0.2	2709±10	4.63±0.01	15.25[c]	0.65	0.94	13
PLZJ50	late M/ early L	Pleiades	135±2	∼120Myr	75.5±0.5	2705±10	4.63±0.01	15.26[c]	0.62	1.50	13
PLZJ23	late M/ early L	Pleiades	135±2	∼120Myr	18.9±7.4	1356±260	4.47±0.16	19.96[c]	0.65	0.95	13
PLZJ93	L/T	Pleiades	135±2	∼120Myr	18.9±7.4	1356±260	4.47±0.16	19.96[c]	-0.02	0.55	13
PLZJ323	L/T	Pleiades	135±2	∼120Myr	19.6±7.6	1417±245	4.48±0.13	19.61[c]	-	-	13
PLZJ721	L/T	Pleiades	135±2	∼120Myr	18.3±7.1	1308±275	4.46±0.16	20.24[c]	-0.23	-	13
PLZJ235	L/T	Pleiades	135±2	∼120Myr	18.7±7.3	1344±265	4.47±0.16	20.03[c]	-0.28	-	13
PLZJ112	L/T	Pleiades	135±2	∼120Myr	18.2±7.1	1301±275	4.46±0.16	20.28[c]	-	-	13
PLZJ100	L/T	Pleiades	135±2	∼120Myr	18.3±7.1	1306±275	4.46±0.16	20.25[c]	-	-	13

Notes:

Distance and mass are from the primary source (see text), unless otherwise stated.

[a]: Perryman et al. (1998), [b]: Perryman et al. (1997), [c]: MKO magnitudes.

1: Bouvier et al. (2008), 2: Hogan et al. (2008), 3: Tinney (1998), 4: Chappelle et al. (2005), 5: Magazzu et al. (1998)

6: Mohanty, Jayawardhana & Basri (2005), 7: Rebolo, Zapatero-Osorio & Martin (1995), 8: Martín, Rebolo & Zapatero-Osorio (1996)

9: Zapatero Osorio et al. (1998), 10: Cossburn et al. (1997),11: Martín et al. (1998), 12: Bihain et al. (2006), 13: Casewell et al. (2007)

6.2.2 UCDs in binaries

A good source of benchmark UCDs, as shown in this work comes from members of binary systems. Those with published, measured age and mass come from resolvable companions to WD and main-sequence stars.

UCD companions to main-sequence stars

The largest complement of benchmark UCDs that have thus far been found are members of widely separated multiple or binary systems with main-sequence stars. The age of the main-sequence primary can be calculated via several methods, including age-metallicity relations, chromospheric or coronal activity (Ca_{II}HK, H_{α}, X-ray), Lithium abundance, rotational or space velocity, or from their location on an HR diagram compared to theoretical isochrones. Included here are 22 such UCDs in binary systems with main-sequence stars where their ages have been constrained using one or more of these methods.

One of the first confirmed BDs was Gl 229B (Nakajima et al. 1995), a T6.5 companion to the M dwarf Gl 229. Aged at a young ∼30 Myr, based on the age estimate for the M1 flare star primary. It is calculated to have $T_{\rm eff}$∼1000±100K, log g≤3.5 and [Fe/H]∼ -0.5 by Leggett et al. (2002b) who compared their high resolution spectra to the AMES DUSTY and COND models (Burrows et al. 1997b; Burrows et al. 2001), suggesting a best fit for both Gl 229A and B comes from a low metallicity solution (Fe/H ∼-0.5), despite its kinematics placing it in the young disc population. The young age estimate is also consistent with the low gravity estimate, which they suggest corresponds to a mass of 25M_{Jup} (Leggett et al. 1999), with a lower limit of >7M_{Jup} (Leggett et al. 2002a).

The multiple system Gl 570, contains a T dwarf companion to K4V, M1.5V and an M3V star members (Burgasser et al. 2000; Geballe et al. 2001). Burgasser (2007) used a technique, whereby they make comparisons of the H_2O and colour ratios of the spectrum, with the same ratios from theoretical model spectra to estimate the age of Gl 570A (K4), which was measured as 2-5 Gyr (2^{+3}_{-1} Gyr), with a $T_{\rm eff}$=810±30, log g=5.0±0.3 and an estimated [Fe/H]=0.01-0.10 (Cayrel de Strobel et al. 1997; Feltzing & Gustafsson 1998; Santos & Piatti 2004; Valenti & Fischer 2005) for Gl 570D.

Kirkpatrick et al. (2001) identified two UCD companions to G type stars (Gl 417B and Gl 584) and used the calculations of Lachaume et al. (1999) to infer ages of 0.08-0.3 Gyr and 1.0-2.5 Gyr for the G dwarfs, respectively. They used the models of Burrows

et al. (1997b) to calculate a mass, based on an average temperature for the UCDs corresponding to spectral type. The primary stars also indicate a metallicity of [Fe/H]=-0.01 and -0.20, respectively. They obtained and measured spectra for three other UCD companions to main-sequence stars, including GJ 1048B/LHS102 (Gizis, Kirkpatrick & Wilson 2001), G 196-3B (Rebolo et al. 1998) and GJ 1001B (EROS Collaboration et al. 1999), calculating ages of 0.6-2.0 Gyr, 0.06-0.3 Gyr and 0.07-0.01 Gyr respectively, based on published ages and inspection of their spectra for Hα and Li, with masses of 70$\pm$10 M_{Jup}, 35$\pm$15 M_{Jup} and 70$\pm$10 M_{Jup}, respectively. Leggett et al. (2002a) also calculated log g for LHS102B as 5.5$\pm$0.5 with solar metallicity, from studies of the primary star.

The G2V star, HD 130948 was found to be a wider multiple system containing a closely separated UCD binary, consisting of an L0 and an L4 dwarf by Potter et al. (2002), who estimated an age for the system of <0.8 Gyr, based on X-ray activity, Li abundance and fast rotation of the G dwarf. The two UCD companions are at a separation of $\sim$48 AU and from Lyon group models they derived masses of <78 M_{Jup} and <68M_{Jup}. Nordstrom et al. (2004) measure an [Fe/H] of -0.15 for the G star primary.

The ϵIndi system (Scholz et al. 2003) has been well studied and through a combination of direct and differential imaging by Geißler et al. (2007) the UCD companion ϵIndiB was resolved into two T dwarfs (T1 and T6). The primary K4.5V star has an age of 0.8-2.0 Gyr (Lachaume et al. 1999) and the mass of the two T dwarfs are given as 47 M_{Jup} and 28 M_{Jup} to 25% uncertainty, as measured by McCaughrean et al. (2004).

Chauvin et al. (2005) discovered a UCD companion to AB Pic, a K2V star, also part of the large Tucana-Horologium association, which has an estimated age of $\sim$300 Myr and [Fe/H]=-0.64. The L1$^{+2}_{-1}$ companion is at a separation of 250-270 AU and from model predictions has a mass of 13-14 M_{Jup} and $T_{\rm eff}$=1500-1700 K (Lyon group DUSTY and Burrows models).

The UCD 2M0025+4759 was resolved into two L4 type UCDs with HST imaging by Reid et al. (2006) and was shown to have common proper motion to the solar metallicity F8V star HD2057 (G171-58/G217-47) at a separation of $\sim$8800 AU. This system is dated at <1 Gyr, from detection of Li in the UCD, however the age of the F8V primary was measured at $\sim$1.1 Gyr, with an upper limit of 3.6 Gyr from its metallicity (Nordstrom et al. 2004). It is however likely that the primary F star is itself a binary (Latham et al. 2002; Balega et al. 2004), and would thus account for the age discrepancy.

Metchev & Hillenbrand (2006) also used this same method of dating for the L7.5 companion to the solar analogue G star HD203030. It is aged at 130-400 Myr and has

a derived mass of 24 M_{Jup}, using the Lyon group and Burrows models. Metchev & Hillenbrand (2004) also identified an L4 companion to the F5V star HD 49197, as part of their AO survey of young solar-type stars. The age was inferred from the activity, presence of Li and kinematics of the primary and the age was estimated from the Lyon group DUSTY models in this case.

Luhman et al. (2007) also report two T dwarf companions, HN pegB (Mugrauer et al. 2006) and HD3651B to G0V and K0V star primaries respectively, from their survey around stars in the solar neighborhood using the Spitzer Space Telescope and date them from studies of the primaries. For HN Peg a metallicity is available from Nordstrom et al. (2004), who measure HN Peg as having [Fe/H]=-0.12 and [Fe/H]= 0.09-0.16 for HD3651 and measured a mass of 40-72M_{Jup} and $T_{\rm eff}$=790-840K (Liu, Leggett & Chiu 2007; Luhman et al. 2007). The separation from the primary is 480AU, and it also has a sub-Saturn mass planetary companion. The age of this system was estimated from measurements of Ca_{II}HK emission from the primary (Wright et al. 2004), an indicator of activity, where main-sequence stars spin down as they lose angular momentum, over time decreasing in activity. This is also seen as a decrease in X-ray emission, which was measured by Hempelmann et al. (1995) for this system, along with high resolution spectral observations from Valenti & Fischer (2005). The age for HD3651A was calculated as 3-12 Gyr (6^{+6}_{-3}) and hence inferred for the age of the T dwarf companion. Burgasser (2007) more recently re-examined this system and derived an age of 0.7-4.7 Gyr using their semi-empirical techniques, which use comparisons of the H_2O and colour ratios of the spectrum, giving a better constraint on the age than the main-sequence host star. These also suggest that the UCD has a $T_{\rm eff}$=790±30, log g=5.0±0.3 and a mass of 34±13M_{Jup}.

An unusually blue L dwarf (2MASS J17114559+4028578) was discovered to be a widely separated companion to the M4.5V dwarf G203-50 (Radigan et al. 2008), which has an age of 1-5 Gyr, estimated from it's activity. The mass of the $L5^{+2.0}_{-1.5}$ companion is calculated from the total mass and mass ratio of the system as 69^{+8}_{-15} M_{Jup} and $T_{\rm eff}$ of 1700^{+210}_{-250}K. The close UCD companion to the binary system Gl 337AB was resolved for the first time by Burgasser, Kirkpatrick & Lowrance (2005) with AO imaging, revealing not a single L8 but two UCDs of nearly equal magnitude at a separation of ∼11 AU from each other and 880 AU from Gl 337AB (G9V + K1V). The age of the primary was measured as 0.6-3.4 Gyr by Wilson et al. (2001) using age indicators (activity, Li, [Fe/H] and kinematics). They also present the discovery of the 1.5-3.0 Gyr old L0 companion to the F7V star, HD89744, which in addition also has an exoplanet companion. Their search

also detected an L dwarf companion to an M0 star (Gl 618.1), however no age constraint could not be placed on this system, thus it can't be considered a benchmark.

All of the above discussed UCD + main-sequence binary systems are shown in Fig. 6.3 - 6.5 as red lower half filled circles and are listed with their parameters in Table. 6.5.

Table 6.5: UCD in binaries

UCD	SpT	Primary	D	Sep	Age	Mass	Teff	log g	Fe/H	J	$J-H$	$J-K$
ID		SpT	pc	AU	Gyr	M_{Jup}	K	dex	dex	2MASS	2MASS	2MASS
Gl 417B	L4.5	G0V	21.76[a]	∼2000	0.08-0.3	36±15	1600-1800	-	-0.01[f]	14.57	1.10	1.88
Gl 584C	L8	G1V+G3V	18.66[a]	∼3600	1.0-2.5	62±15	1300-1600	-	-0.20 [f]	16.32	1.33	2.09
GJ 1048B	L1	K2V	21.2 6[a]	∼250	0.6-2.0	68±10	-	-	-	13.67	0.69	1.35
G 196-3B	L2	M2.5V	∼20.0	∼300	0.06-0.6	38±15	-	-	-	14.90	1.23	2.09
GJ 1001B/LHS102B	L8	M4V	9.556[a]	180	>1.0	73±10	1900-2000	$5.5^{+0.5}_{-0.0}$[e]	0.00 [e]	13.10	1.05	1.70
HD203030B	L7.5	G	40.86[a]	487	0.13-0.40	24^{+8}_{-11}	1206^{+74}_{-116}	-	0.00[f]	18.13	1.28	1.92
HD 49197B	L4±1	F5V	44.6[a]	43	0.26-0.79	62^{+12}_{-25}	-	-	-	15.92	1.30	1.63
HN PegB	T2.5±0.5	G0V	18.4±0.3[a]	795±15	0.3±0.2	22±9	1130±70	-	-0.12[f]	15.86	0.49	0.76
HD 3651B	T7.5±0.5	K0V	11.1±0.1[a]	480	0.7-4.7	53±14	810±50	5.3±0.2	0.19[f]	16.16	-0.51	-0.57
ϵIndiBa	T1	K4.5V	3.626±0.009[a]	1459	0.8-2.0	47±10	-	-	-	12.29[b]	0.78[b]	0.94[b]
ϵIndiBb	T6	K4.5V	3.626±0.009[a]	1459	0.8-2.0	28±7	-	-	-	12.29[b]	0.78[b]	0.94[b]
2M1711+4028	$L4^{+2}_{-1.5}$	M4.5V	21.2±3.9[a]	135±25	1-5	69^{+8}_{-15}	1700^{210}_{250}	-	-1.0[f]	15.00	0.79[c]	1.28[c]
Gl 229B	T6.5	M1-M2	5.7[a]	∼45	∼0.03	7-25	1000±100	≤3.5	∼-0.5[e]	14.20	-0.35	-0.35
Gl 337CD	L8+L8/T	G8V+K1V	20.5[a]	10.9/880[d]	0.6-3.4	40-74	1300-1600[b]	-	-0.29[f]	15.51[b]	0.89[b]	1.47[b]
HD89744B	L0	F7IV-V	39[a]	2460	1.5-3.0	77-80	2000-2200	-	0.17[f]	14.90	0.90	1.30
2M0025+4759	L4+L4	F8	42±2	8800	<1	<65	-	-	-	14.84[b]	1.18[b]	1.94[b]
AB PicB	$L1^{+2}_{-1}$	K2V	$47.3^{+1.8}_{-1.7}$	250-270	0.03	13-14	1500-1700	4.05±0.5	-0.64[f]	16.18	1.49	2.04
Gl 570D	T7.5	K4V+M1.5V+M3V	5.9[d]	-	2^{+3}_{-1}	33^{+18}_{-9}	780^{+45}_{-30}	$5.0^{+0.3}_{-0.2}$	0.01-0.10	14.82	-0.56	-0.72
HD 130948B	L0-L4	G2V	17.9[a]	∼48	<0.8	<78	1950±250	-	-0.15[f]	13.9[b]	0.7[b]	1.6[b]
HD 130948C	L0-L4	G2V	17.9[a]	∼48	<0.8	<68	1950±250	-	-0.15[f]	13.9[b]	0.7[b]	1.6[b]
2M0025+4759A	L4+L4	F8	42±2	∼8800	∼1.1	∼48	-	-	-	14.84[b]	1.18[b]	1.94[b]
2M0025+4759B	L4+L4	F8	42±2	∼8800	∼1.1	∼47	-	-	-	14.84[b]	1.18[b]	1.94[b]

[a]: parallax of primary from Perryman et al. (1997)

[b]: Combined value from unresolved properties of a UCD+ UCD binary system.

[c]: synthetic colours calculated from the spectrum (Radigan et al. 2008).

[d]: 10.9 AU for separation of L8+L8 and at 880 AU from the MS primary.

[e]: Leggett et al. (2002), [f]: Nordstrom et al. (2004).

UCD companions to white dwarfs

There are also a couple of known WDs with UCD companions, these have measured ages (for the WD) and masses (for the UCDs) and are thus good benchmark systems and included here.

The first discovered WD + UCD system, GD165AB (Becklin & Zuckerman 1988) has been the subject of much study and is widely used as a template L dwarf. Kirkpatrick et al. (1999a) calculated a crude age estimate for the system in a similar way to that of GD1400, from the mass of the WD (0.56-0.65$M_{\odot}$), taking into account the cooling age and the main-sequence lifetime, for corresponding progenitor masses of 1.2-3M.0$_{\odot}$. They estimate that the age of the system is 1.2-5.5 Gyr and used the NextGen models to calculate $T_{\rm eff}$ and plot GD 165B in M_K - log(age) space to compare it to model tracks for different mass UCDs to derive a mass for GD 165B as 65-75 M_{Jup}, with a log g=5.0±0.5.

The M8.5 companion (APMPM J2354-3316C/LDS 826C) to the WD + M4 system LHS4039/4040 (Scholz et al. 2004; Farihi, Becklin & Zuckerman 2005) is the most similar system to 2MASSJ0030-3739/2MASSJ0030-3740 discovered in this work, having a separation of ∼2200 AU. The age of the system was estimated at ∼1.8 Gyr by Silvestri et al. (2001) from the M dwarf component, via it's activity and the mass of the UCD was calculated as ∼100M_{Jup} by Scholz et al. (2004), although they don't state how this was calculated. The parallax distance and J- band magnitude was used to re-evaluate the mass of the UCD using the COND and DUSTY Lyon group models, which yield a mass 77±3 M_{Jup} and $T_{\rm eff}$∼2260K, which places it at the stellar/substellar border. This system, as it has a good age constraint is included here. The full list of properties of these benchmark UCD companions to WDs are shown in Table. 6.6 and are plotted as green stars in Fig. 6.3 - 6.5.

Table 6.6: UCD + WD binaries

UCD ID	SpT	Primary ID	D	Sep	Age	Mass	Teff	log g	J	$J-H$	$J-K$
			pc	AU	Gyr	M_{Jup}	K	dex	2MASS	2MASS	2MASS
APMPM J2354-3316C	M9.5	LHS4039/4040	∼21	2200	∼1.8	77±3[a]	∼2260[a]	-	-	-	-
GD 165B	L4	GD 165	∼52	∼120	1.2-5.5	65-75	1900±100	5.0±0.5	15.6	0.90	1.51

[a]: Derived from the Lyon group DUSTY and COND models, [b]: Parallax from Van Altena et al.(1995).

6.2.3 Field UCDs

Although it is a difficult task to calculate the age of field UCDs, on occasion there are indicators, such as the presence of Li in their spectra or from their kinematics (if a distance and a radial velocity measurement are available). Several field UCDs have been identified in this way and an age estimate calculated. The isolated field UCD DENISp-J1228.2-1547 (Delfosse et al. 1997) in which Li was observed by Tinney, Delfosse & Forveille (1997), constraining the age to $\leq$1.5 Gyr. Comparison of the equivalent width measurement of the Li feature compared to the width of this feature seen in young cluster UCDs allowed a lower limit to be placed on the age at $\geq$100 Myr. Several other field UCD + UCD binaries have also been age calibrated in this way including SDSSJ0423-0414 (Geballe et al. 2002), where Li was measured by Burgasser et al. (2005); 2M0850 (Kirkpatrick et al. 1999b), where Li was observed by Reid et al. (2001b) and Kelu 1 (Ruiz, Leggett & Allard 1997). More recently Stumpf et al. (2008) has monitored Kelu1 with high resolution VLT/NACO and HST imaging suggests that it may be a triple system, where Kelu1A is likely to be a spectroscopic binary of type L0.5$\pm$0.5 + T7.5$\pm$1 and Kelu1B a L3pec $\pm$1.5 dwarf. They determined a dynamical mass for the system of 177^{+113}_{-55}M$_{Jup}$ from the orbit of the system. In addition a spectroscopic UCD + UCD binary (2MASS0320-044) in the field was discovered by Blake et al. (2008) where the measured kinematics of the system indicate an age >3.6 Gyr. These benchmark field UCDs are shown in Table. 6.7 and are plotted as purple bows in Fig. 6.3 - 6.5.

Table 6.7: Field UCDs with age estimates

UCD ID	SpT	D	Age	Mass	$T_{\rm eff}$	J	$J-H$	$J-K$
		pc	Gyr	M_{Jup}	K	2MASS	2MASS	2MASS
DENISp-J1228.2-1547	L5[1]	20.2	0.1-1.5	20-68	-	14.37	1.03	1.61
SDSSJ0423-0414a*	L6[2]	15.2±0.4	0.6-3.4	60±19	1250-1575	14.46	1.00	2.19
SDSSJ0423-0414b*	T2[2]	15.2±0.4	0.6-3.4	60±19	1200-1500	14.46	1.00	2.19
KELU1Aa*	L0.5±0.5	18.65	0.3-0.5	61±2$^+$	-	13.41	1.02	1.67
KELU1Ab*	T7.5±1	18.65	0.3-0.5	61±2$^+$	-	13.41	1.02	1.67
KELU1B*	L3pec±1.5	18.65	0.3-0.5	50±2	-	13.41	1.02	1.67
2M0850*	L6	27.70	0.95±0.75	40±20	1295±85	16.46	1.24	1.99
2M0850*	L6	27.70	0.95±0.75	31±16	1180±45	16.46	1.24	1.99
2MASS0320-044*	M0-L0.5	26.2±4.3[3]	>3.6	78-84	2300 ±100	13.26	0.72	1.12

Notes:

*: UCD + UCD Binary-measured colours are shared, $^+$: shared mass estimate

[1]: Dahn et al.(2002),[2]: Burgasser et al.(2005),[3]: Cruz et al.(2003)

6.3 Discussion

The benchmark UCDs identified here are plotted in Fig. 6.3 - 6.5 in mass-age, $T_{\rm eff}$-log g and $T_{\rm eff}$-[Fe/H] space. Fig. 6.3 shows their mass-age distribution, where the distribution of objects are in reasonable agreement with the simulations of Pinfield et al. (2006) (Fig. 6.1). Also obvious is a distance-magnitude limit, where a distance limit of 50pc has been overplotted as an aid to indicate the limits that are currently being probed by the benchmarks. This roughly corresponds to a detection limit of $J{\sim}19$, reflecting the sensitivity of the surveys used to detect these UCDs. Old, very low-mass objects are not expected to be detected by these surveys as they are too faint. The distribution also shows that the most densely populated region in mass-age space is, unsurprisingly at younger ages, where the age can be somewhat more easily constrained, as there are more useful age indicators (e.g. Lithium detection, activity, rotation) for youthful UCDs. The majority of benchmarks in this region are members of clusters or moving groups, where their metallicity is also known. It should also be noted that (omitting the candidate subgiant + UCD and main-sequence+UCD systems presented in this work) only a handful have ages >2 Gyr. Thus if the candidate systems presented here are confirmed they will make an invaluable contribution to the number of older, evolved benchmark UCDs. These also occupy the higher mass end of the diagram. This would also allow, if candidates confirmed, investigations of the mass-luminosity relation as a function of time. Fig. 6.4 shows the spread in $T_{\rm eff}$ and log g of the benchmarks, overplotted with the DUSTY and COND model isochrones (red and blue lines respectively), to show where the benchmarks sit in relation to the model parameter space. Also plotted are the benchmarks with [Fe/H] measurements as a function of $T_{\rm eff}$ in Fig. 6.5. It can be seen that the currently confirmed benchmarks are sparsely distributed, but confirmation of UCD candidate companions to subgiant and main-sequence stars could provide much information for this parameter-space. Indeed, there could be significantly more improvement via the discovery of large additional populations of benchmarks UCDs, with a range in measured properties, in ongoing and new large scale surveys (e.g. UKIDSS, VISTA).

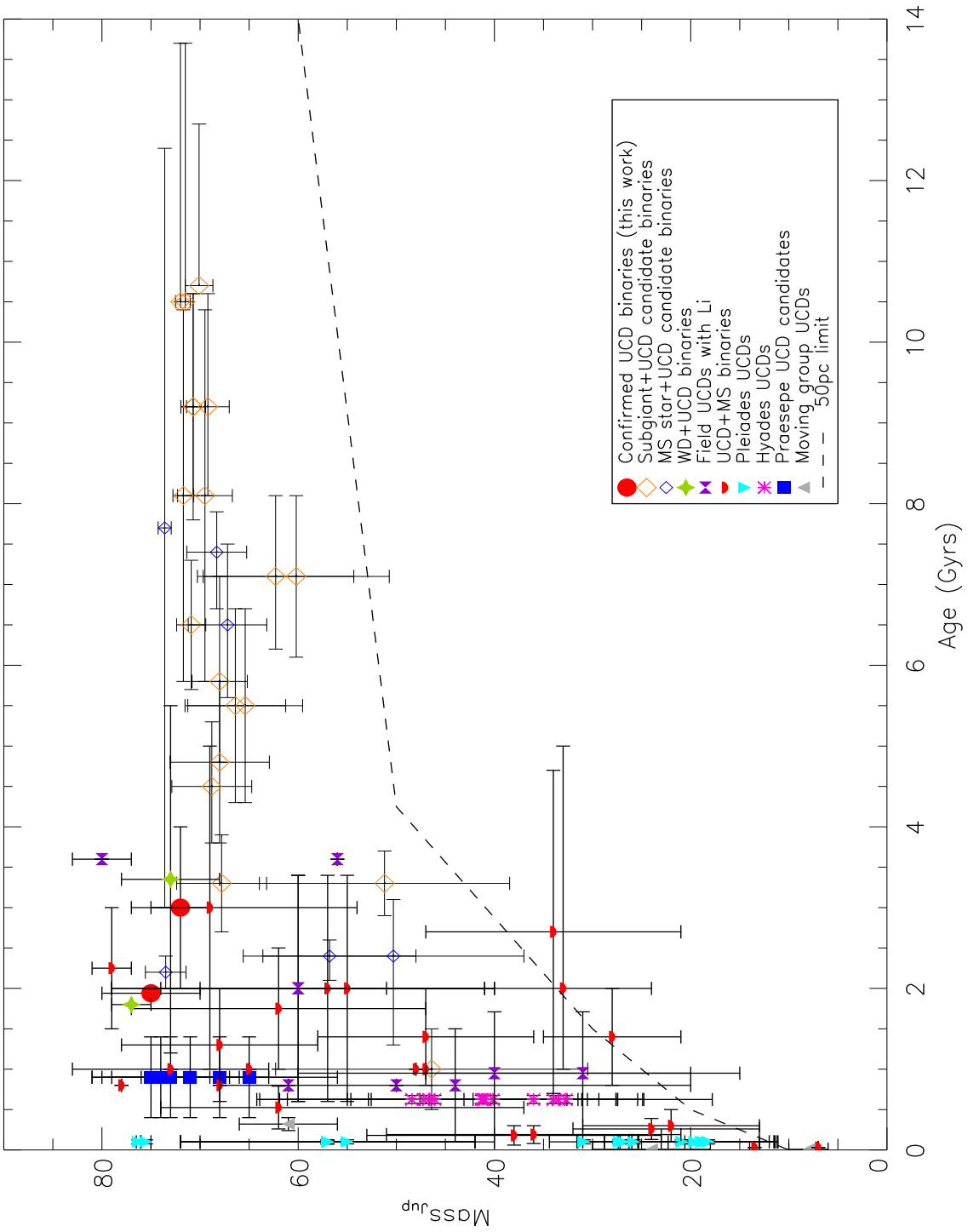

Figure 6.3: The distribution in mass-age space for benchmark UCDs taken from the literature and both confirmed and candidate objects (see text) presented in this work.

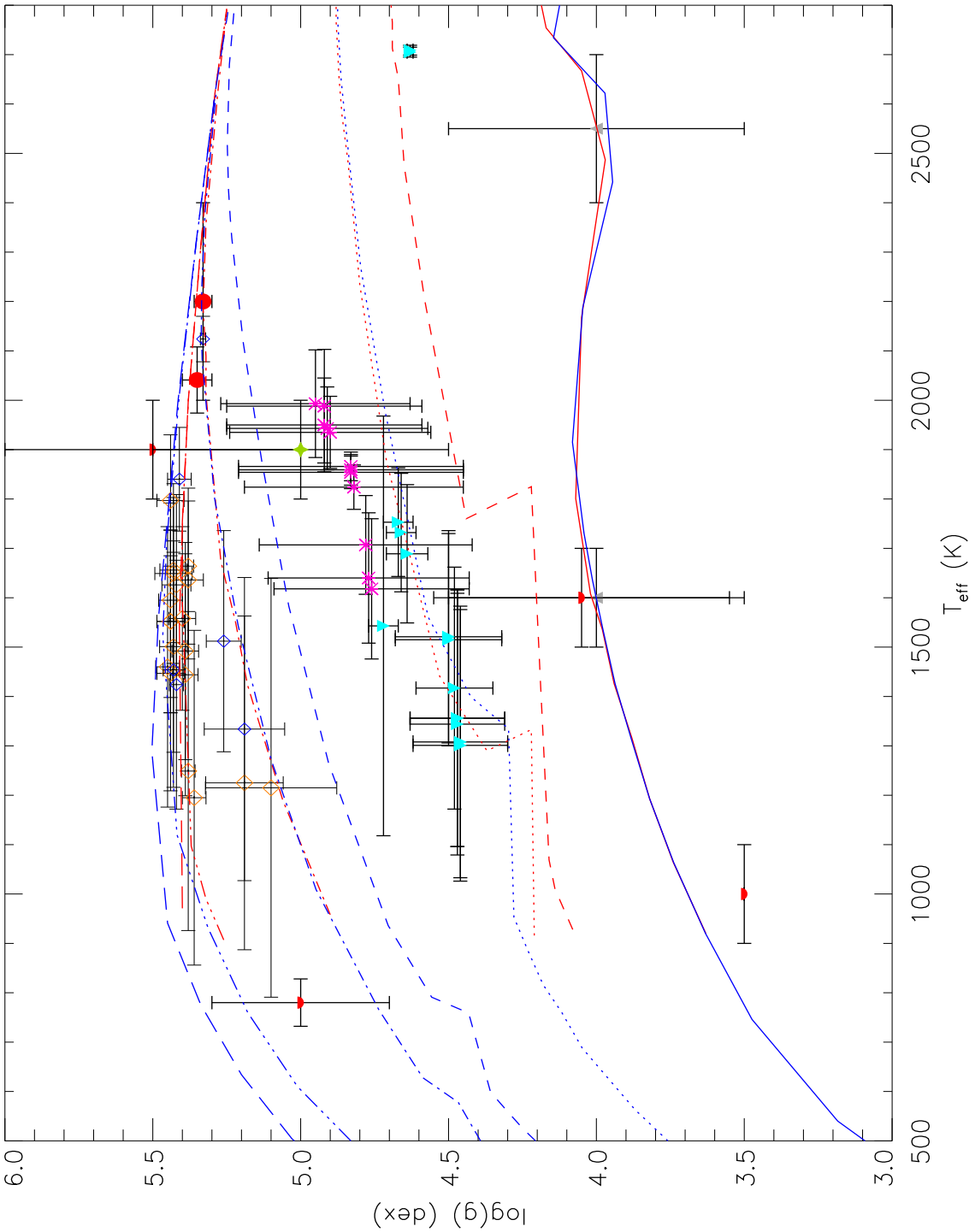

Figure 6.4: $T_{\rm eff}$ against log g for benchmark UCDs taken from the literature and both confirmed and candidate objects (see text) presented in this work. Symbols are the same as in Fig. 6.3. Overplotted with isochrones from the Lyon group DUSTY (red) and COND (blue) models. Solid lines are for models at 10Myr, dashed lines are for models at 100Myr, dotted lines are 500Myr, dot-dashed lines are for 1Gyr and dot-dot-dot-dashed lines are for 5Gyr and the long dashed lines are for 10Gyr models.

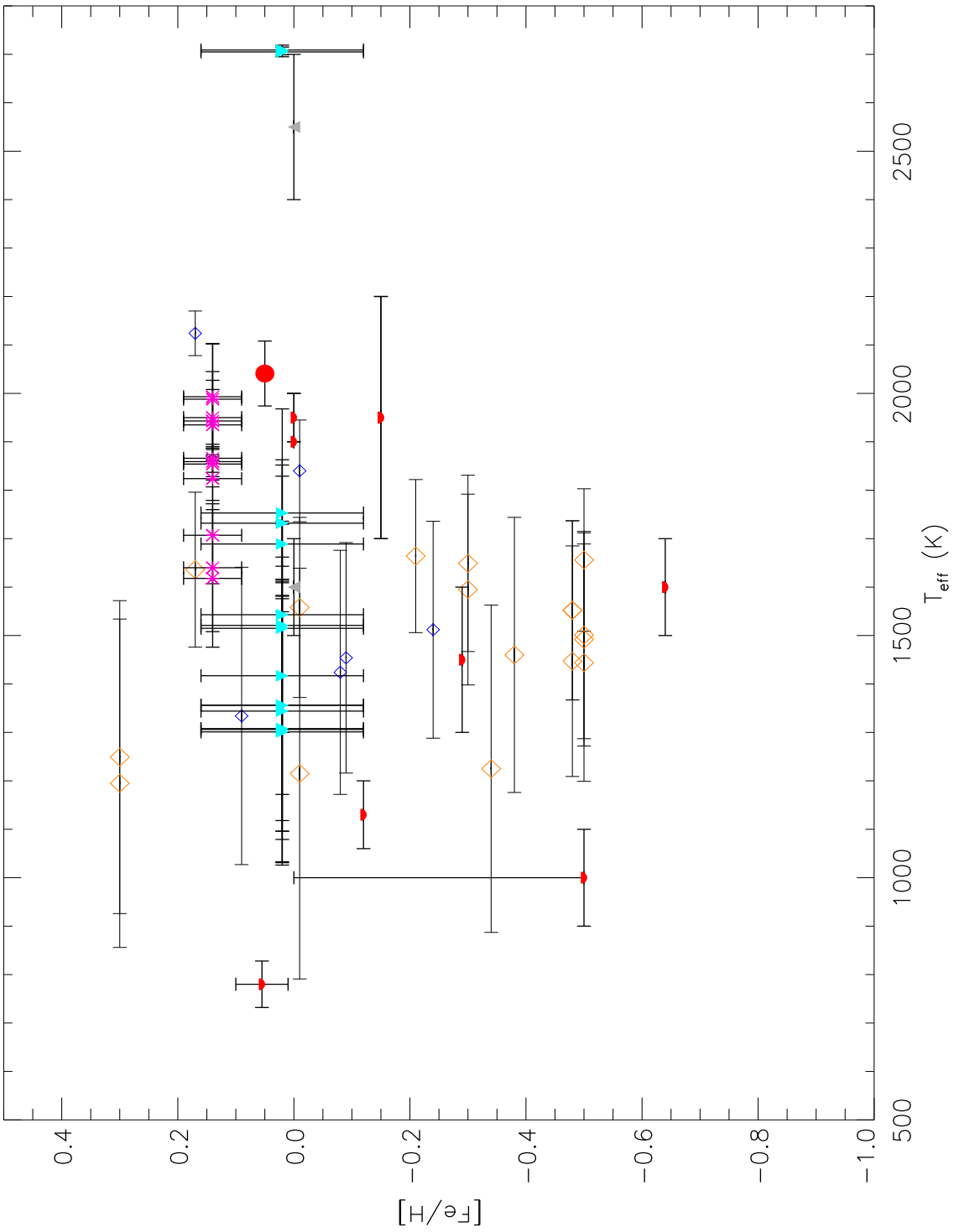

Figure 6.5: $T_{\rm eff}$ against [Fe/H] for benchmark UCDs taken from the literature and both confirmed and candidate objects (see text) presented in this work. Symbols are the same as in Fig. 6.3.

6.3.1 The effects of gravity and metallicity on observed UCD properties

The effects of $T_{\rm eff}$, log g and [Fe/H] on UCDs are important elements of UCD model atmospheres and how they affect the colours of UCDs is still not well understood. Benchmark objects will allow the predictions of current models to be tested and appropriately refined. These benchmarks can be used in two ways, firstly to compare the models with observation and thus facilitate model improvements. Secondly to look for links between observable properties and physical characteristics and potentially calibrate changes in spectroscopic criteria. Both are vitally important for the understanding of UCDs that may enable properties to be well constrained through observational studies (spectroscopy, photometry and parallax). This may ultimatly lead to accurate predictions of UCD properties from their observable (photomteric) properties alone.

In general the theory of UCD evolution is that they cool and fade over time, evolving from L dwarfs, that have dusty atmospheres through to T dwarfs, whose atmospheres are relatively dust-free. The two models most referenced throughout this work are from the Lyon group, the COND (dust-free) and DUSTY models (Chabrier et al. 2000a; Baraffe et al. 2002; Baraffe et al. 2003), which along with other models (Tucson group, Marley, Tsuji) are effective in reproducing the overall observed characteristics of the very red, dusty L dwarfs and those of very cool T dwarfs in the field, but struggle in particular to explain the intermediate L/T transition phase or how the physical properties (surface gravity or metallicity) change with age and what affect this has on their observational characteristics. Burrows, Sudarsky & Hubeny (2006) compared the predictions for colour from the DUSTY and COND model atmospheres. Fig. 6.6 show the predicted colours of L and T dwarfs for different metallicity, which shows a broad variation in predicted colours, especially across the L/T transition. Fig. 6.7 also shows a wide range in $T_{\rm eff}$-$J-K$ colour space, with respect to changes in gravity and metallicity predicted by models.

Knapp et al. (2004) measured accurate J-, H- and K- photometry, spectroscopy and parallaxes for a large selection of L and T dwarfs in order to try and address this question. They show that a large range in NIR colours and a turn over, or brightening effect at the L/T transition, as can be seen in Fig. 6.8. The scatter in the colour sequence is presumably caused by a range of log g and metallicity.

The cool temperatures of UCDs cause their atmospheres to be clouded by dust of iron and silicates, which causes opacity and reddens NIR colours in L dwarfs. The

amount of reddening may vary with the size of the dust grains, how many there are and their distribution in the atmosphere (Ackerman & Marley 2001; Allard et al. 2001; Marley et al. 2002; Tsuji & Nakajima 2003). For T dwarfs dust is thought to form lower in the atmosphere, below the photosphere, such that there is no dust opacities to affect the emergent spectra and results in bluer NIR colours. The mechanism of this sinking or ′raining-out′ of dust clouds that occurs at the L/T transition is as yet not fully understood, as is clearly indicated by the variations in properties predicted by the models. Several cloud models where the composition, size and rate at which condensation occurs have been looked at to try and explain this. A scenario where dust clouds thin as $T_{\rm eff}$ decreases was proposed by Tsuji & Nakajima (2003) suggesting that the reversal in $J-K$ colour (as seen in Fig. 6.8) may be a function of gravity. They suggest that low gravity objects would turn to bluer colours at brighter magnitudes compared to higher gravity objects, indicating there could be different evolutionary tracks for varying gravities. This means that lower mass objects would be brighter at the transition, which would occur earlier at higher $T_{\rm eff}$ and brighter M_J, whereas higher or intermediate mass objects would hit the transition later. This would account for the observed spread in $J-K$ colours observed at the L/T transition.

Another theory is that of ′patchy cloud′ (Ackerman & Marley 2001; Marley et al. 2002; Burgasser et al. 2002; Folkes et al. 2007; Burgasser et al. 2008), where it is suggested that the clouds start to break up, causing holes in the cloud deck due to enhanced collision induced H_2 absorption (CIA). Higher metallicity may also imply a greater production of dust, as more metals are available to condense onto grains, causing an increased opacity and reddening colours in the NIR. In general a trend in metallicity (albeit with a large scatter) would be expected, such that older dwarfs would be expected to have lower metallicity. This would cause a blue-ward turn in colour, suppressing the H- and K- band flux. Indeed this may explain some of the blue L dwarfs seen, such as 2MASSJ0532+8246, identified by Burgasser et al. (2003b) who found it to be a high velocity, metal-poor halo object. This object has been suggested as the first substellar sub-dwarf.

A third suggestion (see Knapp et al. 2004) is a ′sudden downpour′ model. They suggest that at $T_{\rm eff}\sim$1300K the rate of sedimentation becomes more efficient at removing iron and silicate grains from the atmosphere, predicting that lower masses should turn blue-ward earlier than higher masses at around T1-T4. For a T3 type they suggest a log $g\sim$5.4. Comparatively for the patchy cloud theory of the same spectral type, this

should is occur at log g≈5.0, and for the thinning cloud model log g≈4.0. Models in general predict higher surface gravity for older UCDs, which could be tested using these benchmarks by measuring features in their spectrum that appear to be sensitive to changes in gravity, such as the FeH(0.869, 0.989, 1.200 & 1.600 μm), KI(1.169, 1.178, 1.243 & 1.253 μm), NaI(0.818 & 1.268) and TiO(0.705, 0.820 & 0.843 μm) features (McGovern et al. 2004; Allers et al. 2007).

The benchmark UCDs that will be identified through the kinds of studies presented in this work can be used to directly test these assumptions. Measuring accurate colours and flux in the same fashion as Knapp et al. (2004) will make it possible to directly measure, for example if the H- and K- band flux peaks in T dwarfs are really affected by changes in gravity and metallicity, as the observations of halo UCDs (Burgasser et al. 2003b) would suggest. If gravity or metallicity are really to blame for the changes in the strength of atomic absorption lines as suggested by the observations of McGovern et al. (2004). Understanding the true effects of gravity and metallicity would then reveal the mechanisms at play in the L/T transition and if/or how these factors play a part in UCD evolution. Ultimately this would give models real predictive qualities down into new regimes.

6.3.2 Correlations with colour and physical properties

The benchmark population that has been identified here are taken from the literature and confirmed UCDs presented in this work (see §6.2) were used to investigate possible correlations between colours and synthetic (or modelled) physical parameters ($T_{\rm eff}$, log g and [Fe/H]). For the majority of the benchmarks, where all these parameters are known, mainly broadband NIR colours are available and thus are chosen to search for correlations amongst these. However other colours, if available may prove useful in distinguishing useful trends. For example combining NIR with optical photometry, or narrow band colours, such as the CH_4 filters in the H- band. Spectral ratios and line strengths could also be used to investigate correlations between observable characteristics and $T_{\rm eff}$, log g or [Fe/H]. This would ideally be done for each spectral subclass (i.e. L0, L1...T8, T9), however for the limited number of suitable benchmarks currently available this was not possible and for practical reasons these were simply split into L and T. It may be expected that this approach would be optimal given the number of available benchmarks since dusty L dwarfs would be expected to show spectral sensitivities that will be different

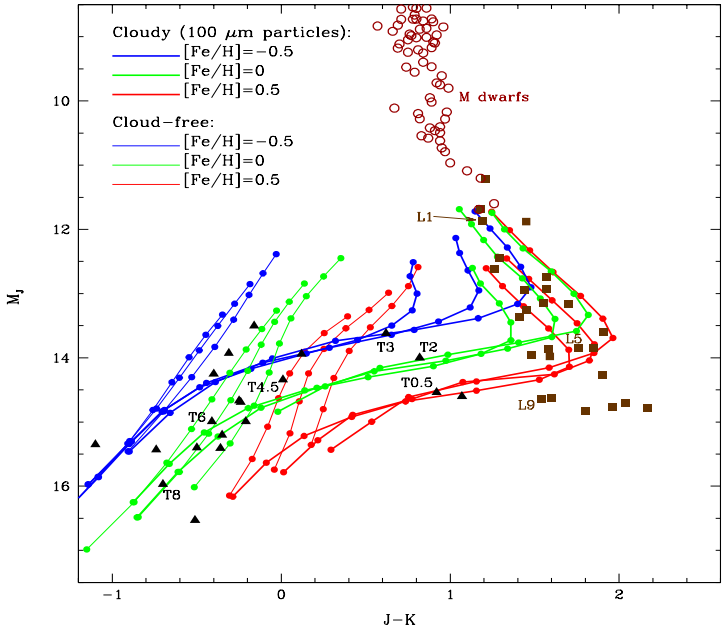

Figure 6.6: M_J-$J-K$ colour space showing the dependence of metallicity and gravity on BD models from Burrows et al. (2006) for their COND (thin lines) and DUSTY (thick lines) models. Overplotted are different metallicities for [Fe/H]=-0.5,0.0, 0.5 (blue, green and red, respectively) and surface gravities $10^{4.5}$, $10^{5.0}$ and $10^{5.5}$ cms^{-1} (the leftmost curve from each model/metallicity set of three id for the highest gravity, and the rightmost for the lowest) . L (filled squares) and T (filled triangles) dwarfs from Knapp et al. (2004) and M dwarfs (open circles) from Leggett et al. (1992) are also overplotted for comparison.

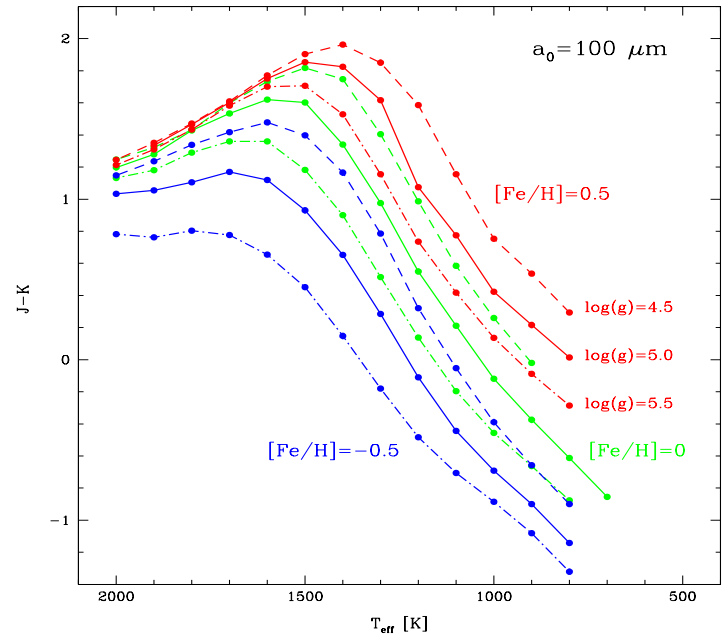

Figure 6.7: $T_{\rm eff}$-$J-K$ space predictions of the DUSTY and COND models from Burrows et al. (2006), for a grain size of 100μm. Shown are the effects of changes in [Fe/H] of 0.5 (red), 0.0 (green) and -0.5 (blue) and log g of 4.5 (dashed lines), 5.0 (solid lines) and 5.5 (dot-dashed lines).

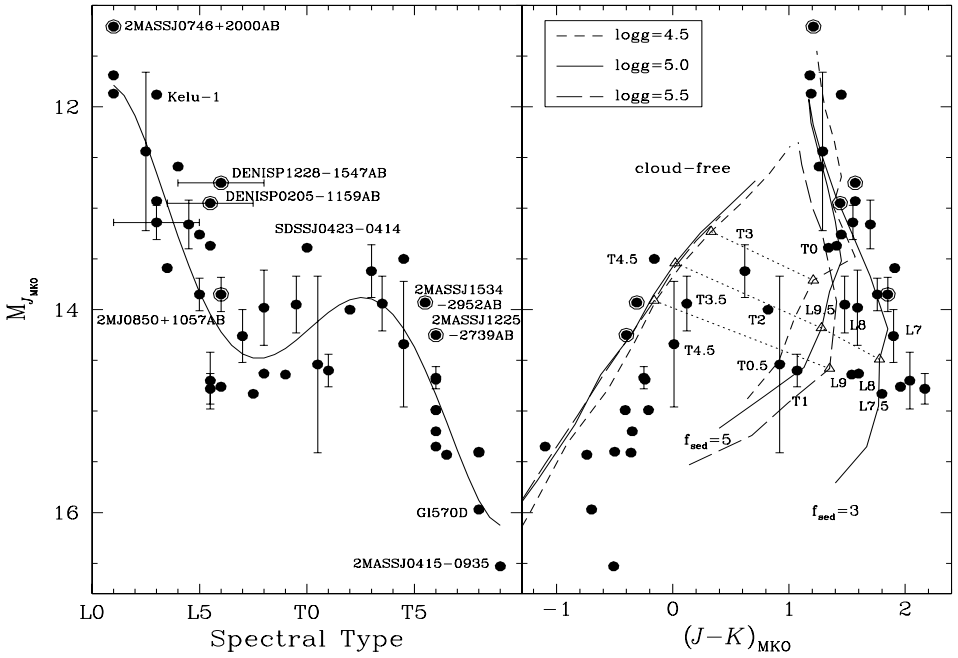

Figure 6.8: Left: M_J as a function of spectral type and Right: M_J as a function of $J-K$ colour for L and T dwarfs from Knapp et al. (2004). Objects circled are known binaries and error bars are shown where the type is uncertain by more than one subclass. Overplotted are the cloud-free models from Marley et al. (2002) for varying values of log g.

to those of the relatively dust-free atmospheres of T dwarfs. In the following sections the steps undertaken to search for property related correlations with broadband colour are explained.

Correlations with colour and $T_{\rm eff}$

The benchmark L's and T's were firstly plotted as a function of $T_{\rm eff}$ against $J-H$, $H-K$ and $J-K$ colour. A least squares fit was made to provide a first approximation fit. For this approximation the L dwarf benchmarks show a linear trend if 1207B is removed from the fit data. 1207B likely suffers from gray dust extinction in the NIR, which causes it to be under luminous (Mamajek 2005). This means that the constraints on log g for 1207B are poor, with an estimate from the available models giving log g over a large range of 4.5-5.5. On reflection this object does not make a good benchmark for assessing colour-property correlations, despite 1207B being a promising object, where an insight into the potential trends for planetary mass UCDs could have been indicated. This object is highlighted in Fig. 6.9 and the fit to the T dwarfs are shown in Fig. 6.10, where again a linear trend provides the best fit.

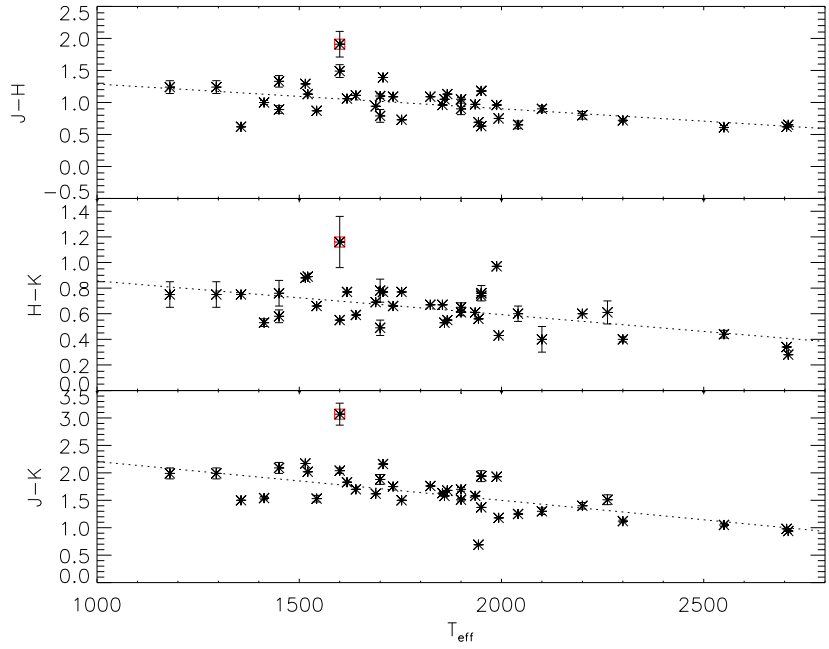

Figure 6.9: $T_{\rm eff}$-colour plot of benchmark L dwarfs with NIR $J-H$, $H-K$ and $J-K$ colours. Overplotted as a dotted line is a least squares fit to the data. Also overplotted is 1207B (as a square), see text.

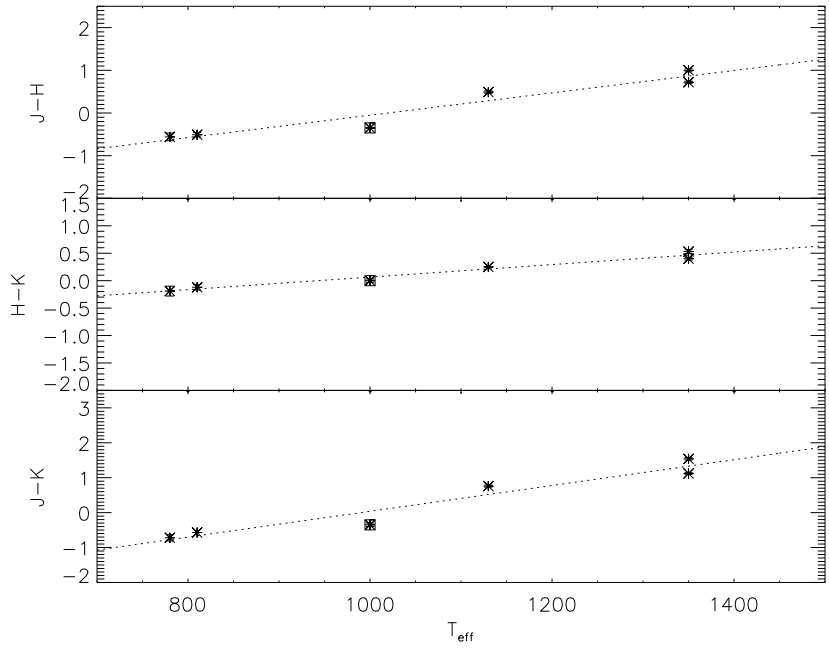

Figure 6.10: $T_{\rm eff}$-colour plot of benchmark T dwarfs from the literature search with NIR $J-H$, $H-K$ and $J-K$ colours. Overplotted as a dotted line is a least squares fit to the data. Also highlighted is Gl 229B as a square as a potential log g and [Fe/H] outlier, with normal T dwarf colours (see text).

Correlations with colour and log g and [Fe/H]

The first approximation fits were used to create a $T_{\rm eff}$ corrected colour, and any trends with log g or [Fe/H] were looked for. For the T dwarfs only four benchmarks had known $T_{\rm eff}$, log g and [Fe/H], one of which is Gl 229B, an unusually low-gravity, metal poor T dwarf (based on the observations and analysis of Leggett et al. 2002a). Models predict that log g should increase as an object cools and contracts, with which metallicity should decrease as more heavier elements are created over time. If colours are dependent on these properties then it may be possible that these contrasting effects could cancel out any correlation with colour. This may be the underlying reason for the apparent normal T dwarf colours that Gl 229B exhibits (highlighted as a square symbol in Fig. 6.10).

There are several more L dwarf benchmarks than T's, however the scatter in colours implies no obvious trend. Most of the objects lie between log $g = 4.5$ and 5.0, with two objects at log $g = 5.5$, GD 165B, a companion to a WD and HD12005C, a companion to a main-sequence star (confirmed in this work). The low gravity end is occupied by ABpicB, a similarly low-gravity metal poor UCD as Gl 229B and the binary 1207AB, where 1207B has large uncertainties (indicated by error bars in Fig. 6.11). There is no obvious trend here, but if the uncertainties on 1207B were smaller then it may indicate a red-ward trend in NIR colour at low log g.

For metallicity the limited number of objects, including Gl 229B, means that a trend could not be fully analysed for the T dwarfs. For the L dwarfs, although the sample numbers with [Fe/H] are larger, the spread in colour is quite large with the majority of objects occupying mainly two metallicity bins; the Hyades L dwarf objects at [Fe/H]$\sim$0.14 and main-sequence companions and Pleiades UCDs with solar metallicity. The spread in colours is also quite sizable here. Therefore, although there may be some relation between broadband colour and metallicity, it would not be possible to see it because neither the sample size nor the range of properties within the population of benchmark L and T dwarfs are available.

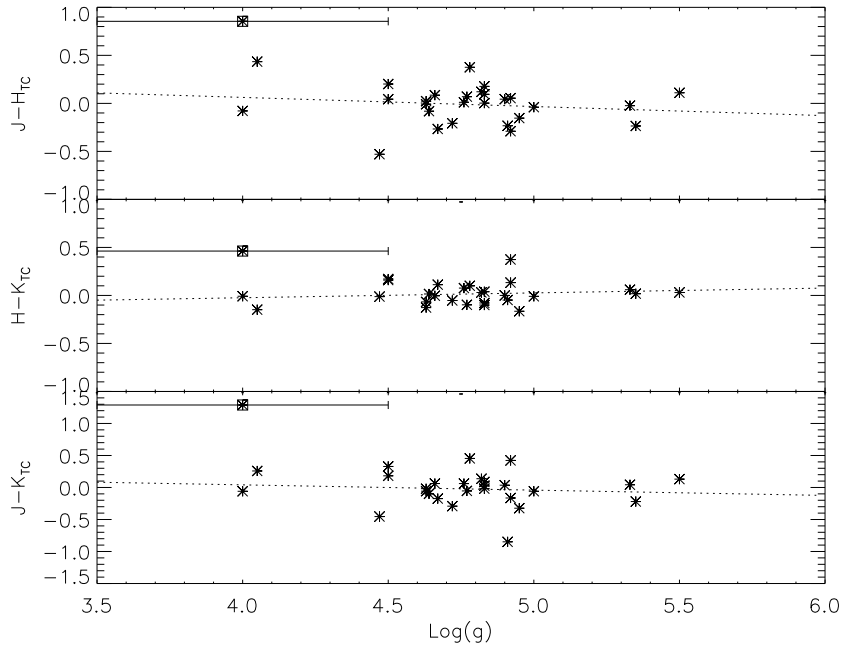

Figure 6.11: Colour against log g, where the colour-$T_{\rm eff}$ trend (see Fig. 6.9) has been subtracted from the colour, for benchmark L dwarfs with NIR $J-H$, $H-K$ and $J-K$ colours. Overplotted as a dotted line is a least squares fit to the data. Also overplotted is the outlier 1207B (as a square) with its error bars (see text).

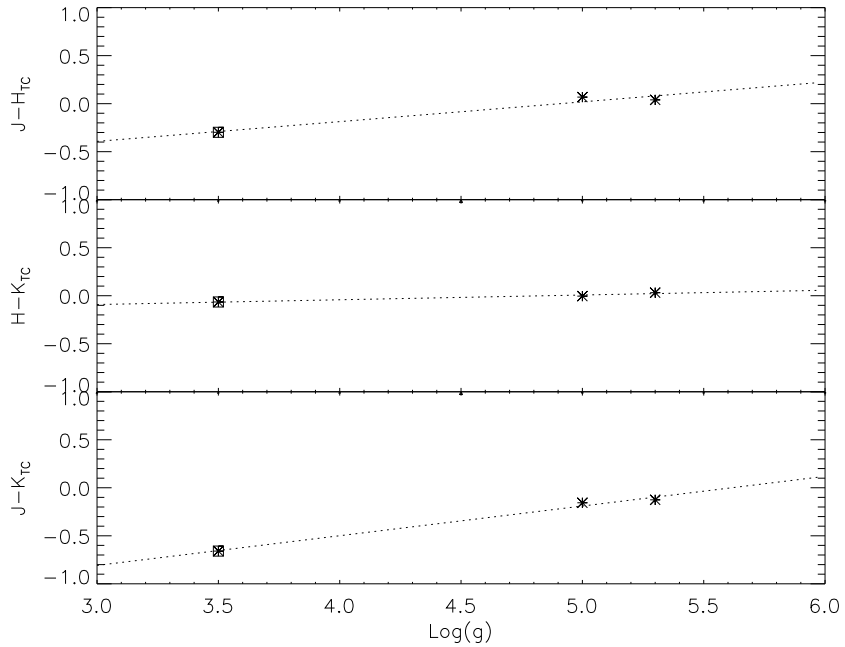

Figure 6.12: Colour against log g, where the colour-$T_{\rm eff}$ trend (see Fig. 6.10) has been subtracted from the colour, for benchmark T dwarfs with NIR $J-H$, $H-K$ and $J-K$ colours. Overplotted as a dotted line is a least squares fit to the data. Also highlighted is Gl 229B as a square, as a potential log g and [Fe/H] outlier (see text).

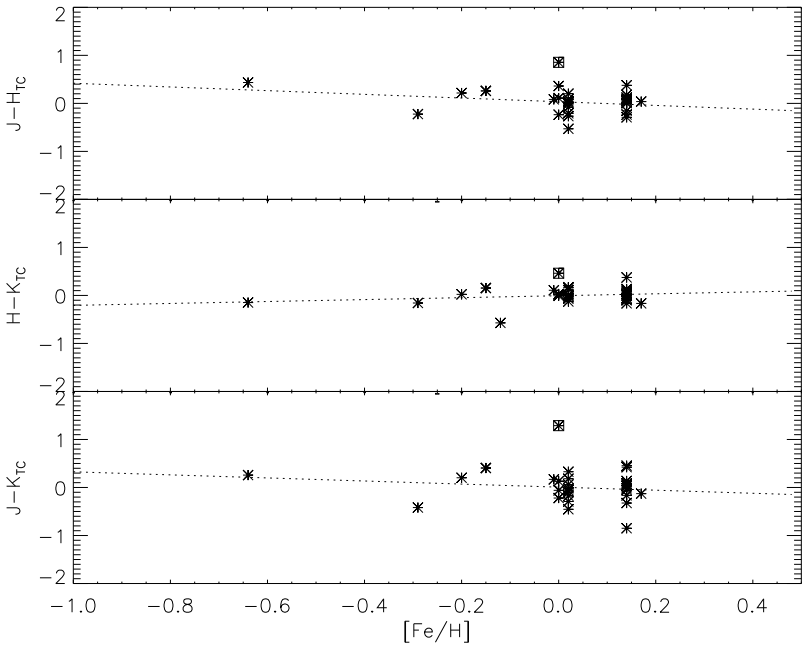

Figure 6.13: Colour against [Fe/H], where the colour-$T_{\rm eff}$ trend (see Fig. 6.9) has been subtracted from the colour, for benchmark L dwarfs with NIR $J-H$, $H-K$ and $J-K$ colours. Overplotted as a dotted line is a least squares fit to the data. Also overplotted are the outliers 1207B (as a square), see text.

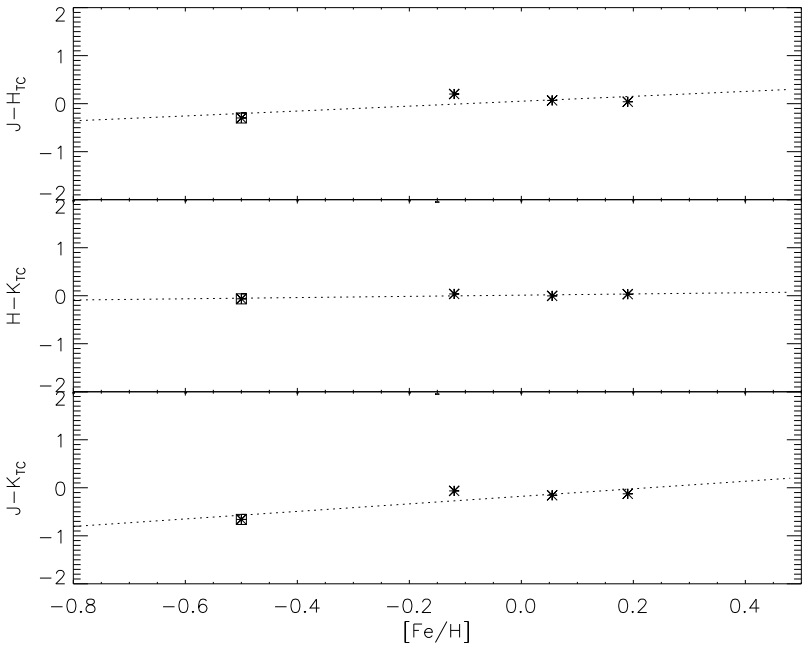

Figure 6.14: Colour against [Fe/H], where the colour-$T_{\rm eff}$ trend (see Fig. 6.10) has been subtracted from the colour, for benchmark T dwarfs with NIR $J-H$, $H-K$ and $J-K$ colours. Overplotted as a dotted line is a least squares fit to the data. Also highlighted is Gl 229B as a square, as a potential log g and [Fe/H] outlier (see text).

Sensitivity of colours to $T_{\rm eff}$

If there had been obvious trends to colour and log g or [Fe/H] then it would be possible to produce improved colour-$T_{\rm eff}$ fits by removing the trends in colour derived for the log g and [Fe/H]. This would be expected to reduce the scatter in the colour-$T_{\rm eff}$ plot. This method is illustrated here, using the essentially zero trend findings for log g and [Fe/H], even though the scatter has not changed. The $'$improved$'$ colour-$T_{\rm eff}$ fit is shown in Fig. 6.15 for the L dwarfs. There appears a fairly linear trend with $T_{\rm eff}$ and colours (overplotted as a dotted line on Fig. 6.15) and in general the scatter is smallest in $H-K$ for both the L and T dwarfs. The range over which the properties are best fit was determined from the level of scatter and the distribution of data points along the fit. For the T dwarfs, objects are fairly evenly distributed in $T_{\rm eff}$ space. However for L dwarfs there are no objects between 2100-2500K and it is possible the trend in that region may not be linear.

A more comprehensive investigation of benchmark sensitivity to physical properties would investigate a much greater range of observable criteria (other than broadband photometry). However, this is limited by the available benchmarks and measurements, and thus it has only been possible to identify trends between $T_{\rm eff}$ and the three NIR colours considered.

These trends were used to calculate a sensitivity index in the applicable $T_{\rm eff}$ ranges, as the rate of change of colour with $T_{\rm eff}$. The equation of the fit is a first order, least squares fit of the form $Colour = a + b(T_{eff})$, where a and b are the coefficients of the fit and the corresponding sensitivity is shown in Table. 6.8 and 6.9. The larger the sensitivity index, the more sensitive the colour is to changes in $T_{\rm eff}$. On inspection of the sensitivity of NIR broadband colours with $T_{\rm eff}$, the benchmarks would indicate that the colours are, in general not strongly sensitive to changes in $T_{\rm eff}$, but that of all the colours $J-K$ might be slightly more sensitive than $J-H$ and $H-K$ colours. From these correlations the $T_{\rm eff}$ of a UCD can also be calculated, such that for a UCD with solar metallicity, log $g\sim$5.0, over the range 750$\leq T_{\rm eff}\leq$1400 (for T dwarfs) and 1600$\leq T_{\rm eff}\leq$2100 (L dwarfs), $T_{\rm eff}$ can be approximated via the following relations.

L dwarf colour-$T_{\rm eff}$ relations:

$T_{\rm eff}$=2830.74-983.95$(J-H)$

$T_{\rm eff}$=2790.22-1438.28$(H-K)$

$T_{\rm eff}$=2907.41-630.03$(J-K)$

Table 6.8: Parameters of fitting equations for colours of T dwarfs.

Colour	Property	a	b	Range	Sensitivity[a]
$J-H$	$T_{\rm eff}$	-2.671	0.0026	750-1400K	0.0026
$H-K$	$T_{\rm eff}$	-1.075	0.0011	750-1400K	0.0112
$J-K$	$T_{\rm eff}$	-3.658	0.0039	750-1400K	0.0375

Notes: The relation equation is: colour=a+b*$T_{\rm eff}$.

[a] Sensitivity is the rate of change of colour with $T_{\rm eff}$.

Table 6.9: Parameters of fitting equations for colours of L dwarfs.

Colour	Property	a	b	Range	Sensitivity[a]
$J-H$	$T_{\rm eff}$	1.879	-0.00049	1600-2100K	0.00050
$H-K$	$T_{\rm eff}$	1.303	-0.00036	1600-2100K	0.00035
$J-K$	$T_{\rm eff}$	3.233	-0.00086	1600-2100K	0.00085

Notes: The relation equation is: colour=a+b*$T_{\rm eff}$.

[a] Sensitivity is the rate of change of colour with $T_{\rm eff}$.

T dwarf colour-$T_{\rm eff}$ relations:

$$T_{\rm eff}=1023.48+353.30(J-H)$$

$$T_{\rm eff}=947.38+845.58(H-K)$$

$$T_{\rm eff}=995.09+252.49(J-K)$$

Although no strong correlation between broadband colour and log g or [Fe/H] are seen, and only a weak relation to $T_{\rm eff}$ has been found in this study, there are indications (i.e. from the remaining scatter in colours and the properties of some outlying objects), these analytical techniques hold promise for the future. With more benchmark UCDs and a greater spread in properties over a range of spectral types it may be possible to provide a way of robustly measuring UCD properties from their observable characteristics. Good relations with colour may also allow reliable mass functions to be calculated with a only a limited amount of spectroscopic follow-up.

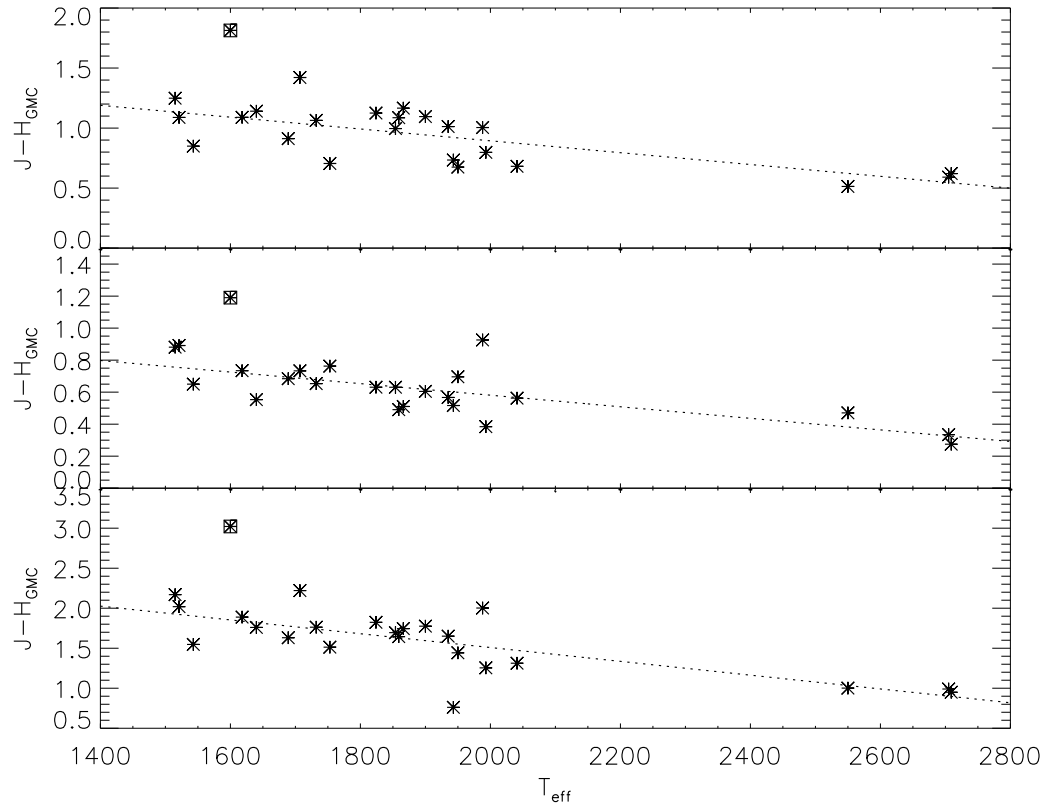

Figure 6.15: Improved $T_{\rm eff}$ against colour plot, where the effects of log g and [Fe/H] (from Fig. 6.11 and 6.13) have been removed for the benchmark L dwarfs with NIR $J-H$, $H-K$ and $J-K$ colours. Overplotted as a dotted line is a least squares fit to the data.

6.4 Future Work

The work in this thesis has presented the discovery of three UCD companions to main-sequence and WD stars, two of which are benchmark systems with constrained ages, along with a large number of candidate UCD + WD, UCD + main-sequence and UCD + subgiant binary systems. The next logical progression would be to follow-up these candidates with a combination of proper motion, parallax and spectral observations. Once confirmed, high S/N or high resolution spectroscopy could be employed to accurately measure such gravity sensitive features as previously mentioned. They could then be used to calibrate properties observationally and place constraints on evolutionary models. Correlations with colour and properties could also be explored, enabling a way to infer the properties of a UCD based on its observable colours.

The large number of benchmarks needed for this task could be found by expanding this work. In the immediate/near future this includes future data releases of large NIR surveys such as UKIDSS and the VISTA hemisphere survey, which is planned to reach a further $\sim$2 magnitudes fainter than UKIDSS (K $\sim$20), over a large portion of the southern hemisphere and will be able to probe deeper and fainter than previously capable and should reveal hundreds of new UCDs and many in new lower temperature regimes, where the question of a BD minimum mass can also start to be addressed.

In addition WISE will be able to follow-up benchmark UCDs by measuring their mid IR flux. This coupled with a parallax distance will enable a direct measurement of luminosity, where combined with age information can give a radius estimate from structure models and will allow $T_{\rm eff}$, mass and log g to be calculated. Another natural expansion of this work would be to extend the subgiant pilot survey, where an accurate measurement of metallicity (if not known) could be calculated from follow-up echelle spectra. The WDs however will not yield this information, but obtaining high resolution spectra will allow accurate determinations of the cooling age to be calculated, placing very accurate constraints on the age of WD + UCD systems. The UCDs discovered through these methods will also allow constraints to be placed on the binary fraction, birth rate and the mass function for ultracool objects. These factors are vitally important for the understanding of the substellar population in the galaxy.

References

Ackerman A. S., Marley M. S., 2001, ApJ, 556, 872

Allard F., Hauschildt P. H., Alexander D. R., Tamanai A., Schweitzer A., 2001, ApJ, 556, 357

Allen P. R., Koerner D. W., Reid I. N., Trilling D. E., 2005, ApJ, 625, 385

Allers K. N. et al., 2007, ApJ, 657, 511

Althaus L. G., García-Berro E., Córsico A. H., Miller Bertolami M. M., Romero A. D., 2009, ApJL, 693, L23

Andersen M., Meyer M. R., Greissl J., Aversa A., 2008, ApJL, 683, L183

Balega I., Balega Y. Y., Maksimov A. F., Pluzhnik E. A., Schertl D., Shkhagosheva Z. U., Weigelt G., 2004, A&A, 422, 627

Baraffe I., Chabrier G., Allard F., Hauschildt P. H., 1998, A&A, 337, 403

Baraffe I., Chabrier G., Allard F., Hauschildt P. H., 2002, A&A, 382, 563

Baraffe I., Chabrier G., Barman T. S., Allard F., Hauschildt P. H., 2003, A&A, 402, 701

Barry D. C., 1988, ApJ, 334, 436

Basri G., 1998, in Rebolo R., Martin E. L., Zapatero Osorio M. R., eds, Brown Dwarfs and Extrasolar Planets. p. 394

Bate M. R., Bonnell I. A., Bromm V., 2003, MNRAS, 339, 577

Bate M. R., 1998, ApJL, 508, L95

Bate M. R., 2005, MNRAS, 363, 363

Becklin E. E., Zuckerman B., 1988, Nature, 336, 656

Benvenuto O. G., Althaus L. G., 1999, MNRAS, 303, 30

Bergeron P., Gianninas A., Boudreault S., 2007, in Napiwotzki R., Burleigh M. R., eds, 15th European Workshop on White Dwarfs. p. 29

Bessell M. S., 1986, PASP, 98, 1303

Bihain G., Rebolo R., Béjar V. J. S., Caballero J. A., Bailer-Jones C. A. L., Mundt R., Acosta-Pulido J. A., Manchado Torres A., 2006, A&A, 458, 805

Blake C. H., Charbonneau D., White R. J., Torres G., Marley M. S., Saumon D., 2008, ApJL, 678, L125

Bochanski J. J., West A. A., Hawley S. L., Covey K. R., 2007, AJ, 133, 531

Boehm-Vitense E., 1992, Introduction to stellar astrophysics. Vol. 3 - Stellar structure and evolution. Cambridge, England and New York, Cambridge University Press, 1992, 300 p.

Bonfils X., Delfosse X., Udry S., Santos N. C., Forveille T., Ségransan D., 2005, A&A, 442, 635

Bouvier J., Stauffer J. R., Martin E. L., Barrado y Navascues D., Wallace B., Bejar V. J. S., 1998, A&A, 336, 490

Bouvier J. et al., 2008, A&A, 481, 661

Briceño C., Luhman K. L., Hartmann L., Stauffer J. R., Kirkpatrick J. D., 2002, ApJ, 580, 317

Burgasser A. J., Burrows A., Kirkpatrick J. D., 2006, ApJ, 639, 1095

Burgasser A. J. et al., 2000, ApJL, 531, L57

Burgasser A. J. et al., 2002, ApJ, 564, 421

Burgasser A. J., Geballe T. R., Golimowski D. A., Leggett S. K., Kirkpatrick J. D.,

Knapp G. R., Fan X., 2003, in Martín E., ed, Brown Dwarfs. p. 377
Burgasser A. J. et al., 2003, ApJ, 592, 1186
Burgasser A. J., McElwain M. W., Kirkpatrick J. D., Cruz K. L., Tinney C. G., Reid I. N., 2004, AJ, 127, 2856
Burgasser A. J., Reid I. N., Leggett S. K., Kirkpatrick J. D., Liebert J., Burrows A., 2005, ApJL, 634, L177
Burgasser A. J., Geballe T. R., Leggett S. K., Kirkpatrick J. D., Golimowski D. A., 2006, ApJ, 637, 1067
Burgasser A. J., Looper D. L., Kirkpatrick J. D., Cruz K. L., Swift B. J., 2008, ApJ, 674, 451
Burgasser A. J., Kirkpatrick J. D., Lowrance P. J., 2005, AJ, 129, 2849
Burgasser A. J., 2004, ApJS, 155, 191
Burgasser A. J., 2007, ApJ, 658, 617
Burleigh M. R., Clarke F. J., Hodgkin S. T., 2002, MNRAS, 331, L41
Burleigh M. R., Hogan E., Dobbie P. D., Napiwotzki R., Maxted P. F. L., 2006, MNRAS, 373, L55
Burleigh M. R. et al., 2006, MNRAS, 373, 1416
Burningham B. et al., 2008, MNRAS, 391, 320
Burrows A., Hubbard W. B., Lunine J. I., Marley M., Guillot T., Saumon D., Freedman R. S., 1997a, in Soderblom D., ed, Planets Beyond the Solar System and the Next Generation of Space Missions. p. 9
Burrows A. et al., 1997, ApJ, 491, 856
Burrows A., Hubbard W. B., Lunine J. I., Liebert J., 2001, Reviews of Modern Physics, 73, 719
Burrows A., Sudarsky D., Hubeny I., 2006, ApJ, 640, 1063
Burrows A., Sudarsky D., Lunine J. I., 2003, ApJ, 596, 587
Burstein D., Heiles C., 1982, AJ, 87, 1165
Carpenter J. M., 2001, AJ, 121, 2851
Casali M. et al., 2007, A&A, 467, 777
Casewell S. L., Dobbie P. D., Hodgkin S. T., Moraux E., Jameson R. F., Hambly N. C., Irwin J., Lodieu N., 2007, MNRAS, 378, 1131
Catalán S., Isern J., García-Berro E., Ribas I., Allende Prieto C., Bonanos A. Z., 2008, A&A, 477, 213
Cayrel de Strobel G., Soubiran C., Friel E. D., Ralite N., Francois P., 1997, A&AS, 124, 299
Chabrier G., Baraffe I., Plez B., 1996, ApJL, 459, L91+
Chabrier G., Baraffe I., Allard F., Hauschildt P., 2000, ApJ, 542, 464
Chabrier G., Brassard P., Fontaine G., Saumon D., 2000, ApJ, 543, 216
Chabrier G., Brassard P., Fontaine G., Saumon D., 2000, ApJ, 543, 216
Chabrier G., 2003, PASP, 115, 763
Chandrasekhar S., 1931, ApJ, 74, 81
Chappelle R. J., Pinfield D. J., Steele I. A., Dobbie P. D., Magazzù A., 2005, MNRAS, 361, 1323
Chauvin G. et al., 2005, A&A, 438, L29
Chiu K., Fan X., Leggett S. K., Golimowski D. A., Zheng W., Geballe T. R., Schnei-

der D. P., Brinkmann J., 2006, AJ, 131, 2722
Claver C. F., Liebert J., Bergeron P., Koester D., 2001, ApJ, 563, 987
Comerón F., Reipurth B., Henry A., Fernández M., 2004, A&A, 417, 583
Cossburn M. R., Hodgkin S. T., Jameson R. F., Pinfield D. J., 1997, MNRAS, 288, L23
Cruz K. L., Reid I. N., Liebert J., Kirkpatrick J. D., Lowrance P. J., 2003, AJ, 126, 2421
Cruz K. L. et al., 2007, AJ, 133, 439
Cushing M. C., Rayner J. T., Vacca W. D., 2005, ApJ, 623, 1115
Dahn C. C. et al., 2002, AJ, 124, 1170
Day-Jones A. C. et al., 2008, MNRAS, 388, 838
De Simone R., Wu X., Tremaine S., 2004, MNRAS, 350, 627
Deacon N. R., Hambl N. C., 2004, A&A, 416, 125
Delfosse X. et al., 1997, A&A, 327, L25
Delorme P. et al., 2008, A&A, 482, 961
Dobbie P. D., Pinfield D. J., Napiwotzki R., Hambly N. C., Burleigh M. R., Barstow Jameson R. F., Hubeny I., 2004, MNRAS, 355, L39
Dobbie P. D., Burleigh M. R., Levan A. J., Barstow M. A., Napiwotzki R., Holberg J. B., Hubeny I., Howell S. B., 2005, MNRAS, 357, 1049
Dobbie P. D. et al., 2006, MNRAS, 369, 383
Dufour P., Fontaine G., Liebert J., Schmidt G. D., Behara N., 2008, ApJ, 683, 978
Dye S. et al., 2006, MNRAS, 372, 1227
Edvardsson B., Andersen J., Gustafsson B., Lambert D. L., Nissen P. E., Tomkin J., 1993, A&A, 275, 101
Eisenstein D. J. et al., 2006, ApJS, 167, 40
Engelbrecht A., Koester D., 2007, in Napiwotzki R., Burleigh M. R., eds, 15th European Workshop on White Dwarfs. p. 289
EROS Collaboration et al., 1999, A&A, 351, L5
Fan X. et al., 2001, AJ, 121, 54
Farihi J., Christopher M., 2004, AJ, 128, 1868
Farihi J., Becklin E. E., Zuckerman B., 2005, ApJS, 161, 394
Farihi J., Becklin E. E., Zuckerman B., 2008, ApJ, 681, 1470
Farihi J., Burleigh M. R., Hoard D. W., 2008, ApJ, 674, 421
Farihi J., Hoard D. W., Wachter S., 2006, ApJ, 646, 480
Farihi J., Zuckerman B., Becklin E. E., 2008, ApJ, 674, 431
Feltzing S., Gustafsson B., 1998, A&AS, 129, 237
Feltzing S., Holmberg J., Hurley J. R., 2001, VizieR Online Data Catalog, 337, 70911
Ferrario L., Wickramasinghe D., Liebert J., Williams K. A., 2005, MNRAS, 361, 1131
Finley D. S., Koester D., Basri G., 1997, ApJ, 488, 375
Fleming T. A., Schmitt J. H. M. M., Giampapa M. S., 1995, ApJ, 450, 401
Folkes S. L., Pinfield D. J., Kendall T. R., Jones H. R. A., 2007, MNRAS, 378, 901
Funayama H., Itoh Y., Oasa Y., Toyota E., Mukai T., 2008, in Santos N. C., Pasquini L., Correia A. C. M., Romaniello M., eds, Precision Spectroscopy in Astrophysics. p. 285
Geballe T. R., Saumon D., Leggett S. K., Knapp G. R., Marley M. S., Lodders K., 2001, ApJ, 556, 373
Geballe T. R. et al., 2002, ApJ, 564, 466

Geballe T. R., Knapp G. R., Leggett S. K., Fan X., Golimowski D. A., 2003, in Brown A., Harper G. M., Ayres T. R., eds, The Future of Cool-Star Astrophysics: 12th Cambridge Workshop on Cool Stars, Stellar Systems, and the Sun (2001 July 30 - August 3), eds. A. Brown, G.M. Harper, and T.R. Ayres, (University of Colorado), 2003, p. 670-675. p. 670
Geißler K. et al., 2007, A&A, 461, 665
Girardi L., Bressan A., Bertelli G., Chiosi C., 2000, VizieR Online Data Catalog, 414, 10371
Gizis J. E., Bharat R., 2004, ApJL, 608, L113
Gizis J. E., Kirkpatrick J. D., Burgasser A., Reid I. N., Monet D. G., Liebert J., Wilson J. C., 2001, ApJL, 551, L163
Gizis J. E., Kirkpatrick J. D., Wilson J. C., 2001, AJ, 121, 2185
Gizis J. E., Reid I. N., Hawley S. L., 2002, AJ, 123, 3356
Golimowski D. A. et al., 2004, AJ, 127, 3516
Goodwin S. P., Whitworth A., 2007, A&A, 466, 943
Green E. M., Demarque P., King C. R., 1987, The revised Yale isochrones and luminosity functions. The revised Yale isochrones and luminosity functions, New Haven: Yale Observatory, 1987
Grether D., Lineweaver C. H., 2006, ApJ, 640, 1051
Guieu S., Dougados C., Monin J.-L., Magnier E., Martín E. L., 2006, A&A, 446, 485
Hambly N. C., Digby A. P., Oppenheimer B. R., 2005, in Koester D., Moehler S., eds, 14th European Workshop on White Dwarfs. p. 113
Hambly N. C., Hodgkin S. T., Cossburn M. R., Jameson R. F., 1999, MNRAS, 303, 835
Hambly N. C. et al., 2008, MNRAS, 384, 637
Hauck B., Mermilliod M., 1985, A&AS, 60, 61
Hauck B., Mermilliod M., 1998, A&AS, 129, 431
Hawley S. L. et al., 2002, AJ, 123, 3409
Hempelmann A., Schmitt J. H. M. M., Schultz M., Ruediger G., Stepien K., 1995, A&A, 294, 515
Hewett P. C., Warren S. J., Leggett S. K., Hodgkin S. T., 2006, MNRAS, 367, 454
Hillenbrand L. A., 1997, AJ, 113, 1733
Hogan E., Jameson R. F., Casewell S. L., Osbourne S. L., Hambly N. C., 2008, MNRAS, 388, 495
Howell S. B., Nelson L. A., Rappaport S., 2001, ApJ, 550, 897
Hubeny I., Lanz T., 1995, ApJ, 439, 875
Hurley J. R., Pols O. R., Tout C. A., 2000, MNRAS, 315, 543
Ibukiyama A., Arimoto N., 2002, A&A, 394, 927
Ireland M. J., Kraus A., Martinache F., Lloyd J. P., Tuthill P. G., 2008, ApJ, 678, 463
Jameson R. F., Casewell S. L., Bannister N. P., Lodieu N., Keresztes K., Dobbie P. D., Hodgkin S. T., 2008, MNRAS, 384, 1399
Jeans J. H., 1924, MNRAS, 85, 2
Jenkins J. S., Jones H. R. A., Pavlenko Y., Pinfield D. J., Barnes J. R., Lyubchik Y., 2008, A&A, 485, 571
Jones H. R. A., Pavlenko Y., Viti S., Barber R. J., Yakovina L. A., Pinfield D., Tennyson J., 2005, MNRAS, 358, 105

Just A., 2003, Ap&SS, 284, 727
Kalirai J. S., Hansen B. M. S., Kelson D. D., Reitzel D. B., Rich R. M., Richer H. B., 2008, ApJ, 676, 594
Kilic M. et al., 2006, AJ, 131, 582
Kilkenny D., Heber U., Drilling J. S., 1988, South African Astronomical Observatory Circular, 12, 1
Kirkpatrick J. D., Allard F., Bida T., Zuckerman B., Becklin E. E., Chabrier G., Baraffe I., 1999, ApJ, 519, 834
Kirkpatrick J. D. et al., 1999, ApJ, 519, 802
Kirkpatrick J. D. et al., 2000, AJ, 120, 447
Kirkpatrick J. D., Dahn C. C., Monet D. G., Reid I. N., Gizis J. E., Liebert J., Burgasser A. J., 2001, AJ, 121, 3235
Kleinman S. J. et al., 2004, ApJ, 607, 426
Knapp G. R. et al., 2004, AJ, 127, 3553
Knox R. A., Hawkins M. R. S., Hambly N. C., 1999, MNRAS, 306, 736
Kroupa P., 2001, MNRAS, 322, 231
Kumar S. S., 1963, ApJ, 137, 1121
Lachaume R., Dominik C., Lanz T., Habing H. J., 1999, A&A, 348, 897
Latham D. W., Stefanik R. P., Torres G., Davis R. J., Mazeh T., Carney B. W., Laird J. B., Morse J. A., 2002, AJ, 124, 1144
Lawrence A. et al., 2007, MNRAS, 379, 1599
Leggett S. K., Toomey D. W., Geballe T. R., Brown R. H., 1999, ApJL, 517, L139
Leggett S. K. et al., 2002, ApJ, 564, 452
Leggett S. K., Hauschildt P. H., Allard F., Geballe T. R., Baron E., 2002, MNRAS, 332, 78
Leggett S. K., 1992, ApJS, 82, 351
Levine J. L., Steinhauer A., Elston R. J., Lada E. A., 2006, ApJ, 646, 1215
Liebert J., Bergeron P., Holberg J. B., 2005, ApJS, 156, 47
Littlefair S. P., Dhillon V. S., Marsh T. R., Gänsicke B. T., Southworth J., Watson C. A., 2006, Science, 314, 1578
Liu M. C., Dupuy T. J., Ireland M. J., 2008, arXiv
Liu M. C., Leggett S. K., Chiu K., 2007, ApJ, 660, 1507
Lodieu N., Dobbie P. D., Deacon N. R., Hodgkin S. T., Hambly N. C., Jameson R. F., 2007, MNRAS, 380, 712
Lodieu N. et al., 2007, MNRAS, 379, 1423
Lodieu N., Hambly N. C., Jameson R. F., Hodgkin S. T., 2008, MNRAS, 383, 1385
Lodieu N., Hambly N. C., Jameson R. F., 2006, MNRAS, 373, 95
Lucas P. W., Weights D. J., Roche P. F., Riddick F. C., 2006, MNRAS, 373, L60
Luhman K. L., Rieke G. H., 1999, ApJ, 525, 440
Luhman K. L., Rieke G. H., Young E. T., Cotera A. S., Chen H., Rieke M. J., Schneider G., Thompson R. I., 2000, ApJ, 540, 1016
Luhman K. L., Briceño C., Stauffer J. R., Hartmann L., Barrado y Navascués D., Caldwell N., 2003, ApJ, 590, 348
Luhman K. L., Stauffer J. R., Muench A. A., Rieke G. H., Lada E. A., Bouvier J., Lada C. J., 2003, ApJ, 593, 1093

Luhman K. L. et al., 2007, ApJ, 654, 570
Luhman K. L., 2004, ApJ, 602, 816
Luhman K. L., 2007, ApJS, 173, 104
Magazzu A., Rebolo R., Zapatero Osorio M. R., Martin E. L., Hodgkin S. T., 1998, ApJL, 497, L47+
Mamajek E. E., 2005, ApJ, 634, 1385
Marley M. S., Seager S., Saumon D., Lodders K., Ackerman A. S., Freedman R. S., Fan X., 2002, ApJ, 568, 335
Marsakov V. A., Shevelev Y. G., 1995, Bulletin d'Information du Centre de Donnees Stellaires, 47, 13
Martín E. L., Basri G., Zapatero-Osorio M. R., Rebolo R., López R. J. G., 1998, ApJL, 507, L41
Martín E. L., Delfosse X., Basri G., Goldman B., Forveille T., Zapatero Osorio M. R., 1999, AJ, 118, 2466
Martín E. L., Rebolo R., Zapatero-Osorio M. R., 1996, ApJ, 469, 706
Maxted P. F. L., Napiwotzki R., Dobbie P. D., Burleigh M. R., 2006, Nature, 442, 543
McCaughrean M. J., Close L. M., Scholz R. D., Lenzen R., Biller B., Brandner W., Hartung M., Lodieu N., 2004, A&A, 413, 1029
McCook G. P., Sion E. M., 1999, ApJS, 121, 1
McGovern M. R., Kirkpatrick J. D., McLean I. S., Burgasser A. J., Prato L., Lowrance P. J., 2004, ApJ, 600, 1020
McLean I. S. et al., 2000, ApJL, 533, L45
McLean I. S., McGovern M. R., Burgasser A. J., Kirkpatrick J. D., Prato L., Kim S. S., 2003, ApJ, 596, 561
Metchev S. A., Hillenbrand L. A., 2004, ApJ, 617, 1330
Metchev S. A., Hillenbrand L. A., 2006, ApJ, 651, 1166
Miller G. E., Scalo J. M., 1979, ApJS, 41, 513
Mohanty S., Jayawardhana R., Huélamo N., Mamajek E., 2007, ApJ, 657, 1064
Mohanty S., Jayawardhana R., Basri G., 2005, ApJ, 626, 498
Monet D. G., Dahn C. C., Vrba F. J., Harris H. C., Pier J. R., Luginbuhl C. B., Ables H. D., 1992, AJ, 103, 638
Monet D. G. et al., 2003, AJ, 125, 984
Monteiro H., Jao W.-C., Henry T., Subasavage J., Beaulieu T., 2006, ApJ, 638, 446
Moraux E., Bouvier J., Stauffer J. R., Cuillandre J.-C., 2003, A&A, 400, 891
Muench A. A., Lada E. A., Lada C. J., Alves J., 2002, ApJ, 573, 366
Muench A. A. et al., 2003, AJ, 125, 2029
Mugrauer M., Seifahrt A., Neuhäuser R., Mazeh T., 2006, MNRAS, 373, L31
Mullally F., Kilic M., Reach W. T., Kuchner M. J., von Hippel T., Burrows A., Winget D. E., 2007, ApJS, 171, 206
Nakajima T., Oppenheimer B. R., Kulkarni S. R., Golimowski D. A., Matthews K., Durrance S. T., 1995, Nature, 378, 463
Napiwotzki R. et al., 2001, Astronomische Nachrichten, 322, 411
Napiwotzki R., Green P. J., Saffer R. A., 1999, ApJ, 517, 399
Nordstrom B. et al., 2004, VizieR Online Data Catalog, 5117, 0
Padoan P., Nordlund Å., 2002, ApJ, 576, 870

Panei J. A., Althaus L. G., Benvenuto O. G., 2000, A&A, 353, 970
Perryman M. A. C. et al., 1997, A&A, 323, L49
Perryman M. A. C. et al., 1998, A&A, 331, 81
Pinfield D. J., Dobbie P. D., Jameson R. F., Steele I. A., Jones H. R. A., Katsiyannis A. C., 2003, MNRAS, 342, 1241
Pinfield D. J., Jones H. R. A., Lucas P. W., Kendall T. R., Folkes S. L., Day-Jones A. C., Chappelle R. J., Steele I. A., 2006, MNRAS, 368, 1281
Pinfield D. J. et al., 2008, arXiv, 806
Pollack J. B., Hubickyj O., Bodenheimer P., Lissauer J. J., Podolak M., Greenzweig Y., 1996, Icarus, 124, 62
Potter D., Martín E. L., Cushing M. C., Baudoz P., Brandner W., Guyon O., Neuhäuser R., 2002, ApJL, 567, L133
Pravdo S. H., Shaklan S. B., Lloyd J., 2005, ApJ, 630, 528
Prialnik D., 2000, An Introduction to the Theory of Stellar Structure and Evolution. An Introduction to the Theory of Stellar Structure and Evolution, by D. Prialnik. ISBN 052165937X, Cambridge University Press, 2000.
Radigan J., Lafrenière D., Jayawardhana R., Doyon R., 2008, arXiv
Rebolo R., Zapatero Osorio M. R., Madruga S., Bejar V. J. S., Arribas S., Licandro J., 1998, Science, 282, 1309
Rebolo R., Zapatero-Osorio M. R., Martin E. L., 1995, Nature, 377, 129
Reid I. N. et al., 1999, ApJ, 521, 613
Reid I. N., Burgasser A. J., Cruz K. L., Kirkpatrick J. D., Gizis J. E., 2001, AJ, 121, 1710
Reid I. N., Gizis J. E., Kirkpatrick J. D., Koerner D. W., 2001, AJ, 121, 489
Reid I. N., Lewitus E., Allen P. R., Cruz K. L., Burgasser A. J., 2006, AJ, 132, 891
Reipurth B., Clarke C., 2001, AJ, 122, 432
Ribas I., 2003, A&A, 400, 297
Rocha-Pinto H. J., Scalo J., Maciel W. J., Flynn C., 2000, ApJL, 531, L115
Roxburgh I. W., 1989, A&A, 211, 361
Ruiz M. T., Leggett S. K., Allard F., 1997, ApJL, 491, L107+
Salpeter E. E., 1955, ApJ, 121, 161
Santos Jr. J. F. C., Piatti A. E., 2004, A&A, 428, 79
Saumon D., Marley M. S., Lodders K., Freedman R. S., 2003, in Martín E., ed, Brown Dwarfs. p. 345
Saumon D. et al., 2007, ApJ, 656, 1136
Scalo J. M., 1986, in de Loore C. W. H., Willis A. J., Laskarides P., eds, Luminous Stars and Associations in Galaxies. p. 451
Scholz A., Jayawardhana R., 2006, ApJ, 638, 1056
Scholz R.-D., McCaughrean M. J., Lodieu N., Kuhlbrodt B., 2003, A&A, 398, L29
Scholz R.-D., Lodieu N., Ibata R., Bienaymé O., Irwin M., McCaughrean M. J., Schwope A., 2004, MNRAS, 347, 685
Scholz A., Jayawardhana R., Brandeker A., 2005, ApJL, 629, L41
Schröder K.-P., Pauli E.-M., Napiwotzki R., 2004, MNRAS, 354, 727
Schuster W. J., Nissen P. E., 1989, A&A, 222, 69
Schwartz M. J., Becklin E. E., 2005, AJ, 130, 2352
Silvestri N. M., Oswalt T. D., Wood M. A., Smith J. A., Reid I. N., Sion E. M., 2001,

AJ, 121, 503
Sion E. M., Greenstein J. L., Landstreet J. D., Liebert J., Shipman H. L., Wegner G. A., 1983, ApJ, 269, 253
Skrutskie M. F. et al., 2006, AJ, 131, 1163
Slesnick C. L., Hillenbrand L. A., Carpenter J. M., 2004, ApJ, 610, 1045
Stark M. A., Wade R. A., 2003, AJ, 126, 1455
Steele P. R., Burleigh M. R., Dobbie P. D., Barstow M. A., 2007, MNRAS, 382, 1804
Stumpf M. B., Brandner W., Henning T., Bouy H., Koehler R., Hormuth F., Joergens V., Kasper M., 2008, arXiv
Tej A., Sahu K. C., Chandrasekhar T., Ashok N. M., 2002, ApJ, 578, 523
Thorén P., Edvardsson B., Gustafsson B., 2004, A&A, 425, 187
Tinney C. G., Delfosse X., Forveille T., 1997, ApJL, 490, L95+
Tinney C. G., Burgasser A. J., Kirkpatrick J. D., McElwain M. W., 2005, AJ, 130, 2326
Tinney C. G., 1998, MNRAS, 296, L42+
Tokunaga A. T., Vacca W. D., 2005, PASP, 117, 421
Tsuji T., Nakajima T., 2003, ApJL, 585, L151
Tsuji T., Nakajima T., Yanagisawa K., 2004, ApJ, 607, 511
Tsuji T., Ohnaka K., Aoki W., 1996, A&A, 305, L1+
Valenti J. A., Fischer D. A., 2005, ApJS, 159, 141
VandenBerg D. A., Stetson P. B., 2004, PASP, 116, 997
Warren S., Hewett P., 2002, in Metcalfe N., Shanks T., eds, A New Era in Cosmology. p. 369
Warren S. J. et al., 2007, MNRAS, 381, 1400
Weidemann V., 2000, A&A, 363, 647
Weights D. J., Lucas P. W., Roche P. F., Pinfield D. J., Riddick F., 2008, arXiv
West A. A., Hawley S. L., Bochanski J. J., Covey K. R., Reid I. N., Dhital S., Hilton E. J., Masuda M., 2008, AJ, 135, 785
Whitworth A. P., Goodwin S. P., 2005, Astronomische Nachrichten, 326, 899
Whitworth A. P., Stamatellos D., 2006, A&A, 458, 817
Wilking B. A., Meyer M. R., Robinson J. G., Greene T. P., 2005, AJ, 130, 1733
Wilson J. C., Kirkpatrick J. D., Gizis J. E., Skrutskie M. F., Monet D. G., Houck J. R., 2001, AJ, 122, 1989
Wright J. T., Marcy G. W., Butler R. P., Vogt S. S., 2004, ApJS, 152, 261
Yi S., Demarque P., Kim Y.-C., Lee Y.-W., Ree C. H., Lejeune T., Barnes S., 2001, ApJS, 136, 417
Yong D., Lambert D. L., 2003, PASP, 115, 796
Zapatero Osorio M. R. et al., 1998, in Rebolo R., Martin E. L., Zapatero Osorio M. R., eds, Brown Dwarfs and Extrasolar Planets. p. 51
Zuckerman B., Becklin E. E., 1992, ApJ, 386, 260